DEVELOPMENT OF CUBESAT ANTENNA SYSTEMS FOR IONOSPHERIC SOUNDING

By

GRAHAM KIRKBY MSci

A thesis submitted to

The University of Birmingham

For the Degree

DOCTOR OF PHILOSOPHY

Space Environment and Radio Engineering Group

Electronic, Electrical and Systems Engineering

College of Engineering and Physical Sciences

University of Birmingham

March 2018

ABSTRACT

There are many uses for space based VHF/UHF synthetic aperture radar (SAR) systems; however, there are significant obstacles which must be addressed to develop operational systems. One of these is the impact of the ionosphere on the relatively low frequency radar signal. To aid the design of future SAR satellites, the ionospheric propagation environment must be fully understood; however measurements of scintillation affecting the VHF/UHF signal, at sufficient bandwidth, have not yet been made. To address these issues the Wideband Ionospheric Sounder CubeSat Experiment (WISCER) is being developed. The satellite will quantify ionospheric distortion on a radar signal by transmitting a wideband (100MHz) sounder signal. Two antenna candidates have been analysed: the crossed Moxon and the conical helix antenna. Improvements to the crossed Moxon antenna design, yielding the WCM antenna, have led to an increase in bandwidth from 65 MHz to 105 MHz. A prototype of the conical helix antenna has been launched on a sub-orbital sounding rocket, providing a proof of concept and a de-risking flight opportunity for that antenna and its strain rigidisation. A trade-off analysis has been conducted to compare the two antenna candidates with the result that the WCM antenna is the preferred WISCER antenna.

To,

Jessica, Steven, Kay, Rachel, Sam and Rodney

ACKNOWLEDGEMENTS

The work undertaken in this thesis would not have been possible without the support and guidance of a wide array of people. Firstly, my parents have been a constant source of support and encouragement throughout my entire education. Without their lessons I would never have reached this point. They have inspired me whilst allowing me to follow my own unique interests and passions. My partner, Jessica, has provided me with unwavering support despite suffering the most. My gratitude for her patience and advice is infinite; I could not imagine a life without her.

I undertook my PhD within the Space Environment and Radio Engineering (SERENE) research group at the University of Birmingham after completing my Physics MSci there too. My experience at the university over the course of seven years has been truly amazing and has greatly transformed me into the person I am today. I would particularly like to thank Paul Cannon OBE, David Hoyland and Sean Elvidge for their advice and feedback on my work. Thanks also go to my fellow students James Churm and Chris Mannix for their advice, contributions and distractions.

Finally, I would like to thank my PhD supervisor Matthew Angling for his support, guidance and giving me the opportunity to work on an incredible project. To be able to test my ideas in milligravity was truly inspiring and I hope the whole department continues to be successful far into the future.

Contents

List of Figures

List of Tables

CHAPTER 1) INTRODUCTION

Synthetic Aperture Radar (SAR) satellites currently orbit the Earth, imaging the surface using several different frequencies for different applications. These applications are crucial to society and range from the monitoring of climate change to fulfilment of military defence. However, the Earth's atmosphere poses an obstacle to obtaining clear and focused radar images.

Ionising radiation from the sun liberates electrons from the neutral atoms of the upper atmosphere creating a region called the Ionosphere. These free electrons can then influence the propagation of radio waves through this region leading to distortions in a radar image. This phenomenon is dependent on frequency and so must be carefully considered before the launch of a new type of SAR satellite imaging in a new frequency range.

Currently, there is a desire to develop satellite based Foliage Penetrating (FOPEN) radar. This type of radar uses wideband transmission in the VHF/UHF radio frequency range to achieve the FOPEN effect. Unfortunately, these frequencies are heavily affected by the ionosphere and their propagation through it is not fully quantified. Of interest is the post sunset equatorial ionosphere due to the ionospheric structures in that region that cause the most severe degradation to radar signals.

To address these issues the Wideband Ionospheric Sounder CubeSat Experiment (WISCER) is being developed. The satellite will measure and quantify ionospheric distortion on a radar signal by transmitting a wideband sounder signal. This signal will propagate through the ionosphere and the one way distortion will be measured on the ground. The benefit of such a one way technique over a two way technique is that it does not require data storage and relay capacity on the highly restricted satellite platform, and

the resulting signal distortion is simpler to process and analyse having not been distorted by a reflection from the ground and a second pass through the ionosphere.

The objective of this work is to progress the design of the WISCER antenna to show that the space based system is viable within the limits of a 3U+ CubeSat. To achieve this, two antenna candidates have been analysed and optimised for the mission requirements: The crossed Moxon antenna and the conical helix antenna. The effect of these antennas on the host CubeSat has also been investigated with attention given to the attitude perturbations arising from the large antennas. Finally, a prototype of the conical helix antenna was launched on a REXUS sounding rocket, providing a proof of concept and a de-risking flight opportunity for that antenna (Figure 1).

Figure 1 shows the inflated conical helix antenna prototype during flight on the REXUS 19 sounding rocket.

CHAPTER 2) INTRODUCTION TO THE IONOSPHERE AND SPACE BASED SYNTHETIC APERTURE RADAR

2.1) Introduction

To fully describe the requirement of the WISCER mission as a precursor to a FOPEN SAR satellite we must first understand the ionosphere, its structure and its impact on the propagation of radio waves. This chapter will explain in detail these concepts and give a brief introduction to the principle of operation of a SAR satellite.

2.2) Ionosphere

During the initial design of any spacecraft, knowledge of the space environment is used to ensure the satellite will function as intended. The satellite itself must be shielded from damaging environmental effects, but it is also important to consider the satellite's radio frequency (RF) systems. Space environments can have a range of effects on a transiting signal causing distortion and/or degradation of signal strength. The ionosphere is one such environment that must be considered for signals passing from a satellite to the ground and vice versa.

The ionosphere refers to a region of the Earth's atmosphere that extends from approximately 50km to 1000km altitude (Knipp, 2011). Within these altitudes solar radiation generates a significant number of free electrons by ionizing atmospheric atoms and molecules. These ions and electrons will recombine and be replaced by newly ionized particles, thus an equilibrium density of charged particles is achieved dependent on the strength of the ionizing source. The ionosphere is an electrical conductor and so it can affect the passage of radio waves through it. Due to the energy requirements of such

ionization only photon energies at UV and higher frequencies can split the electrons from their parent atoms.

2.2.1) Structure of the Ionosphere

Ionospheric conditions vary with position above the Earth due to the varying levels of solar radiation that generate them. The vertical structure however is relatively stable, and a typical electron density profile is shown in Figure 2. The electron densities vary greatly with altitude allowing categorisation into four primary regions.

The first layer from 50km to 90km is called the D region and is created by hard x-rays that have penetrated all other layers of the atmosphere to reach this point. The electron density in this region is normally very low, however, so its effects are minimal under most circumstances. The electron density is low due to the high atmospheric density causing a high collision frequency and hence absorption rate. Ions and free electrons collide frequently and recombine quickly.

The second layer known as the E region has a higher electron density and occurs between the altitudes of 90km and 150km. The main ion contributors are O_2^+ and NO^+ (shown in Figure 2) and are generated by soft x-rays (1-10nm) and far ultraviolet radiation (122-200nm).

The third and fourth layers are called F1 and F2 which form the densest part of the ionosphere. The two layers are produced by the high flux of hydrogen Lyman alpha UV radiation (Chamberlain & Hunten, 1987) produced by the abundant hydrogen of the sun. The F1 layer extends from approximately 200km in altitude and transitions to the F2 region, which then ends at approximately 500km. The final region, the topside of the F2 layer, lies above 500km and is generated by ionization from extreme UV radiation. It has

no real upper boundary as the ionospheric plasma slowly transitions into the plasmasphere above it. Here atomic hydrogen and helium progressively replace oxygen as the parent atom for the free electrons.

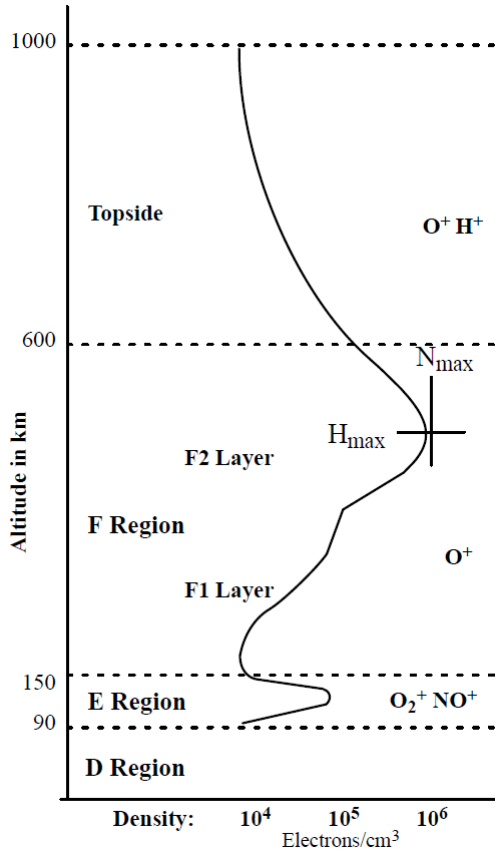

Figure 2. The vertical structure of the ionosphere from (Anderson & Fuller-Rowell, 1999).

There are four main regions of the ionosphere when differentiated by latitude. They are: the polar region (~75° to 90° North and South); the auroral region located (~60° to ~65° North and South), the mid latitudes (~35° to 55° North and South) and the equatorial region (0° to 30° North and South).

The polar regions connect directly to the solar wind, as the Earth's magnetic field lines extend vertically in this region. Some ionisation is therefore contributed by solar protons but EUV still contributes most significantly to the ionosphere's electron density. Due to this a seasonal variation of electron density is observed here. When sunlight is continuous

in the summer the electron density peaks but during the dark winter months it drops to very low values and is known as the polar hole. The uppermost layers of the ionosphere persist however due to the low recombination rates at that altitude and the extended periods of sunlight exposure.

The auroral region is the most well-known due to the visible light (i.e. the aurora) given off at altitudes of 90km to 150km but can be observed to extend to more than 500km (Kallenrode, 2004). This light is generated via impact excitation of oxygen and nitrogen by charged particles from the sun spiralling down from the magnetosphere. The magnetosphere here referring to the region around the Earth where its magnetic field is dominant over that of the sun and the solar wind. These impacts also cause ionisation contributing to the ions of the ionosphere at this latitude and above. The oval shaped auroral region expands, shifts and contracts as the energy state of the magnetosphere varies. The incoming particles are initially accelerated by reconnection events in the magnetotail. They are then accelerated to energies of greater than a few keV (Knipp, 2011) by voltage variations along the magnetic field lines, which they are being guided by, and impact the ionosphere. Electrons are the dominant source of auroral energy in calm conditions but during strong geomagnetic events protons can contribute a large fraction too. Due to this source of energy the electron density in the auroral ionosphere remains high even during the night.

The equatorial ionosphere (~0° to 30° North and South) is characterised by the strong electron density gradients found in this region. The Earth's equator receives the greatest incident flux of solar energy. Therefore, our instinctive expectation would be that we should observe the greatest electron density trailing the noon equator. We must however consider the Earth's magnetic field which is parallel to the surface at the nearby geomagnetic equator. Solar heating of neutral atoms lifts the ionosphere, forcing the

plasma to cross the geomagnetic **B** field lines. This generates an electric field (**E**=-**v**×**B**, where **v** is the velocity vector of the charged particles) that is orientated eastward during the day time. The overall result is a fountain effect where the ionosphere rises, and the embedded plasma is forced out north and southwards. This depletes the electron density at the magnetic equator and enhances it at approximately ±15° magnetic latitude as seen in Figure 3.

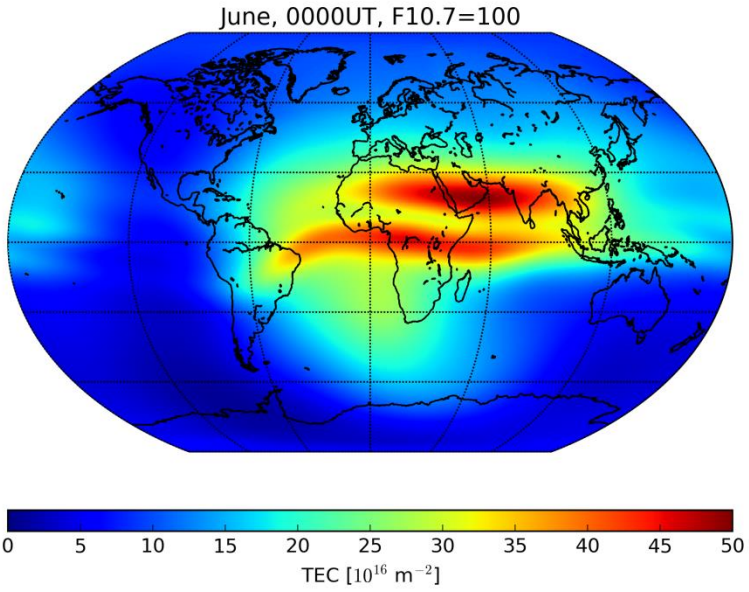

Figure 3.The figure shows an electron density map of the globe showing the effects of equatorial anomaly. The map was produced using the NeQuick Ionospheric model (Nava, Coisson, & Radicella, 2008).

Signals passing through the equatorial region are affected by both the strong electron density gradients and the turbulent time varying electron density distribution across the area. The mass relocation of plasma naturally causes patterns of uneven distribution and turbulence that result in a widely varying scale of structures (from tens of metres to hundreds of kilometres). These structures can scatter and/or scintillate the trans-ionospheric signals.

2.2.2) Variability of the Ionosphere

The electron density of the ionosphere can change significantly due to any change in the source of the ionization causing a shift in the equilibrium between ionization and recombination. Figure 4 shows how the diurnal and solar cycle variation in solar radiation affects electron density within the layers.

The diurnal cycle has the greatest impact. During the night the reduced ionisation leads to the almost complete loss of the E and D regions, and the merger of the of the F layers into single layer. Within these regions the electron density is a product of the equilibrium between the incoming ionising radiation and recombination due to ion-electron collisions. Without the sustained ionization provided by direct sunlight the high collision frequency quickly reduces the electron density at these altitudes. During the night the F1 and F2 layers become indistinguishable forming a single layer as the electron density reduces. In the F2 region and above, the atmospheric density is lower giving the electrons and ions much longer mean free paths (lower collision frequencies). They therefore have much longer lifetimes and response less to the diurnal cycle with increasing altitude.

Long term variation of the ionosphere also occurs due to the 11 year solar cycle. The increased EUV flux during solar maximum increases electron density whilst the reduced flux during solar minimum leads to a reduced electron density.

Short term ionospheric variability can be driven by solar flares which produce large bursts of x-rays and other high energy radiation. As this radiation reaches the ionosphere large fluctuations in electron density can be observed in the D and E layers. Variability can also be driven due to geomagnetic effects.

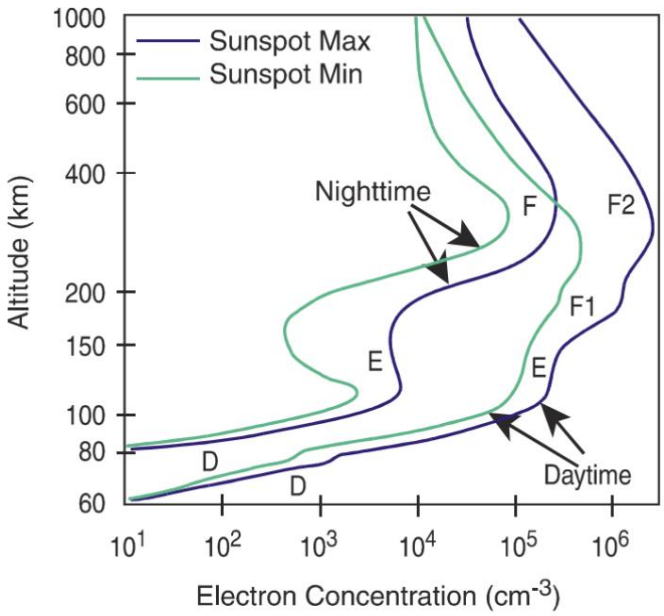

Figure 4 Graph showing the changing electron density of the ionosphere under solar and diurnal cycles. (Angling, Cannon, & Bradley, 2007)

Table 1 shows properties of the ionosphere and how they vary with the diurnal and solar cycles. The total electron content (TEC) given in Table 1 is the electron density, N_e, integrated along a line as given by Equation 1.

$$TEC = \int_{s_0}^{s_1} N_e ds,$$

Equation 1

It is a measure of the effect the ionosphere will have on a signal travelling along that line and is used to quantify the variability with time.

Ionospheric Parameter	**Diurnal (Mid-Latitude)**	**Solar Cycle (Daytime)**
N_{max}	1×10^{-1} to 1 electrons/m^3 Factor of 10	4×10^{-1} to 2 electrons/m^3 Factor of 5
Maximum Usable Over the Horizon Frequency	12 to 36 MHz Factor of 3	21 to 42 MHz Factor of 2
Total Electron Content	5×10^{16} to 5×10^{17} electrons/m^2 Factor of 10	1×10^{17} to 5×10^{17} electrons/m^2 Factor of 5

Table 1 Differences in properties of the ionosphere between day and night and solar cycle. (Anderson & Fuller-Rowell, 1999)

2.2.3) Radio Propagation in the Ionosphere

The ionosphere is an electrical conductor and therefore will affect radio waves passing through it. The waves interact with the free electrons in the ionospheric plasma and are attenuated, distorted and even for some frequencies completely reflected during their passage. The F layer contains the greatest electron density so if a radio signal can penetrate this layer it will continue to propagate out into space. Signals with frequencies below the plasma frequency of a particular ionospheric region however cannot penetrate it and are reflected. This reflection can be exploited in order to obtain increased range of HF (3-30MHz) radio frequencies and was heavily used for communications before the advent of satellite communications. However due to the variability of the ionosphere this is not a reliable method of communication. The highest frequency that can be effectively reflected by the ionosphere is related to the plasma frequency given by Equation 2 (where n is electron number density, e is the electron charge, ε_0 is the permissively of free space, m is the effective electron density and ω_p is the plasma frequency for electrons). As the electron density of the ionosphere varies with time this frequency limit therefore also varies. This can lead to interruptions in forms of communication that depend on this reflection, when they are no longer below the limit. Early ionospheric propagation predictions of this effect contributed to the prediction of the Sun's 11-year solar cycle (Bilitza, Rawer, Bossey, & Gulyeava, 1993).

$$\omega_p = \sqrt{\frac{ne^2}{\varepsilon_0 m}}$$

Equation 2

All trans-ionospheric signals below 2GHz are in some way affected by passage through the ionosphere (Xu, Wu, & Wu, 2004). As the frequency of the trans-ionospheric signal is

lowered the effects tend to increase. The key effects of the ionosphere on radio waves include Faraday rotation, group delay, dispersion and scintillation.

To aid in the understanding it is useful to describe the refractive index of a plasma, which is given by Equation 3 (where n_i is refractive index, n is electron density, e is electron charge, m_e is electron mass, ε_0 is vacuum permittivity, ω is angular frequency and the equation is the magnetic field free approximation). Electron behaviour dominates the refractive index of the plasma due to the electron's small mass compared to the ions. Increasing the electron density decreases the refractive index.

$$n_i = \sqrt{1 - \frac{ne^2}{\varepsilon_0 m_e \omega^2}}$$

Equation 3

Group delay occurs since the presence of charged particles, which are the primary driver of the plasma's refractive index, causes the signal propagation speed to slow down. The time delay difference between the free space travel time and the measured travel time is called the group delay t, which can be calculated from the TEC using Equation 4 (where f is frequency in MHz). Group delay times of 0.5 to 500ns have been measured for TEC values from 10^{16} to 10^{19} e/m^2 (ITU-R, 2007). One example of this effect is for single-frequency GPS receivers, where it is imperative to correct for the delay of the GPS signal as it propagates through the ionosphere from GPS satellites to the receiver on the ground.

$$t = 1.345 \, \frac{TEC(slant)}{f^2} \times 10^{-7}$$

Equation 4

As a consequence of the group delay magnitude depending on frequency, a wideband radar signal will experience dispersion during its transionospheric passage. The differential delay between the frequencies used is proportional to the integrated electron density along

the ray path. For a fixed bandwidth signal, the dispersion is inversely proportional to the frequency cubed and therefore it is key to consider dispersion for large bandwidth signals.

When propagating through the ionosphere, Faraday rotation is the measured rotation of a signal's plane of polarisation by a ground station compared to that with which it was transmitted. The effect arises due to the anisotropy of the ionospheric plasma combined with the presence of Earth's geomagnetic field. The angle θ of Faraday rotation, as given by Equation 5 (ITU-R, 2007), is dependent on the radio wave frequency f and the average magnetic field strength B_{av}. Due to this effect, many satellite systems use circular polarisation, as will WISCER.

$$\theta = 2.36 \times 10^{-14} \frac{B_{av} n_e}{f^2} \qquad \textbf{Equation 5}$$

The final and most problematic effect of the ionosphere is scintillation of the phase and amplitude of the transiting signal. Embedded within the ionosphere are electron density structures of varying scales. The differing electron densities expose the transiting signals to varying refractive indices on their path through the ionosphere. This causes differential diffraction (scattering) of the passing wave inducing phase variations along the phase fronts of the signal. Figure 5 shows this process and the resulting amplitude distortion that is the result of interference between the multiple scattered signals.

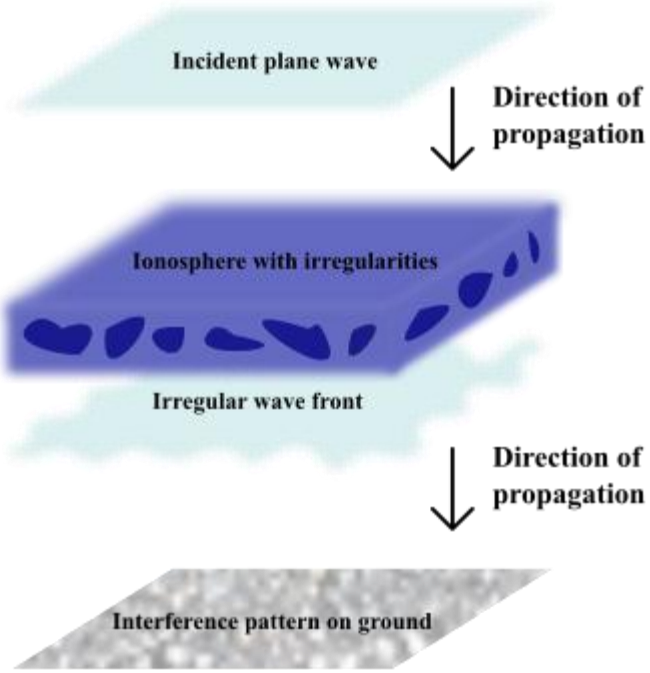

Figure 5. This diagram shows the effect of scintillation on a trans-ionospheric signal.

Scintillation is strongest in the F layer of the ionosphere between 250-400km and occurs most predominantly in the post sunset equatorial region but also occurs to some extent at high latitudes (e.g. auroral scintillation). The magnitude of scintillation levels is described using S4 (amplitude scintillation) and σ_φ (phase scintillation) (NOAA, 2019). These metrics are commonly used to predict how much distortion can be expected on a signal but do not contain the required information to determine the nature of the distortion process. Scintillation disturbances are intense for ultra-high frequency (UHF) and very high frequency (VHF) frequencies used by satellite communication (Groves et al., 1997) and foliage penetrating radar. It is the small scale irregularities in the ionospheric plasma that cause a loss of contrast in a radar image.

2.3) Space Based Synthetic Aperture Radar (SAR)

The potential future satellite system under consideration in this work is VHF/UHF space based radar. From our knowledge of the ionosphere we immediately see that it will have

an impact on image quality and must be taken into consideration during the early design stages of such a satellite to ensure minimum image requirements are met. The necessary measurements of the ionospheric effect on a wideband VHF/UHF radar like signal has not yet been investigated sufficiently to inform the design of such a radar satellite. The details of an experiment to collect this data will follow in subsequent chapters but first we must understand the operation of the radar system in question: a space based synthetic aperture radar (SAR).

Space based SAR, at different frequencies than those considered here, have been flown on many spacecraft for observation and mapping purposes. Such past space craft include: the Magellan Venus mapper (Saunders & Pettengill, 1991), the Advanced Land Observing Satellite (ALOS) with the PALSAR payload (JAXA & EORC, 2006) and ESA's Earth observer ENVISAT (Bruzzi, Louet, & Pfeiffer, 1995).

The resolution of any electromagnetic receiver is limited by diffraction at its aperture. If X/R (where R is the range to the objects to be resolved and X is the distance between them) is less than λ/D (where D is the receiver aperture and λ is the incident wavelength) then the two objects cannot be differentiated. For example, a radar satellite orbiting the Earth at 750km, equipped with a 10m aperture and using a 0.5m wavelength signal will have a maximum resolution of 37.5km.

The SAR processing technique aims to improve upon this resolution limit by making use of the relative motion of the radar system with respect to the target. This work does not require detailed knowledge of SAR processing and so it will not be explained fully here. It is however important to understand the basic principles behind the method in order to fully appreciate the nature of the experimental system requirements that will be given in chapter three.

There are two primary parts to the SAR process: improving range resolution and improving azimuthal resolution. The first, which is known as range vision, uses the fact that return signals that have reflected from targets at different ranges have different flight times. If short pulses are used the signal return delays can be measured, allowing the radar image to be plotted in the range axis. However very short powerful pulses are difficult to generate and so long coded pulses are used to emulate short ones via a pulse compression method (Stimson & Griffiths, 2014).

Ideally, we would point a radar system in the nadir direction (straight down) to eliminate shadowing but SAR forces us to maximise the range difference within our image to get good results. If two separate target objects have very similar or equal ranges, we cannot differentiate them. Unfortunately, even looking somewhat horizontally we still see this effect on slopes facing the incoming radar beam. The effect warps mountain peaks towards the radar due to the range not being as far as we would predict based on its horizontal position. The radar return from the slope is therefore overlaid at a single location creating a bright spot, which can be seen in Figure 6.

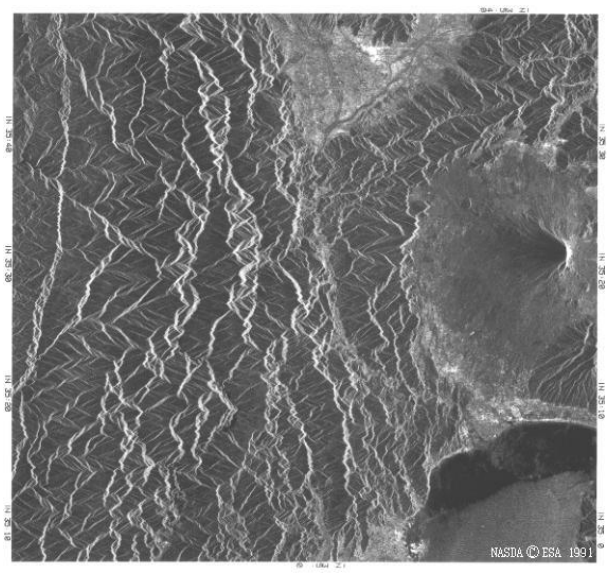

Figure 6. This figure is an SAR image captured by the European Remote Sensing Satellite No.1 (ERS-1) from an orbital altitude of 780km. Within the image is Mount Fuji, which shows clear signs of range distortion due to the steep slopes.

The second part of SAR processing addresses improving resolution in the azimuth direction. Figure 7 shows a diagram that illustrates this method where the distance L is the diffraction limit length for the radar system. As a SAR system travels the length L it emits a series of pulses, the distance between the points at which they were transmitted being p_a. Since we know the radar wavelength λ, the observation range R_0 and the width of the illuminated ground area L we can use the phase of the reflections to process the image and get better resolution than L.

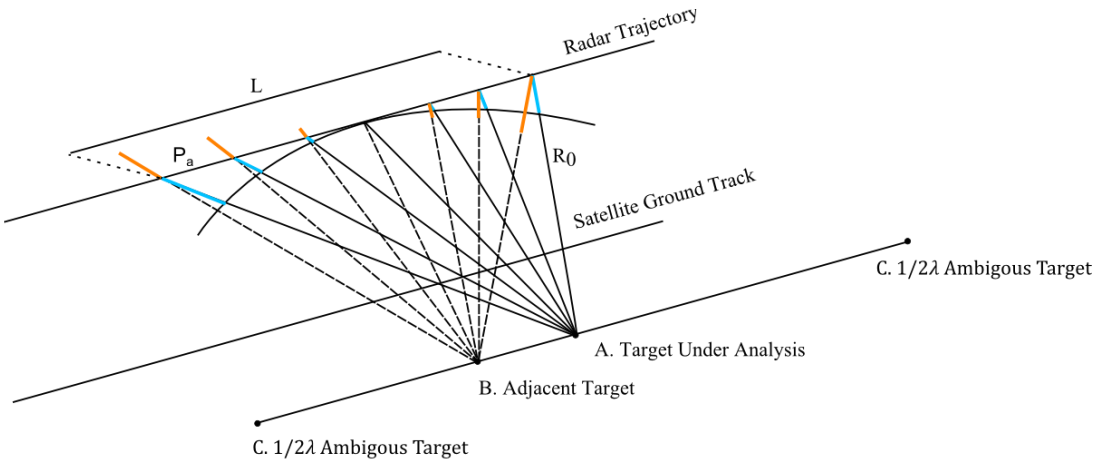

Figure 7. This is a signal path diagram that shows how adjacent azimuth targets are processed out of the SAR image using phase information.

Take target A in Figure 7; if we adjust the phases for the signal range to A, the signals from the target will combine constructively. Conveniently however, if we take Target B and perform the same adjustment the contributions from opposing sections of the trajectory cancel out. The condition for this destructive interference is that there is $\frac{1}{2}\lambda$ phase shift in the full round trip. If a full 2π phase shift, corresponding to a change in phase path of λ, occurs during the signal's flight the processing will treat that signal no differently than the signal from A. These ambiguous C target locations are shown in Figure 7. These two constraints combine to give Equation 6 and then using the diffraction limit relationship we see in Equation 7 that p_a should be equal to half the aperture diameter. This result is counter intuitive as it means that smaller antennas get better azimuth resolution (Pillai, Li, & Himed, 2008).

$$p_a \geq \frac{\lambda R_0}{2L}$$

Equation 6

$$p_a = \frac{D}{2}$$

Equation 7

From Equation 7 we also note that resolution does not depend on range. The amount of processing required does however depend on range due to the number of necessary samples equalling L/p_a (which can also be expressed as $2\lambda R_0/D^2$). The azimuth processing also introduces a time resolution limit. As the method combines measurements from all the pulses performed whilst the radar travels the distance L, transient targets that take place within this time frame are not resolved. For satellites with L of 5km this time frame is only 0.6 seconds due to their high speed.

As described in the previous section scintillation caused by the ionosphere results in distortion to the phase and amplitude of a radio signal passing through the ionosphere. Due

to the phase information based processing technique used by SAR it is particularly susceptible to these distortions. An example of the effect scintillation has on a SAR image can be seen in Figure 8 where two images of the same location are compared. Scintillation acts to reduce contrast and distort the image with the interference pattern generated by the ionospheric structures. The scintillation of phase is particularly damaging to the azimuthal processing technique. The phase alterations caused by the ionosphere obscure the original phase of the signal and therefore remove the information being used to locate the target within the final image. However, if the channel impulse response is known or can be predicted to some degree of accuracy these effects can be accounted for and potentially significantly reduced (Mannix, Belcher, Cannon, & Angling, 2016) (Mannix, Belcher, & Cannon, 2014) (Mannix, 2016).

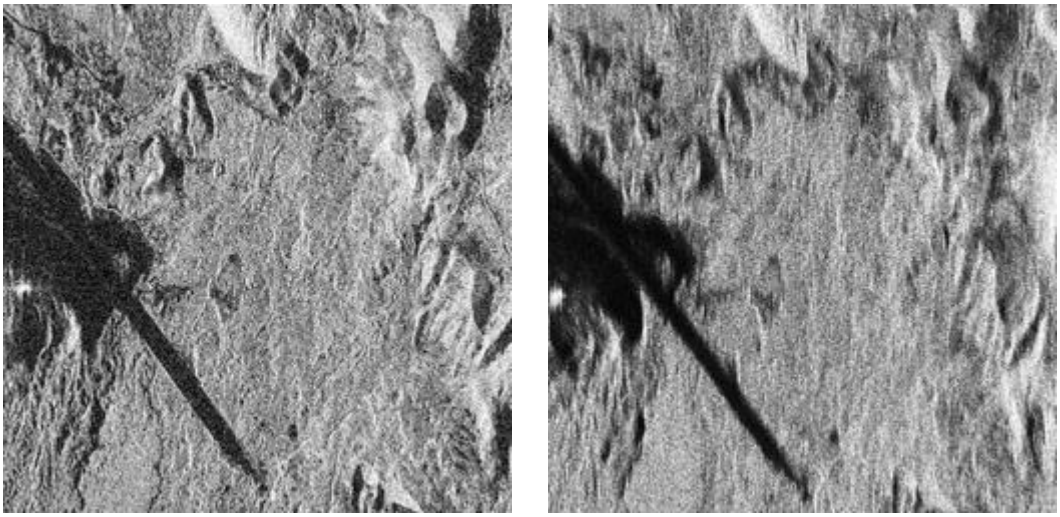

Figure 8. Images from the JAXA SAR satellite PALSAR. (Left) This image was taken during a period with minimal scintillation distortion. (Right) This is an image of the same landscape with scintillation effects present. Note the blurring and loss of contrast (C. Mannix, 2016).

If UHF/VHF radio waves are used on a SAR system, the ability to make foliage penetrating observations becomes a possibility due to the transparency of foliage at these frequencies. However, the ionospheric distortion of these signals is significant and has not been fully characterised. Distortions also arise from foliage attenuation and internal clutter motion (Davis, 2009) but foliage characterization makes use of these distortions in order to

identify the type of foliage present (Quegan et al, 2012). This technique makes possible new global measurements of vegetation.

2.4) Conclusions

In this chapter the ionosphere and its structure have been introduced in order to provide a foundation of understanding for the challenges of implementing a FOPEN SAR satellite. During the design process for WISCER it is imperative that these ionospheric impacts are understood and that the experiment is designed in such a way as to generate accurate measurements of the relevant distortions. In the next chapter, when outlining the intended method of operation for WISCER, previous ionospheric measurement campaigns will be reviewed to inform the design.

CHAPTER 3) INTRODUCTION TO CUBESATS AND WISCER

3.1) Introduction

A basic CubeSat is a 10cm cube satellite with a maximum mass of 1.33kg. This basic unit can then be repeated to make larger CubeSat versions. The aim of the CubeSat specification is to provide a standard design for picosatellites that reduces their cost and development time (Munakata, 2009). This provides a viable platform for technology demonstration and an array of scientific measurements. The Wideband Ionospheric Sounder CubeSat Experiment (WISCER) will use a 3U+ (10x10x34cm plus top hat section) CubeSat. The following chapter introduces the CubeSat platform in detail and describes the WISCER concept.

3.2) History and development of CubeSats

CubeSats have opened up access to space for low cost projects. This is shown by the long list of countries for which a CubeSat has been their first national satellite. For example, Swiss cube-1 was Switzerland's first satellite and was launched by the Indian space agency (ISRO). It demonstrated an atmospheric sensor, which measured air glow of Earth's upper atmosphere.

The CubeSat project first started in 1999 at California Polytechnic State University (Cal Poly). The CubeSat project evolved out of the OPAL project at Cal Poly. Whilst we will not list the primary objectives of the OPAL mission here, one of the goals of OPAL was to deploy small daughter satellites. These picosatellites measured 10.1 x 7.6 x 2.5cm and lead to an investigation into what the size of the smallest practical free flying satellite could be. Difficulties in designing the ejection system for OPAL lead to the selection of a 10cm cube

being optimal for a CubeSat. This simplified the ejector to a 10x10cm pusher plate with a spring loaded door. This design was the start of the Poly-PicoSatellite Orbital Deployer (P-POD) which is in current use for CubeSat deployment at the time of writing.

The first CubeSat was launched in 2003 on a Russian Eurockot and 75 had been launched by 2012. On 4th Oct 2012, the first CubeSats were launched from the ISS after being delivered to the station by a resupply mission. CubeSat payloads were predominantly academic until 2013 but the majority from 2014 onwards have been commercial (Swartwout, 2017). While writing this thesis 292 CubeSats were launched taking the overall total to 753 as of July 2017, showing the dramatic adoption of this satellite class.

One strength of CubeSats is their relatively inexpensive nature. This allows for large constellations of these satellites to be flown and a wide array of applications to be exploited for both scientific and commercial purposes. One such scientific constellation is the QB50 project. The aim of this project is to launch 48 (planned capacity of 50) CubeSats which will make in-situ measurements of the lower thermosphere (90-350km). Each QB50 CubeSat will have its own unique payload but also carry one of three thermospheric measurement experiments. One third of the CubeSats will carry an Ion-Neutral Mass Spectrometer (INMS), one third will carry a Flux φ Probe Experiment (FIPEX) and the final third will carry a Multi-Needle Langmuir Probe (m-NLP). All the CubeSats will also carry thermistors/thermocouples/RTD (TH) to measure temperature. The orbits of all the CubeSats will be closely monitored to investigate thermospheric drag and re-entry dynamics.

The largest commercial constellation to date is operated by Planet Labs. Their business model makes use of many CubeSats in low polar orbits to image the entire Earth every 24 hours. Each one of the CubeSats is known as a "Dove" with "Flocks" being deployed at

regular intervals to account for system failure and re-entry losses. Low orbits at first appears to be a disadvantage; however, this low altitude allows for similar image resolution to that of larger satellites but with much smaller and cheaper equipment. The programme is ongoing with 32 Doves having been launched as of 2016.

CubeSats, mainly the larger sizes, are also now finding use in deep space making use of spare payload capacity on probes. For example, the twin MARCO CubeSats will provide additional communications relay during the atmospheric entry of the Insight Lander on Mars.

3.3) Current specification

The current design specification for all CubeSat sizes is given by CDS REV13 (Munakata, 2009). The basic 10cm cube is known as a 1U CubeSat, with the larger versions of 1.5U, 2U, 3U, 3U+ and 6U in common operation. The primary purpose of the specification is to provide information on the interface between the CubeSat (responsibility of the operator) and the Launcher (responsibility of the launch provider) in order to minimise the risk of damage or failure to the launcher or primary satellite payload. The standardised restraint and deployment mechanism is the Poly Picosatellite Orbital Deployer (P-POD) and is shown in Figure 9. A spring loaded door restrains the CubeSats and the pusher spring until the correct orbit has been achieved. Access panels provide access to the CubeSats prior to launch.

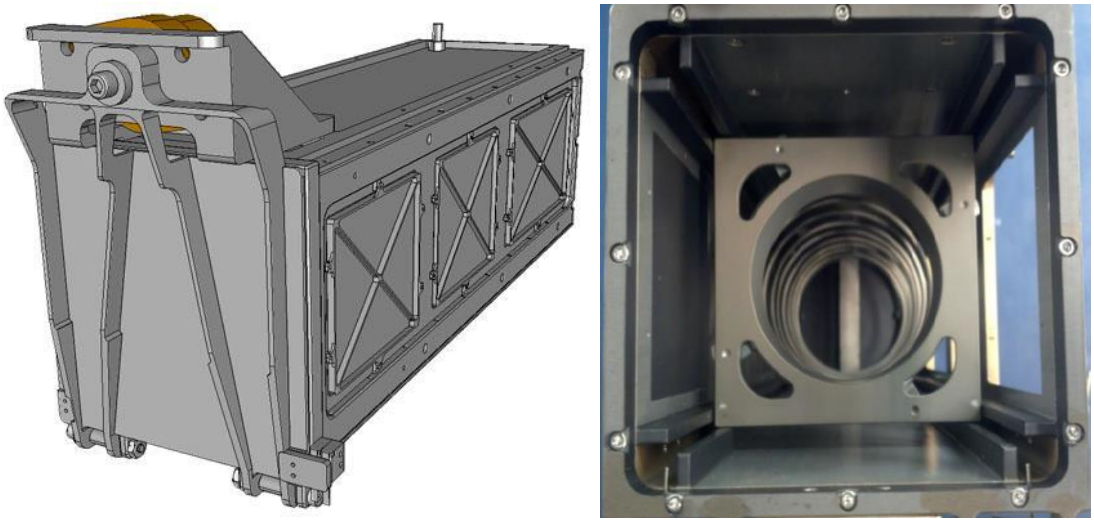

Figure 9 shows the P-POD CubeSat deployer used to eject the CubeSats once the correct orbit has been achieved. The standard P-POD deployer is capable of holding up to a 3U+ CubeSat or any complete combination of the smaller sizes (Munakata, 2009).

This work will focus on the 3U+ CubeSat size, since this will be used by WISCER. This is due to it being the largest size that fits within the most common P-POD deployer. To further explain this decision, it is important to note that most CubeSats are secondary payloads on launch vehicles. This means that their deployment can only take place once they pose no threat to the success of the primary payload. This often dictates that secondary payload deployment occurs after the successful deployment and clearance of the primary. Generally, the upper stage of the launch vehicle does not perform orbital adjustment manoeuvres due to limits on engine re-starts, delta-V and navigation systems. From this we can see that ensuring that the CubeSat is compatible with as many launch vehicles as possible creates the greatest opportunity for deployment into the optimum orbit.

Figure 10 shows a schematic of the 3U+ CubeSat. The 3U+ specification is largely identical to the 3U design except for the addition of the top hat that fits within the compressed pusher spring prior to deployment. Both the 3U and 3U+ have a maximum mass of 4kg and are required to have their centre of mass within 7cm of the CubeSat's

geometric centre. It is important to note, within the CDS REV13 (Munakata, 2009), that the CubeSat will be powered down (via a deployment trigger switch) whilst it is within the P-POD. Diagnostics and charging can take place whilst the CubeSat is in the P-POD, but the CubeSat will not activate until deployment. Therefore, under standard operation there is no pre-launch telemetry and post-deployment contact comes at a minimum of 45 minutes after deployment due to transmission restrictions. This method of operation significantly simplifies the P-POD device and, since it is unlikely a secondary payload can scrub a launch attempt, ground telemetry in this situation is unnecessary.

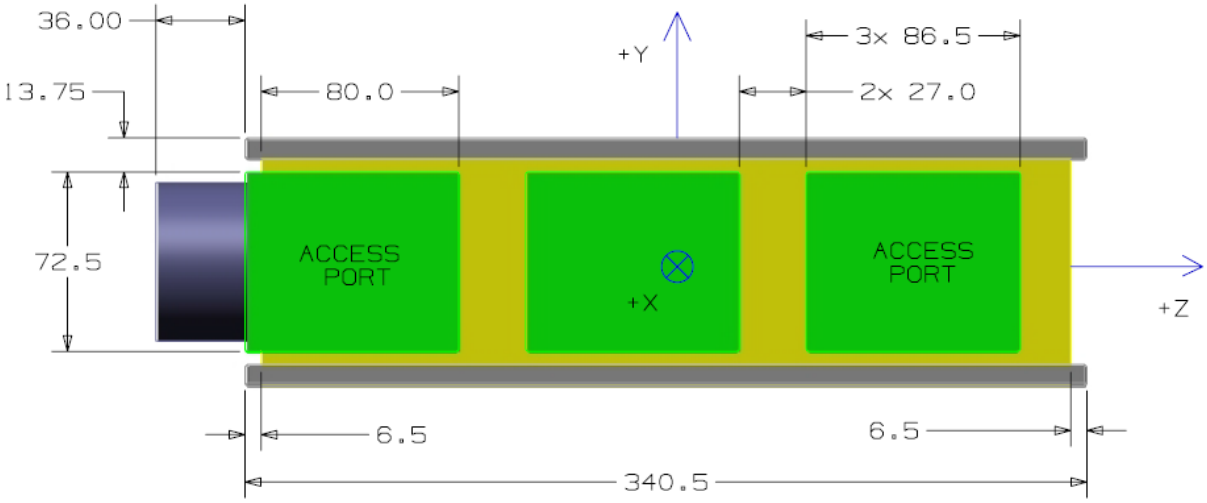

Figure 10 shows a diagram of the 3U+ CubeSat form factor to be used by WISCER. The dimensions given are in mm (Munakata, 2009).

3.4) Wideband Ionospheric Sounder Experiment (WISCER)

The previous sections of this chapter have introduced the concept and uses of CubeSats. Here the CubeSat mission specific to this work is introduced. This section will describe the overall WISCER mission and aims, then go on to give the specific objectives of this project.

There are a wide range of potential uses for space based VHF/UHF synthetic aperture radar (SAR) systems however; there are significant obstacles which must be dealt with in

order to develop an operational system. One of these obstacles is the impact of the ionosphere on the relatively low frequency radar signal. In order to mitigate this impact, and aid the design of future SAR satellites, it must be fully understood. Measurements of scintillation affecting the VHF/UHF signal, at sufficient bandwidth, have not yet been made.

Preliminary studies have been conducted using ground radars and calibration spheres, but further information can be obtained using a CubeSat as the transmit end of a wideband radio sounder. The wideband signal propagates through the ionosphere and the distortion is measured at a ground station. This configuration removes the problems of limited on-board data storage and data downlink rate.

WISCER will be comprised of a wideband (approximately 100MHz) beacon operating at a centre frequency of approximately 450MHz. In combination with a ground station, the system will measure the channel impulse response (CIR) of the post sunset equatorial ionosphere. The post sunset equatorial ionosphere is of interest due to the prevalence of small scale ionospheric structure that can cause scintillation of the trans-ionospheric signal. Such scintillation impairs the performance of SAR (see chapter 2). WISCER would operate for one year providing significant data across a range of time scales and conditions.

The signal transmitted from the WISCER antenna should be representative of the generated signal (e.g. minimise antenna dispersion), with a homogeneous forward gain (smooth angular variation within ±3dB), for simple recovery of the ionospheric data by the ground station. Some gain is also desirable due to the constrained power of the system. However, the pointing capability of the satellite platform is likely to be limited due to the CubeSat mass and volume budgets. Therefore, the WISCER antenna must provide a

smooth gain pattern over a wide angle. These factors have led to relatively large novel antenna designs for the CubeSat. Preliminary work led to the down selection to two candidate antennas: the conical helix antenna and the crossed Moxon antenna. These antenna candidates will be described in detail in chapters 6 and 7.

3.4.1) Measuring the Ionosphere with the WISCER satellite

The aim of the WISCER experiment is to measure the ionospheric disturbance on a wideband UHF/VHF SAR radar signal. These measurements will allow for the evaluation of the viability of such a system and allow insights into the issues that will need to be overcome in its implementation. A benefit of the current WISCER design is that the ground station will then receive the signal as WISCER passes overhead to make the measurements, thus eliminating the need to download large amounts of data from the satellite.

The effect of any transmission medium can be described by the complex impulse response (CIR). (Cannon, Groves, Fraser, Donnelly, & Perrier, 2006) developed and implemented a method to make measurements of the ionospheric CIR at bandwidths of 7 MHz and 18MHz at VHF and UHF frequencies respectively using the ARPA Long-Range Tracking and Instrumentation Radar (Altair) at the Ronald Reagan Ballistic Missile Defence Test Site (RTS). This was achieved using a 42m diameter dish with a power input of 6MW and using orbiting calibration spheres to reflect the signal. However, these bandwidths are significantly smaller than the 100MHz that would be implemented on a space based SAR system. In order to design a future FOPEN SAR satellite, accurate measurements of a much wider bandwidth signal are required. Applying the method used by (Cannon et al., 2006) the signal spread in the delay and Doppler domains can be determined from the CIR by calculating the channel scattering function (Angling et al., 1998).

A complete description of the method will not be repeated here since for the design and optimisation of the WISCER antenna we only need to know the characteristics of the signal to be transmitted. The measurement method requires the production of a deterministic signal which uniformly occupies the channel bandwidth. The deterministic signal will be a pseudo-random (PN) bit sequence, which is spectrally shaped to ensure it remains within the required band limit and then PSK modulated onto a baseband carrier. This baseband signal is then mixed up to the required transmission frequency. The resulting signal is then amplified and fed to the antenna. The antenna, therefore, sees a continuous pseudo-random signal spanning the required frequency band. When the PN bit sequence is received on the ground it is pulse compressed, compared to the original and any changes in the signal record the effect of the ionosphere. It is immediately apparent therefore that the antenna should both preserve the pulse of the signal (minimise distortion). Repeated measurements of the signal may then be used to probe the complete characteristics of the post sunset equatorial ionospheric propagation channel.

In order to make these measurements whilst operating within the capabilities of the CubeSat platform the satellite antenna must meet the requirements shown in Table 2. These requirements were determined in a prior study (Angling et al., 2013).

Reference	Requirement	Notes
REQ-ANT-01	Antenna signal should be circularly polarised.	To avoid Faraday losses
REQ-ANT-02	Antenna shall have bandwidth greater than or equal to waveform bandwidth (min 60MHz).	The waveform bandwidth will preferably be 100MHz. (For the conical helix antenna, see section 6.3.1 & 6.5.3. For the WCM antenna, see section 7.5 and the development work in chapter 7)
REQ-ANT-02b	Antenna transmit power should not vary by more than 3dB across the operational bandwidth.	Data analysis will be more complex if the transmitted signal strength varies strongly with frequency. (For the conical helix antenna, see sections 6.3.1 & 6.5.3. For the crossed WCM antenna, see section 7.5)
REQ-ANT-03	Antenna gain pattern shall not vary by more than 3dB across the operational forward beam width.	CubeSat attitude determination and pointing accuracy are limited. Measurement accuracy will be impacted if signal strength varies strongly with satellite attitude.
REQ-ANT-03b	Antenna -3dB beam width shall be greater than the combined 3σ error of attitude determination and pointing accuracy.	Receiver should remain within the beam footprint despite attitude errors. (For pointing accuracy predictions, see section 5.4)
REQ-ANT-04	Antenna dispersion should be less than 0.02μs across the operating bandwidth.	This is required to limit multipath spreading of the correlation peak. If this value cannot be met, some form of equalisation will be required. (See section 6.3.1 and section 7.5)

Table 2 Antenna requirements for the WISCER CubeSat mission.

3.4.2) WISCER development objectives

The primary objective of this work was to progress and investigate the candidate antenna concepts in order to best inform the final selection. In order to achieve these primary objectives a four step plan was executed:

1. Simulate and prototype candidate antennas in order to determine their performance with respect to the WISCER requirements.

2. Simulate the overall system performance for each candidate antenna in order to perform a trade-off analysis. (Attitude and orbital disturbances were covered by this work).

3. Investigate broadening the bandwidth of the narrowband crossed Moxon candidate antenna.

4. Undertake in flight validation of the riskier deployment method for the conical helix antenna type.

Completion of these steps would allow for an informed down selection to one of the candidate antennas going forward into the final satellite design phase.

The WISCER payload does not place any specific requirement on the host satellite, the choice of a CubeSat was purely to ensure minimal required development time and cost. The UKube platform by Clyde Space, shown in Figure 11, was chosen as the initial design reference platform. The UKube platform acts as the satellite bus providing all necessary support services to the experiment payload. Using this approach allows the WISCER experiment and payload interface design to be completed independently of the satellite bus, meaning that any other sufficiently large CubeSat capable of achieving the necessary interface requirements can be used.

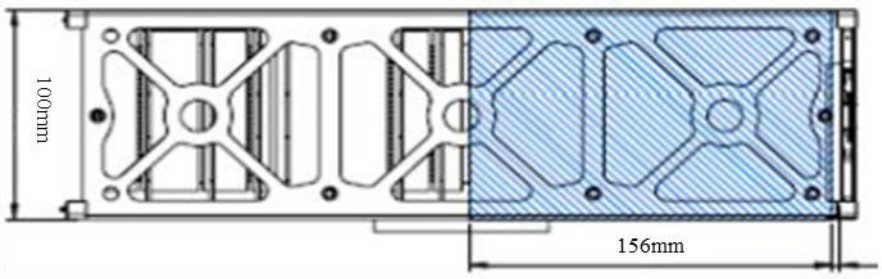

Figure 11 shows that UKube service module to payload split. The UKube platform was used as the starting design reference for WISCER concept validation.

The challenge imposed by the selection of the CubeSat standard for WISCER is the limited available volume and power. One goal of this work was to show that a sounder payload that met the requirements for the WISCER experiment could fit within these budgets.

3.5) Key subsystems

In this section the key subsystems of WISCER, listed below, will be outlined and the requirements upon them discussed. When considering viable antenna candidates, the volume budget of the highly restricted CubeSat form factor is of key importance. If the remaining volume after allocation to critical subsystems is insufficient to store the deployable antenna during launch, that antenna is not a viable option. Many key sub-systems are all readily available as inter-compatible COTS products from companies such as Clyde Space Ltd, for example:

- Power generation and conditioning system,
- Attitude control system,
- Communications system (making use of the primary antenna),
- Experiment payload,
- Thermal control system.

Solar panels and power conditioning units are a staple of the satellite industry including CubeSats. A wide array of deployable solar panels are commercially available providing good design flexibility whilst meeting the power budget requirement. Utilising triple deployable solar panels Clyde Space Ltd can offer a peak power generation rate of 55W at the time of writing (ClydeSpace, 2018b).

Attitude control is again a common product and fully integrated attitude determination and control systems in multiple configurations are available (CubeSat Shop, 2018).

Communications are a crucial system for all CubeSats and, despite the sounder experiment setup, WISCER would be no exception. Health checks, sounding campaigns and fault recovery are just a few of the critical tasks an on-board communications system will be required to achieve. As the primary WISCER antenna functions at frequencies applicable for communication it is expected that the antenna will be used for both the sounding work as well as communications.

Most CubeSats make use of passive thermal control due to their small size and limited power budgets. WISCER however will require the use of an inefficient class A power amplifier which will generate significant heat during the sounding transmissions (Angling et al., 2013). In order to prevent overheating, it is expected that a bespoke heat sink will be required. Preliminary thermal modelling of such a system will be detailed in chapter 8.

3.6) Review of relevant CubeSat missions with deployable antennas

The ability to fly large antennas on a CubeSat has a wide range of potential applications. It is, therefore, a topic of ongoing research within the field. Basic tape spring dipole antennas are used on almost every CubeSat with standard communication requirements, due to their reliability, simplicity and essentially omnidirectional radiation pattern. However, due to the low gain this antenna type limits CubeSats to only operating in low Earth orbit unless a relay satellite can be used.

To overcome this problem a highly directional reflector antenna has been proposed (Babuscia et al., 2013), with further testing of the design being completed during the course of this thesis (Babuscia et al., 2014). The antenna design uses a reflector setup but

makes use of a novel inflatable shape to achieve the correct reflector curvature. As for the WISCER conical helix antenna, it is therefore critical to maintain this curvature despite micrometeorite impacts, material relaxation and attitude disturbances. To limit the antenna radiation losses the mass and material of the inflatable membrane between the reflector and the CubeSat are carefully controlled. This precludes the use of other proposed rigidisation techniques such as resin based methods. A continual supply of gas has been suggested (Babuscia et al., 2013) as a means by which to maintain the reflector shape and counteract the leak rate. This obviously leads to a finite antenna lifetime based on gas reserves but is an appealing option due to its simplicity and flexibility. If the initial inflation did not achieve the correct shape, a second inflation with the gas reservoir could be used to attempt to correct the problem.

Inflatable deployment methods have been proposed for a wide variety of applications, including quite commonly truss and boom segments. A complete summary and description of recent work in this area is presented by Schenk et al. (2014).

An alternative to inflatable deployments are complex mechanical methods. Such techniques build on the commonly used tape spring designs by developing increasingly complex deployment patterns. Background and an example of a conical helix antenna design are presented by Olson et al. (2012) and Sakovsky et al. (2015) respectively. These designs have the advantage that once deployed they are stable and they do not require the gas generation system of an inflatable design, but they are susceptible to potential deployment failures due to snagging of their many components.

3.7) Conclusions

In order to ensure an appropriate design for future FOPEN SAR satellite the ionospheric distortion effects on the radar signal should be understood and quantified. Previous experiments have provided initial results towards this goal, but with a maximum bandwidth of 18MHz these results are not representative of a much wider (~100MHz) SAR signal. The WISCER method is proposed to achieve the necessary bandwidth and measurement resolution, whilst reducing the analysis complexity due to the single transionospheric pass.

This thesis will specifically look at the antenna design optimisation needed to achieve the mission goals. A full system level approach, including the interaction and optimisation of the antenna with the CubeSat systems will be considered. Particular attention will be given to the attitude perturbations generated by the large deployable antenna required for the directional UHF signal. The next chapter will detail the relevant antenna theory needed to investigate these areas before results are presented.

CHAPTER 4) ANTENNA THEORY

4.1) Introduction

The requirements for the WISCER antenna were laid out in Table 2. These requirements lead to the necessary parameters the antenna system must have, to successfully complete the proposed experiment. The problems specific to the WISCER mission, that are relevant here, are summarised below:

- Limited volume for the stored antenna
- Desire to minimise antenna size to minimise attitude disturbance torques
- Desire to minimise antenna mass
- Desire to maximise antenna power efficiency
- Desire to maximise antenna bandwidth (at least 100MHz).

4.2) Antenna electromagnetics

To design an antenna that meets, or potentially exceeds, these needs we must first understand the antenna theory and verification techniques for suitable antennas.

Gauss' law for electricity

$$\nabla \cdot \boldsymbol{E} = \frac{\rho}{\varepsilon_0}$$ **Equation 8**

Gauss' law for magnetism

$$\nabla \cdot \boldsymbol{B} = 0$$ **Equation 9**

Faraday's law of induction

$$\nabla \times \boldsymbol{E} = -\frac{\partial \boldsymbol{B}}{\partial t}$$ **Equation 10**

Ampere's Law

$$\nabla \times \boldsymbol{B} = \mu_0 \boldsymbol{J} + \mu_0 \varepsilon_0 \frac{\partial \boldsymbol{E}}{\partial t}$$ **Equation 11**

The most basic description of an antenna is a device that converts electrical oscillations into electromagnetic radiation and vice versa. To understand the process by which this is achieved we turn to the mathematical description of electromagnetism provided by Maxwell's equations. These equations, given in their vector-differential form in Equation 8 to Equation 11, completely describe electromagnetism. The first two equations describe the divergences of electrical and magnetic fields. When looking at inertial fields this helps us to understand how electric fields, created by charged particles, behave. The second two equations are very useful for understanding the principles of antennas. In vector differential notation they describe how the curl (a mathematical description of rotation in a vector field) in one of the fields is generated by a change in the opposing field. Equation 11 states Ampere's law which describes how a magnetic field is generated around a flowing current. From Equation 11 and Equation 8 we note that to maximise the generated EM fields (and hence the amplitude of the radiated EM wave) we must maximise the current and charge distributions of the antenna elements.

4.3) Antenna simulation methods

Analytical solutions for Maxwell's equations are essentially impossible for all but the simplest antennas. Modern computing capability, however, has enabled the use of finite element models for accurate predictions of even complex antenna geometries. The modelling software selected for use in this thesis is Computer Simulation Technology – Microwave Studio (CST MWS). Specifically, the transient (also known as time domain (TD)) solver is used due to its applicability for wideband antennas. There are three other available antenna simulation solver methods available within CST MWS. Both the ray

tracing and integral solvers are not applicable for WISCER due to the wideband nature and complex antenna geometry. The third is the frequency domain (FD) solver which, as the name suggests, operates in frequency space. Due to this, the simulation becomes computationally expensive for wide bandwidths due to the necessity to compute for individual frequencies across the frequency band of interest. Both the FD and TD methods use a Yee grid mesh which unfortunately does not lend itself well to the complex geometry and multi-scale structure of the conical helix antenna. In order to capture the detail and make accurate antenna performance predictions a fine mesh with many cells is required. In this situation the TD method is preferred as it is the computationally less costly of the two. As the method works in the time domain it also lends itself well to producing the dispersion results important to the mission objectives of WISCER.

4.4) Narrow band antennas and the simple dipole

To understand the wideband antennas to be used by the WISCER experiment we must first understand the basic principles of antennas and their simplest designs.

Narrowband antennas make use of a resonance condition within the antenna in order to radiate efficiently. The driving signal and the resonating signal in the antenna arms are in phase producing large voltages that radiate radio frequency (RF) waves strongly. The voltage and current distributions during the peaks are shown in Figure 12 for a dipole antenna. In order to achieve this resonance condition, the physical dimensions of the antenna elements are carefully controlled. The desired frequency of operation is used to calculate the antenna arm length required to match the standing wave condition. This leads to a real impedance value for the antenna at this frequency. If the source used to drive the antenna is matched to this impedance (or the antenna is designed to match the source impedance) then maximal power is delivered to the antenna.

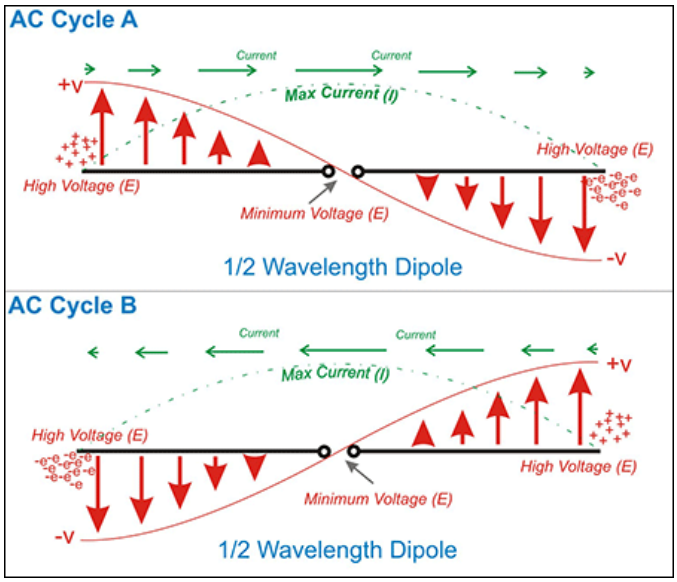

Figure 12 shows the voltage and current distributions of a 1/2λ dipole antenna (Turner, 2018).

4.5) Antenna Q value

An important quantity for comparison of antennas is the Q value. The Q value of an antenna is a measure of the bandwidth of the antenna (considering the centre frequency). It allows for the comparison of antennas, when a range of frequencies are required during operation. The defining equation of Q is given in Equation 12 where f_c is the centre frequency, f_1 is the lower 3dB frequency and f_2 is the upper 3dB frequency.

$$Q = \frac{f_c}{f_2 - f_1}$$

Equation 12

The Q of an antenna is very similar to the Q in mechanical systems. It determines how long the antenna "rings", or in more quantitative terms how much energy is lost per oscillation (Equation 13). These two definitions are not necessarily equal for small Q and so the frequency definition should be used as standard for antennas, but it helps to provide a more intuitive description for those unfamiliar with the concept. As with mechanical resonators, antennas with high Q are narrowband and resonate at a sharp peak in

frequency. Low Q antennas are wideband responding well to a range of input frequencies. A useful way to think of this when designing a feed-antenna system is that the higher the Q value, the more sensitive the input impedance is to small changes in frequency.

$$Q = 2\pi \times \frac{Energy\ stored}{Energy\ dissipated\ per\ cycle}$$

Equation 13

Different geometries of antennas have different Q values. They also come with a range of other properties e.g. radiation pattern. It is, therefore, common to attempt to alter the Q value of a given antenna type to more accurately fulfil the requirements placed on it.

4.5.1) Modifying the Q value

One method for altering the Q value of an antenna is to apply "loading". Here we treat the antenna as an RLC circuit. Every antenna has natural RLC contributions from its design but if further physical RLC components are added the overall properties can be changed. Loading coils and capacitance hats are commonly used to reduce the required physical size of an antenna when it is to be used in a confined space such as on a vehicle (Huang & Boyle, 2008). Actively modifying this loading through, for example, the use of variable inductors can even be used to shift the resonant frequency of a high Q antenna (Kraus, 1988).

Directional wideband antennas are relatively large. Therefore, if we wish to lower the Q value of a small antenna, to achieve a wider bandwidth (without seriously affecting the antenna efficiency through absorption), we must determine how the addition of resistive, inductive and capacitive loading will affect the antenna.

In order to evaluate the antenna, and any loading we include, we can treat it as a sum of small sections. For each small section, the reactance can be determined using Equation 14

and Equation 15. It is important to note here that the Q of an individual reactive component depends on the applied frequency. This is usually the resonant frequency of the circuit in question. Without exact knowledge of this we are therefore limited to only knowing if the overall Q will be increased or decreased by the addition of the loading.

Equation 14 describes the Q of an inductor, including the inherent series loss. Where X_L is the inductive reactance, R_L is the series resistance (Ohms), ω_0 is the resonance frequency (rads/s) and L is the inductance (Henrys).

$$Q_L = \frac{X_L}{R_L} = \frac{\omega_0 L}{R_L} \qquad \textbf{Equation 14}$$

In the same way Equation 15 describes the Q of a capacitor, also including its inherent series loss. X_C here is the capacitive reactance, R_C is the series resistance, ω_0 is the resonance frequency (rads/s) and C is the capacitance (Farads).

$$Q_C = \frac{X_C}{R_C} = \frac{1}{\omega_0 C R_C} \qquad \textbf{Equation 15}$$

Equation 16 shows how the overall system Q can be calculated. This is a general result independent of whether their losses come from series resistance or otherwise (Di Paolo, 2000).

$$Q = \frac{1}{\frac{1}{Q_L} + \frac{1}{Q_C}} \qquad \textbf{Equation 16}$$

From these equations we can see that decreasing the inductance and increasing the capacitive loading of the antenna will increase the Q value of the antenna. Increasing the resistance will also decrease the Q and is described in further detail in subsequent sections.

Applying loading in this manner will alter the antenna Q favourably but there will also be side effects as this loading affects other antenna properties. As previously stated, the loading can have a strong effect on the resonant frequency. Adding capacitance and reducing inductance has the effect of increasing the resonant frequency for a simple dipole. This leads to the need for a larger antenna to regain the desired operating frequency.

4.6) Wideband antenna theory

The previous section described narrowband antennas using the simple dipole antenna as a starting point. It went on to show how such narrowband antennas may be modified to increase their operating bandwidth. This section will detail the theory of wideband antennas, looking at the features that allow them to radiate effectively across a wide range of frequencies.

One design philosophy is to create an antenna that is determined by angles and not lengths. The antenna will then have scalable sections that can radiate at the different frequencies. This concept is known as Rumsey's principle and is stated as: *The impedance and pattern properties of an antenna will be frequency independent if the antenna shape is specified only in terms of angles* (Kraus, 1988). In practice, such antennas would be infinite in size so there must always be a maximum and minimum length in their definition. The driving signal is reflected from the ends of the antenna resulting in modified pattern and impedance properties from that of the infinite antenna. These two lengths therefore determine the range of operating frequencies of the antenna. The bandwidth is improved, over that of the simple theory, by the fact that in a real system the current along the antenna is attenuated. If the current is negligible at the point of truncation then there is no significant reflection to affect the antenna properties. Attempting to provide a matched termination can also improve the frequency independent nature. John D. Dyson

implemented Rumsey's principle in 1958 (Huang & Boyle, 2008) to invent the first practical frequency independent spiral antennas, one of which is being used in this work, the conical spiral.

Another design method is to use slow transitions from the feed line to free space. The gradual transition slowly varies the impedance and does not produce any coherent reflections. The overall input impedance of the antenna therefore is very flat allowing a wide range of frequencies to be matched and radiated by the antenna. Examples of this antenna type include the twin alpine horn antenna and the volcano smoke antenna (Kraus, 1988).

Due to the constraints of launch, minimising the size of a satellite antenna is beneficial. However, once the antenna becomes electrically small (Equation 17) it is commonly recognised that further reduction of the antenna size will compromise the efficiency, Q factor or both (Huang & Boyle, 2008). Work on the limitations of electrically small antennas has spanned over half a century, starting with the maximum achievable 'power factor' work of Wheeler (1947) and Chu (1948). This work was then expanded in the 60's and 70's by Harrington (1960), Collin & Rothschild (1964) and Schwering (1976), the later formulating the Fano-Chu limits. This was then expanded upon again and made more accurate in the 90's by McLean (1996). The full outcome of this work has broad ranging implications for a variety of situations, but three concepts are useful and directly relevant here.

Firstly, the aforementioned Fano-Chu limit suggests that increasing the metal present in any radiating antenna configuration, within a set antenna volume, yields a higher gain (Huang & Boyle, 2008). Gain is crucial for WISCER and so this should be taken advantage of wherever possible.

Secondly is the relation between the volume of a sphere that completely encloses a given antenna and that antennas bandwidth (Huang & Boyle, 2008). The relationship is given by Equation 18 and shows that, as the size of the sphere decreases the Q value must increase if efficiency is to be maintained.

$$In\ the\ case\ that:\ \frac{r}{\lambda} \leq \frac{1}{2\pi} \qquad \textbf{Equation 17}$$

$$Q_0 = \eta_A \left(\frac{1}{(\beta r)^3} + \frac{1}{\beta r} \right) \qquad \textbf{Equation 18}$$

$$Q_0 \approx \eta_A \left(\frac{1}{(\beta r)^3} \right) \qquad \textbf{Equation 19}$$

Equation 18, where Q_0 is the Q factor of the antenna as well as any external component used to bring it to resonance, η_A is the antenna efficiency, β is the wavenumber and r is the radius of the minimum enclosing sphere, can be simplified to a good approximation (Equation 19) using the fact that for electrically small antennas βr is always less than or equal to 1. This equation allows us to determine the minimum radius that yields a suitable Q factor and efficiency combination. Using the optimal signal bandwidth of 100MHz from chapter 2 and some simple calculation the minimum enclosing radius is shown to be 17.2cm. This can use used as the theoretical lower bound before the antenna efficiency must be compromised. Consideration must be taken of the breakdown of Equation 12 in providing an accurate value of Q as an antenna becomes more wideband (Q<1). If significant improvement in bandwidth is made this Q value definition will no longer provide an accurate guiding limit.

The third concept is that of broadening the bandwidth of a pre-existing narrowband antenna to achieve the desired operational frequency range. There are many methods for

achieving this depending on the starting antenna, but they all fall into one of two categories: modifying the antenna itself by changing its shape or adding further radiating elements; or adding other passive electrical components to the antenna circuit. As shown in the previous section adding capacitance, resistance or inductance can alter the Q of an antenna. However, these circuits themselves resonate at a given frequency and so high order setups (many components) are preferable. In practice, there is a limit to the order which can be achieved and therefore a limit to the broadening that can be achieved. Adding such components also adds further mechanisms for the loss of energy from the antenna and so begin to reduce the antenna efficiency the further they are applied.

Using these concepts will guide simulation efforts towards improving the WISCER antenna performance. Antenna S11, input impedance as a function of frequency, and efficiency are useful metrics by which to perform an optimisation of the antenna's bandwidth, but the added complexity, cost and practicalities of use must be considered when making further conclusions.

4.6.1) Specifics of improving Pulse Radiation and Bandwidth

WISCER will utilise short transient pulses as probing signals to investigate the ionosphere. It is, therefore, important to minimise the late time ringing of the wideband antenna in order to prevent the ionospheric effects on the signal from being masked.

Late time ringing occurs within an antenna when multiple reflections of the excitation signal occur between the ends of the antenna and the feed. Since this period is prolonged it narrows the bandwidth. Consequently, reduction of this ringing is important for maintaining the bandwidth of the antenna.

The most common technique for increasing the bandwidth of an antenna is resistive loading. Including resistance quickly damps signals within the antenna and prevents effective transmission of the ringing signals. However, it also introduces inefficiencies to the transmission of the desired excitation, which must be factored into any alterations of the antenna design to ensure improved overall performance. The optimal profile for purely resistive loading on a cylindrical antenna is described by Wu & King (1965) with improvements for a double exponential current distribution from Guo & Shi (2006). However, despite being optimised it still gives poor radiation efficiency performance at around 30% (Montoya, Member, & Smith, 1996). Distributed capacitive loading was also introduced with a number of differing profiles (Rao, Ferris, & Zimmerman, 1969) in order to achieve non-dissipative loading. Whilst distributed capacitive loading does keep the radiation efficiency high it has been shown by Montoya et al. (1996) that there is still relatively strong ringing within the antenna when compared to resistive loading.

A combination of distributed resistive and capacitive loading was therefore suggested as a possible solution. A series of sources, including Kanda (1983) and Lestari, Yarovoy, & Ligthart (2004), have used this technique, again with a number of different capacitive profiles in order to achieve efficiencies in the range of 40 to 60%.

A common application for this loading method is ground penetrating radar, where it is used on a bow tie antenna. The antenna sits very close to the target of interest so any dispersion of the antenna signals can quickly limit the accuracy of the distance measurement. Space based radar systems do not generally have this problem but multipath spreading within the ionosphere causes dispersion of the signal. To be able to quantify the dispersion caused, an aim of WISCER seen in Table 2, the sounder waveform should be as free from antenna generated dispersion as possible. The level of loading required to meet

the requirements of the WISCER experiment will be evaluated within this work and used to inform the final design of the chosen antenna.

4.7) Transmission lines and matching

In order to achieve desired performance of any chosen WISCER antenna the transmission line that feeds that antenna must be considered. A brief introduction to transmission lines and antenna feed lines will be given here followed by more detail on the significant points when dealing with wideband antennas.

A transmission line has the ability to direct energy along its length. They have become very common in our everyday lives and include electrical power lines, optical fibres or even just simple wiring. For this project we are concerned with RF energy and so coaxial cables and microstrips are the most relevant transmission lines. Such electrical circuits fall into two categories; lumped element systems and distributed element systems. It is important to determine which kind of system is being designed in order to prevent unwanted behaviour. The distinction between the two systems depends on the wavelength of the electrical signal being used. If the wavelength is much longer than the length of the transmission line, then the current and voltage can be considered unchanged along the line's length. Such a transmission line can therefore be treated just like a regular wire in a DC circuit and is known as a lumped circuit. However, if the wavelength of the signal becomes approximately equal to or smaller than the length of the transmission line it becomes a distributed element system. The variations of voltage and current as a function of distance can no longer be ignored. Transmission line theory has been developed in order to deal with such systems.

Transmission line theory states that a distributed system can be modelled by dividing the line into many (ideally an infinite number) segments. Each segment has a length Δz and is therefore much smaller than a wavelength and can be represented by a set of lumped elements as shown in Figure 13.

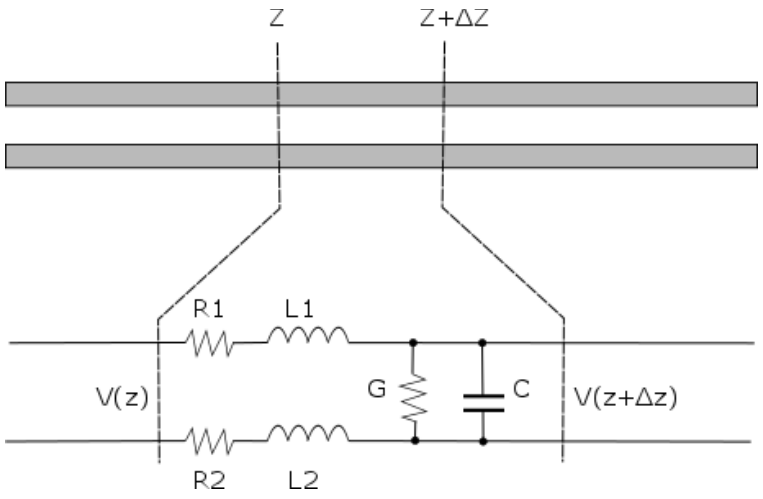

Figure 13 shows the transmission line model for a two-wire balanced line (Huang & Boyle, 2008).

A full description and analysis of the results of the theory are not required here but it is important to note some key points. The variation of current and voltage along a transmission line are a function of the length but the impedance of a homogenous transmission line is constant along its length. Specifically, for the 1-0.5m wavelengths used by WISCER, small circuits such as those on a small PCB can be approximated as a lumped system. However, the feed lines that carry the signal from these circuit boards to the antennas approach λ and therefore distributed system effects must be considered.

The transmission line case relevant to the feeding of antennas in general is that of a terminated transmission line. The setup can be seen in Figure 14 and comprises of three main sections: the RF source, the transmission line itself and the load. Each section has its own characteristic impedance.

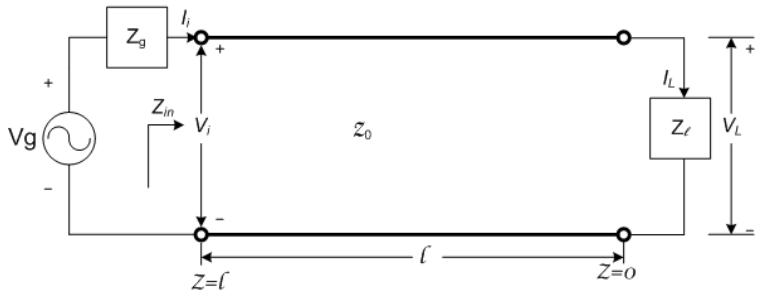

Figure 14 shows the general form of a terminated transmission line which is applicable to an antenna feed (Huang & Boyle, 2008).

A full mathematical derivation of this case is widely available in books such as (Huang & Boyle, 2008). An important result of the mathematical description is that of the equation for the reflection coefficient Γ given in Equation 20, where Z_0 is the transmission line impedance and Z_L is the load impedance. This equation is used to determine the level to which a system must be impedance matched to perform effectively. Discontinuities in the impedance along a transmission line and at the load lead to reflections from those points. This in turn leads to ineffective power transfer if the reflection coefficient is a significant fraction of the signal being delivered.

$$\Gamma_0 = \frac{Z_L - Z_0}{Z_L + Z_0} \qquad \textbf{Equation 20}$$

From Figure 14 we see that there are four important cases to consider for this transmission line arrangement:

- **Matched case:** $Z_L = Z_0$

  For this case the impedance of the load matches the impedance of the line. The input impedance is, therefore, not a function of the line length.

- **Open Circuit:** $Z_L = \infty$

  When the transmission line is terminated without connection the load can be represented by an infinite resistance. When this is the case the input impedance will be:

$$Z_{in}(l) = Z_0 \frac{1}{j\tan(\omega\sqrt{LC}l)}$$ **Equation 21.**

The impedance at the input has no real resistance only reactance, which is capacitive for small lengths like that expected on WISCER. It is important to be able to recognise and distinguish this behaviour to prevent confusion between real results of an operational antenna and a system that has a fault. It is also important for calibration purposes of a spectrum analyser in an experiment setting.

- **Short Circuit:** $Z_L = 0$

When the transmission line is terminated with a short the load can be represented by zero resistance. When this is the case the input impedance will be:

$$Z_{in}(l) = j\,Z_0\tan(\omega\sqrt{LC}l)$$ **Equation 22.**

The impedance in this case also has no real resistance only reactance, which is inductive for small lengths like that expected on WISCER. Again, it is important for fault checking and calibration to be able to identify this system response.

- **Quarter-wavelength case:** $l = \lambda/4$

This case is known as the quarter-wavelength transform due to the outcome that the load impedance is converted to the input impedance over the length of the transmission line. From Equation 22 below it can be deduced that if the line impedance matches the load impedance, the input impedance will always match the load.

$$Z_{in}(l) = \frac{Z_0^2}{Z_L}$$ **Equation 23**

The quarter wavelength for this case does not have to be directly attached to the load to be effective. If there are an integer number of wavelengths before the $\lambda/4$ section, then the effect is still present. This practice is commonly used for impedance matching for narrowband antennas. For wideband antennas however, there is no singular quarter-wavelength due to the range of frequencies. If the bandwidth is sufficiently narrow compared to the frequency it can still be used as an approximation, but this is not applicable for the 0.5m to 1m wavelength range planned for WISCER which is too wide.

After considering each of the cases above we see that achieving the matched case is required on WISCER. Removing the dependence of the input impedances on feed line length is very useful and removes design constraints.

Due to the expected impedance of the antenna candidates for WISCER it was known at an early stage that the transmission line and signal source impedance could not be matched using COTS components. Research showed that there were two relevant types of wideband impedance matching. The first, using microstrip tapers, was immediately ruled out due to wavelength considerations. Calculation for such a microstrip taper (Klopfenstein, 1956) yielded the result that the taper length is approximately equal to $\lambda/4$ which is 1.25 times the width of a CubeSat for even the lowest frequency. The second option is to use transformers. Transformers are commonly used in wideband applications and are readily available as COTS products. There are many types and configurations of transformer; to choose the appropriate type for WISCER we must consider: frequency, compactness, impedance of the antenna and impedance of the source/transmission line. A type A transformer (DC isolated primary and secondary, centre-tap secondary) (Mini-Circuits,

2018) was selected as being most suitable. The exact transformer used in prototyping is detailed in Appendix 1.

4.8) Baluns

Radiation from the antenna feed line can alter the radiation pattern of the antenna depending on the exact feed line configuration. There are several techniques for feeding antennas with balanced lines without affecting their pattern characteristics, the simplest of which is to use unbalanced lines for each antenna element. Due to the deployment requirement and the need for the two candidate antennas to be fed from their respective forward end, unbalanced feeding was chosen for simplicity. In order to take the output of the WISCER signal generator and feed the antennas with multiple unbalanced lines a balun is required.

A balun takes a balanced signal and converts it to an unbalanced signal or vice versa. Strictly in this situation the correct device is an "Unun". Which converts an unbalanced signal into multiple other unbalanced signals but the term balun is commonly used as an umbrella term for this family of devices and shall be used here. There are many different types of baluns, but they fall under two primary categories; transformer type or delay line type. The delay line type baluns depend on transmission lines of specific lengths for their operation. They therefore only operate for specific frequencies and are not suited to the wideband operation of WISCER. The transformer types are largely frequency independent and can operate in a wideband system. Both types can also transform impedances or add a phase shift to one of the output signals. This means a single component can impedance match the antennas and generate the correct phase shift (0°-180° for the conical and 0°-90°-180°-270° for the crossed Moxon).

The type of balun chosen for testing the antenna designs was a BALH-003 high power balun by Marki Microwave. This is a transformer type balun which allows for wideband operation (200 kHz to 3 GHz).

4.9) Conclusions

To conclude, features and design principles of wide bandwidth antennas have been presented. The antenna simulation methods that will be used in the following results chapters have been outlined. In the following results chapters the work undertaken on the candidate antennas will be described in detail, including the predicted attitude perturbation interactions with the CubeSat system.

CHAPTER 5) WISCER ATTITUDE DETERMINATION AND CONTROL SYSTEM (ADCS)

5.1) Introduction

A consideration for the WISCER mission is the control of the CubeSat attitude. Many CubeSats do not actively control their attitude. They are left to either freely tumble or use passive systems such as permanent magnets and hysteresis damping. For WISCER the power limitations imposed by the limited solar energy collecting potential of the CubeSat form factor, leads to the need to efficiently radiate that energy when transmitting. The wideband signal required for WISCER is energy intensive and is also compounded by the inefficiency of the type A wideband amplifier required. This low efficiency, at best 30%, leads to large amounts of heat. Thermal control is the focus of a parallel WISCER work package, but it is immediately apparent that minimising the transmission power is critical. To do this the antenna should be made directional. The pointing accuracy for a CubeSat with extremely limited payload mass is necessarily going to be poor and therefore candidate antennas with a half beam width of approximately 60° have been chosen.

In this chapter, the challenges facing WISCER relating to attitude control will be discussed and results from attitude simulations of the WISCER candidate antenna variants will be shown. After initial research, it became apparent that a magnetic only attitude control system would provide significant mass advantages over the alternative system, which would include reaction wheels. However, due to the large deployable antennas under consideration it was decided that a simulation was necessary to determine if the torque of a magnetic only system would be sufficient to overcome in orbit attitude perturbations and maintain antenna pointing.

5.2) Perturbation torques

In order to readily understand the results of the following chapter, knowledge of perturbation torques acting on satellites in LEO is required. This section provides relevant detail on the torques arising from atmospheric drag, radiation pressure and gravity gradients, as they generate the largest contributions in this case.

5.2.1) Atmospheric Drag

As we have already seen, the majority of the ionosphere actually exists above the commonly quoted beginning of space, which is known as the Karman line at 100km (Córdoba, 2013). While it is true that the atmosphere is already very tenuous by this point, we must note that it is still present and continues to die away with ever increasing altitude. Even at an altitude of 260km the GOCE satellite (Drinkwater et al., 2007) was aerodynamically shaped to minimize drag, yet still needed a dedicated electric propulsion unit to maintain its orbit.

Atmospheric drag, for LEO satellites is the determining factor of satellite life time. The small drag force combines over time in the retrograde direction, to decay a satellite's orbit and return it to Earth. The exact lifetime is difficult to compute as it depends strongly on the chosen altitude and solar weather conditions. This is actually a very useful feature of LEO as it naturally removes unwanted space debris. Within the CubeSats community a common consensus is that lifetimes should be maintained below 25 years. Whilst this rule is not yet formally enforced, there has been significant development into end of life de-orbit devices. These devices reduce the ballistic coefficient of the satellite. Simple approximations for a 3U WISCER design show that this must be considered for the orbital altitudes in the upper ionosphere.

When considering spacecraft attitude, it is the torque exerted on the spacecraft by aerodynamic forces that must be considered. At LEO altitudes, atmospheric drag can be considered as a particle based problem due to the low pressure as opposed to a fluid based one. Atmospheric atoms and molecules arrive, interact and leave without interacting with any others, simplifying the calculation of drag and torque. The particles can either be immediately reflected by the spacecraft or adsorbed and reemitted later. If atomic oxygen is adsorbed to the external surface of a spacecraft it can react chemically with it (Reddy, 1995). Therefore, a considered choice of external materials is required to prevent such damage to exposed critical components. The low pressure particle interaction with the spacecraft simplifies calculation of the forces and torques generated. The result is that the processing requirements are much less than that of computational flow dynamics (CFD) simulations and can be performed without specialised computer hardware.

5.2.2) Radiation Pressure

Photons of light have momentum that can be transferred when they interact with a surface. The momentum of a photon, p, is given by the equation below:

$$p = h/\lambda \qquad \textit{Equation 24.}$$

In Equation 24 h is the Planck constant and λ is the photon wavelength. Classical mechanics can then be used to calculate the forces acting on the spacecraft due to light from the two main sources in LEO, the sun and Earth. The Earth however needs to be treated as two sources by the model, as it has significant emission in two spectral bands. The sources are therefore, in order of descending flux: direct sunlight, reflected sunlight from the earth and thermal photons from Earth.

The direct solar flux at 1 A.U. is 1360.8 ± 0.5 W m^{-2} (Kopp & Lean, 2011). Using simple computer models and assumptions (based on common construction materials of a satellite) it can be shown that this leads to a force on the order of 10^{-6} N for objects with an area (normal to the incident solar flux) of approximately $1m^2$.

With an average albedo of 0.3 (Goode, Qiu, Yurchyshyn, & Hickey, 2001) reflected light from the Earth makes up one quarter of the total light falling on a satellite and should not be considered a small effect.

Thermal and RF radiation emitted from the satellite itself will also contribute to the forces and torques generated. Whilst comparatively small, they should be included for high precision modelling due to the cumulative effect they can have.

5.2.3) Gravity Gradients

The Earth's gravitational field strength decreases with radial distance from the planet. Therefore, lower parts of the spacecraft will experience a stronger gravitational force than the upper sections. This gravity gradient leads to the centre of gravity being offset from the centre of mass. A restoring torque is generated that has the effect of returning the centre of gravity to its equilibrium position.

To calculate the gravitational forces and torques on a spacecraft several limiting and simplifying restrictions need to be made, which are listed here:

- Only the Earth is considered.
- The Earth possesses a spherically symmetric mass distribution.
- The spacecraft size is much smaller than the distance to the centre of mass of the Earth.

- The spacecraft consists of a single rigid body.

We can then calculate the gravitational forces and torques for a spacecraft (labelled β in Figure 15) using Equation 25 and Equation 26.

$$f = -\mu \int_{\beta} \frac{dm}{R^2} \qquad \textit{Equation 25}$$

$$g = -\mu \int_{\beta} \frac{r \times R}{R^3} dm \qquad \textit{Equation 26}$$

The symbols above have meaning as depicted in Figure 15. Supplementary to this, μ is the standard gravitational parameter, f is the total force acting on the spacecraft and g is the gravity gradient torque. Another form of the gravitational torque equation can be seen in Equation 27. Where I is the moment of inertia of the spacecraft and $\hat{o}$ is the local nadir unit vector. We can see that the gravitational torque will provide a restoring force that acts to keep the axis of minimum moment of inertia aligned vertically with respect to the planet. To describe this in a more intuitive way we can conceive of a telephone pole like object in orbit around Earth. The differing strength of gravity at the top and bottom of the pole lead to a torque that attempts to align the pole towards the ground. However, in space without a damping force this would lead to oscillations around this attitude.

$$g = 3\left(\frac{\mu}{R_c}\right)\hat{o} \times \mathrm{I} \cdot \hat{o} \qquad \textit{Equation 27}$$

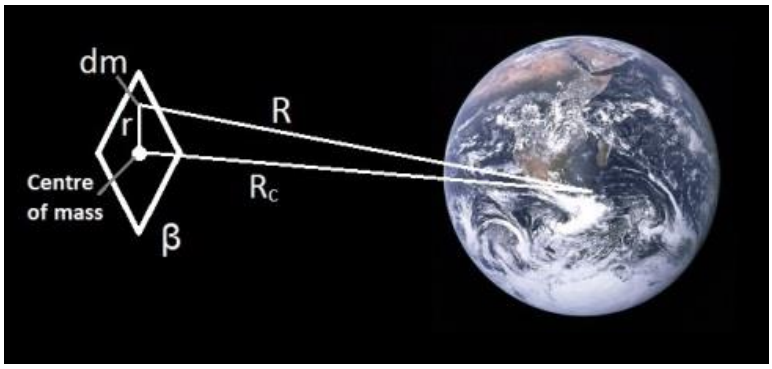

Figure 15 A spacecraft in the gravitational field of earth, ignoring the effect of the moon and other gravitational sources.

There are many other sources of perturbation torque that will not be listed here in detail, as they provide only small contributions. The objective of this piece of preliminary work was to quickly access the magnitude of different torques. The knowledge generated then, not only determined which attitude control system was required, but aided design decisions to minimise the total torque generated. In the results section of this chapter, the contributions of these main torque sources will be analysed.

5.3) WISCER Attitude Control System (ACS) Simulation Method

The WISCER experiment requires that the CubeSat passes over the equatorial ground station at roughly 22:00 local time in order to observe the post sunset equatorial ionosphere. It is, however, largely independent of the orbit it is inserted in to, with the exact orbit only determining the frequency of such passes. Both equatorial and sun synchronous orbits would be ideal as they generate the most frequent passes. To maximise the number of launch opportunities, all orbit types should be considered and reasonable mitigating steps taken, if challenges for a particular orbit arise.

For the following simulations three representative orbit types are used. These orbits, outlined in Table 3, make up the reference orbits, against which a launch opportunity can

be evaluated. Visualizations of the low, mid and sun synchronous inclination orbits are shown in Figure 16.

Orbit	Orbit type	Inclination	Altitude	Local time of descending node
O1	Low inclination	7°	750 km	N/A
O2	Mid inclination	60°	750 km	N/A
O3	Sun synchronous	99.4843°	750 km	2200

Table 3 lists the candidate orbits of the WISCER Satellite.

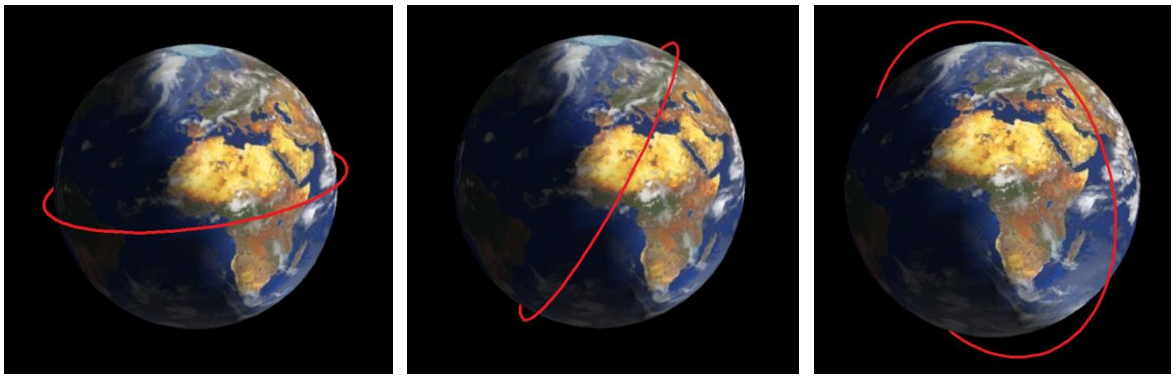

Figure 16 shows the low, mid and high inclination candidate orbits for WISCER.

The objective of the attitude simulations is to determine the magnitude of disturbance torques expected for the large deployable antennas needed for the WISCER mission and verify the suitability of a magnetic only attitude control system. A staged approach was devised to obtain all the required results whilst ensuring the reliable functionality of the individual code segments. The key steps are listed below:

- Initially disturbance torques were estimated for each WISCER variant and for each candidate orbit with nadir pointing of the satellite enforced. This provides baseline torque estimates that may be compared to the torque that can be provided by a magnetorquer attitude control system.

- Secondly, the nadir pointing constraint was removed and replaced with a physics simulation of the CubeSats rotation (if no attitude control were imposed). In this case, the satellite is initialised with the correct angular momentum that would, if there were no disturbance torques, maintain nadir pointing. The satellite's current attitude is then used to calculate the disturbance torques. Integrating these torques throughout the orbit and updating the satellite rotation rate provides a simulation of the satellite's expected attitude evolution.
- The third stage implemented a realistic magnetic attitude control system to simulate the active control of the satellite in orbit. The available torque limits of a representative system were included allowing for a determination on whether the WISCER variant would be stable in the given orbit.

The following subsections describe the functionality and accuracy limitations of the implemented model. Section 5.4 then goes on to present the results from the final round of simulation using the most up to date predictions for the WISCER variant form factors. Only the final simulation results are presented for conciseness. The third stage simulation was repeated throughout the PhD work whenever a significant change to the WISCER design dimensions arose (e.g. change of conical helix dimensions or the reduction of the crossed Moxon drag sail size). It is expected that only the presented results will be relevant for future work, however all other data is available from the author.

5.3.1) Simulation Package and Coordinate system

In order to achieve the stated objectives quickly the use of an external satellite MATLAB toolbox was used. The Princeton Satellite Systems (PSS) Spacecraft Control Toolbox (SCT) is a library of MATLAB code scripts relevant to spacecraft simulation. Work is ongoing at PSS to expand the libraries capability and build out the interconnectivity and

modularity of these scripts. Due to this and the unique objective, each stage of the WISCER attitude simulation is therefore a combination of PSS SCT functions and bespoke code written by the author.

The chosen coordinate system for the simulations will be a LVLH (local vertical, local horizontal) inertial coordinate system combined with the use of the body frame of the satellite. The axes are defined so that the x axis is in the ram direction, the z axis points downwards, and the y axis is orientated so that the coordinate system is right handed (Figure 17). The body axes of the two WISCER variants are shown in Figure 18 and Figure 19.

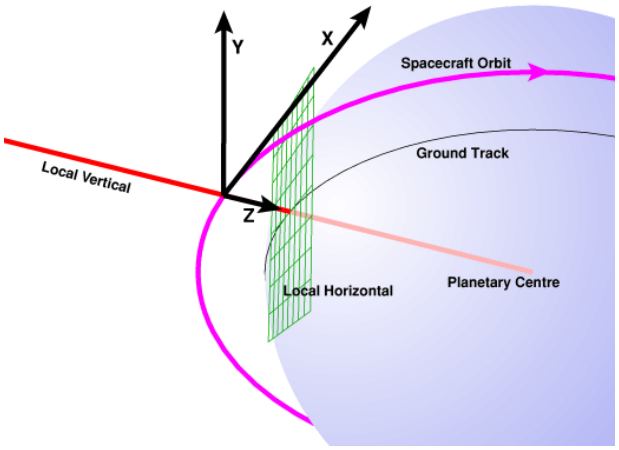

Figure 17 shows the coordinate system used in the SCT simulations based on the body frame of the satellite.

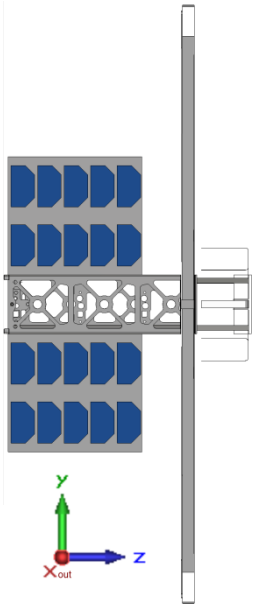

Figure 18 shows the orientation of WISCER (cross-Moxon) with respect to the coordinate system used in the attitude simulations. The blue shapes are individual solar cells. Image is shown to scale with Figure 19.

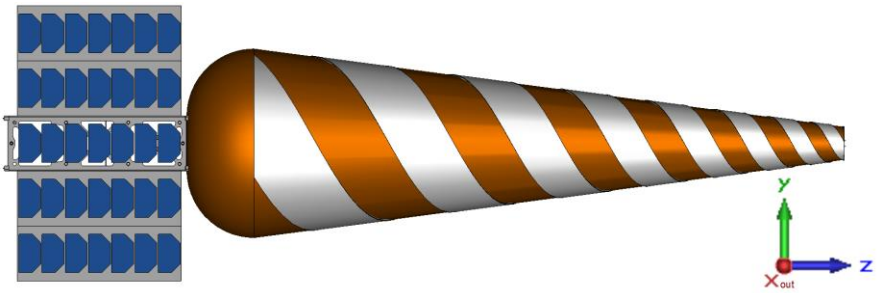

Figure 19 shows the orientation of WISCER (conical helix) with respect to the coordinate system used in the attitude simulations. The blue shapes are individual solar cells. Image is shown to scale with Figure 18.

5.3.2) Attitude simulation and calculation of disturbance torques

The first stage simulation simply calculated all disturbance torques using a satellite "on rails". For each iteration step along the orbit, the nadir pointing quaternion for the satellite was generated and set at the current satellite attitude (body to LVLH conversion). From this the current disturbance torques could be calculated, using the WISCER variant CAD models and environmental data.

Data was collected for the two WISCER variants in all candidate orbits across a range of altitudes. From these results it was possible to determine that below 550km atmospheric drag quickly became the dominant disturbance torque with decreasing altitude. Above 550km the disturbance torque from optical radiation pressure dominates both cases, as seen in Figure 20 and Figure 21. The simulation uses the J70 atmospheric model as an approximation and so we must regard this value as an approximation also. The real value will vary in time depending on solar activity as well as the exact materials used on the spacecraft.

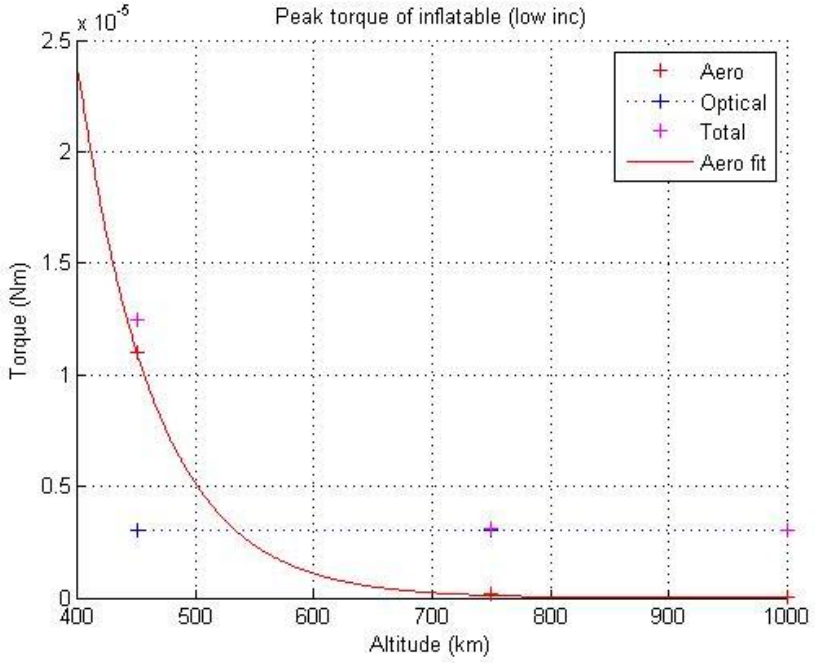

Figure 20 shows the peak aero, optical and total torques experienced by the conical helix WISCER variant in a low inclination orbit.

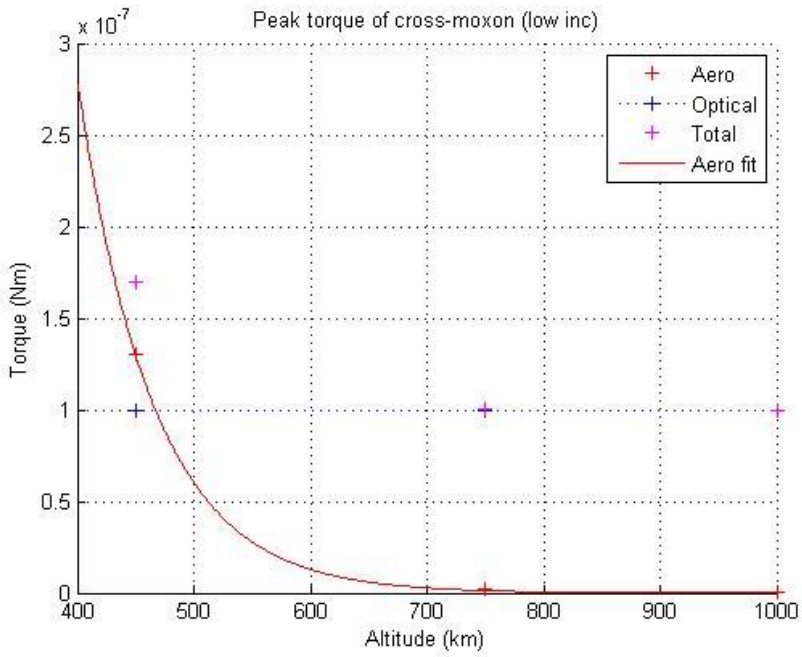

Figure 21 shows the peak aero, optical and total torques experienced by the crossed Moxon WISCER variant in a low inclination orbit.

Stage two of the implementation developed the code structure to simulate the physics of the CubeSat rotation. For each iteration along the orbit the disturbance torques were integrated to give the change in angular rates. These evolving angular rates then determine the evolution of the CubeSat attitude during the orbit. Figure 22 shows a flow diagram of the code structure including the location of the code block of the next stage which includes the attitude control system.

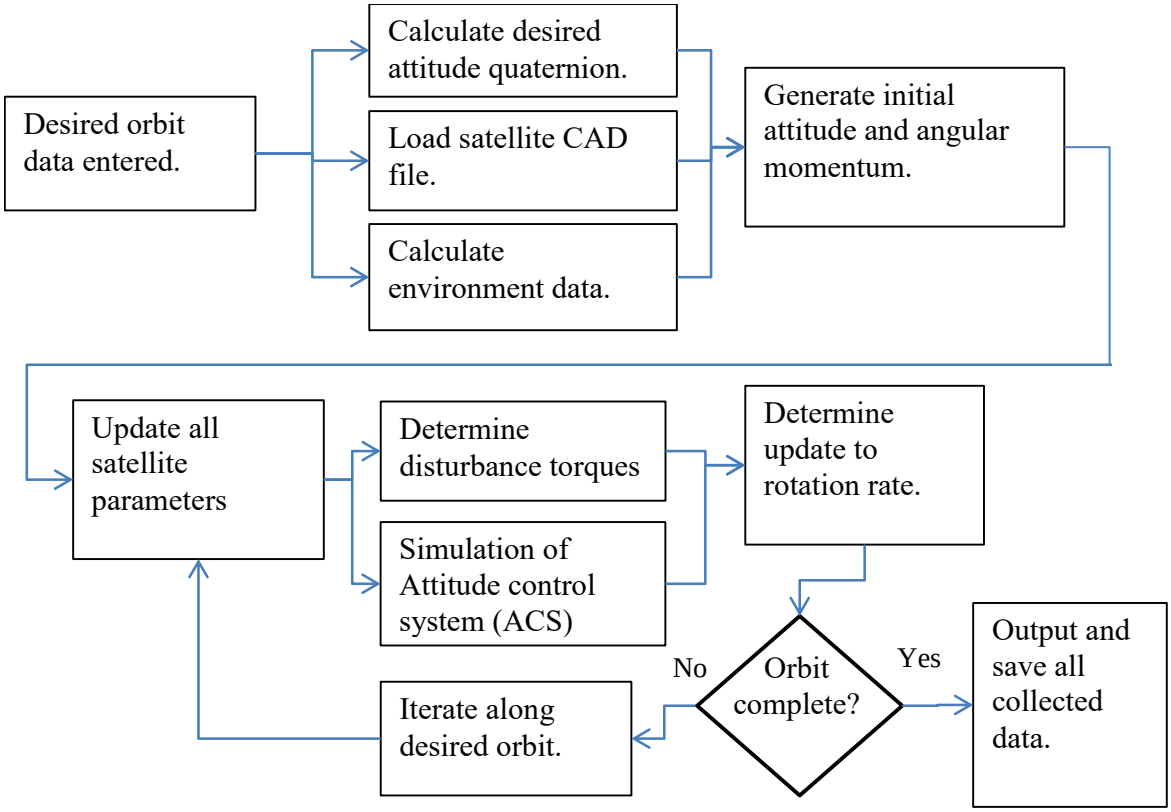

Figure 22 is a flow diagram of the code structure used to calculate the predicted disturbances torques that the WISCER satellite will experience in orbit.

Before continuing it is important to note that this simulation allowed for a better understanding of the other disturbance torques and their relation to the satellite attitude. For the first stage implementation, the gravity gradient torque acting on both variants remained effectively constant due to the constant attitude. In stage two, as the satellite rotates the gravity gradient torque magnitude changes based on the current attitude. For the conical helix, this means that the long axis is no longer aligned with the nadir direction. The effect of this is a restoring force towards the nadir direction. For the expected mass distribution of the conical helix this restoring force is not sufficient to hold nadir pointing. If the distribution was altered to weight the tip of the antenna with approximately 1kg the increase in the gravity gradient and the reduction in the other torques yields an oscillatory yet stable passive configuration. This weighting is almost certainly unfeasible for the 4kg

CubeSat but shows that gravity gradients must be considered as a non-insignificant contributor.

5.3.3) Implementation of a simulated three axis magnetic Attitude Control System (ACS)

In the previous section a propagating simulation of the satellite attitude which is perturbed by external torques was completed. Now we move on to simulate the available torque from the ACS. This will allow the simulation to be used to determine if the intended ACS can maintain the pointing of the satellite. If the ACS has insufficient torque available to it then then nadir pointing will be lost, and the satellite will tumble.

Three axis magnetic control uses three or more electromagnets, called magnetorquers, to control the satellite's attitude using Earth's magnetic field. COTS magnetorquer systems exist for CubeSats. They are most commonly used alongside reactions wheels, with the magnetic system used to dump any build-up of momentum (Li, Post, Wright, & Lee, 2013). The two systems complement each other to produce a system that requires no physical consumables to maintain attitude in regions with strong magnetic fields such as LEO.

The operating principle of the magnetic system relies on the interaction between the space craft dipole and the Earth's magnetic field. The magnetorquers are aligned orthogonally in the body axes of the satellite. The on-board computer, at discrete points along the orbit, measures the Earth's magnetic field strength and direction. Using this information, the computer can determine the required magnetic dipole for each of the magnetorquers (given also a corrective torque target). The computer sends the current needed to produce the correct dipole in each magnetorquer. The maximum torque is determined by the maximum current that can flow in the magnetorquer without damage. It is also therefore apparent that

the maximum available ACS torque will depend on the Earth's magnetic field strength and direction at that location.

Note here, that if any one of the body axes in which the magnetorquers are orientated becomes aligned with the field direction, no torque will be available about that axis. However, the variability of Earth's magnetic field minimises the issue caused by this effect. As the satellite moves quickly through Earth's magnetic field it may lose torque about one of the body axes momentarily but then regain it a few minutes later.

A second but more subtle problem can be seen upon inspection of Equation 28.

$$\tau = m \times B \qquad \textbf{Equation 28}$$

Where τ is torque, m is the magnetic dipole moment and B is the external magnetic field. We wish to determine m from knowledge of B and τ, which requires us to perform the inverse of a cross product. However, the answer for m cannot be constrained in all three dimensions at a single point in time. Not only this but a range of values will also satisfy the two other dimensions leading to the need to choose them based on a minimisation of the resulting dipole moment magnitude.

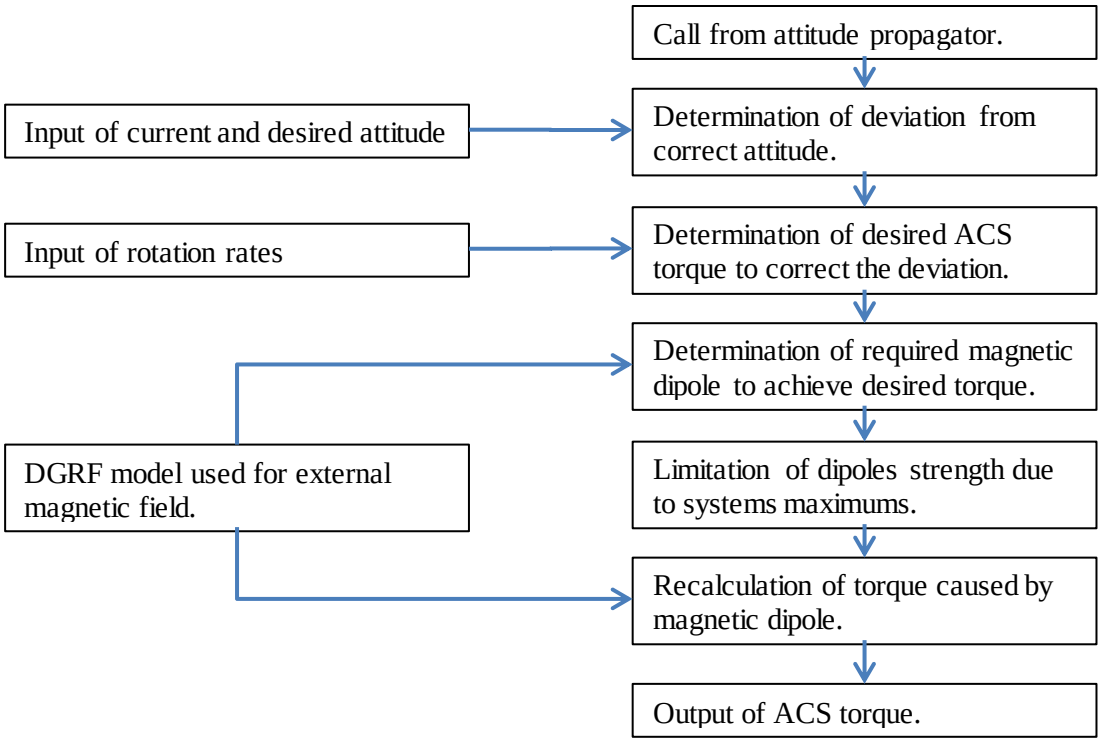

Figure 23. A flow diagram showing the key processes of the basic magnetic ACS system.

It became apparent that implementing a three-axis magnetic ACS is a complex task and that the SCT did not have a dedicated function suite. However, using the PSS SCT function MagControlThreeAxis it has been possible to construct a simulation of a simple three axis magnetic ACS. Figure 23 shows the code structure used to achieve this.

Upon being called, the ACS program takes values for the current and desired attitudes, rotation rates and the current external magnetic field. From the current and desired attitudes, the program determines the correcting rotation direction. A simple proportional differential controller then determines the magnitude in this direction of the desired ACS torque. The proportional part applies a corrective torque proportional to the magnitude of the difference between the current attitude and the desired attitude. The differential part acts as a damping term to reduce any rotation rate of the satellite. This rotation rate is measured with reference to the rotating nadir direction and therefore the required rotation to maintain nadir pointing is not damped.

Now that that the desired torque has been generated it is passed to the part of the program that simulates the magnetorquers, along with the value for Earth's magnetic field. The MagControlThreeAxis function is called to determine the required dipole strengths that will generate the desired torque. Due to the problems previously described in this section a magnitude profile for each dipole must be generated over the propagation time interval of the program in order to constrain the requirement of all three dipole moments. Applying the resulting dipole vector, over the time step, creates the desired torque in all three axes. The MagControlThreeAxis function does this, whilst also minimising the dipole strength to its lowest required value, by minimising the weighted sum of the cost functional in Equation 29.

$$\boldsymbol{D} = \left(\boldsymbol{t} + (\boldsymbol{B} \times \boldsymbol{m})\right)'\left(\boldsymbol{t} + (\boldsymbol{B} \times \boldsymbol{m})\right)' + \boldsymbol{m}'\boldsymbol{m} \qquad \textbf{Equation 29}$$

Where D is the final minimized dipole vector array, m is the current dipole vector array and t is the constant desired torque over the period for which b is entered.

Once this array of dipoles vectors has been generated, it is checked by a limiter to ensure that at no point does it exceed the maximum value of two Clyde Space magnetorquers, which is 2×0.2 Am^2. If at any point this value is exceeded the whole profile is scaled down. This process is repeated if other axes are found to still exceed the maximum value. The whole dipole moment profile is scaled down, rather than just the exceeding point, to maintain the proper resulting net dipole moment direction and therefore the correct torque direction. Once the check has been completed the net torque is calculated and outputted from the program to be included in the next update step of the main program.

5.4) Simulation results

In this section, the results from the attitude simulations will be presented. Due to the volume of raw data only a selection will be presented to illustrate the available data and how it is analysed. One candidate orbit for each WISCER variant has been selected. For the conical helix antenna variant, the sun synchronous, 750km altitude orbit was selected as it provides the best operational environment for the magnetic ACS. Even in this best case the attitude control of the conical helix will be shown to be unstable. For the less challenging crossed Moxon design, the 60^0 inclination 750km orbit has been chosen. All Moxon orbits were stable but this orbit yields the largest angular deviation from the target pointing for this set of simulation runs. It therefore shows the worst-case simulation for the crossed Moxon and illustrates the reasons for pointing error most clearly.

5.4.1) Conical Helix Antenna WISCER Variant

The conical helix antenna poses obvious challenges when considering attitude stabilisation. The use of a large, much greater in size than the original CubeSat form factor, inflatable antenna provides a large surface area on which aerodynamic and radiation pressure forces can act. The combination of these forces with a centre of mass that is still within the body of the CubeSat after inflation, leads to relatively large torques being generated.

Another factor that will not be investigated here but should be noted in future work is that the flexible connection between the CubeSat body and the antenna will lead to significant non-rigid body motions. Any ACS on the final CubeSat should take this into account to prevent potential oscillations. Results in chapter 5 suggest that this flexibility may be minimal whilst there is gas pressure within the antenna.

Figure 24 below shows the CAD model as used for this set of simulation runs. Small details in the CAD model are omitted to improve simulation performance as they would not contribute significantly to the calculated disturbance torque values. Repeating the simulations would be advised however, if there is significant alteration to the main surface materials, their locations or to the position of the spacecraft centre of mass.

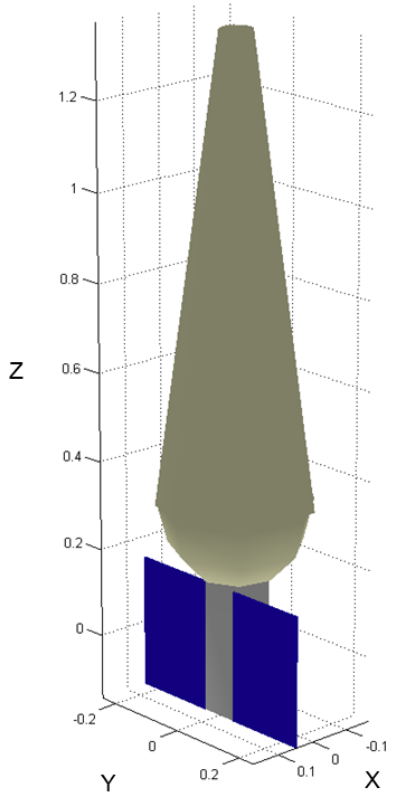

Figure 24 shows the CAD model used in the final conical helix WISCER attitude simulation. The body axes defined will be used by the graphs in this section.

Figure 25 through to Figure 33 show the results for the conical helix variant of WISCER in a sun synchronous 750km circular orbit around the Earth. All disturbance torques, including thermal and reflected radiation torques, are included but any RF torques are not calculated due to their uncertainty, position dependence and near negligible effect.

Figure 25 shows the predicted attitude trace of the conical helix in this orbit. The red lines are the X body axis, the green lines are the Y body axis and the yellow lines are the Z body axis. This axis set is shown for multiple points throughout the orbit to visually illustrate the evolution of the angular deviation. This three-dimensional plot allowed rapid insight to the disturbance processes affecting the simulation run. It is obvious that despite the efforts of the ACS the attitude is unstable, and errors are increasing throughout the orbit. Previous results without the attitude control show multiple complete rotations within this single orbit due to disturbance torques. Whilst the addition of the ACS is a significant improvement, it does not prevent unacceptable tumbling of the CubeSat. This simulation therefore represents a failure for the magnetic ACS. The following figures show the error cascade effect originating from the failure causes.

Figure 26 through to Figure 28 show the most significant disturbance torques acting on the CubeSat and deployed antenna. Figure 29 then shows the total of these torques throughout the orbit. It is this total that, in the simple sense, the ACS system must oppose to maintain the satellite's attitude. Note how the gravity gradient torque acts to oppose movement from nadir pointing, reducing the demand on the ACS.

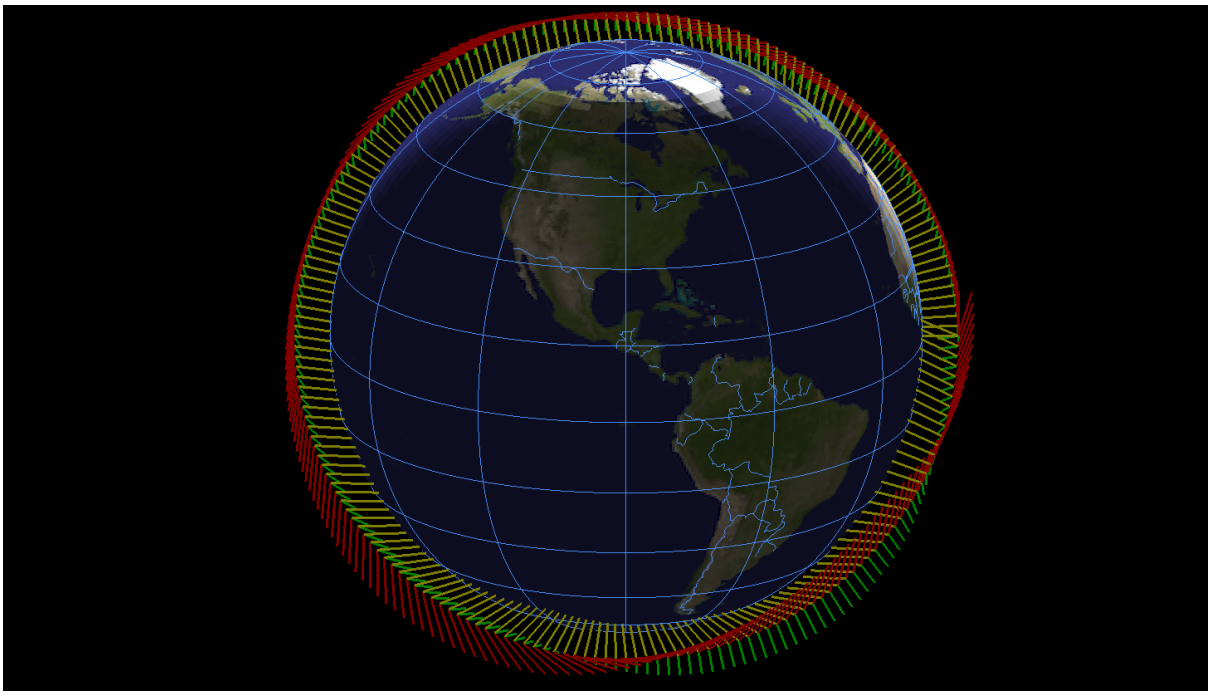

Figure 25 shows the attitude trace of the conical helix WISCER variant in a 750km sun synchronous orbit. The spacecraft body axes are as follows: Red is X, Green is Y and Yellow is Z.

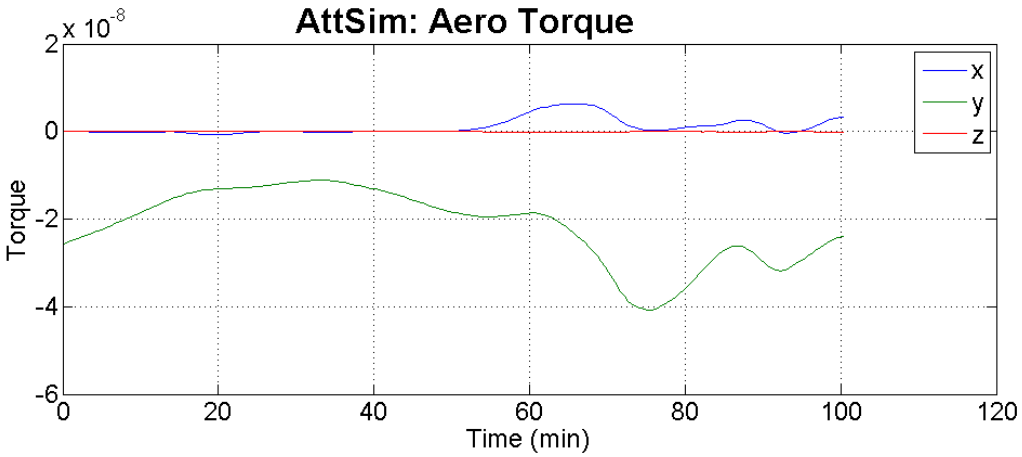

Figure 26 shows the aerodynamic drag torque acting on the conical helix WISCER variant throughout its 750km sun synchronous orbit. Axes are defined in Figure 24.

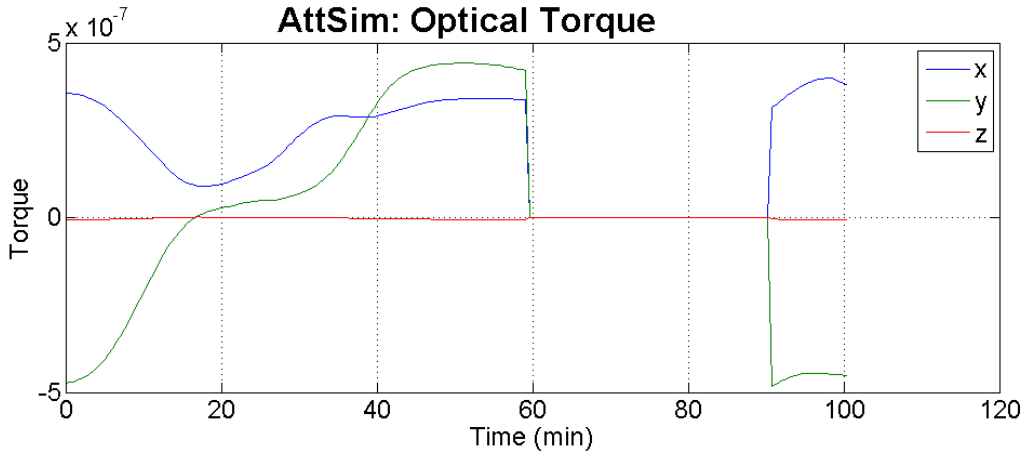

Figure 27 shows the optical radiation pressure torque acting on the conical helix WISCER variant throughout its 750km sun synchronous orbit.

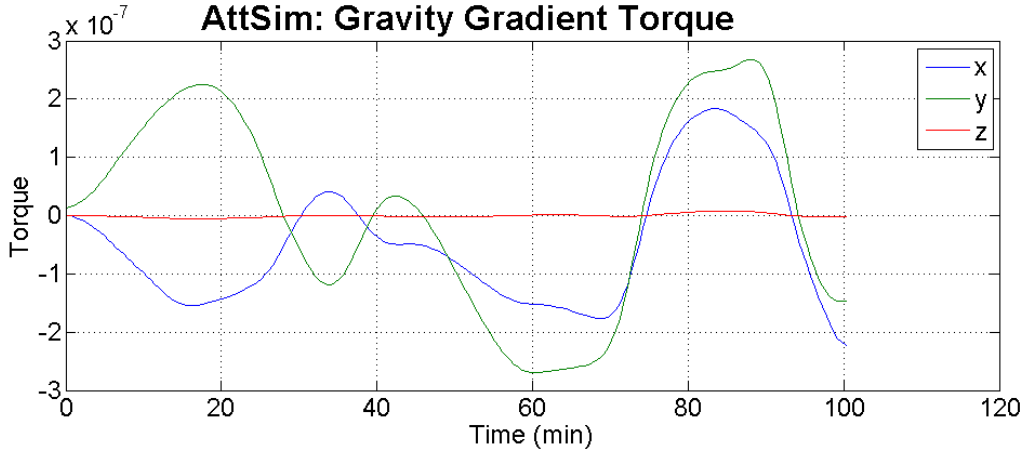

Figure 28 shows the gravity gradient torque acting on the conical helix WISCER variant throughout its 750km sun synchronous orbit.

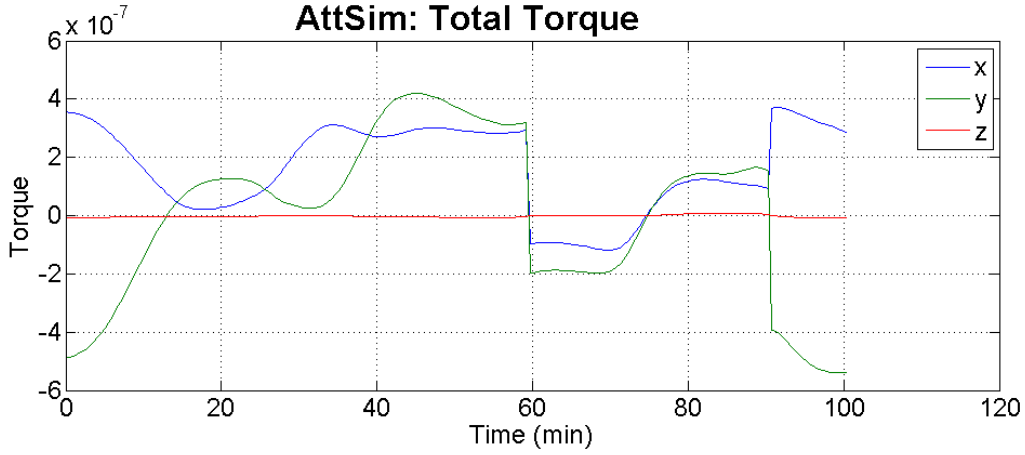

Figure 29 shows the total disturbance torque acting on the conical helix WISCER variant throughout its 750km sun synchronous orbit. Axes are defined in Figure 24.

The Proportional-Differential (PD) controller generates a corrective torque request, Figure 30, for each point in the orbit. The ACS uses this with a measurement of local planetary field strength and direction to determine the magnetic dipole required to achieve that torque. Figure 31 shows the axial contributions of this desired dipole. Immediately we see that the dipole strength is near constantly maxed out in at least one axial direction. This means that for the requested dipole at least one of the magnetorquers would exceed the maximum allowable current of 0.2A. In order to maintain the direction of the correction torque all three axes are scaled down. This disparity between that requested and achieved torques leads to the observed attitude drift.

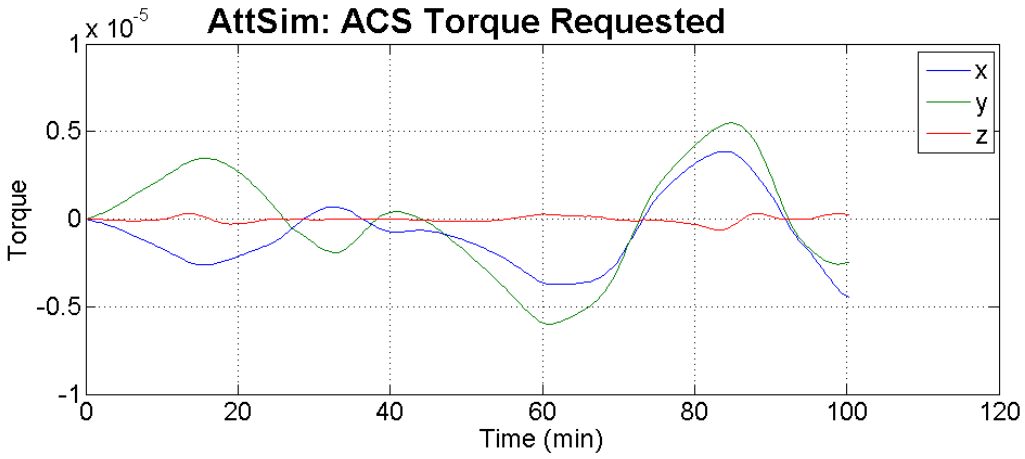

Figure 30 shows the ACS corrective torque requested by the conical helix WISCER variant throughout its 750km sun synchronous orbit.

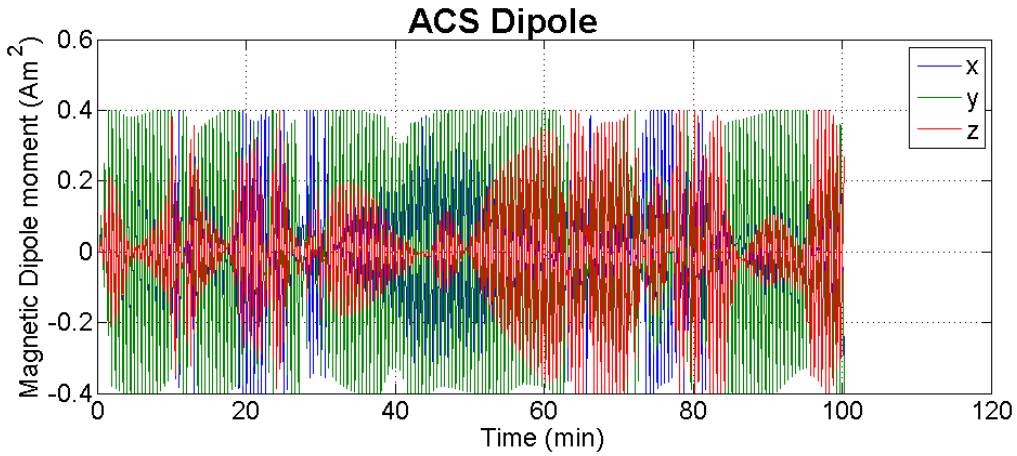

Figure 31 shows the magnetic dipole generated by the conical helix WISCER variant throughout its 750km sun synchronous orbit, considering any limiting effects.

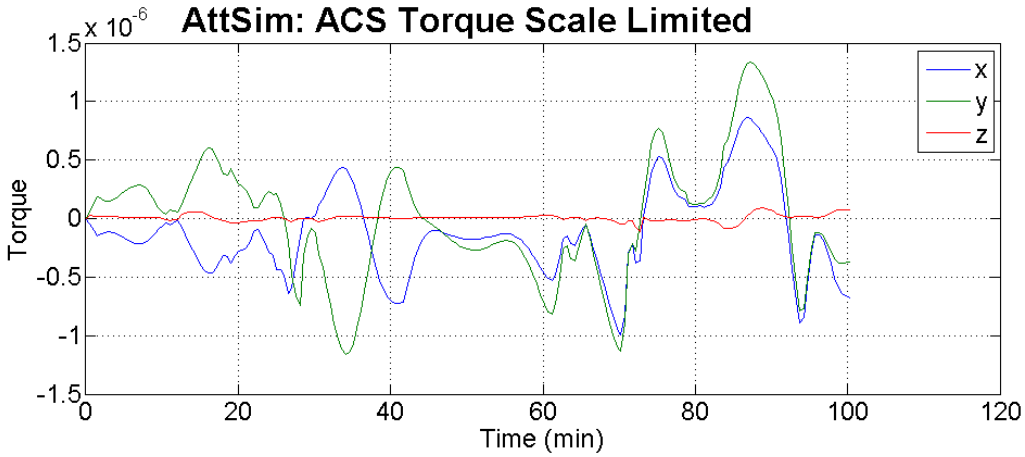

Figure 32 shows the resulting torque, after applied limits, achieved by the ACS system of the conical helix WISCER variant throughout its 750km sun synchronous orbit.

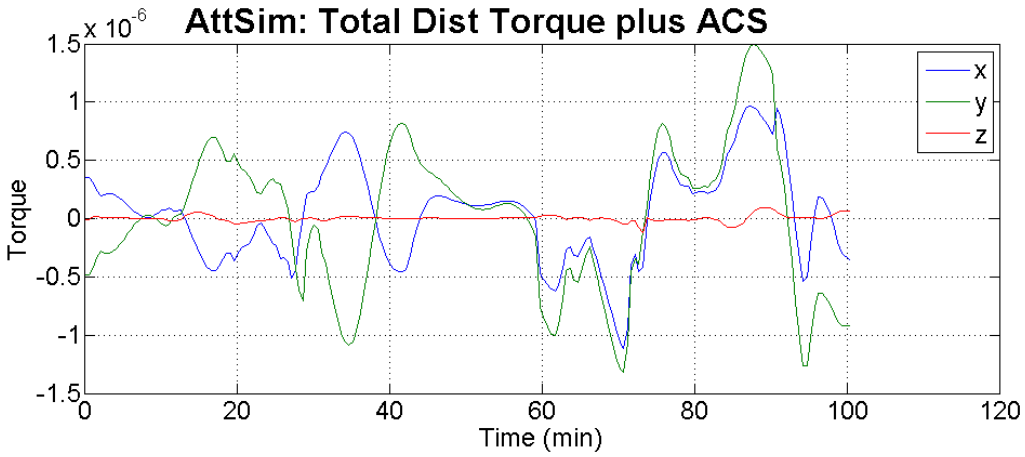

Figure 33 shows the total resultant torque acting on the conical helix WISCER variant throughout its 750km sun synchronous orbit, including both the disturbance torques and achieved ACS torque.

Figure 31 leads to the applied torque we can see in Figure 32, the resulting torque achieved by the total generated magnetic dipole. Figure 33 then shows the final net torque acting on the CubeSat. Ideally this would be near zero with all disturbance torques near completely cancelled out however in this case there are significant residuals leading to the undesirable rotations. Figure 34 shows the angular deviation of all three of the candidate inclinations. The sun synchronous orbit is the third (1.72 rads) graph and is by far the best case. The low inclination orbit shows an almost complete failure of the ACS to oppose the disturbance torques (as compared to a simulation where is it deactivated). This is due to the alignment of the equatorial magnetic field with the primary rotation axis of the disturbance torques.

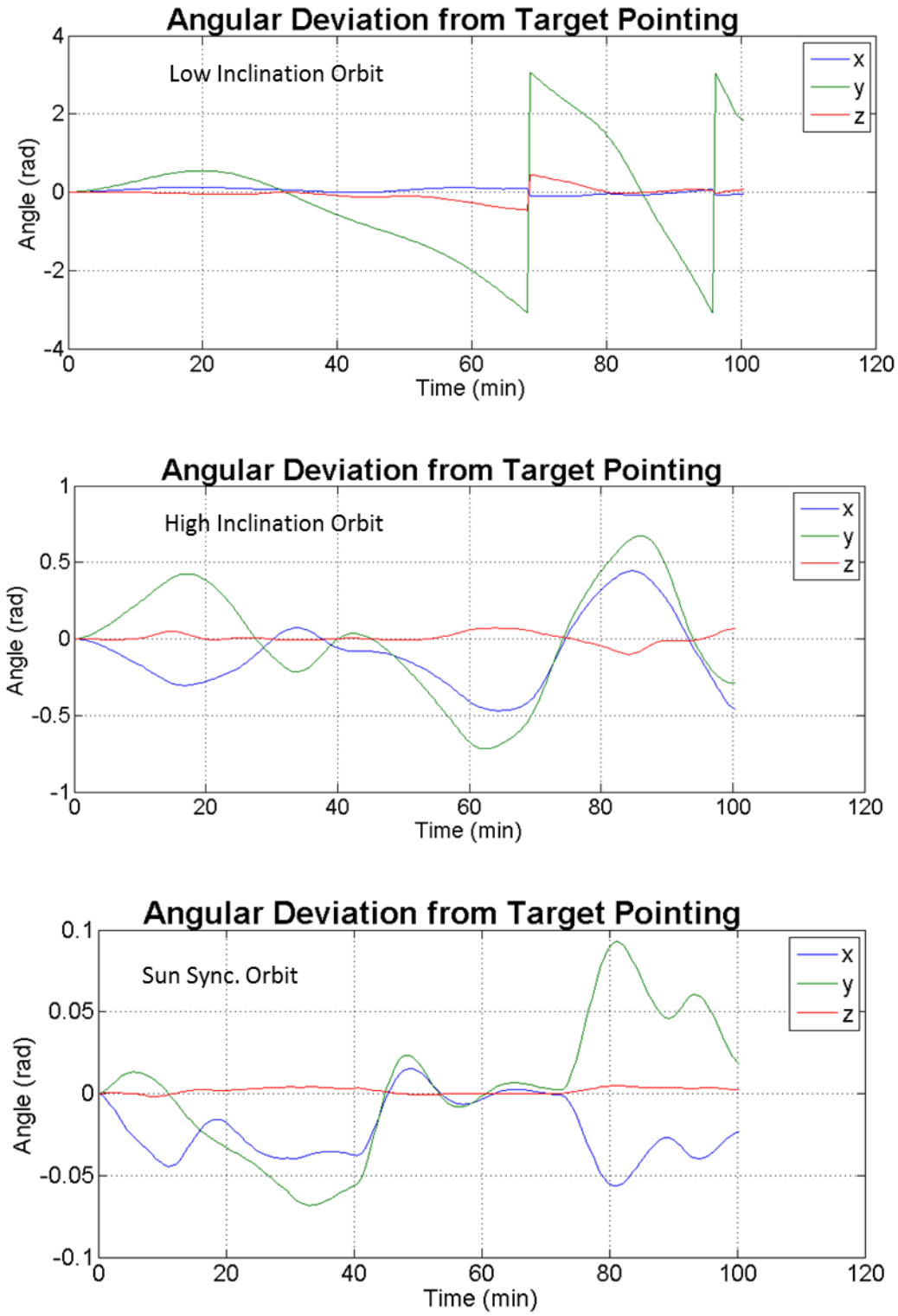

Figure 34 shows the angular deviation for all candidate orbits for the conical helix WISCER variant. Figures prior to this have only shown data for the Sun synchronous orbit. Axes are defined in Figure 24.

In an equatorial orbit with the antenna pointing nadir aerodynamic and radiation pressure torques combine to rotate the satellite in the y axis (LVLH, seen as vertical in the inertial

frame trace of Figure 25). If the alignment was perfect there would be no possible dipole the ACS can use to oppose the rotation. Since the simulation uses the DGRF model of Earth's magnetic field (Bilitza & Papitashvili, 2015), the simulated inputs to the field sensors see a much more complex and realistic field than the simple dipolar view commonly imagined. The deviation in alignment and fluctuations around the orbit lead to at least some corrective torque being generated by the ACS. To achieve this the currents within the magnetorquers needs to be high to provide the reaction against the small axis component of the field. This leads us to notice a compounding issue with the use of a magnetic only control system: the more strain that is placed on the ACS the more power is used. This results in an undesired positive feedback loop when considering that the CubeSat's power source is solar panels which themselves depend on correct attitude for their efficiency.

In conclusion, it is therefore recommended that a magnetic only 3 axis ACS is not applicable to the conical helix antenna WISCER variant due to the nature and magnitude of the disturbance torques. For stable attitude control the use of reaction wheels is recommended. Magnetic control is still applicable for momentum dumping as most integrated contributions from radiation pressure cancel out (Figure 27). Aerodynamic torques will constantly build up angular momentum in the system for a constant nadir pointing attitude but dumping momentum periodically, in a streamlined attitude mode, can mitigate this.

High inclination orbits are most suitable due to the varying magnetic field. Equatorial orbits suffer due the effects of a persistent near alignment with one body axis of the CubeSat. Higher inclination orbits should therefore be considered preferable even if reaction wheels are included. If the final CubeSat design includes a magnetic component

of the ACS another simulation run should be performed to provide further systems engineering data to appropriately size the system.

5.4.2) Crossed Moxon Antenna WISCER Variant

This section presents the results from the simulation run on the crossed Moxon antenna WISCER variant. The CAD model used in these simulations can be seen in Figure 35 and represents a final configuration of the 3U crossed Moxon variant that will be discussed further in later chapters. Note however that the antenna elements are shaped to give a "worst case" scenario for element area. This was chosen for two reasons: the antenna element area is small, providing only a small torque contribution and the final element shape depends on yet to be determined deployment limits.

From Figure 35 it is immediately apparent that we would expect the crossed Moxon to perform much better in the simulation due to the much-reduced surface area over that of the conical helix. Prior to antenna design changes the original drag sail antenna design (Outlined in Chapter 7) with its large surface area posed much more of a concern. Simulations conducted for all the crossed Moxon variants were conducted but this model is believed to be most relevant at this time for future work.

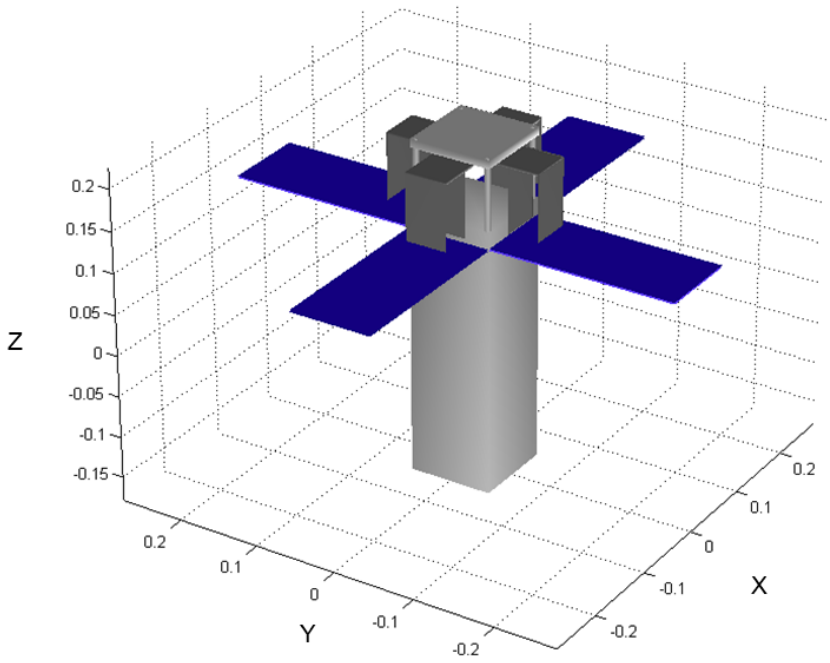

Figure 35 shows the CAD model used in the final crossed Moxon WISCER attitude simulation. The body axes defined will be used by the graphs in this section.

In Figure 36 the attitude trace of the 60° inclination orbit simulation is shown. This inclination was chosen for the example as it has the greatest angular deviation for the chosen simulation settings. This is an arbitrary choice however as all simulations show stable attitude control and minimal pointing error (<1°). Minor changes to the orbit, time or PD controller settings could change this result.

The most significant disturbance torques are shown in Figure 37 through to Figure 40. Note that there is a significant reduction in all three compared to the conical helix, which is due to the reduced surface area of the crossed Moxon. The resulting gravity gradient and aerodynamic torques also have a much smaller fractional contribution to the total disturbance torque. For the gravity gradient, this is due to the near perfect nadir alignment throughout the orbit but also the shorter length of the satellite when compared to the conical helix. The aerodynamic torque is reduced to a similar level mainly due to the much smaller cross section of the antenna and solar panels in the ram direction. This changes if

the attitude control is lost and an angle of attack is presented by the solar panels. This must be considered when we observe the remaining dipole budget.

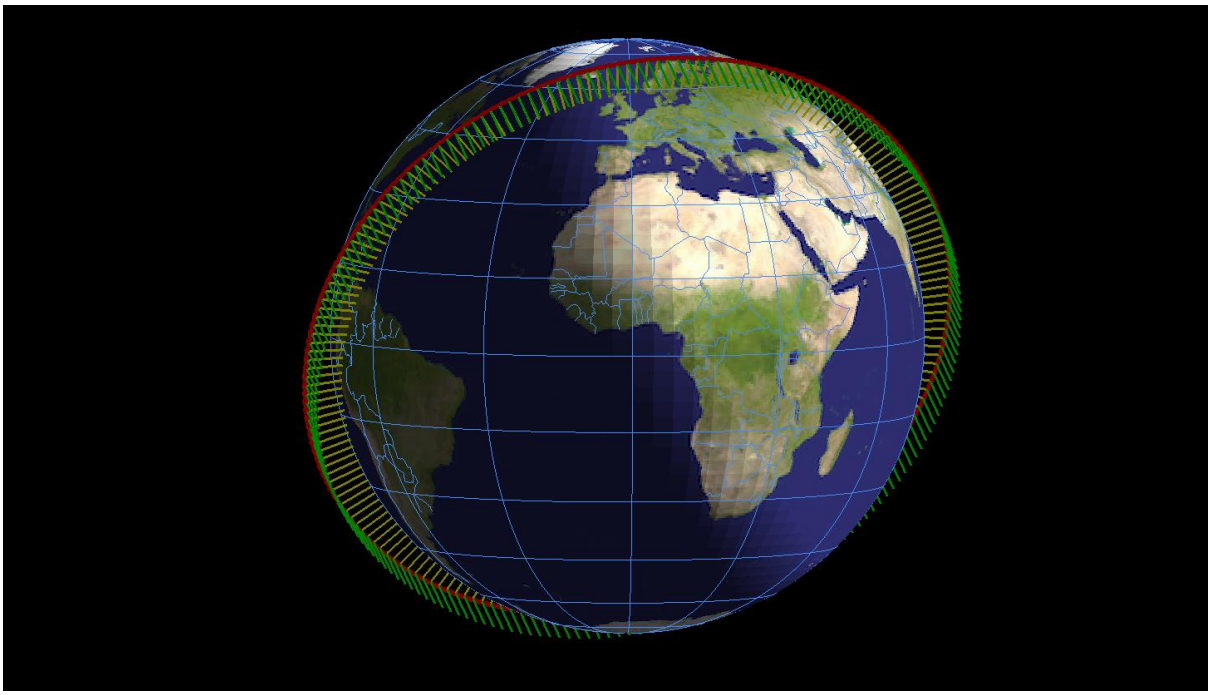

Figure 36 shows the attitude trace of the crossed Moxon WISCER variant in a 750km 60º inclination orbit. The spacecraft body axes are as follows: Red is X, Green is Y and Yellow is Z.

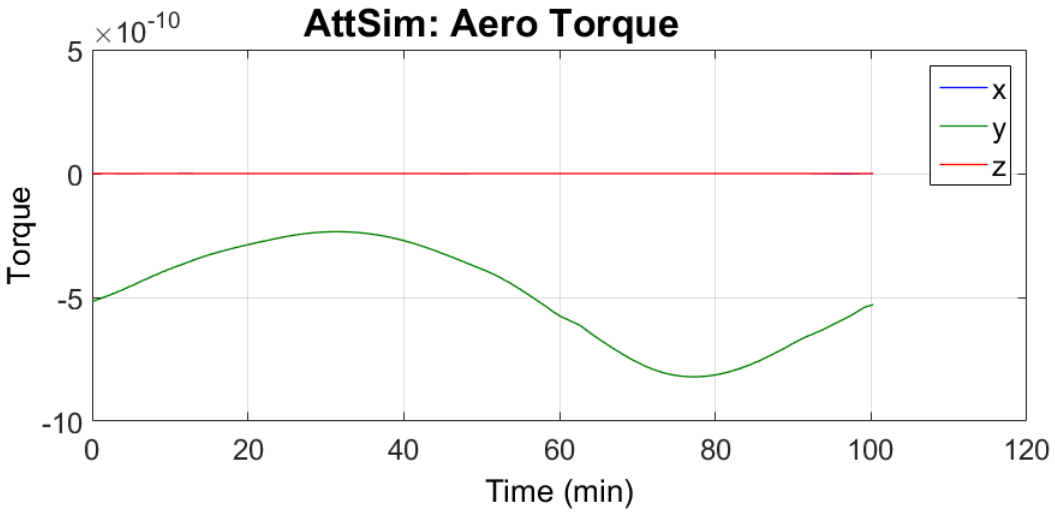

Figure 37 shows the aerodynamic drag torque acting on the crossed Moxon WISCER variant throughout the 750km 60º inclination orbit.

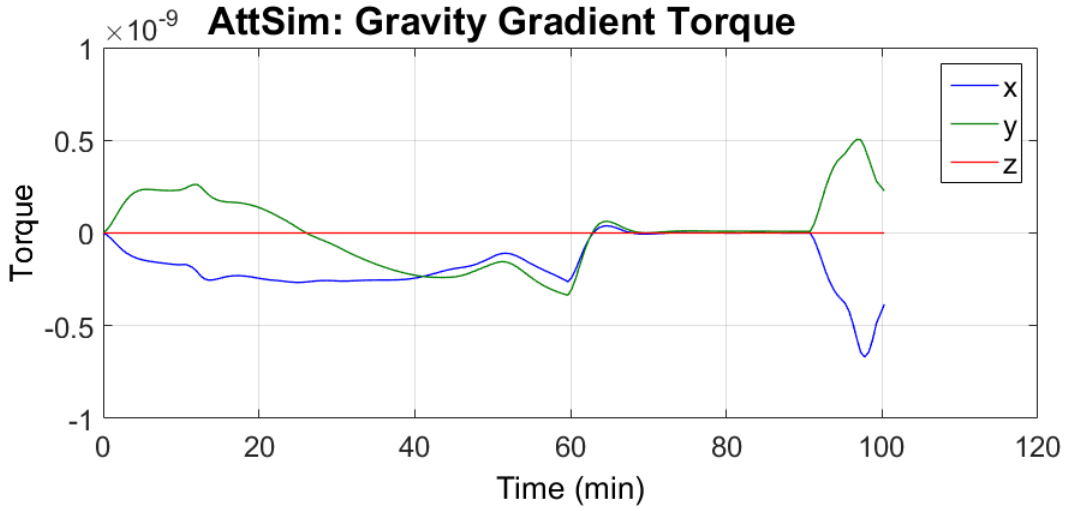

Figure 38 shows the gravity gradient torque acting on the crossed Moxon WISCER variant throughout the 750km 60º inclination orbit.

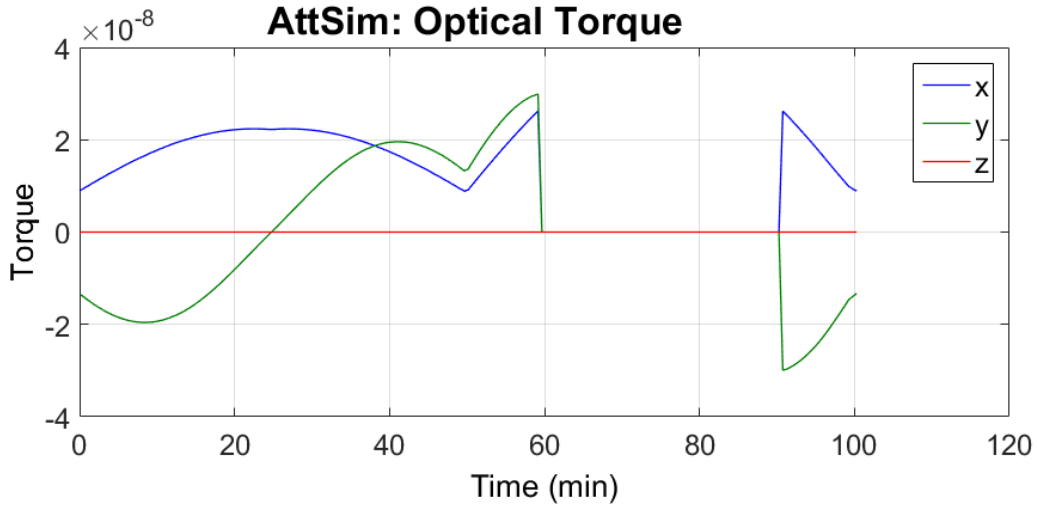

Figure 39 shows the radiation pressure torque acting on the crossed Moxon WISCER variant throughout the 750km 60º inclination orbit.

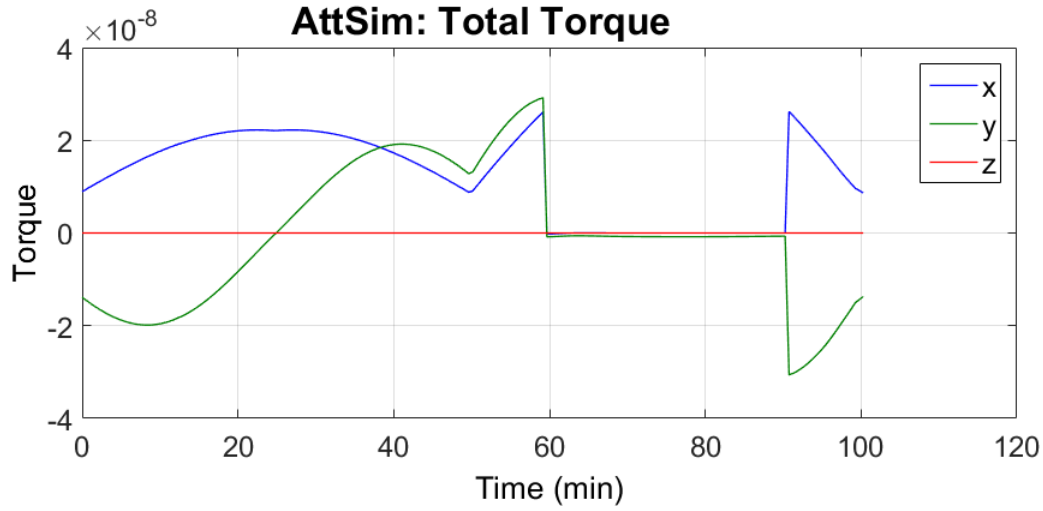

Figure 40 shows the total disturbance torque acting on the crossed Moxon WISCER variant throughout the 750km 60º inclination orbit.

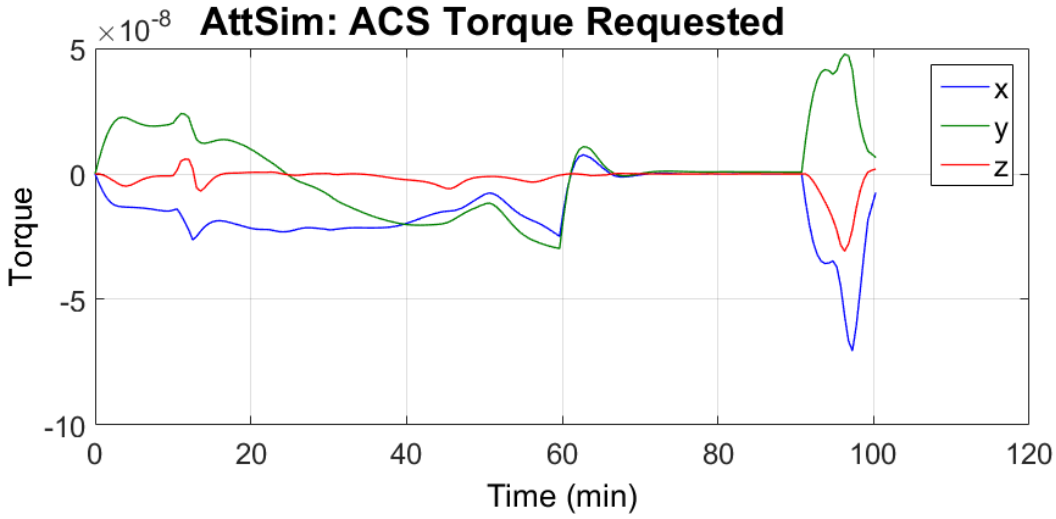

Figure 41 shows the requested torque by the modelled ACS for the crossed Moxon WISCER variant throughout the 750km 60º inclination orbit.

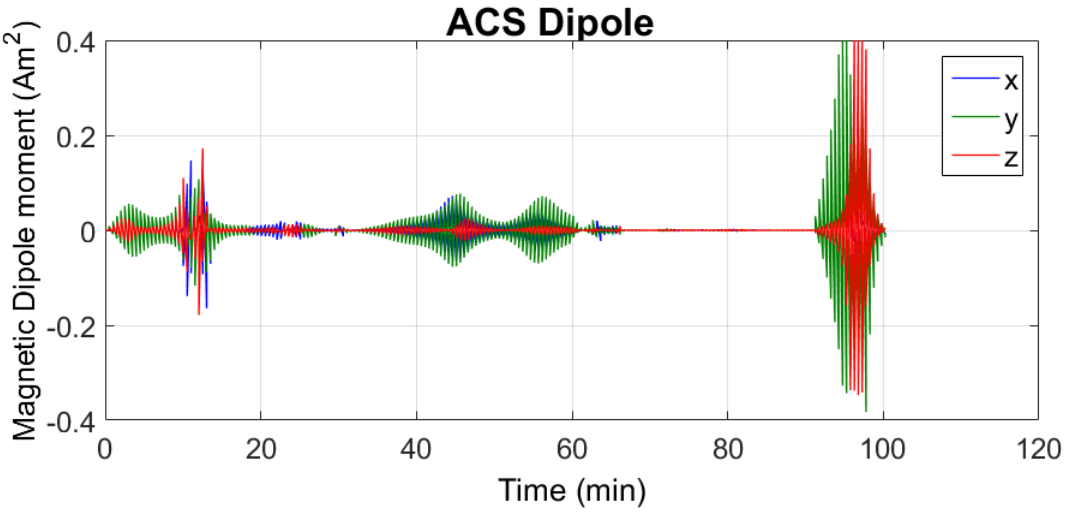

Figure 42 shows the dipole that was calculated by the ACS to achieve the requested torques. All limits are included in the results.

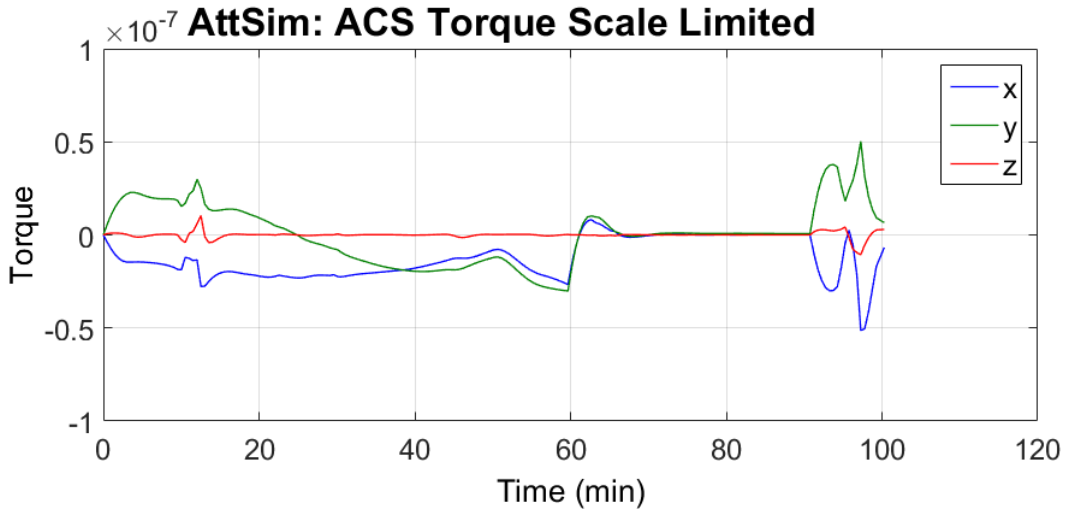

Figure 43 shows the torque achieved by the ACS as calculated from the magnetic dipole with limits.

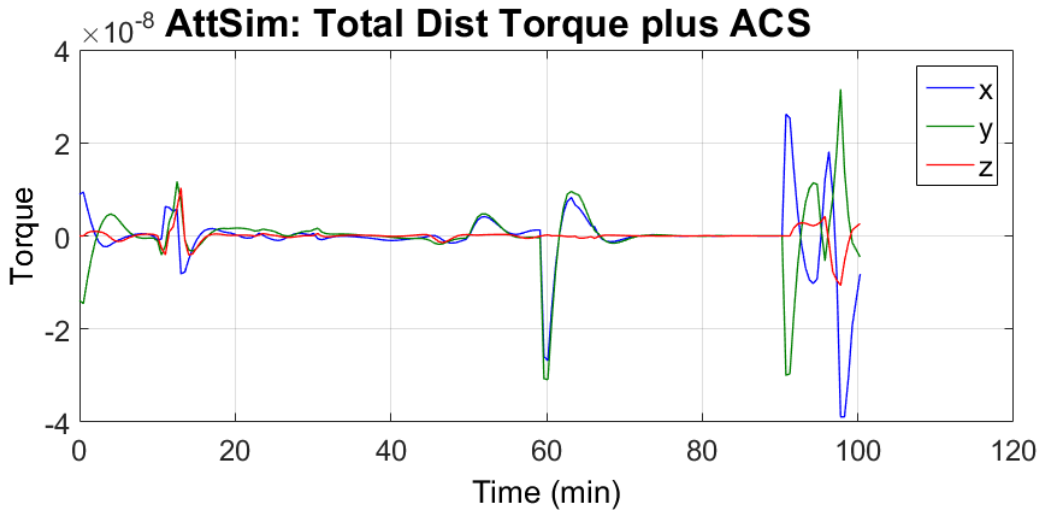

Figure 44 shows the final net torque acting on the satellite including the disturbance torques and the achieved ACS torque.

In Figure 41 through to Figure 43 we see the ACS operating in a stable regime. The requested torque in Figure 41 closely matches the total disturbance torque (primarily the radiation pressure of Figure 39) showing that the PD constants were tuned sufficiently accurately. From this the required dipole is calculated and presented in Figure 42. From this we can see that there was an instance where the dipole limits were applied. However, it was fleeting and therefore most likely caused by a momentarily bad alignment with the Earth's magnetic field. The effect of this is seen to be minimal in Figure 43 where the applied ACS torque is shown. In the stable case, the achieved ACS torque very closely matches the requested torque as would be expected.

Due to the nature of the analytical ambiguity in the calculation of the required dipole and the need for interpolated field measurements, there is also some resolution discrepancy in the system itself when determining the dipole. Initially, this had a significant impact on the simulation before the number of interpolated field measurements was increased. In a real system however, with continuous field measurement and further processing, improvement here should be possible.

Figure 44 shows the resultant torque acting on the CubeSat combining all disturbance and ACS torques. Again, as the attitude is stable there is a near complete reduction of the disturbance torques as they are opposed. Note the two periods however, as the CubeSat enters and exits eclipse. The sudden removal and introduction of light generates a discontinuity in the disturbance torque that is not countered by the ACS until the effect propagates into the angular deviation. It is on exit from the eclipse that there is an unfavourable magnetic field alignment leading to the largest observed angular deviation. Even though the dipole is briefly saturated, stability is maintained due to the disturbance

torque still being smaller than the available ACS torque. Comparison of Figure 40 and Figure 43 show that the margin was small.

Figure 45 shows the resulting angular deviation traces for all three candidate orbit inclinations. The angular deviation in all cases is small and well within the requirements for WISCER. However, if we note Figure 46 we see that a significant fraction of the available dipole is being used in both cases. The equatorial orbit uses a significant dipole proportion for much of the orbit, including one saturation event. Energy usage is therefore high and should be considered in the overall system analysis.

In conclusion, the use of a simple PD control setup for a WISCER ACS simulation has yielded useful insight into the capability of a magnetorquer only system. The limits of such a system and the practicalities of implementation have been explored. At the level of detail and resolution in this simulation, an attitude hold for the crossed Moxon variant, in the worst case orbit of 0.57° from the target pointing, was achieved. The conical helix antenna variant was not stable in any candidate orbit with the applied dipole limits. This disparity is due to the difference in surface area presented to the solar radiation flux, and hence differing disturbance torque magnitudes. Even in the crossed Moxon case the ACS is somewhat unstable due to the variations of Earth's magnetic field through the orbit. A seemingly stable system can become unstable if high disturbance torque coincides with a poorly aligned B field direction. It is, therefore, recommended that WISCER does not rely solely on magnetorquer actuators. The implications of this conclusion for the overall WISCER satellite will be discussed in chapter 7.

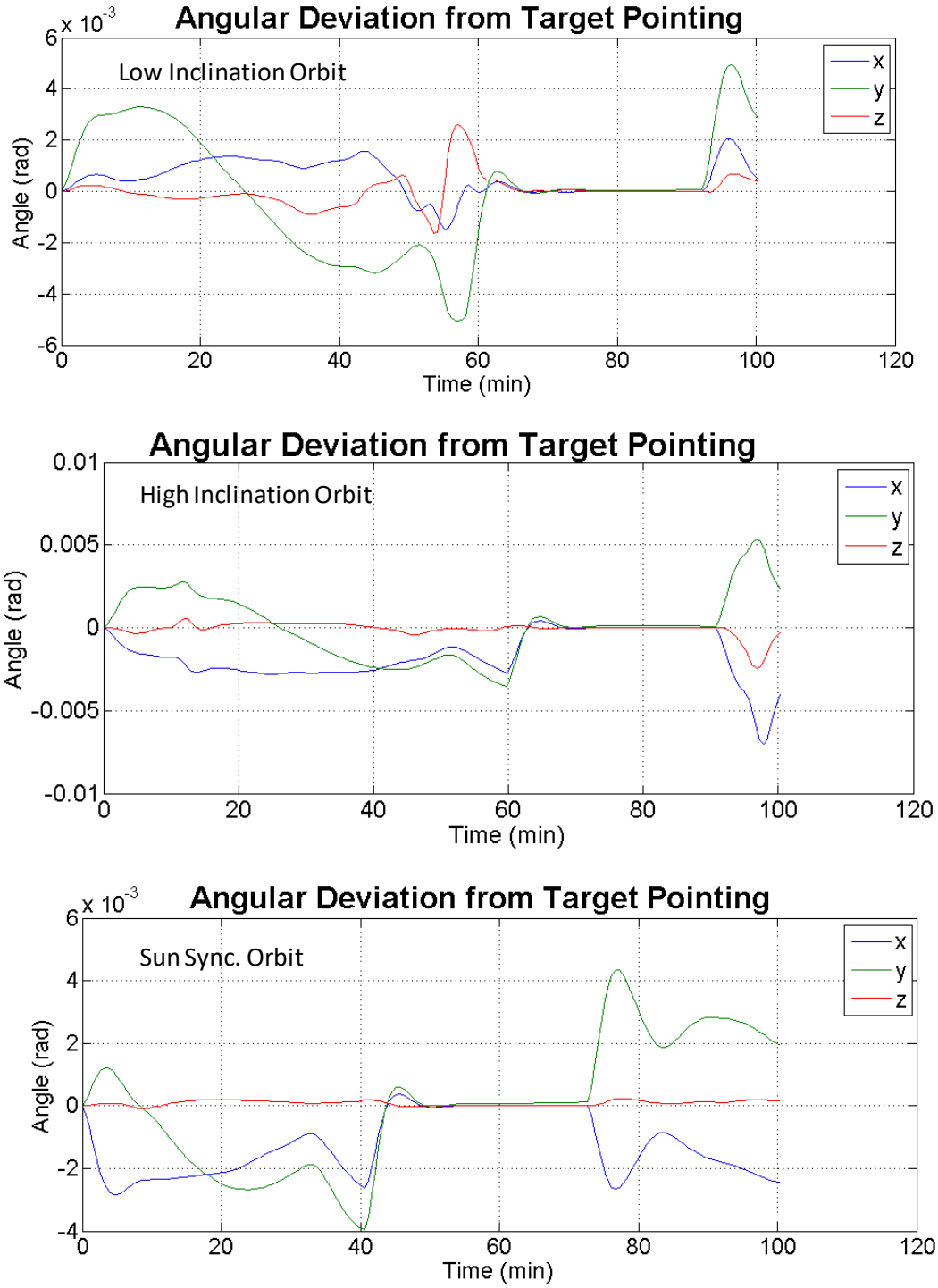

Figure 45 shows the angular deviation for the three candidate orbits at 750km altitude

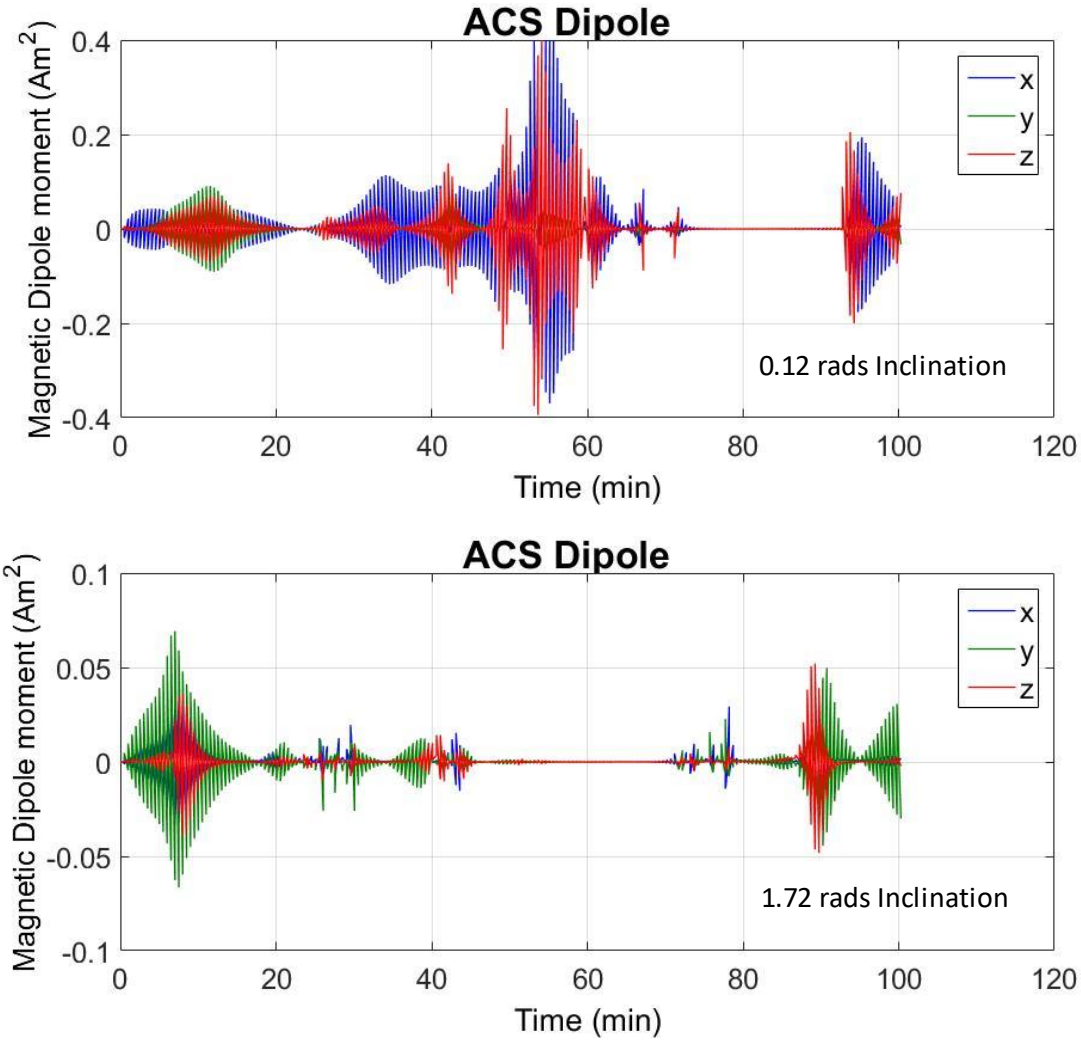

Figure 46 The ACS dipoles for the equatorial and sun synchronous candidate 750km orbits.

CHAPTER 6) LOG-SPIRAL CONICAL HELIX ANTENNA

6.1) Introduction

This chapter describes the development of the inflatable conical helix antenna candidate for the WISCER mission. The down selection to the conical helix and the crossed Moxon was made by Angling et al. (2013) via the comparison of a number of antenna types. A description of the classical conical helix antenna type is provided, outlining required design parameters and the basis for the values that have been initially selected. This section then proceeds to detail the work done to create a simulation of the antenna in the CST Microwave Studio suite. The aim of this simulation is to provide confidence that the specific design alterations necessary for WISCER do not negatively affect the antenna performance. Simulation then also allows optimisations of the antenna to be rapidly explored.

In the second half of the chapter the technology of deployment and practicalities of construction will be addressed. Results will be presented from experimentation with two basic prototypes of the conical helix antenna. These prototypes allowed remaining design questions to be addressed before a design was finalised for a flight opportunity on the REXUS 19 sounding rocket. The results and analysis from the Prototype Inflatable Conical Antenna REXUS Deployment (PICARD) experiment is then presented, following its successful sub-orbital launch in March 2016.

6.2) Log-Spiral Conical Helix antenna

This antenna is formed of two active elements which are shaped into a conical helix. The element's width and wrap follow a logarithmic spiral pattern leading to arms that widen

towards the base of the cone. The antenna parameters are shown in Figure 47 and the dimension of the arms are defined by Equation 30 and Equation 31. The antenna is directional and radiates in the apex direction if fed from that location. The primary parameters used in the definition of the antenna are:

- θ_0 is the cone angle
- α is the rate of wrap of the arms
- δ is the angular width of the exponentially expanding arms
- f_{max} is the maximum required operating frequency
- f_{min} is the minimum required operating frequency

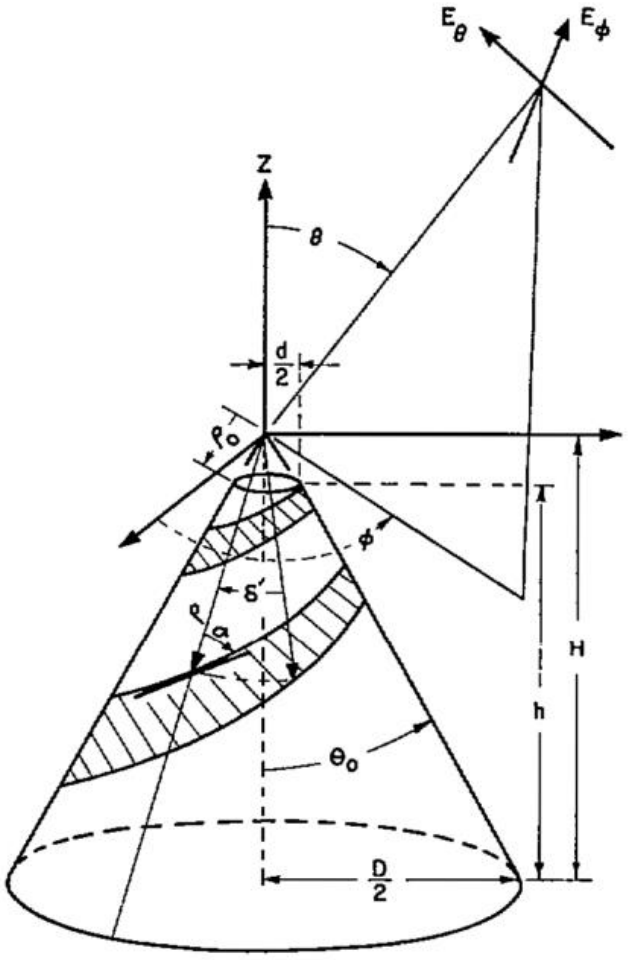

Figure 47 shows the conical antenna with associated parameters (Dyson, 1965).

$$\rho(\varphi) = \rho_0 e^{b(|\varphi| - \delta)}$$ **Equation 30**

Where:

$$b = \frac{sin\ \theta_0}{\tan \alpha}$$ **Equation 31.**

This type of antenna was first characterised by Dyson (1965) with further improvements by Hertel & Smith (2002). These sources were used to determine the initial antenna parameters that should fulfil the operating frequency requirements of WISCER and can be seen in Table 4. The relationship between the antenna frequency extremes and the cone end radii are given by Dyson (1965).

Antenna property	Requirement	Parameter	Initial value chosen
Beam width	120°	Θ_0, α	7.5°, 60°
Min frequency	300MHz	R_{base}	350mm
Max frequency	600MHz	R_{apex}	30mm
Arm Width	No requirement	δ	90°

Table 4 shows the required antenna performance properties and the antenna design properties required to achieve them for the initial conical helix antenna design.

It is proposed here that the use an inflatable deployment method is well suited for the conical helix antenna with the stated parameters. Due to the circular cross section of the cone there will be no pillowing of the inflatable and therefore no deviation of the elements from their correct shape, due to the inflation. The inflatable design will allow the relatively large antenna to be packed into a very confined space for launch (<1U), providing a

significant benefit to the volume budget. Figure 48 shows the inflated conical helix antenna in its deployed state.

For any such inflatable antenna design the metal elements will be necessarily thin to achieve the required flexibility. To provide strength and protect against atomic oxygen erosion the antenna elements are sandwiched between an inflatable bladder and an exterior protective Kapton layer. Further details of the construction techniques used for the PICARD antenna prototype will be outlined later in the chapter.

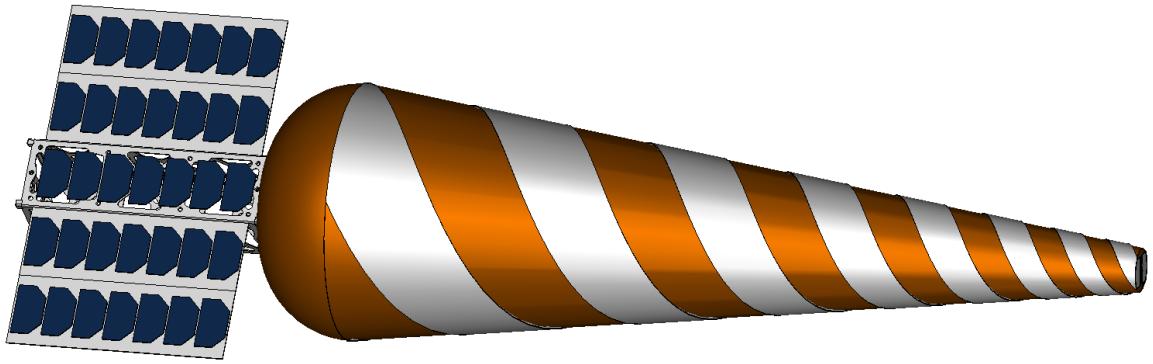

Figure 48 shows the fully inflated conical helix antenna with attached CubeSat and one possible configuration of solar panels.

Figure 49 shows a possible stowed configuration of the inflatable prior to deployment (Angling, Cruise, Hoyland, Harkness, & Drysdale, 2012). Compressed gas is not permitted aboard CubeSats during launch and so an alternative is required to inflate the balloon. Cool gas generators (CGG) will, therefore, be used to provide the necessary quantity of gas for inflation, from a solid powder contained within them. Figure 50 shows an example of such a COTS cool gas generator.

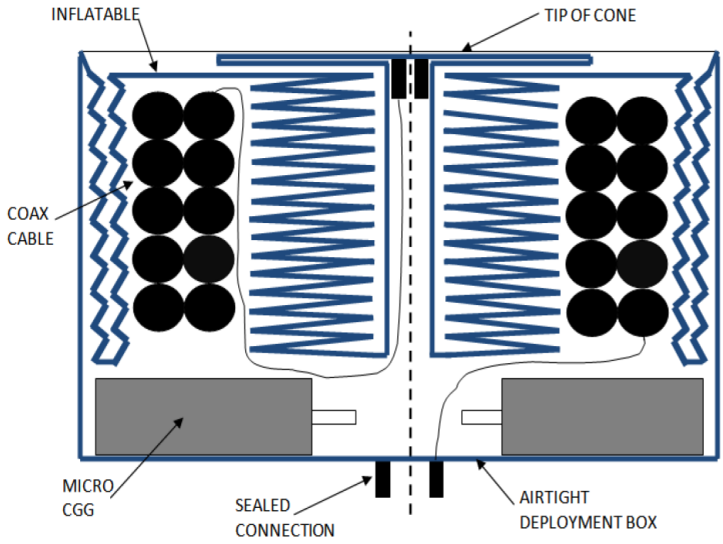

Figure 49 shows the stowed configuration of the antenna prior to deployment (Angling, Cruise, et al., 2012).

Figure 50 shows a cool gas generator to scale against a 1 Euro coin.

Figure 49 also shows the feed line for antenna. As the antenna feed point is at the apex of the inflatable, the cabling will be required to deploy along the interior length. The two feed line configurations available for the apex fed conical helix are: A single coaxial cable feed where the shielding is bonded to one of the antenna arms and a dual coaxial cable feed where the shielding of each line is bonded together. The second configuration requires a balun but is expected to provide an advantage in manufacture and so was selected. Both configurations will require impedance matching at the antenna apex if standard coaxial cable impedances are used. More detail is available on the configurations themselves in Hertel & Smith (2002) and Dyson (1965) respectively with section 6.4.2 also providing further details on the design selected for prototyping.

6.3) Simulation of the Conical Helix Antenna

In this chapter the properties of the conical helix will be evaluated using the CST Microwave studio package. Parameterised simulations were conducted to investigate different aspects of the design. For conciseness, only the main results will be shown here and the outcome of the other simulations will be briefly described where relevant.

A CAD model of the most basic conical helix antenna (Dyson, 1965) was first evaluated to provide a baseline with which to compare the modifications required for the WISCER deployment and experimental requirements. The antenna support structure was then be added to the CAD model.

6.3.1) Basic conical helix design

To create a baseline result for further work a simple model of the conical helix antenna was created using the parameters in Table 4. The antenna elements for this simulation were generated using an analytic face feature within the CST software using the Cartesian form of Equation 30, shown by Equation 32 through to Equation 36. The base and apex are then both cropped to the end diameters calculated from the intended frequency range, giving the CAD model seen in Figure 51.

$$X = \rho_0 e^{b(u-v)} \sin(\theta_0) \cos(u) \qquad \textbf{Equation 32}$$

$$Y = \rho_0 e^{b(u-v)} \sin(\theta_0) \sin(u) \qquad \textbf{Equation 33}$$

$$Z = \rho_0 e^{b(u-v)} \cos(\theta_0) \qquad \textbf{Equation 34}$$

$$\text{for, } 0 < u < \varphi + \frac{\pi}{2} \qquad \textbf{Equation 35}$$

and, $0 < v < \frac{\pi}{2}$ **Equation 36.**

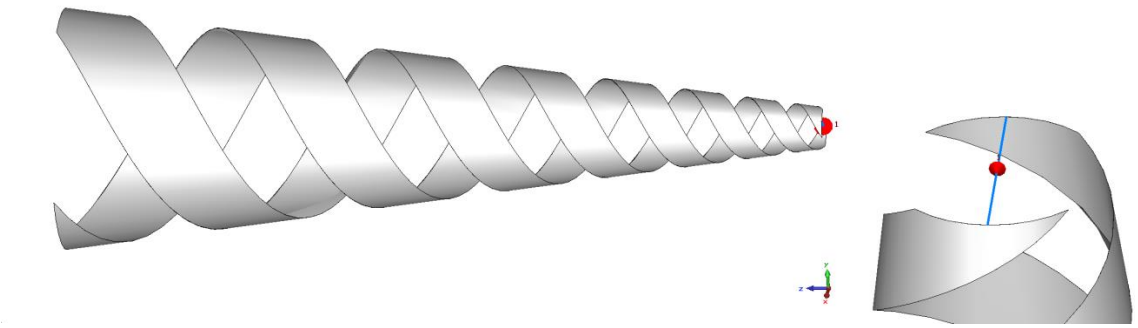

Figure 51 shows a CAD model of the conical helix in its most basic form defined by the values in Table 4. The material used for the elements is aluminium. The antenna feed position is shown on the right.

Figure 52 shows the left hand circularly polarised farfield pattern of the antenna. The pattern is very smooth with a 3dB beam width of 116.4° and a peak directivity of 5.69dBi. These properties are well suited to a low pointing accuracy CubeSat mission.

The antenna feed position was chosen carefully in Figure 51 in order to obtain the flat impedance performance as a function of frequency seen in Figure 53. Movement of the end positions of the dipole feed in either direction along the apex edge causes a deterioration of the flatness of the impedance response at frequencies higher than 300MHz. It can therefore be inferred from this result that the optimum way to feed the antenna is down the centre of an arm. Any physical feed setup should attempt to be symmetrical about the centre line of the antenna arm to achieve this. The results match very well with those presented in Hertel & Smith (2002) lending confidence to the validity of this simulation.

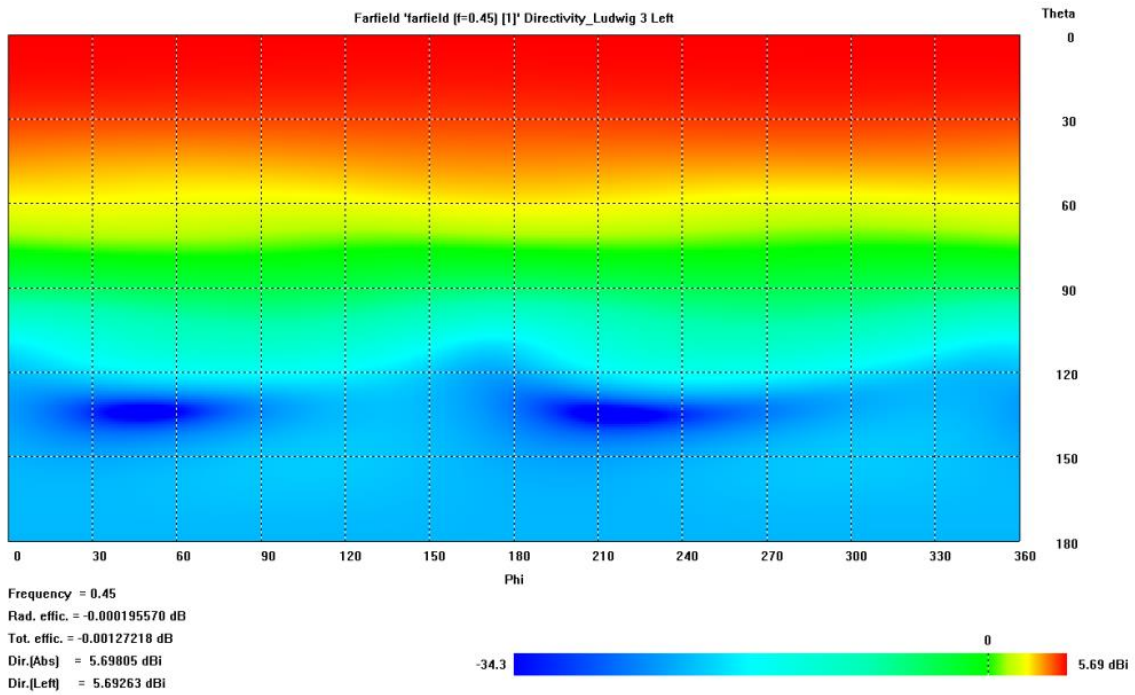

Figure 52 shows both the 2D (Ludwig) left hand polarisation farfield pattern of the basic conical helix antenna.

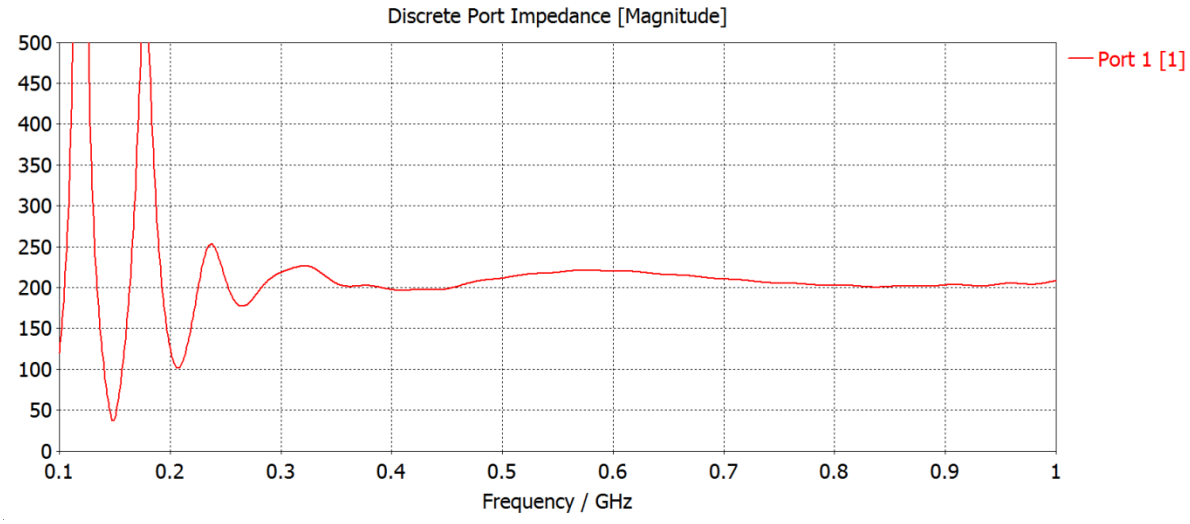

Figure 53 shows the impedance as seen from the discrete port feeding the antenna as a function of frequency.

Figure 54 shows the S11 response of the antenna given that the impedance of the feed is set to 200Ω. S parameters are used to describe the input-output relationship in electrical systems. S11 represents the power reflected into the input port. The simplified conical helix antenna model is shown to be wideband over the frequencies considered and has a very low S11, also known as the reflection coefficient, of approximately 0.05 above

250MHz. This suggests that a smaller antenna could fully fulfil the operating bandwidth requirements of WISCER (300-600MHz).

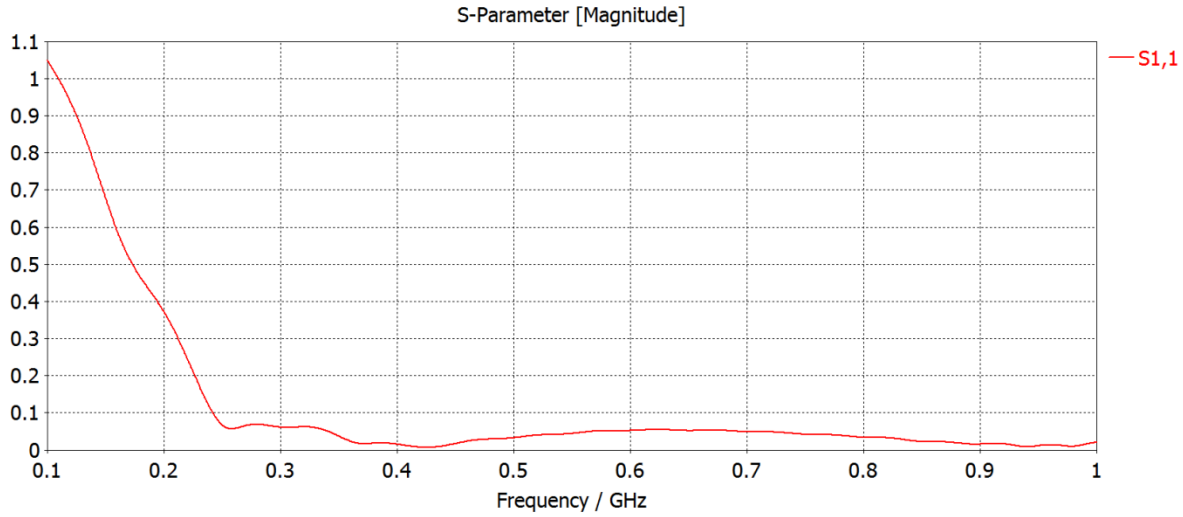

Figure 54 shows the antenna S11 response when the discrete port feed has a characteristic input impedance of 250Ω.

The trans-ionospheric signal from WISCER is to be used to investigate a range of ionospheric effects. In order to measure multipath spread, there are two requirements on the antenna time domain dispersion, that come from Table 2.

- The waveform should be capable of measuring multipath spread of 5μs minimum.
- The waveform should be capable of measuring multipath with a resolution better than 0.02μs minimum.

This leads us to the requirement to minimise the antenna time domain dispersion in order to achieve these measurements and accuracies.

Figure 55 shows the signals seen at the input port of the antenna. The red line is the incident power signal on the antenna from the port. This driving pulse has a length of 5ns with a Gaussian amplitude profile. The green line shows the reflected signal back into the port. The impedances are well matched at 200Ω with minimal energy being reflected to the

input. Around the 20ns mark we can see a signal that is the reflection from the base of the antenna. Work in this thesis has not focused on minimising this effect but initial mitigating possibilities are outlined in (Hertel & Smith, 2002).

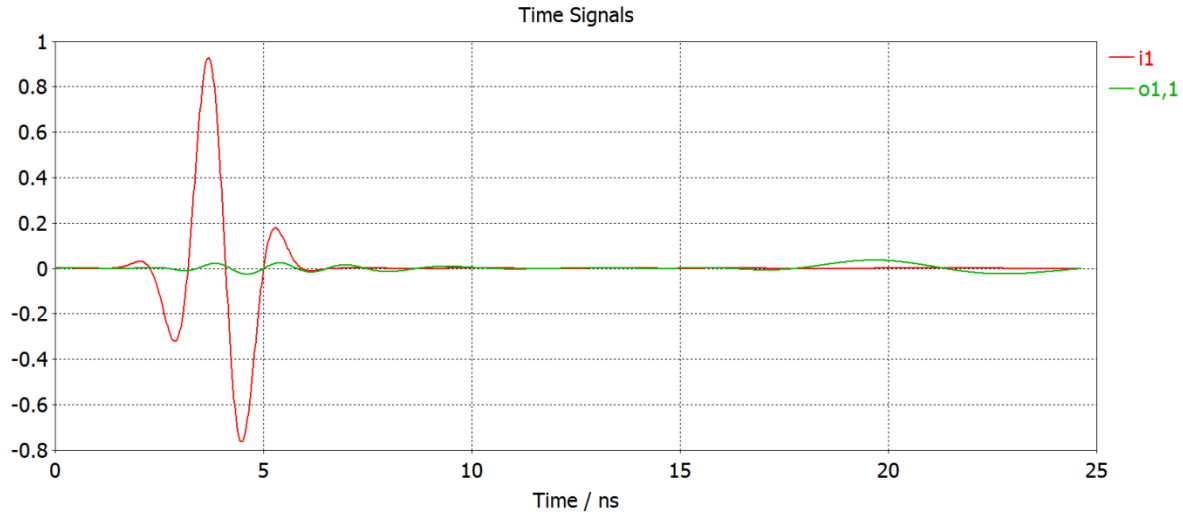

Figure 55 shows the time domain port signals for the conical helix with the input pulse in red and the returned signal in green. Note the reflection from the base of the antenna at 20ns.

Figure 56 shows the time domain E field signals as calculated at a point directly in front of the antenna, along the antennas axial vector. The circular polarisation can clearly be seen in the combination of the x and y components. As shown in these results, and in agreement with Hertel & Smith (2003), the conical helix antenna has the interesting property of dispersing different frequencies in the time domain. The high frequencies are radiated first by the tightly spiralled section near the antenna feed. As the feeding signal travels down the antenna to sections with larger radii the lower frequencies are then emitted. This leads to time domain dispersion on the order of the time it takes the signal to travel down the antenna elements for the whole signal. Using the dispersion measurement technique of Schantz (2004), a value of 0.014µs was determined. This is sufficiently within the requirement and so the conical helix is suitable for WISCER in this respect.

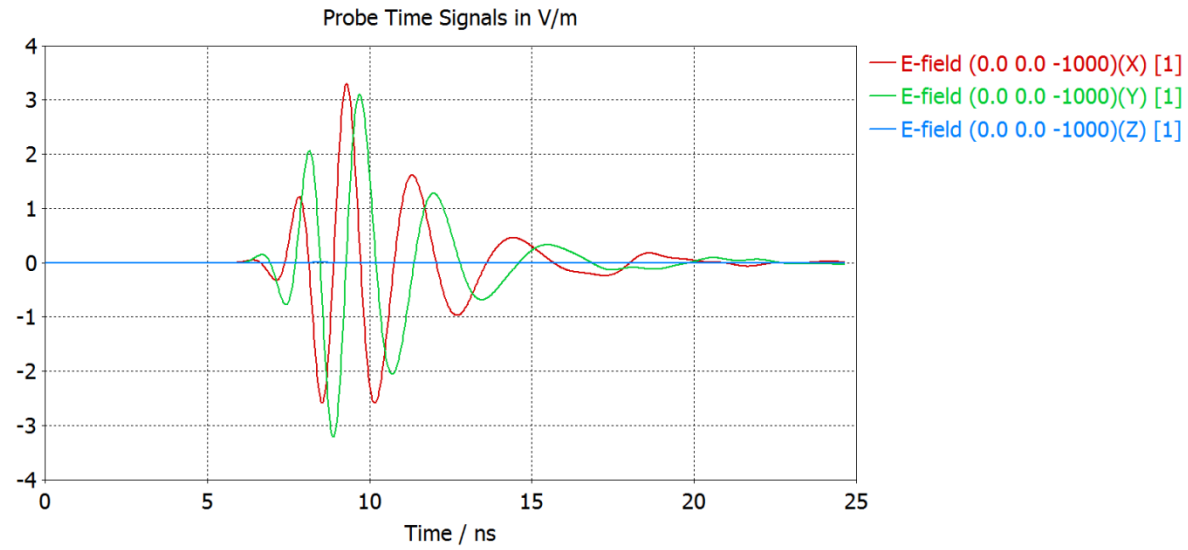

Figure 56 shows the time domain E field signals from the conical helix as measured by a near field probe.

6.3.2) Structure for inflatable deployment

In the previous section the simulated properties of the free space conical helix antenna were presented. For the WISCER experiment however there will need to be additional supporting structures and components. Their addition may affect antenna performance negatively and therefore must be investigated. The three most likely sources of impact are:

- the material of the inflatable itself due to its close proximity to the antenna elements,
- the antenna feed structure as it is possibly in the path of forward radiation,
- the coaxial feed line running from the base of the antenna,
- the CubeSat body itself.

The simplest addition to the previous model is to add the inflatable material. Figure 57 shows the CAD model of this design. The antenna elements are 25µm thick with the protective Kapton layer set to 50µm thick. The materials dispersive properties are

approximated using a very similar polyamide material contained within the CST material library. The feed remains identical to that in Figure 51.

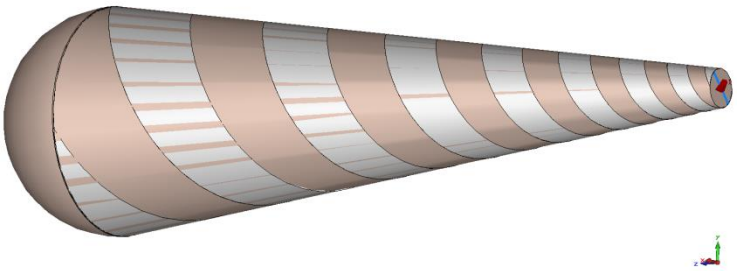

Figure 57 shows the conical helix antenna with the Kapton inflatable included.

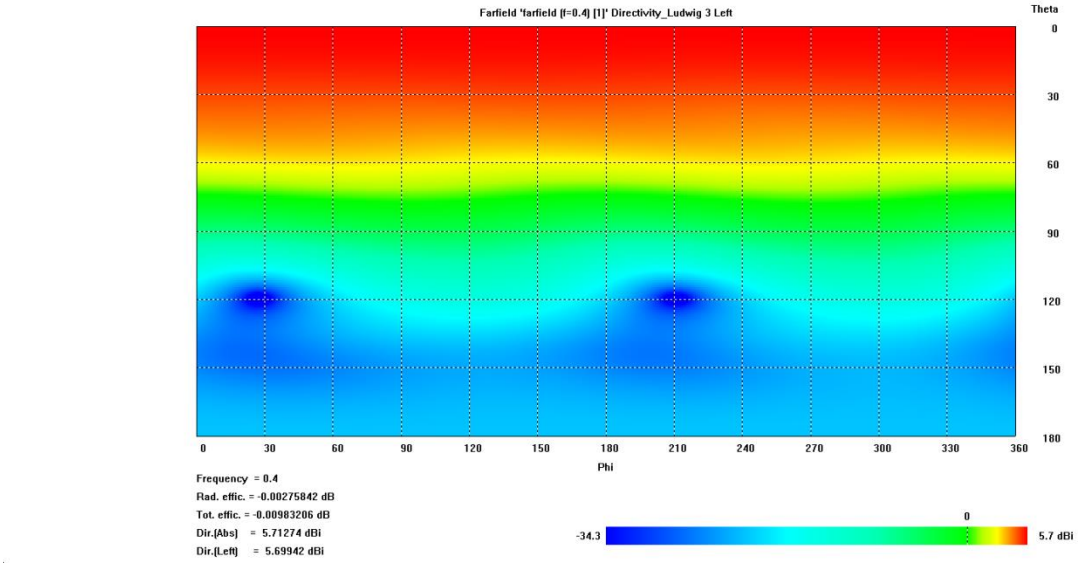

Figure 58 shows the left hand circularly polarised farfield pattern of the conical helix antenna with the addition of a Kapton inflatable.

Figure 58, Figure 59 and Figure 60 show the minimal effect on the antennas properties due to the addition of the structure. The farfield pattern and S11 response remain almost identical, with the only notable difference being the increase in input impedance at high frequencies (above those intended for WISCER). Based upon these simulations it is therefore not expected that the balloon will have a meaningful impact upon the antenna. Further models were created including the feed support structure, coaxial feed cable

(running in free space down the centre of the balloon) and the addition of the CubeSat body with the solar panel configuration seen in Figure 48. All these models also showed minimal impact to the antenna performance.

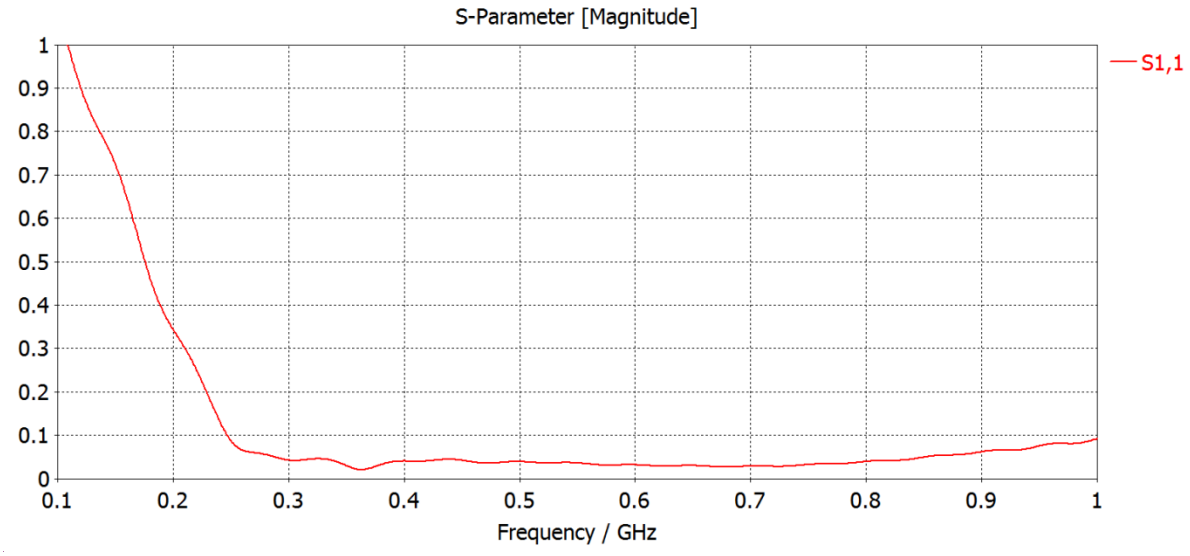

Figure 59 shows the S11 plot of the left hand circularly polarised farfield pattern of the conical helix antenna with the addition of a Kapton inflatable.

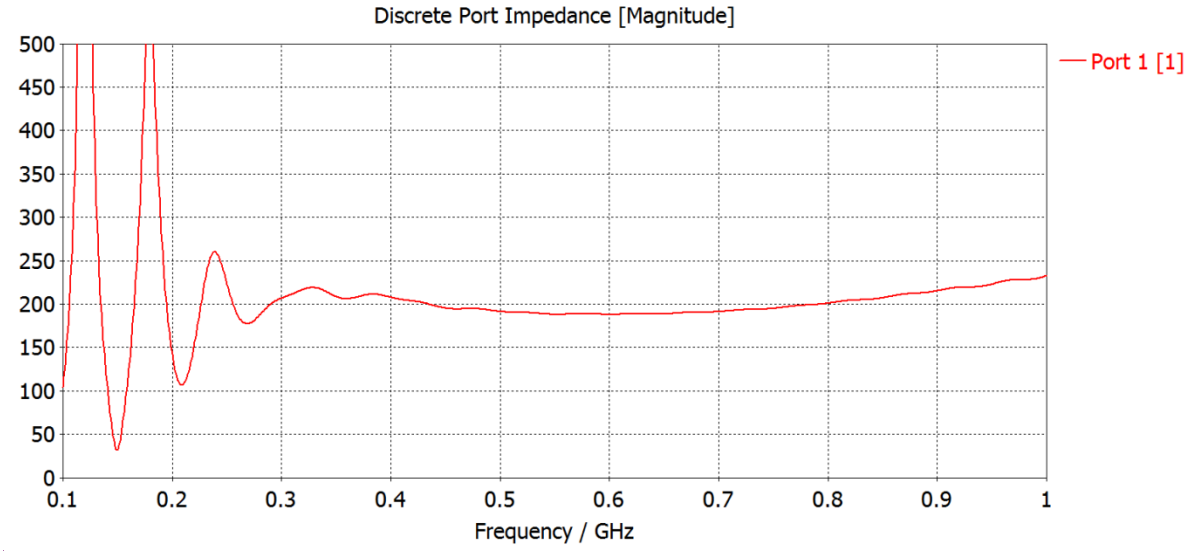

Figure 60 shows the impedance at the feed point as a function of frequency for the conical helix antenna with the addition of the Kapton inflatable.

6.4) Initial testing - Reduced Scale Prototype

Computer modelling of antennas allows for rapid development of their design. However, the process of manufacture and practicality of construction should be included in the design process from the start. For the novel structure and deployment of the conical helix WISCER antenna, this is of key importance. Therefore, an initial prototype of the conical helix antenna was produced. The objective was to facilitate experimentation with construction and test the basic antenna operation. Creating such a prototype provided confidence that the simulations were producing results accurate enough to further inform design choices. Experimentation with the feed setup was also required to gain an understanding of the applicability of designs such as that in Hertel & Smith (2002). This section will describe this work and the construction of two antenna prototypes.

A one third scale antenna was required to raise the operating frequency for these tests, as the largest anechoic chamber at the University of Birmingham has a minimum frequency of 800MHz. Full scale chamber tests or tests at an outdoor range would be required for the final flight design, but this was not possible in this project.

The first consideration is the accuracy to which the antenna elements can be manufactured. To generate the correct curve for the helical antenna elements (Equation 30) on a flat net it is necessary to transform from a conical surface to a 2D Cartesian coordinate system.

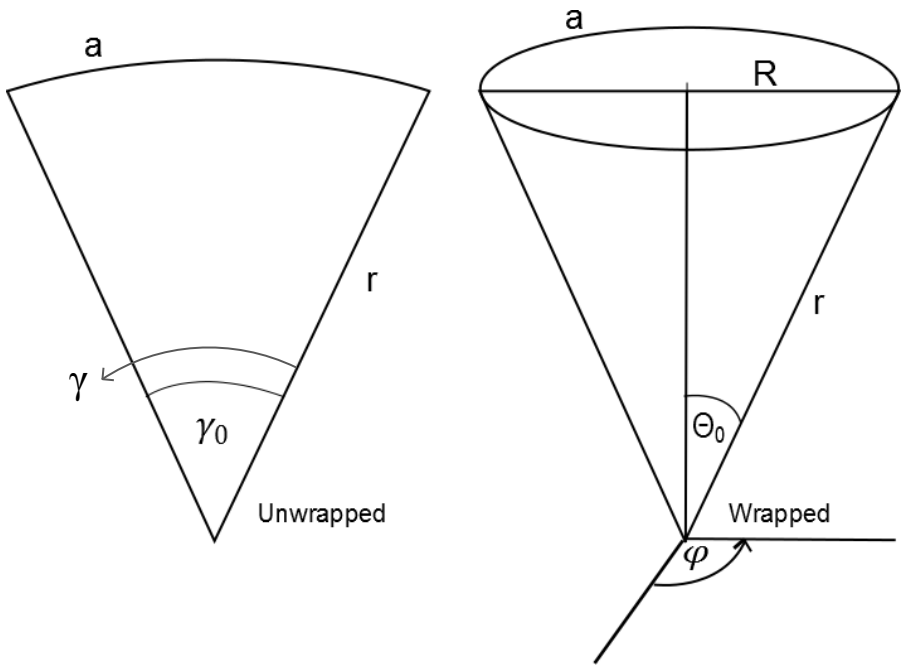

Figure 61 shows a diagram of the wrapped and unwrapped conical geometries.

The conversion process is simplified due to the polar coordinate system used in Equation 30. From Figure 61 we can see that r will remain the same for each coordinate system but φ must be mathematically unwrapped to form γ. Equation 37 shows the conversion from φ to γ but yields the requirement for knowledge of γ_0. Equation 38 through to Equation 41 shows how this can be found based on knowledge of φ and θ_0. Equation 42 shows the final relation which was used to derive the conversion to Cartesian coordinates for Equation 43 and Equation 44.

$$\gamma = \frac{\gamma_0}{2\pi}\varphi \qquad \textbf{Equation 37}$$

$$a = r\gamma_0 \qquad \textbf{Equation 38}$$

$$a = 2\pi R \qquad \textbf{Equation 39}$$

$$R = r\ sin\theta_0 \qquad \textbf{Equation 40}$$

$$\gamma_0 = 2\pi \sin\theta_0$$ **Equation 41**

$$\gamma = \varphi \sin\theta_0$$ **Equation 42**

$$X = \rho_0 e^{b(|\varphi| - \delta)} \cos(\varphi \sin\theta_0)$$ **Equation 43**

$$Y = \rho_0 e^{b(|\varphi| - \delta)} \sin(\varphi \sin\theta_0)$$ **Equation 44**

Figure 62 shows the resulting net that when wrapped on to the conical surface forms the correct antenna structure. The cut in the net design spirals in along the edge of one of the antenna arms. This allows the cone to be wrapped onto the cone without the need to join the antenna elements, leaving them in a single undisturbed piece. The circular sections of the net, at the top and bottom of the spiral, act as cutting guides but also as tabs with which are used to attach the antenna to the feed line.

There are many ways in which the antenna elements and balloon structure could be manufactured. For this prototype, an etching method was selected primarily due to its size. Commercial etching and metal printing services are increasingly available for flexible substrates. These services provide rapid and accurate production but only for limited substrate sizes and on a limited number of substrate materials. Kapton is a frequently used substrate due to its heat resistance. The net size of the third scale prototype was just within the capabilities of Printech Circuit Laboratories (PCL) Limited and they produced both prototype nets. At the time of writing it was not possible for PCL to print the full size antenna net without multiple prints and joins. An alternative supplier would be favourable for larger antennas, as joins are undesirable. The computer controlled etching used here allows the manufacturing tolerances to be reduced (<0.1mm) and, therefore, effectively removes this variable from this test (alterations of less than 1mm to the antenna elements

do not show significant results deviation in simulation). This is beneficial as it reduces the number of confounding variables that must be considered when validating the CST results.

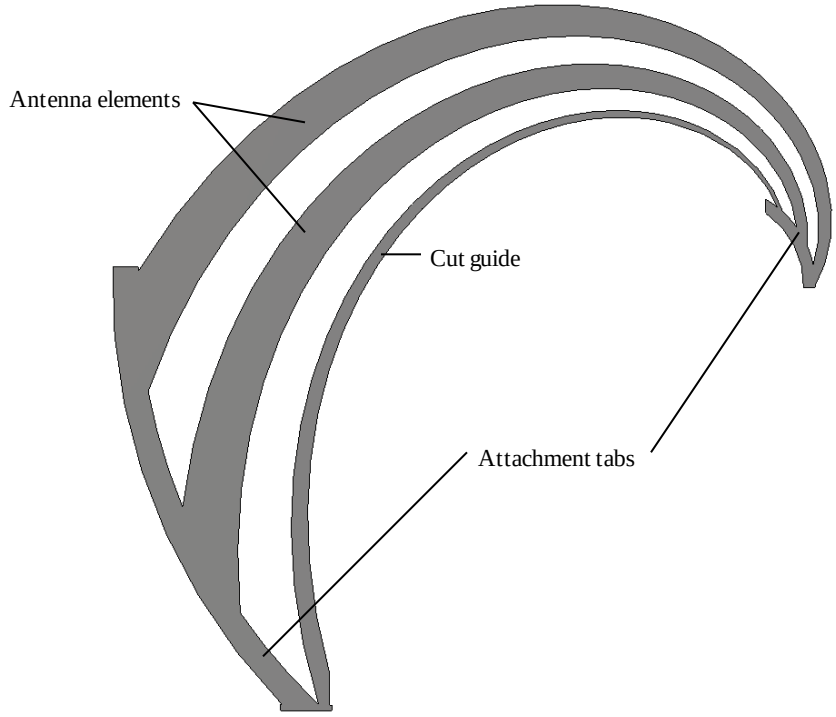

Figure 62 is an image of the prototype net design that has been created. The spiral will wrap onto the exterior of the balloon with no need for joining. Excess tabs at both ends allow for easy electrical connections and cutting guidance.

Multiple feed designs have been suggested in previous works (Hertel & Smith, 2002) (Sakovsky et al., 2015) (Dyson, 1965). Two feed designs were selected for testing: a bonded dual coaxial cable and balun setup, and a single coaxial cable with the sheath bonded to the second antenna element. As the exact feed line setup could not be determined in all cases beforehand, a simplified CAD model of the antenna was created to provide a coarse prediction for the tests. This model included copper antenna elements with a CST dipole feed but did not include the structure of the balloon. These results can be seen in Figure 63 through to Figure 66 and clearly show that the combination of design parameters from Dyson (1965) and Hertel & Smith (2002) have been correctly rescaled as the antenna is active across the intended 900-1800 MHz bandwidth.

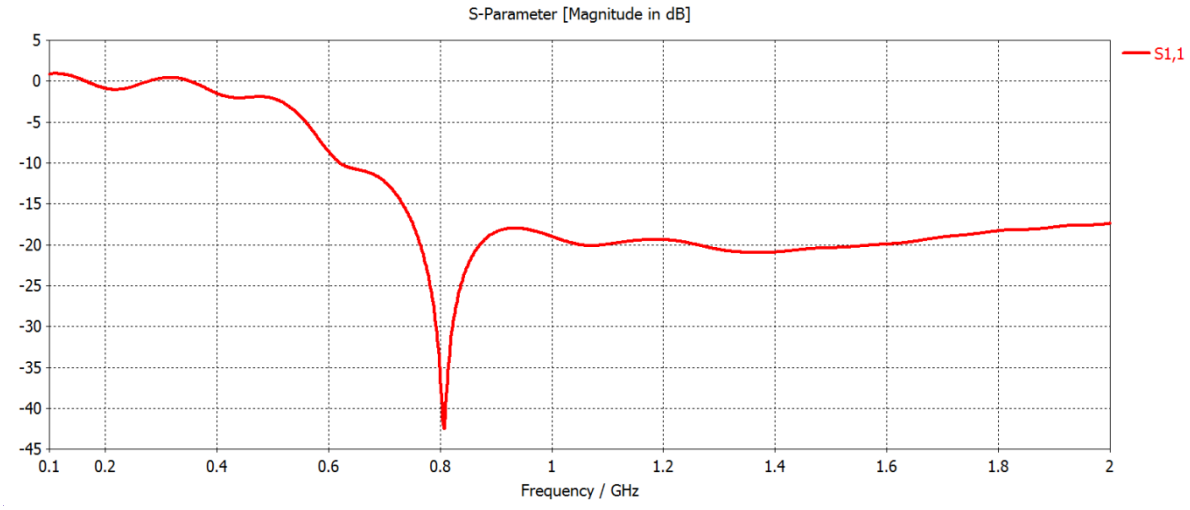

Figure 63 is a prediction of the S11 profile for the Prototype 0.93-1.50 GHz conical helix antenna.

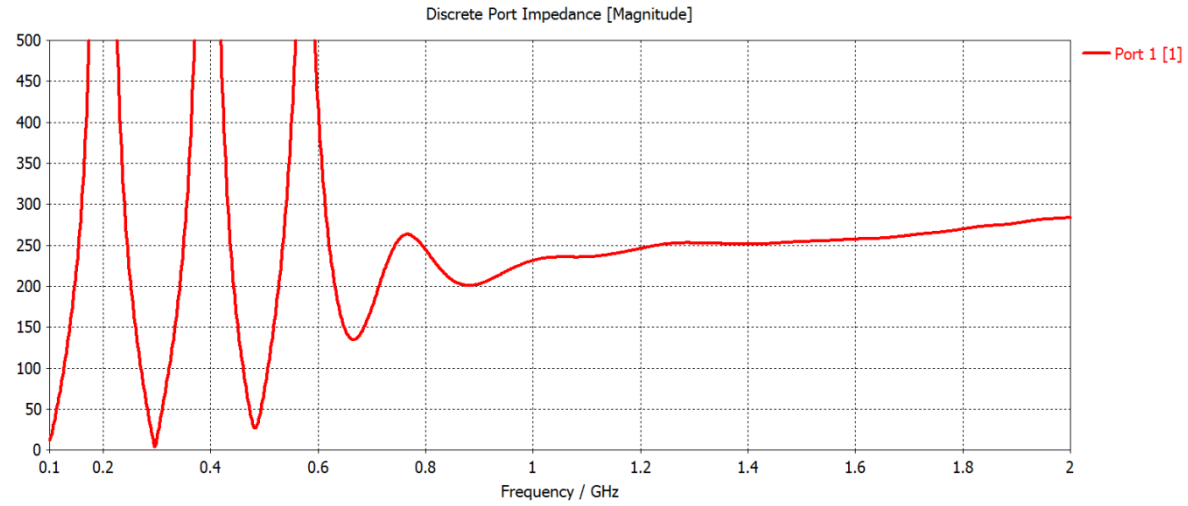

Figure 64 shows model results for the predicted impedance of the prototype conical helix antenna.

There are several differing factors between the simulation and the prototype configuration. Therefore, the S11 profile in Figure 63 is not expected to closely match the physical results, but it provides a reference in order to determine if there is a significant discrepancy in the antenna's central frequency. Figure 64 shows the expected antenna impedance of approximately 250Ω. This predicted value is not expected to be accurate enough to provide a perfect match to the real antenna. Therefore here, easily obtainable 50Ω components were used and the mismatch measured.

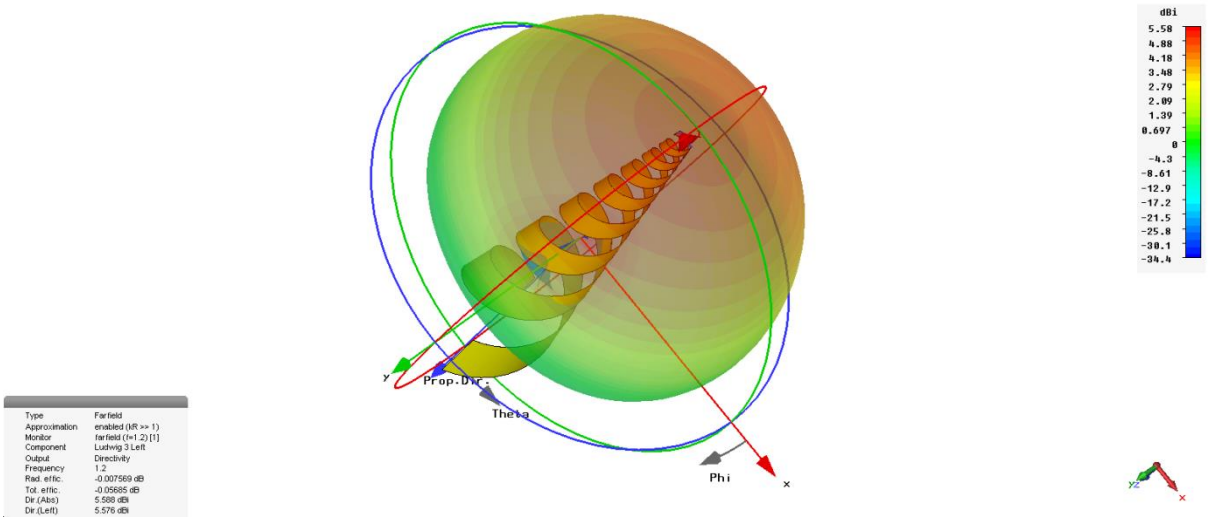

Figure 65 shows the farfield radiation pattern for left hand circular polarised radiation of the prototype conical helix antenna.

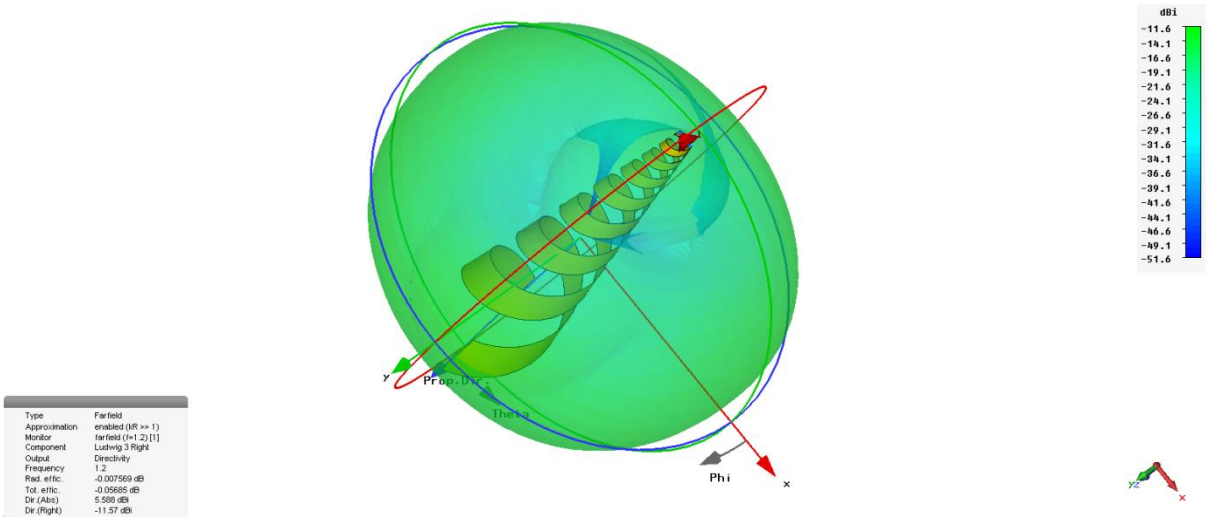

Figure 66 shows the far field radiation pattern for right hand circular polarised radiation from the prototype conical helix antenna.

Measurement of the antenna radiation pattern is possible within the University of Birmingham anechoic chamber, although some distortion should not be ruled out due to the use of the chamber at its lower frequency limit. Figure 65 and Figure 66 show, respectively, the simulated left and right handed polarised far field radiation patterns of the antenna model. It is expected that the feed will have minimal impact on the antenna

radiation pattern if implemented correctly (Hertel & Smith, 2002) and so these simulation results are expected to closely match with the physical prototypes.

6.4.1) Prototype antenna performance results

This section details the results from the conical helix prototypes. Two Kapton substrate prototypes were produced, one with the antenna elements on the interior of the substrate and the other on the exterior. The Kapton substrate was 100µm thick, the minimum available from the supplier PCL. With the copper antenna elements, it can support itself under normal gravity. A simple corrugated plastic scaffold was therefore used to provide support in the anechoic chamber, without impacting the results. One of the test setups can be seen in Figure 67.

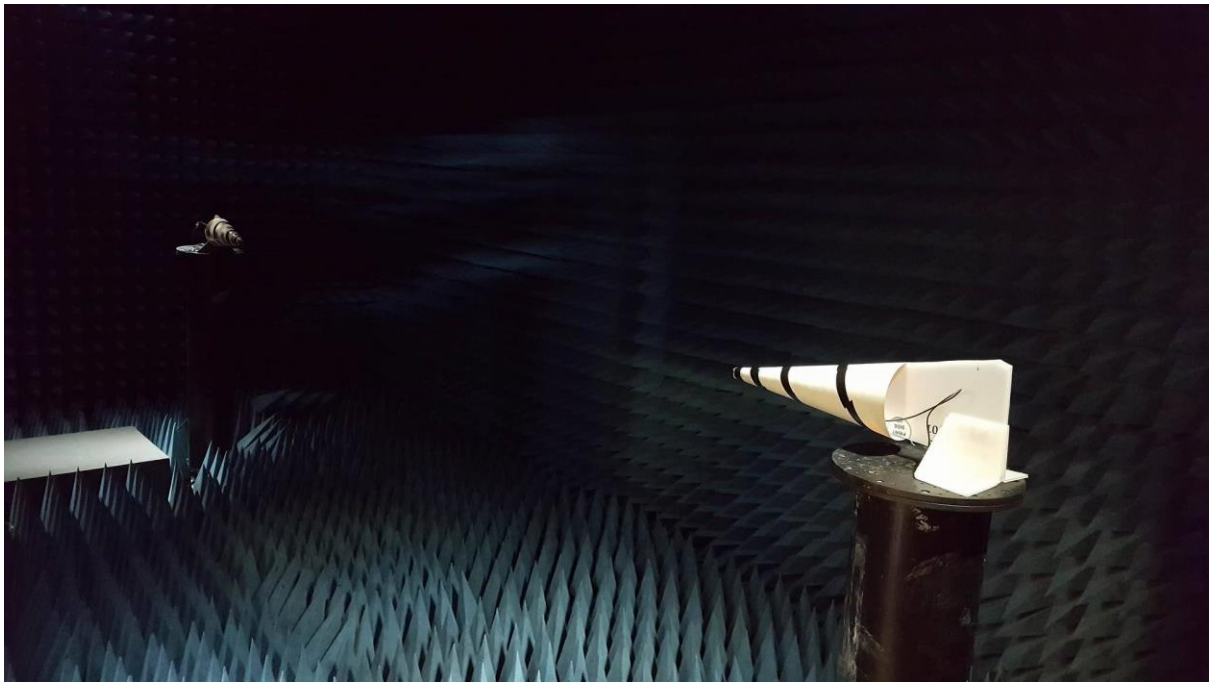

Figure 67 shows anechoic chamber testing of the 1/3 scale conical helix antenna prototypes.

The area at the tip of both the prototype antennas is a circle of 10mm in diameter. In this limited space multiple, different connection methods to the feed were experimented with but directly bonding the coaxial cables to the antenna tabs proved most effective. The setup schematic of the two feed designs is shown in Figure 68. For the dual cable setup,

the shielding of the cables was electrically bonded every 5cm, but in practice is in almost constant electrical contact along the length to the balun.

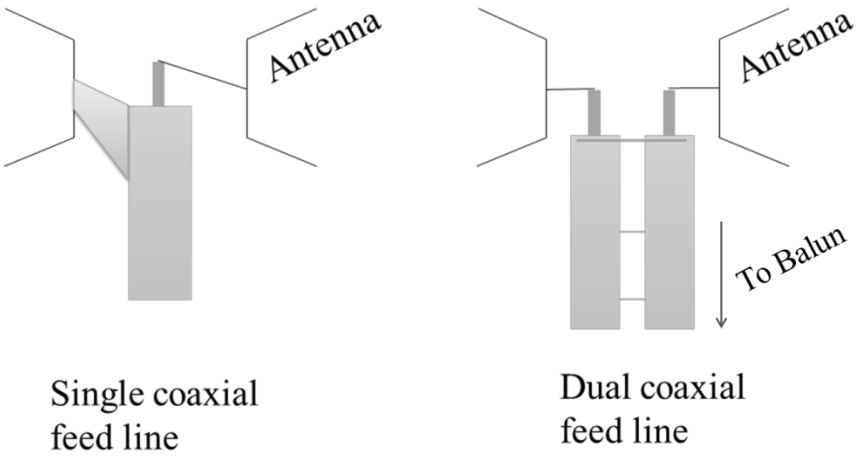

Figure 68 shows a schematic of the feed setups used for both prototype antennas.

The single feed was implemented first as it was the simpler of the two. Figure 69 shows the S11 results for the interior and exterior arms. These graphs show that there is indeed a resonance occurring at the frequencies predicted by the simulations. Energy is therefore being received and radiated by the antenna, but to interpret the results further the radiation patterns must also be considered, which can be seen in Figure 70.

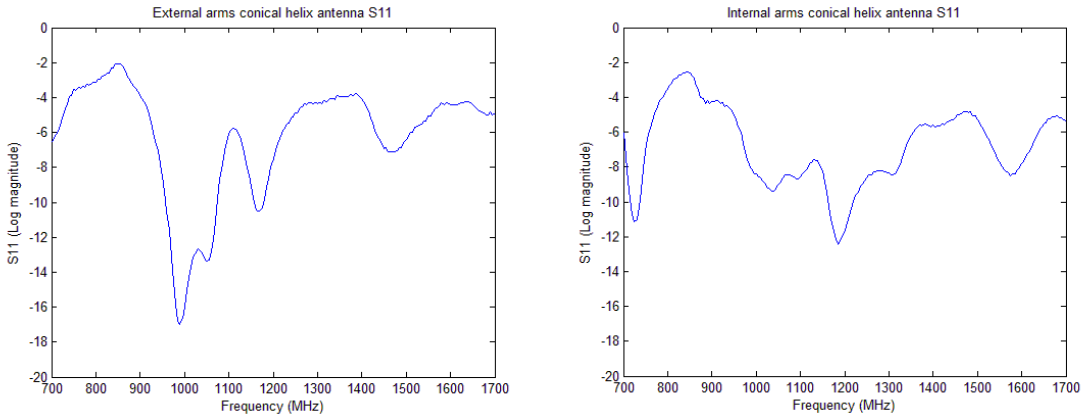

Figure 69. These graphs show the S11 of the, split coax cable fed, conical helix antenna prototypes.

The measured radiation patterns are not as smooth as predicted in the simulations. To provide a potential hypothesis for why this may be the case, the practicalities of the setup

should be considered. As the antenna tapers to its tip, it is not possible to access it by hand. It is therefore not possible to accurately position the feed line as recommended by Hertel & Smith (2002), to the axial axis. When combined with the fact that the coaxial shielding has intentionally been used to carry a signal to one of the antenna arms, a plausible theory is that it is radiating in a way that modifies the antenna characteristics. Whilst the antenna is radiating as expected, shown by the S11 results, the radiation from the feed line significantly alters the characteristics of transmission for the lower frequencies. Low frequencies are preferentially radiated by the feed line and so the expected radiation pattern does not form until a higher frequency than predicted.

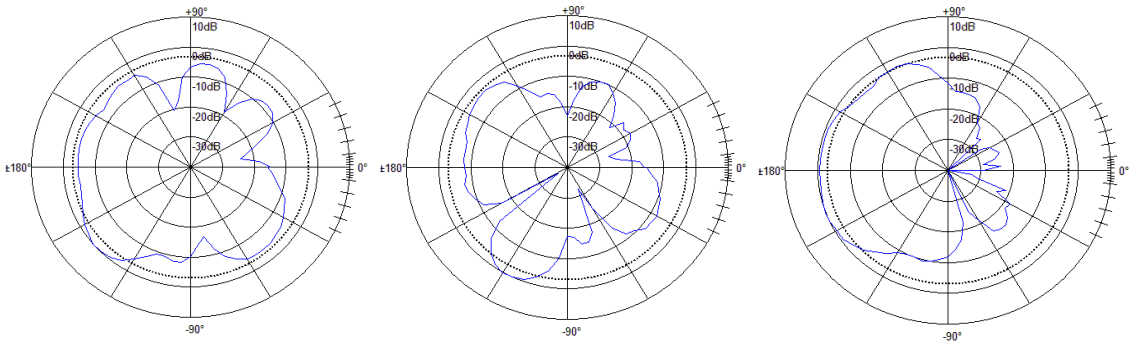

Figure 70. Normalised radiation patterns of the external arms conical helix antenna prototype, spanning its operational frequency, are shown here. 1GHz (Left), 1.2GHz (Centre) and 1.4GHz (Right) are shown as samples with the antenna apex pointing direction at 180°. The dashed line is -3dB of the peak value. The internal arms antenna patterns showed no significant difference.

The differences between the patterns of the interior and exterior antenna variants were negligible and most likely within the experimental error of this test. As the material on any flight antenna would be much thinner than used here it was hoped that an upper bound could be placed on the generated impact. But given the considerations of the radiating feed, this is not possible.

If the radiating feedline theory is correct it should be largely mitigated by the dual line configuration. The feed setups were therefore changed over at this point to the second setup. The S11 results can be seen in Figure 71 and the farfield patterns in Figure 72.

Whilst the far field patterns look much more promising than the previous results, the S11 data exhibits significant frequency dependant features.

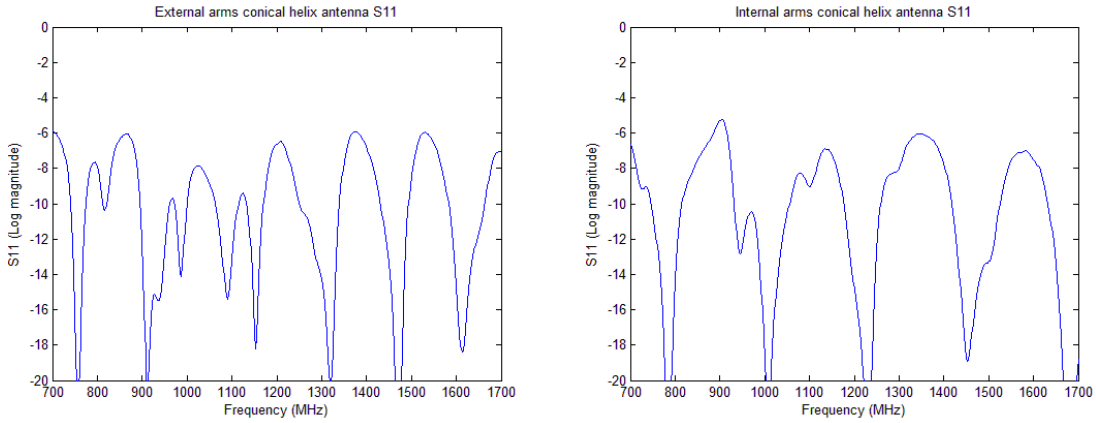

Figure 71. These graphs show the S11 of the conical helix antenna prototypes with a balun feed setup.

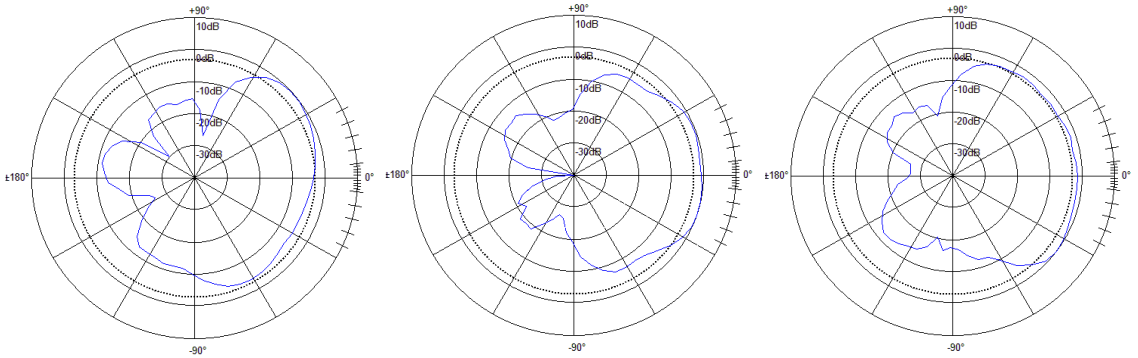

Figure 72. Normalised radiation patterns of the balun fed external arms conical helix antenna prototype, spanning its operational frequency, are shown here. 1GHz (Left), 1.2GHz (Centre) and 1.4GHz (Right) are shown as samples of the full data set. The antenna apex pointing direction is set to 0°. The interior arms again showed identical results.

Due to the addition of a balun and the dual coaxial feed, repeated dips in the S11 pattern are observed. With this knowledge, it was immediately recognised that this was a feature of the feed setup. Due to the work schedule for the REXUS launch the phenomena was not fully investigated prior to launch but was analysed afterwards. The effect arises due to two factors: the length of coaxial cable required to traverse the antenna's length and the impedance mismatch between the feed line and antenna. It is caused by the impedance mismatch generating reflections back down the transmission line. This effectively changes the transmission line impedance at the input, dependant on frequency. The resulting

standing waves then cause the features seen at the signal analyser. Calculations were carried out that confirmed that the frequency of the dips matched the predicted behaviour due to the feed cable lengths used. A more detailed explanation of the cause for the features seen in Figure 71 will be given in section 6.5.9 when similar features are detected in the PICARD results.

Despite the limitations of the S11 results from the dual feed setup, the far field patterns showed a significant improvement over the previous results. Based on this, we know that the energy being delivered to the antenna was being radiated in line with the simulation predictions. The feed does not contribute to radiative emission and the antenna forms a smooth symmetrical, forward radiating pattern when fed in this manner.

As with the single feed setup, the differences in far field pattern between the interior and exterior arms were negligible and are well within the experimental error. This upper bound on the impact of the structural material (the flight antenna will have much thinner material) supports the conclusion that it does not pose any significant considerations for the design of the antenna. Theory dictates that a small amount of absorption should occur, but it is not detectable here. It is therefore expected that the antenna elements can be shielded within a Kapton protective layer without any significant detriment to the performance.

6.4.2) Antenna feed point evaluation

The results of the previous section clearly display that when trying to optimise the antenna efficiency the feed setup is of key importance. The feed design must ensure that there is a good impedance match and that any radiation of the feed does not significantly affect performance.

For the full-scale antenna, there is sufficient room to include a PCB at the balloon apex. The addition of a very small tab was implemented to fold over the tip and make the connection with this PCB. Whilst this addition will have an insignificantly small impact on the radiation performance it will have a noticeable effect on the input impedance of the antenna. For a PCB, it is ideal to have as large an area as possible between the tabs to ease manufacture but there may be benefits to reducing the separation of these points. For example the taper that naturally arises by reducing the separation will have properties of a Klopfenstein taper (Klopfenstein, 1956). The true form of such a taper for this bandwidth is too long to fit onto the balloon apex, but the shape was expected to alter the impedance seen by a matching circuit located on the apex of the balloon.

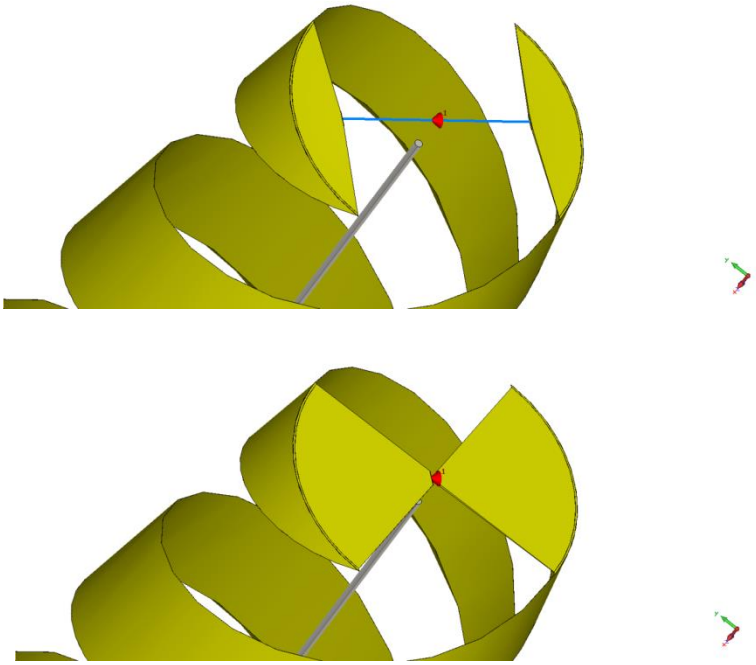

Figure 73 shows the two extremes of the conical helix feed separation width parametric sweep.

To determine the impact of this effect and any other influence at the apex, a parametric sweep simulation was run. The separation of the connection points was varied from 50mm to 2mm in 10 steps and the impedance spectra recorded for each separation. An illustration

of the antenna and the results of this sweep can be seen in Figure 74. Some degree of matching is occurring, especially at the higher frequency range.

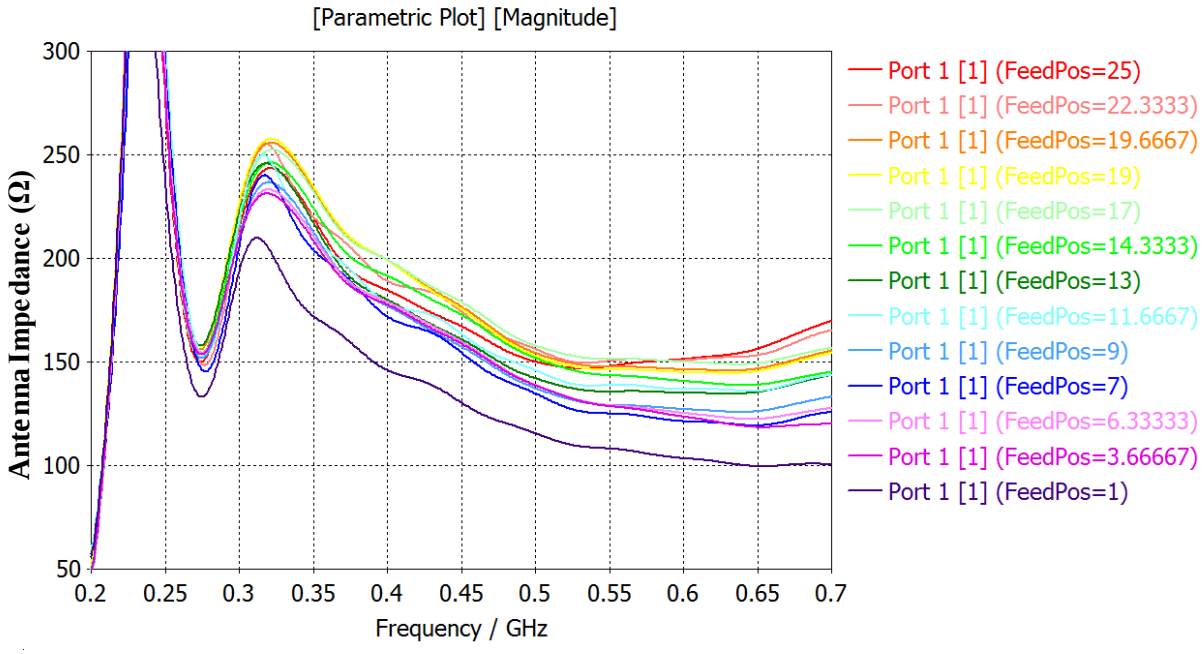

Figure 74 (Top) the widest separation used between the two feed attach point at the apex of the antenna. (Middle) The narrowest separation used in the parametric simulation. (Bottom) A graph of the 10 resulting input impedance values. FeedPos is half of the separation distance between the connection points.

In Figure 75 we see that, with the discrete port impedance set to 200 ohms, the S11 magnitude increases as the separation is decreased just as expected for the impedance mismatch created. Therefore, from this we move on to Figure 76 where the discrete port impedance has been changed to 100 ohms (being an easily achievable value using 50Ω cabling). In this figure, we see that the matching with the antenna we had hoped for has not been achieved. The S11 performance is worse than the 200 ohm case by a significant amount. Whilst the input impedance value has changed at the connection point, power is still being reflected before it enters the antenna itself.

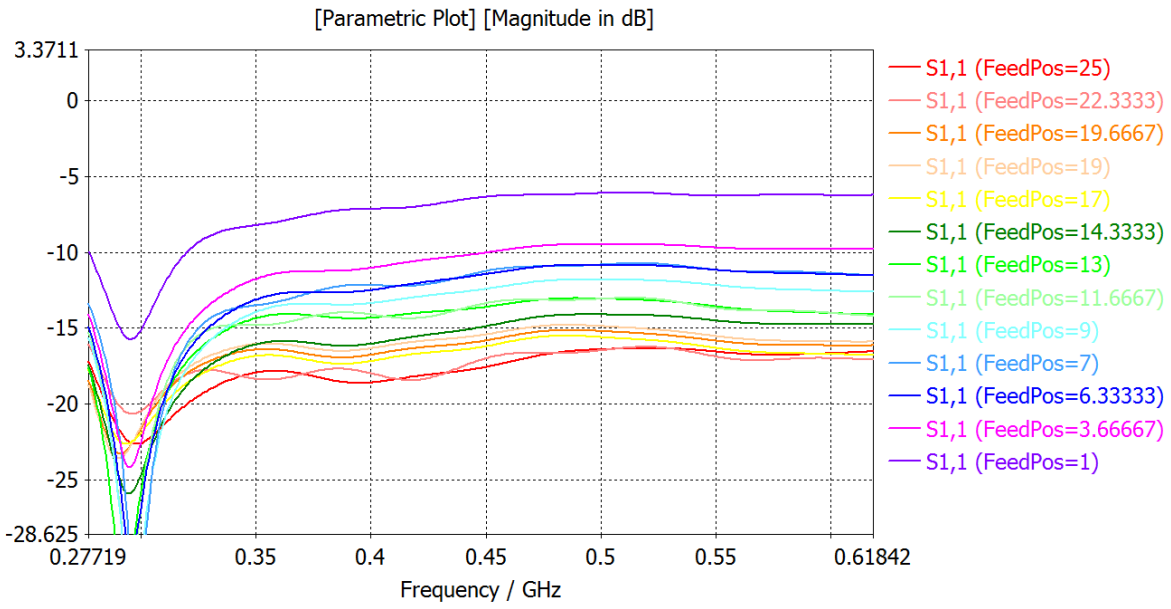

Figure 75 A graph of the parametric sweep of the feed point separation showing the generated S11 results. The input impedance of the discrete port is set to 200 ohms for this sweep. FeedPos is half of the separation distance between the connection points.

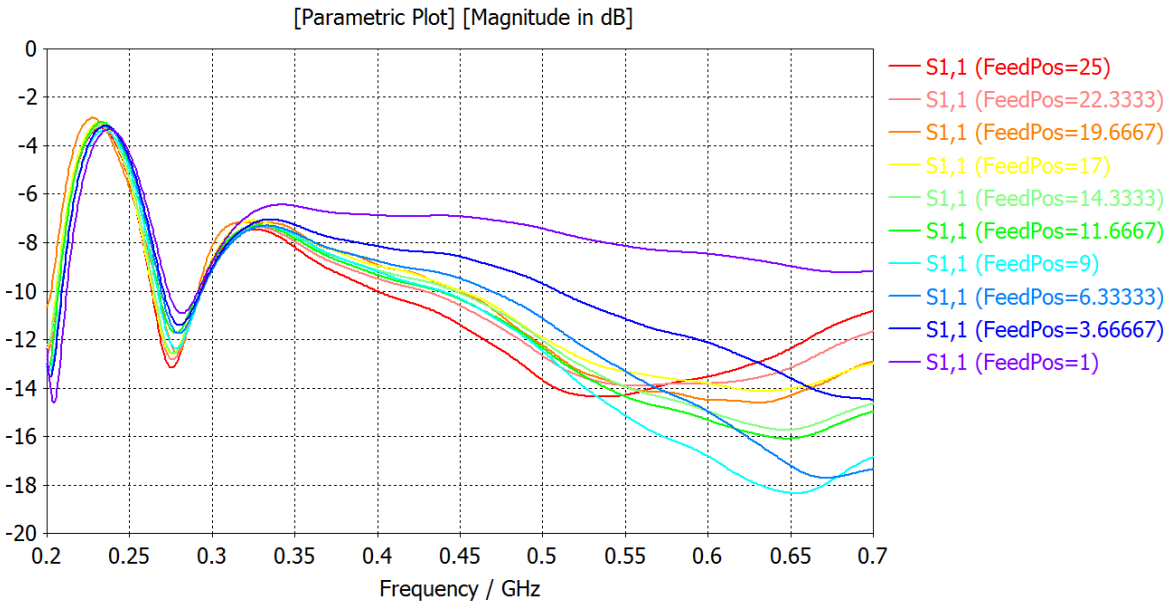

Figure 76 A graph of the parametric sweep of the feed point separation showing the generated S11 results. The input impedance of the discrete port is set to 100 ohms for this sweep. FeedPos is half of the separation distance between the connection points.

Despite the negative result there is good information with which to design the appropriate feed shape for WISER. The maximum separation investigated, of 50mm between the feed

connections, appears the most favourable due to it having the best S11 profile. This is effectively the maximum possible separation due to the need to bond the antenna elements to the PCB. Therefore, a PCB forming the apex of the balloon will have this 50mm to incorporate two coaxial cable connections and a matching transformer for each arm, with the balun mounted in the body of the spacecraft. It would also be possible to use a 2:1 transformer balun at the apex itself. The surface mounted Anaren B0205F50200AHF, used by Sakovsky et al. (2015), is a potential option for WISCER. The results of this simulation directly informed the design of the PICARD antenna feed, which will be detailed in the next sections.

6.5) Prototype Inflatable Conical Antenna REXUS Deployment (PICARD)

A prototype of the WISCER antenna was selected to fly on a suborbital sounding rocket. The launch was provided as part of the REXUS ESA educational program which allows students to develop their engineering skills with real world experience. The program was setup as a jointly funded partnership between the Swedish National Space Board (SNSB) and the German Space Agency (DLR). The program is run by the European Space Agency (ESA) and proposals from students of all ESA participating states are considered under the excess contribution from the SNSB. The following section details the design and results of the experiment.

6.5.1) Introduction to the PICARD project

The Prototype Inflatable Conical Antenna Rexus Deployment (PICARD) experiment was designed to demonstrate the performance of an inflatable antenna deployment and

rigidisation system intended for use on a CubeSat nanosatellite platform such as WISCER. It flew on a REXUS sounding rocket in March 2016 (mission RX19).

On orbit inflatable structures have emerged in the last few decades as a solution to the problem of launch vehicle payload size restrictions (Bernasconi, 2002). Inflatables do however have their own set of challenges which must be considered. A major issue is depressurisation over time caused by leaks, resulting from micrometeorite damage. One solution is where the inflatable structure is rigidised post deployment with a metal-polymer strain technique as used on the Echo series of satellites in the late 1950's to early 1960's.

Figure 77 shows a test inflation of one of the strain rigidised Echo satellites launched by NASA. The inflatable spheres were used as relays to directly reflect radio signals. (Source NASA)

Large antennas are commonly deployable structures when used in satellite operation to reduce launch volume; the requirement for the antenna to be large is a product of the need for high gain and low frequencies. The new developments in inflatable technology present potentially superior solutions to the deployment of antennas which are poorly suited to mechanical deployment methods. A notable achievement in this area was the successful deployment of the Inflatable Antenna Experiment (IAE) from the Space Shuttle in May 1996 (Freeland, 1998) (Figure 78).

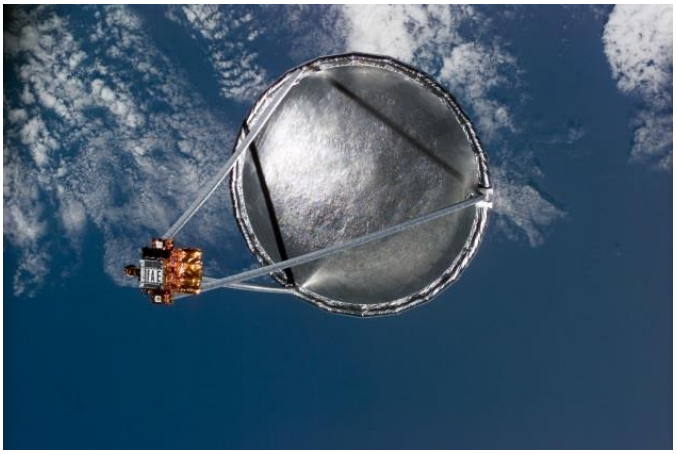

Figure 78 Inflatable Antenna Experiment (IAE) deployed in 1996 (Source NASA).

6.5.2) PICARD experiment and systems overview

The objective of the PICARD experiment was to validate the deployment and rigidisation of a prototype inflatable conical helix antenna in milli-gravity conditions. If the antenna deployment was successful, the secondary objective was to then verify the expected performance of the antenna.

The experiment was located underneath the ejectable nose cone of the REXUS rocket, mounted to the nose cone adapter bulkhead (Figure 79). The antenna inflates into free space once the nose cone has been ejected.

The PICARD experiment is split into four subsystems: the control electronics; the deployment system; the ejection system and the radio frequency (RF) electronics. Once launched the control system operated autonomously through the flight to operate the other subsystems. After the REXUS service module ejects the rocket nose cone, the antenna inflation begins. Upon completion of the inflation the RF system immediately activates the antenna and records the performance. Antenna performance data is then continuously recorded until re-entry. The exposed inflatable is ejected to prevent it from interfering with the recovery system and parachute.

The goal of the RF subsystem was to make a measurement of the antenna S11 during the flight. This provided evidence that the antenna deployed correctly, without significant damage to the active antenna elements. The ejection of the antenna also allowed for an in-flight comparison of the data against an open circuit. Due to the highly constrained mass and volume budgets for this subsystem a miniaturised network analyser was created specifically to measure the antenna S11. A full account of the subsystem design, produced as part of this project work, is included in Appendix 1.

Multiple strain sensors were embedded within the inflatable in order to determine if the required strain for rigidisation was reached. Combined with temperature, pressure, accelerometer and video data of the inflatable, the success of the deployment can be critically assessed. Measurement of the antenna S11 profile by the RF subsystem is then intended to supplement these results to provide verification that the antenna is still operational after the deployment process. This point is crucial as without this check there is no guarantee that the deployment process is compatible with the antenna design. There are several scenarios where the mechanical aspects of the deployment are met but the electrical ones are not. All the data from the experiment was sampled for downlink during flight but also recorded on board the rocket for later recovery and analysis, the two methods being used simultaneously to provide redundancy.

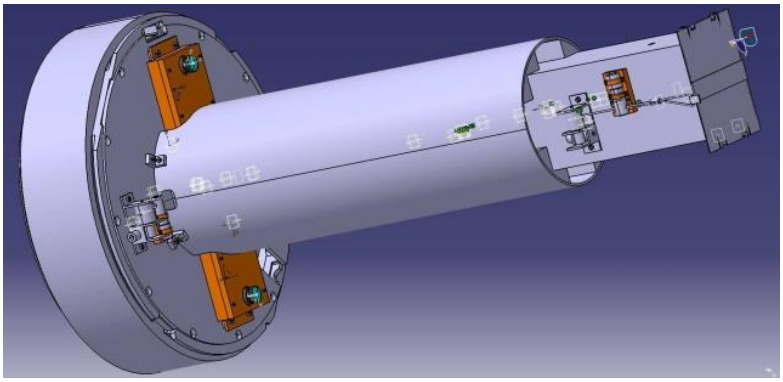

Figure 79. CAD model of the PICARD experiment seen without the nosecone attached. Mechanical design and construction of the structure and deployment mechanisms was performed by the University of Strathclyde.

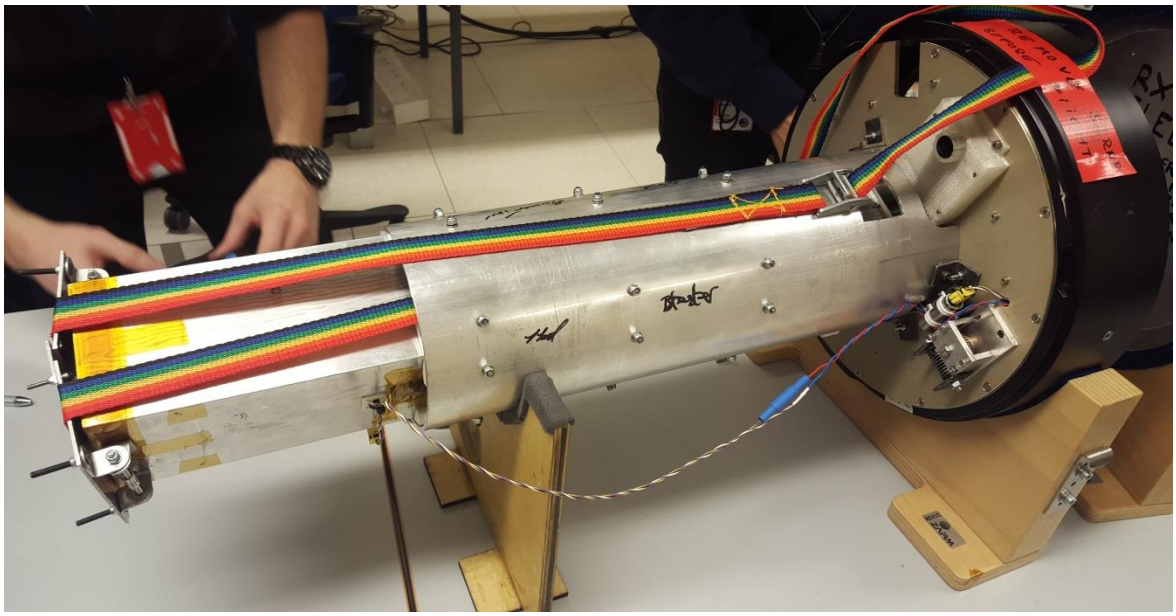

Figure 80. The PICARD experiment shown during pre-flight checks.

6.5.3) PICARD Antenna and predicted performance

The antenna design for PICARD is a prototype for WISCER. Hence the design was made as flight representative as possible, to ensure that not only the performance would be comparable but also that the intended manufacturing process was achievable.

Modifications to the size of the preliminary antenna design were made based on the results from early antenna bandwidth modelling in CST. The reduction in size reduces not only the antenna mass, but also the volume required to store it and the mass/volume needed for the inflation system.

The dimensions chosen for the new antenna can be seen in Figure 81 and the CST simulation results are shown in Figure 82 through to Figure 86. Before proceeding it is noted that simulations including the structural materials were also implemented but showed no significant changes. Increasing the wrap angle of the antenna arms was also investigated as a method to reduce the size, with the number of helical rotations held constant. This significantly degraded the radiation pattern and so was not pursued.

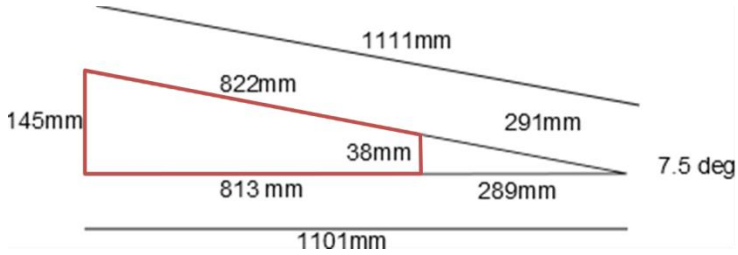

Figure 81. Dimensions shown are those of the updated PICARD conical helix antenna. The size has been reduced from (Angling et al., 2013) without significant impact on the antenna properties.

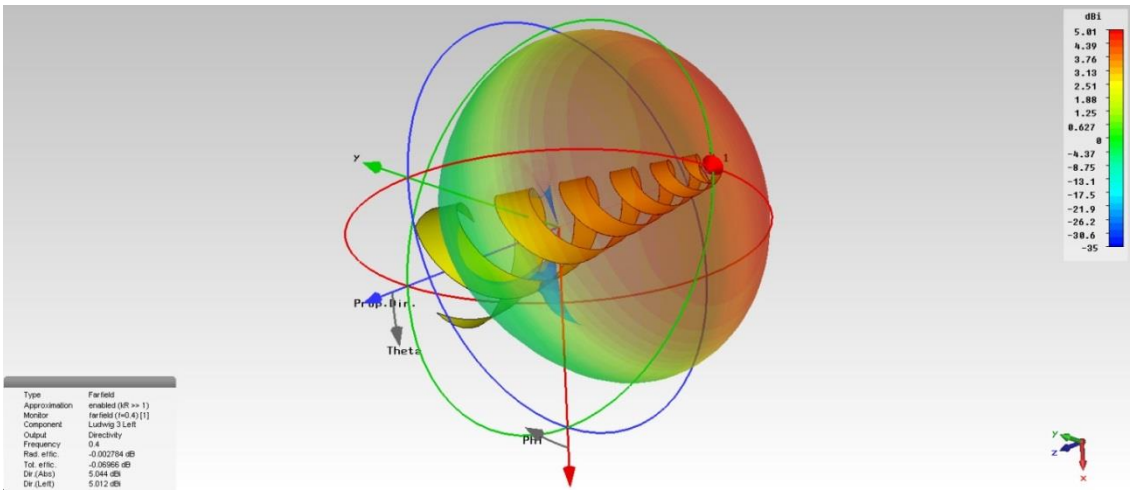

Figure 82. PICARD conical helix antenna 3D radiation pattern for left hand circularly polarised radiation.

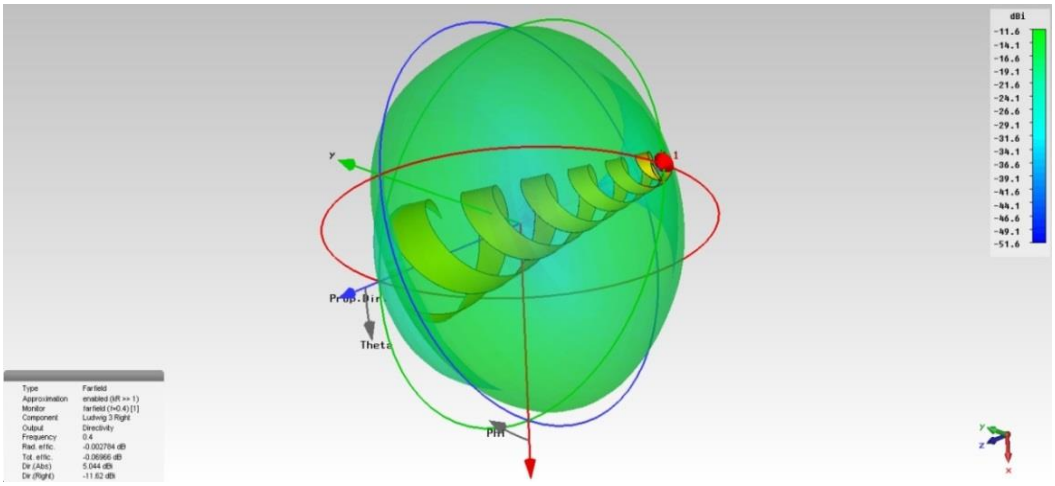

Figure 83. PICARD conical helix antenna 3D radiation pattern for right hand circularly polarised radiation.

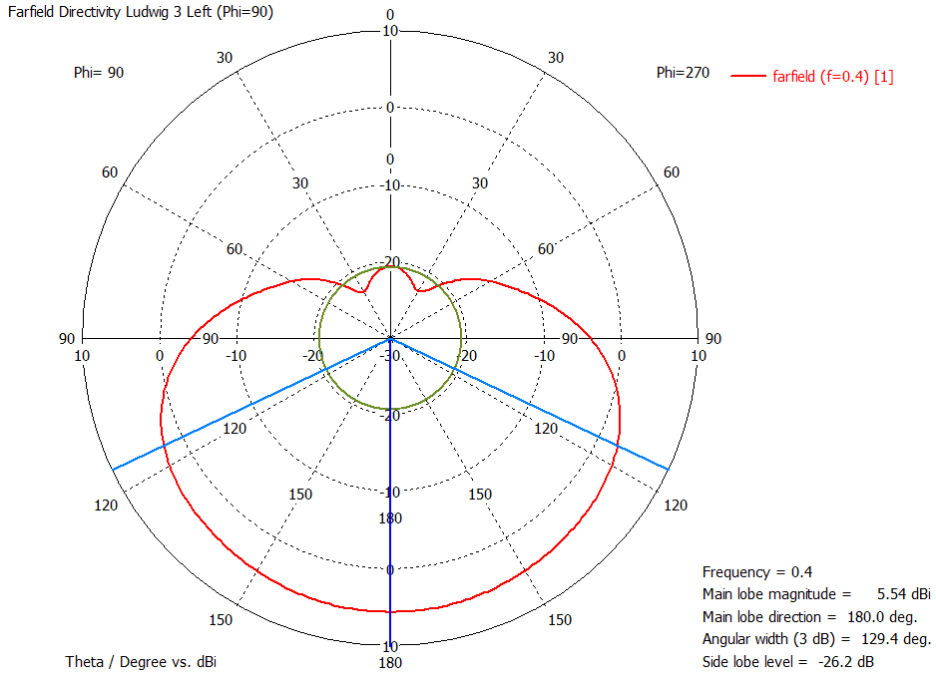

Figure 84. Polar plot of the left hand circularly polarised radiation pattern from the PICARD conical antenna. 180° is the antenna forward direction for this simulation.

Figure 82, Figure 83 and Figure 84 show the radiation pattern results from the simulation. Only negligible differences to the original antenna pattern can be discerned. Figure 85 shows the impedance of the antenna at the input port. The impedance is again high and will require matching to a 50 Ohm coaxial feed.

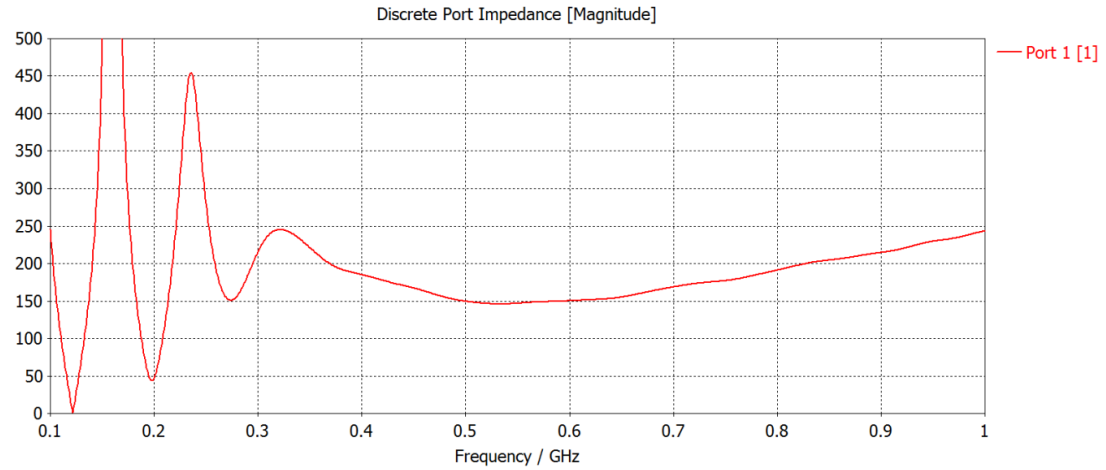

Figure 85. Simulated impedance of the PICARD conical helix antenna. The impedance varies across the intended frequency range.

Figure 86 shows the S11 response of the PICARD antenna. The data shows the S11 response for a matched system (200Ω input to the antenna) without the effects of the balun and bi-directional coupler considered. This simulated S11 therefore provides a good baseline for the expected performance. In the real system the feed setup will introduce multiple impedance interfaces creating unaccounted for signal reflections. The simulation predicts a relatively flat response over the planned frequency range, but the real S11 magnitude will not be as low and smooth as this ideal case.

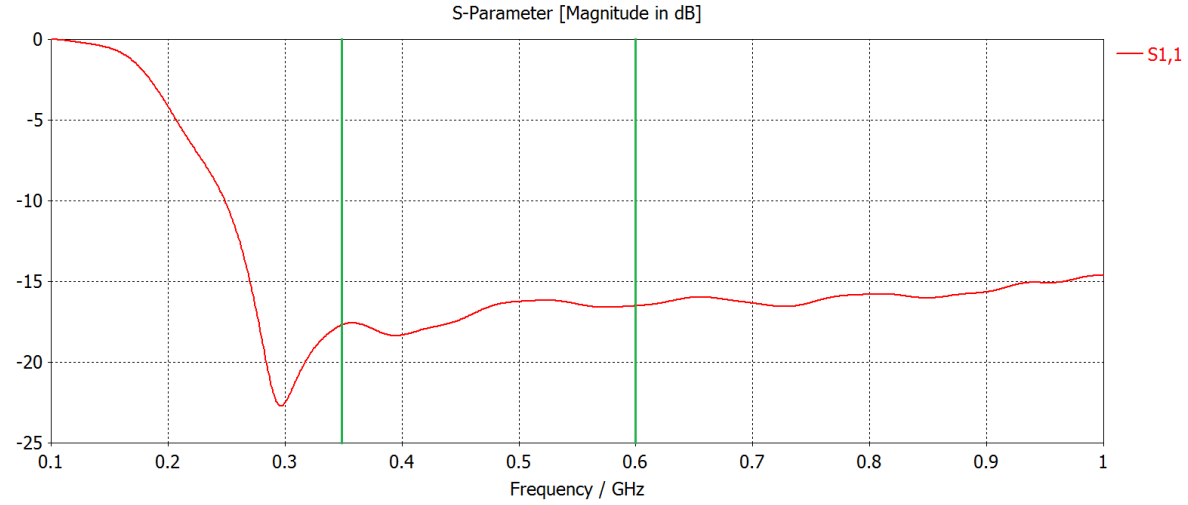

Figure 86 shows an S11 plot for the PICARD conical helix antenna. The green lines show the operational frequency range.

Simulations of possible failure modes of the antenna were also conducted to understand how they may influence the S11 results and if any modes could be identified from this parameter. From the results shown in Figure 87 and Figure 88 it was concluded that it would be very difficult to identify a particular damage mode due to the variance of the S11 for a real system. However, a major failure of the antenna would be detectable, and the antenna ejection provides a direct open circuit reference. This allows for direct confirmation that the antenna elements are intact after deployment, rather than inferring it from a successful deployment.

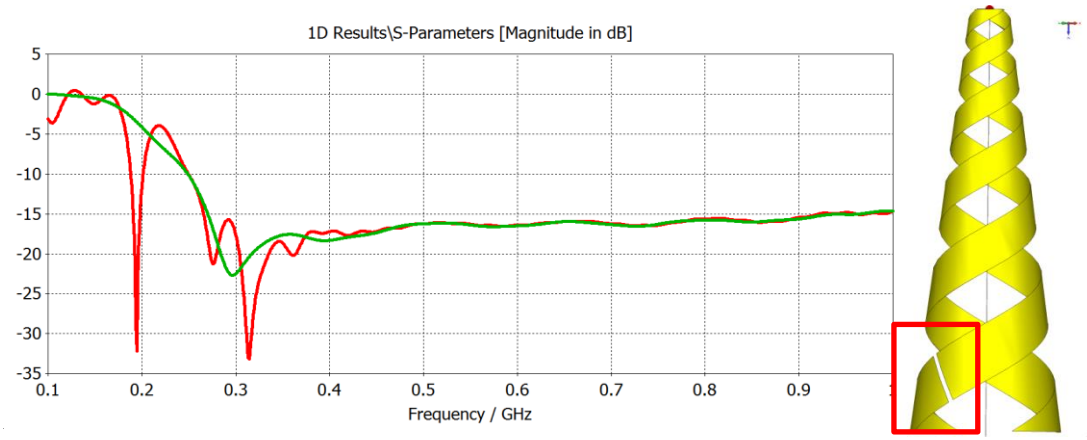

Figure 87 shows the predicted S11 plot given a complete break in the lower section of the conical antenna. Red is the damagedS11.

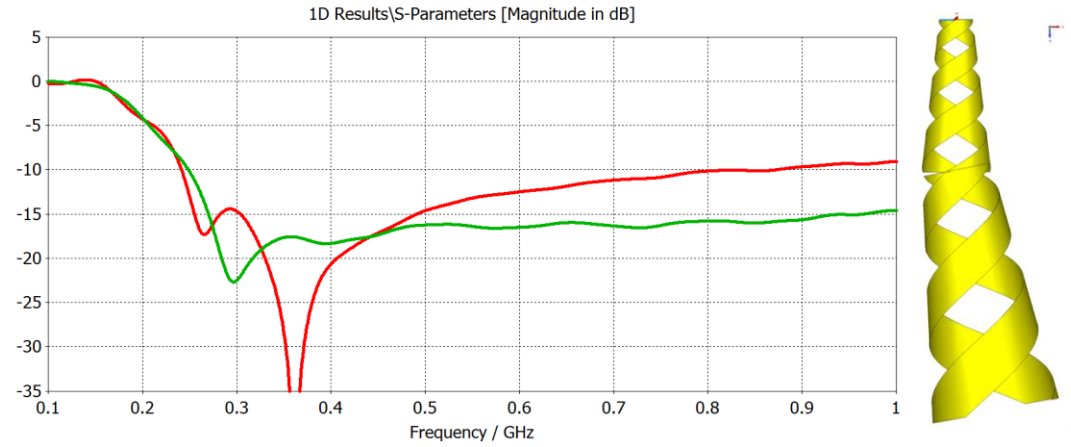

Figure 88 shows the predicted S11 plot given an incomplete deployment of the antenna (Limitations on the CAD environment have also led to splitting of the antenna elements which is likely causing most of the changes seen). Red is the damaged S11.

Many test models of the antenna were created for experimentation with the manufacturing process and inflation dynamics. The identical model created just prior to the flight antenna was designated as a flight spare and RF test model. Measurements of antenna S11 and farfield pattern were performed in the anechoic chamber at the University of Birmingham. It should be noted here that the chamber is only rated to function to 800MHz minimum frequency, and the results below range from 200MHz to 700MHz. The results are presented here despite this, as they provide background to the final flight results and limited evidence that the intended radiation pattern is being achieved.

The measured S11 in Figure 89 again shows the transmission line impedance mismatch pattern generated by the balun feed. The farfield pattern of the antenna, however, shows clearer correlation with the predicted results.

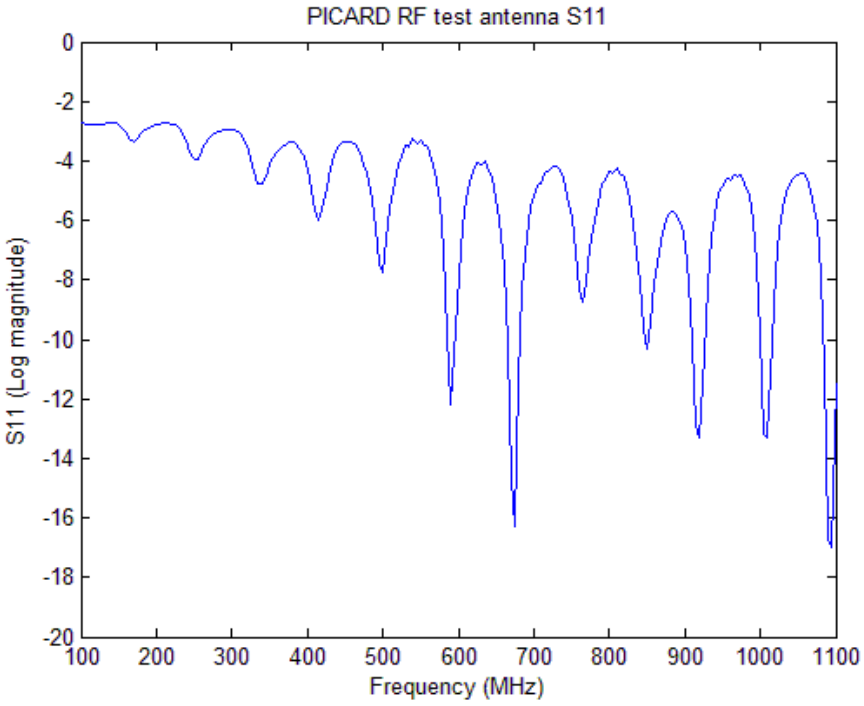

Figure 89 shows the S11 of the PICARD RF test model antenna, inclusive of the feed balun.

Figure 90 shows the recorded farfield patterns for PICARD antenna test model. At the upper end of the frequency range, the expected radiation pattern is clearly visible. It is

uniform in the transmission direction and shows the expected shape for frequencies higher than 500MHz. Below this frequency though it is heavily distorted and appears to show no dominant forward gain. There are two possible explanations for this: either the antenna is not radiating those frequencies as predicted, or the antenna is functioning as predicted but the chamber performance is so quickly degraded at lower frequencies that the signal is completely scattered. Without access to an anechoic chamber rated down to at least a minimum frequency of 200MHz, it is impossible to discern which is correct. To further verify the antenna and distinguish between the two possibilities, access to further facilities is recommended.

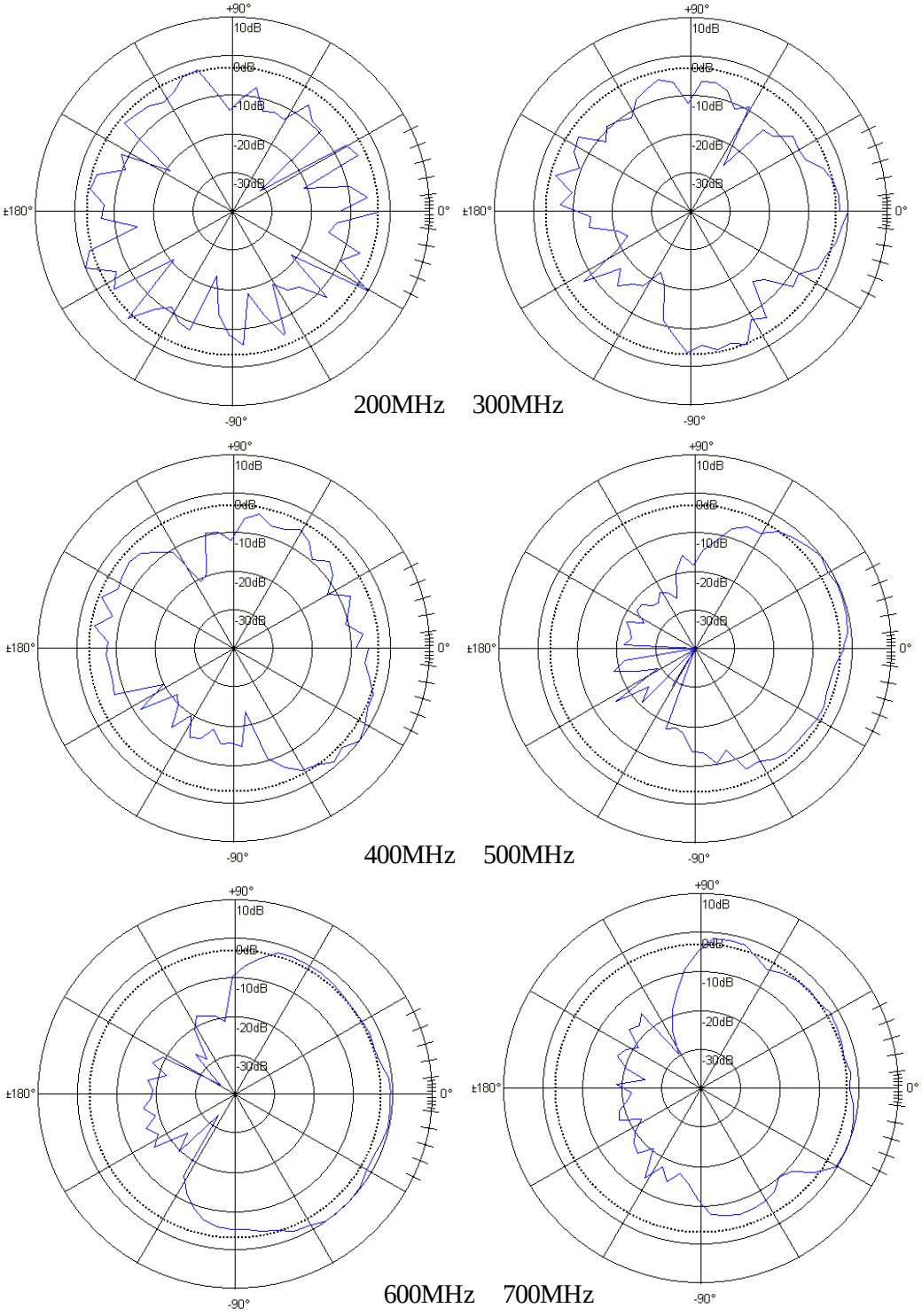

Figure 90. These polar plots show the normalised radiation pattern of the PICARD RF test article antenna for a range of frequencies. The anechoic chamber in which this test was conducted has a recommended operational minimum of 800MHz, which must be considered when making conclusions from these plots.

6.5.4) Antenna Structure Rigidisation

To counteract the inherent structural weakness and vulnerability of an inflatable structure after deflation, it is common to apply some form of rigidisation to the structure if pressure cannot be maintained during the usage lifetime. There are several different methods which have been previously used or proposed; the two methods considered for the WISCER mission were a UV-cured resin and metal-polymer strain rigidisation. A UV-cured resin would grant a great deal of strength to the structure; however, if the UV light for the curing is provided solely by the Sun, it may take several hours to fully cure. Metal-polymer strain rigidisation provides immediate rigidity and is a passive property of the structure (provided sufficient inflation pressure is reached during the deployment). Due to limited duration of the milli-gravity phase of the sounding rocket flight, the metal-polymer rigidisation technique was selected for PICARD.

Strain rigidisation of a metal-polymer composite for deployable structures in space is a relatively old concept. NASA's Project Echo utilised this concept for the ECHO 2 satellite (a 41m diameter spherical balloon launched in 1964), which was used as a passive communications reflector satellite. To successfully rigidise, the composite must be strained such that the metallic layer begins to deform plastically but the polymer layer remains in its elastic deformation regime. When the pressure is released, the polymer remains under tension as the metal resists compression. Therefore, the structure remains in a stressed state. One limitation of strain-based rigidisation is that of shape; whilst simple shapes such as spheres and cylinders have constant uniform strain across the entire surface, the strain in more complex shapes varies significantly across the surface. This can lead to non-uniform rigidisation and potentially under or over strained sections. The conical shape used in our antenna design will suffer from these effects to some extent. However, the strain will vary smoothly with the cross-sectional radius, so will not produce localised stress points. The

increased stress at the base of the antenna acts as a limiting factor in deciding the final peak inflation pressure.

For the PICARD design, Kapton and aluminium are used as the polymer and metal layer respectively. There is an additional bladder layer that is made of polyurethane and attached to the main composite only at the tip and base of the cone. This layer is included to prevent leakage during inflation. A benefit of strain rigidisation is that the peak pressure is only required momentarily and so high leak rates can be tolerated, leading to simplified manufacture. In addition to providing structural strength the Kapton acts as a barrier to reduce degradation of the aluminium antenna elements from interaction with atomic oxygen.

A key difference between previous strain rigidisation methods and the PICARD design is the introduction of only partial metal layer coverage due to the constraints of the antenna. Where the metal layer is not present, a second layer of Kapton is used to maintain structural integrity. The development and validation of this technique is crucial to determining the applicability of strain rigidisation to deployable antennas.

6.5.5) Antenna Packaging

Research into folding patterns for the PICARD antenna packaging was performed by S. Creiche of the University of Strathclyde and is described in Kirkby et al. (2015). The candidates were then tested for suitability and the findings are presented in this section. The design impact on WISCER is also discussed.

Three inflatable packing methods were down selected for study during the PICARD development phase. These were: an origami folding method, concentric/telescopic folding and controlled crumpling. The two primary criteria for the methods were the final stowed

volume and the reliable deployment from the stowed configuration. The stress/strain imparted to the antenna was also initially considered but it was determined that it would be similarly high for any sufficiently compact folding method and so was not a deciding factor.

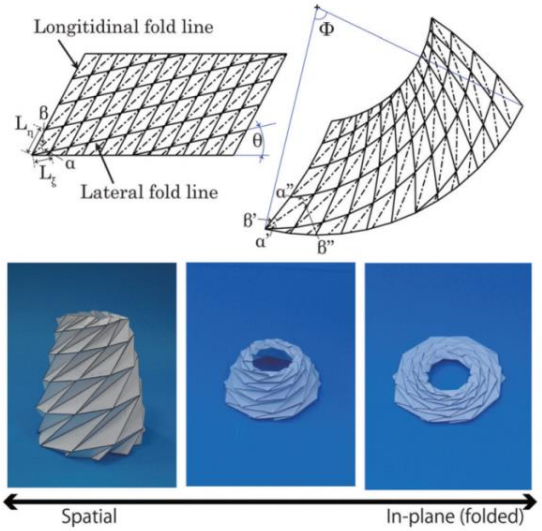

Figure 91. Illustration of the twist-buckled folding pattern for a cone (Ishida, Nojima, & Hagiwara, 2014).

Figure 92. PICARD antenna partially folded according to Origami pattern.

The origami method makes use of a conformal mapping technique (Ishida, Nojima, & Hagiwara, 2014) to adapt a twisting-buckling folding pattern for a cylinder (Hunt & Ario, 2005). The resulting pattern can be seen in Figure 91 and achieves high packing efficiency as a flat disc. Once the fold lines have been imparted to the antenna it can be easily and repeatedly compressed. This leads to very repeatable dynamics of inflation from this state,

but due to the constraints of the stowage volume available of WISCER being a cube, further folding of the disc was required. Due to this, the method did not perform reliably during deployment tests. The tip of the antenna would inflate prematurely due to the central void and cause excessive friction with the container walls. An alternate container design, similar in concept to a rocket payload fairing, was proposed to solve this problem but could not be designed, integrated and tested in time for launch.

The second method uses a concentric/telescopic folding pattern. This pattern has seen extensive development by the company L'Garde for use in many applications, including inflatable boom arms for solar sails. The pattern gives repeatable and reliable results when inflated from the configuration shown in Figure 93.

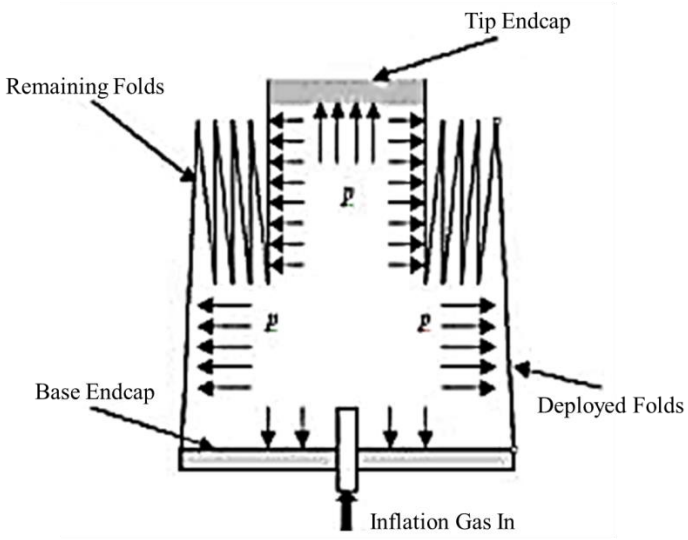

Figure 93 details the concentric/telescopic folding method.

Generally, for this folding pattern the storage container takes on the outer diameter of the base inflatable cone. When combined with small cone angles this produces high packaging efficiencies. However, the cone angle for the WISCER antenna is relatively large and the CubeSat width is much smaller than the base of the antenna. In order to achieve high packaging efficiencies complex extra folds are required. Development of this technique was abandoned based on positive results with the third method and the knowledge that this

folding pattern would be affected by the same friction issue as the origami pattern based on the central void.

Figure 94 is an image of a PICARD antenna after it has undergone controlled crumpling.

Controlled crumpling was the third method used and yielded the best results under testing. Instead of pre-folding the antenna so that it follows organised fold lines, it is simply guided into the storage container under a compressive force. This makes the process simple and offers significant time savings. The compressive force is controlled by hand and the antenna is guided continuously to avoid packing voids. The inflatable is repeatedly compressed then allowed to relax back out of the container so that modifications to the initial crumpling pattern can be implemented. This continues until the entire antenna is contained and the lid is closed. A more detailed procedure is included in Table 5 for reference.

Step Reference	Description
P-FP-01	Slowly evacuate the polyurethane bladder to prevent it impeding the antenna folding.
P-FP-02	Lightly compress the inflatable radially until it is roughly the same width as the container.
P-FP-03	Begin to insert the inflatable into the container, ensuring a concertina fold is naturally adopted as it progresses.
P-FP-04	As each section of the antenna enters the container, apply compressive force to remove any voids. Remove the compressive force and unpack small sections of the antenna as necessary to ensure no packaging voids develop and no areas are over stressed to failure.
P-FP-05	Compress the apex cap into the container and allow 5mins continous compressive force for the inflatable to settle.
P-FP-06	Immediately close container doors and latch. This prevents any natural elasticity from prematurely deploying the antenna.

Table 5 lays out the procedure steps used in the controlled crumpling method specific to the PICARD inflatable.

As the antenna is initially crumpled concertina like folds are induced in order to prevent the formation of a central void. Upon inflation this prevents the friction issues seen in the other two folding patterns as the base of the antenna inflates first, pushing the rest of the antenna out of the container. It is probable that this is the crucial factor in the success of this packaging method, given the use of a solid side wall container. The antenna did not

fail to deploy or rupture during any of the preliminary tests run at ambient pressure, unlike the other patterns.

Despite the random nature of the folds, the method produced very repeatable deployments when integrated to the sounding rocket flight configuration. During the tests that were performed, reliability was not an issue but it was noticed that the random folding can yield crossing fold lines where the material stress is high. It is expected that at these highly localised locations the stress may exceed that required for rigidisation. Further research is suggested to ensure that these areas do not cause ruptures in the thinner materials appropriate for an orbit class antenna.

Due to the random nature of this folding pattern there is a reduction in the theoretical packaging efficiency when compared to that of an ideal telescopic case. However, since the storage volume and shape is so heavily constrained by the CubeSat form factor, the packaging efficiency is very similar to the other two methods implemented (when considering the necessary extra folds to form the correct storage shape).

Based upon the above results the controlled crumping method was selected for a vacuum deployment test. Due to the damping effect of ambient air the dynamics of inflation were expected to differ between that of a vacuum inflation and one performed in atmosphere. Combining this with the incompatibility of the flight inflation system with a double pressure run (atmospheric plus over pressure) and the unknown impact of residual gas in the antenna, a vacuum test was the most logical next step.

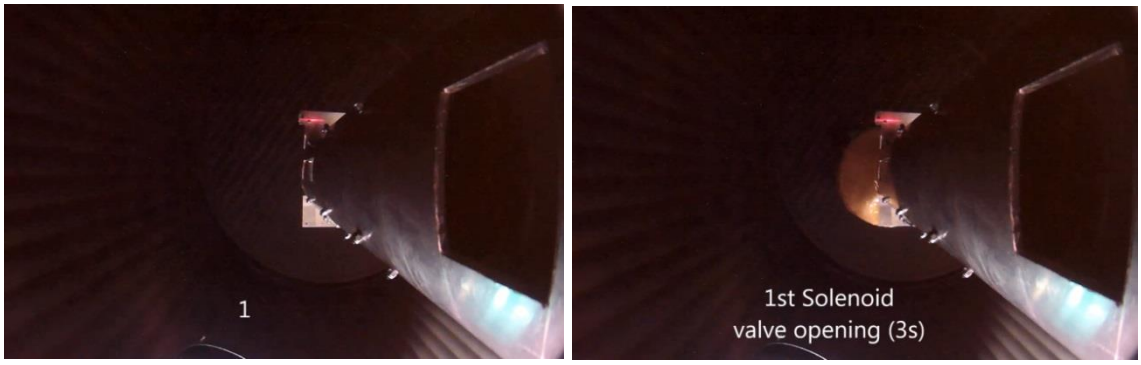

Figure 95 The left image shows the inflation test setup inside the chamber as seen by the flight cameras prior to inflation. The right-hand image shows the inflated antenna 0.8 seconds later when the antenna is fully inflated.

As can be seen in Figure 95 due to the sudden, yet short, first opening of the solenoid gas valve and without the resistance of ambient air, the antenna inflated to completion within 0.8 seconds, thus yielding a successful deployment from the container. It is suggested that for WISCER more control over the inflation pressure profile is required in order to minimise the risk to the structure. Due to the available chamber size the antenna could not be inflated to full working pressure and so a pre-flight rigidisation test was not possible.

6.5.6) Inflation system

To provide the required gas for deployment of a potential WISCER inflatable antenna it is proposed to use Cool Gas Generators, as flown and used in the InflateSail mission (Viquerat, Schenk, Sanders, & Lappas, 2014). These devices provide a large volume of gas from a small compact design, utilising the decomposition of a solid compound. Due to the budget restrictions of PICARD and the less restrictive launcher guidelines of REXUS, the system flown on the test used a conventional compressed gas system. Whilst this is far heavier than the Cool Gas Generators and not suitable for a CubeSat mission, it still allows for the verification of the effectiveness and reliability of the antenna structure and packing method. As the operation of cool gas generators have already been verified, they were not required to achieve the objectives of this experiment.

The PICARD inflation system was comprised of: a gas reservoir, an electronically controlled solenoid valve, a manual valve and associated fittings. The gas flow into the inflatable was solely driven by the over pressure of the reservoir until the antenna and reservoir reached equilibrium. To achieve the intended post inflation antenna-reservoir system pressure, the reservoir simply had to be filled to a pre-calculated pressure. The pressure profile for inflation therefore represents a worse case and acts to validate the structural integrity of the design for all profiles.

A restricting orifice was used to control the flow rate along with multiple separate openings of the valve to allow the antenna to settle, prior to rigidisation.

6.5.7) Antenna Fabrication

The fabrication process investigated as part of this thesis for the third scale antenna prototypes was expanded upon in order to create a design applicable to the PICARD experiment. Factors that influenced these changes included the change to the strain rigidisable structure, folding pattern considerations, cost and further practicalities of manufacture.

The polyurethane bladder is constructed first using two parts. The first makes up the conical section with the use of a conic net, sealed along the long edge using the flexible when dry, low outgassing epoxy adhesive Scotch-weld 2216 B/A Grey. The second part makes up the base of the antenna and for easy of manufacture is again another cone. The two pieces are joined forming the gas tight bladder.

To manufacture the antenna a two piece construction was again used. For strength the base consisted of a dual layer Kapton cone, constructed using the same method as that for the bladder. For the antenna section of the structure a more complex process was required.

Following the conic net method in section 5.3 a single piece of Kapton is cut to form the complete outer layer of the inflatable. This Kapton layer forms the substrate upon which the antenna is created. The antenna elements are then cut, following the conic pattern, as single pieces from a sheet of aluminium. They are then bonded to the substrate layer in the correct positions. The spaces between the elements are reinforced with a second layer of Kapton to prevent the rigidisation pressure causing a rupture when inflated. The resulting construction can be seen in Figure 96 prior to being wrapped onto the former seen in Figure 97. The former is used to ensure the antenna shape is held exactly to the antenna requirements during application and setting of the adhesive. After this, the former is removed and the Kapton base section is added. The bladder can then be inserted via either end ready for the mating to the end caps.

Figure 96. Spiral net pattern used to form the PICARD antenna

Figure 97. PICARD antenna formed around conical mould.

To proceed and seal the inflatable the apex cap and container base cap are required. The apex cap consists of 3 parts: the outer cap, the RF and accelerometer PCB and the inner cap. These additive layer manufactured (ALM) cap pieces can be seen in Figure 98. The antenna elements are then first bonded to the patches on the PCB using silvered adhesive. For WISCER it is planned that the antenna elements would be bonded to the edge of the apex PCB along the full length of the section arc. It is recommended that a rivet/crimp solution should be investigated for use on WISCER as testing of soldering and the use of conductive adhesive in the flight design yielded only satisfactory results from the mechanical and electrical bond.

The two caps then enclose the PCB, pinning the full circumference of the bladder and Kapton structure inside. Using adhesive on the inner surface of the caps yields an airtight seal. The RF coaxial cable can then be attached to the base and the apex before the base is sealed. For the base cap, the same process is repeated producing the fully enclosed inflatable. The inflation and pressure transducer feedthroughs should remain clear of

adhesive during this process and should be checked before setting occurs. Note the dual use of the container cap as the floor of the container. This allows for efficient use of mass/volume budget and easy integration.

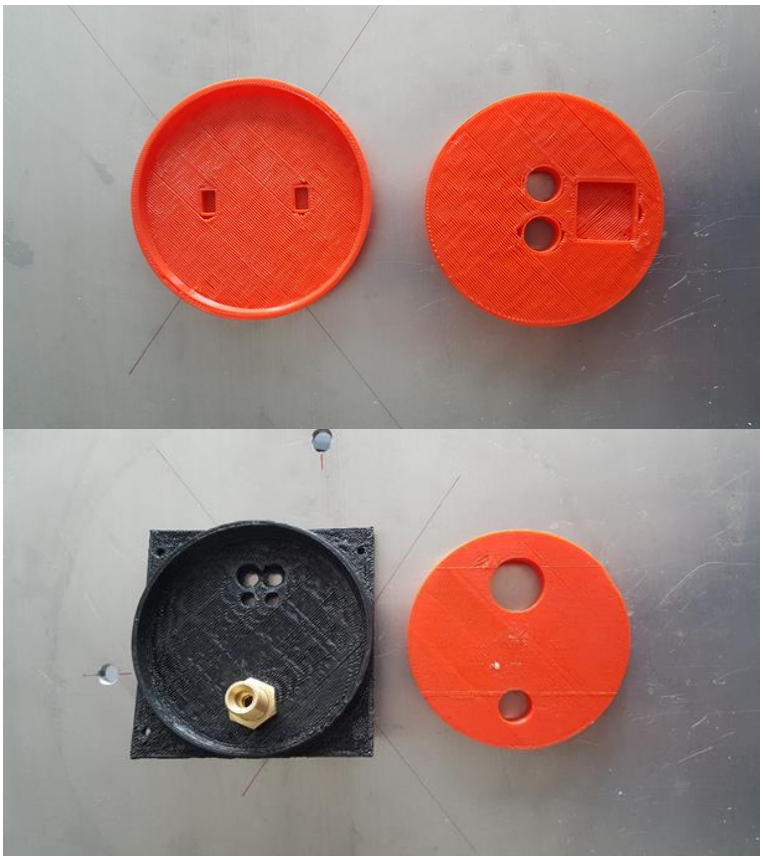

Figure 98 shows the pieces of the ALM caps for the inflatable PICARD antenna.

6.5.8) Flight Results of antenna deployment

In this section the mechanical performance results of the PICARD antenna deployment will be presented and analysed. Then once the key flight events have been described and the state of the inflated balloon known, the subsequent section will detail the RF performance of the antenna.

Table 6 details the key flight events for the PICARD experiment. After the rocket launch and ascent phase, the motor was ejected and the experiment body de-spun, achieving a

milli-gravity environment. The nose cone was then ejected at T+195s and the PICARD experiment proceeded into its active phase as planned.

Time	**Flight Event**
T+0s	Lift-off
T+26s	Motor Burn Out
T+66s	Payload-Motor Separation
T+98s	Yo-Yo De-Spin and Nose Cone Ejection (milli-gravity phase begins)
T+103s	Antenna Door Release
T+105s – T+106s	1st Opening of the Solenoid Gas Valve
T+108s – T+113s	2nd Opening of the Solenoid Gas Valve
T+115s – T+125s	3rd Opening of the Solenoid Gas Valve
T+125s – T+245s	RF Data Collection
T+195s	Antenna Ejection
T+245s	Re-entry
T+300s	Main parachute deployment (All payloads powered down)

Table 6 details the key flight events for the PICARD experiment aboard the REXUS 19 flight.

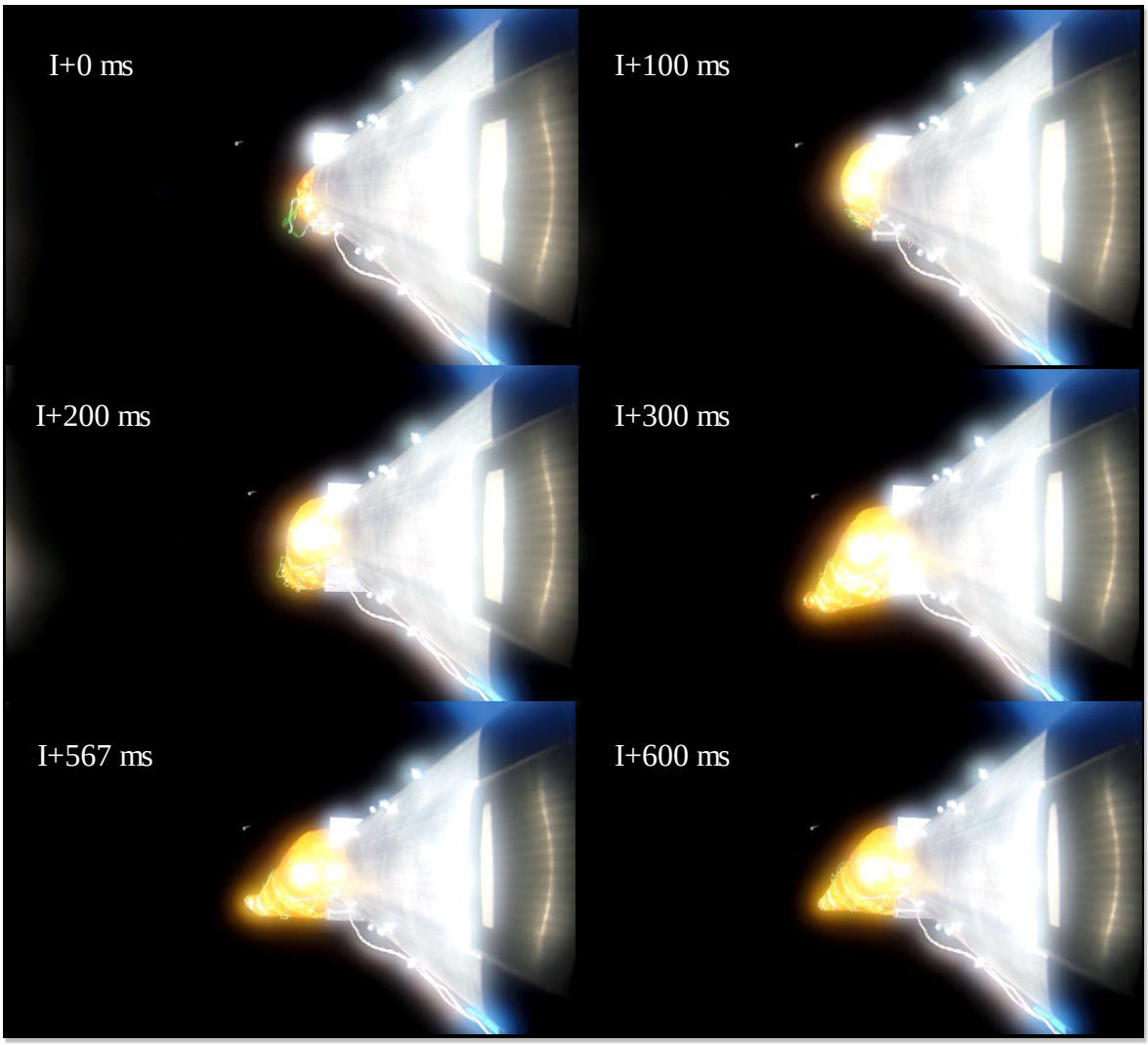

Figure 99 shows screen captures of key antenna inflation events during the suborbital REXUS 19 flight. The included time stamps were determined from the video frame numbers.

Figure 99 shows the successful inflation and rigidisation of the inflatable antenna. The images presented are screen captures from the on-board video and represent a fraction of a second after the first opening of the compressed gas reservoir valve. The first frame shows the moment the antenna is first seen on the video. The images then precede as follows: the base section of the antenna inflating first (I+100ms), the mid-section unfurling (I+200ms), a pressure excess (seen as a pause in the deployment) when the mid-section has inflated but the tip section has not yet unfurled (I+300ms), followed by the unfurling of the tip section (I+567ms) and then finally complete antenna deployment at I+600ms. It should be

noted that a snag of the strain sensor wires causes the antenna to inflate off the radial axis. This allowed the length of the antenna to be observed during deployment, until the over pressure self corrects the antenna shape and alignment by breaking the cables during the 2nd solenoid valve opening.

The successful inflation is immediately apparent from the video footage but evidence of successful rigidisation requires analysis of the recorded pressure and strain data. Figure 100 shows the relative antenna pressure as compared to the ambient pressure throughout the flight. Proceeding through the data in chronological order, it is first noted that there was not significant residual over pressure within the balloon during ascent. This was a concern during mission planning as the volume of trapped gas and leak rate could not be accurately predicted. The restraining door was designed to resist any residual pressure until it was safe to inflate at the time the door was released. From the video it can be shown that there was no significant premature expansion and the relative antenna pressure at this time was zero. Therefore, the trapped volume of gas is believed to have been very small and the leak rate (seen in Figure 100) high enough to dissipate it within 90 seconds of launch.

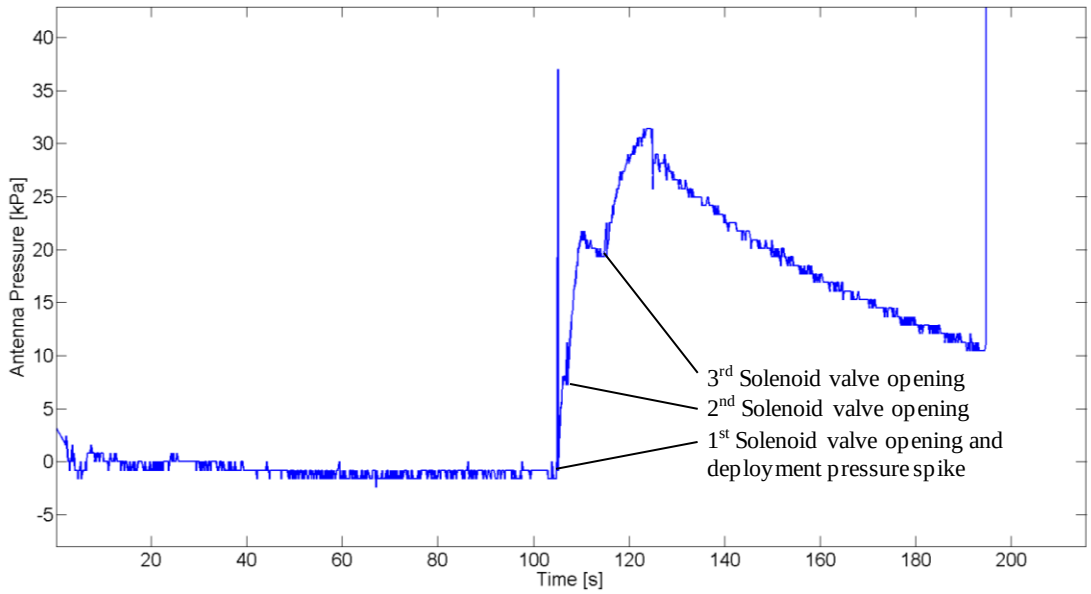

Figure 100. The graph shows the logged differential pressure between the interior of the antenna bladder and external pressure. Time is flight time in seconds; antenna inflation takes place from T+ 100s to T+125s.

At the moment of the first valve opening there is a transient pressure spike to 37kPa. As the pressure sensor was connected to a separate port to the antenna interior, to that of the gas input, it is expected that this is a true pressure spike within the antenna rather than an inflow transient. The most probable theory is that this spike occurred within the antenna base, creating enough pressure to overcome friction and push the antenna out of the container, as planned. With the container walls to support and the reinforced construction of the pressure bladder at the antenna base there is no chance of rupture at this measured pressure.

Following the initial pressure spike the antenna rapidly unfurls within 0.8 seconds. Following the deployment, the pressure within the antenna steadily rises as gas from the reservoir flows in to the antenna.

Upon the closure of the valve after its third opening sequence, the antenna reached the targeted peak pressure of 33kPa. Figure 101 shows the state of the inflatable at this moment. Following this peak, the pressure decayed due to the leak rate. Given the pressure

measurement and the known antenna construction it can be directly calculated, via hoop stress analysis, that the stress within the antenna elements exceeded the 325MPa value required for rigidisation. Unfortunately, due to the damage to the strain sensor wires during inflation, a direct measurement of strain could not be obtained to corroborate this result. The time available until re-entry was also not sufficient to observe the antenna with zero internal pressure. The leak rate could have been increased to show this behaviour, but during mission planning it was determined that this would generate too much risk with regards to achieving the peak pressure.

Figure 101 shows the inflatable antenna at the moment of peak pressure. It is at this point that the antenna was strained and rigidised.

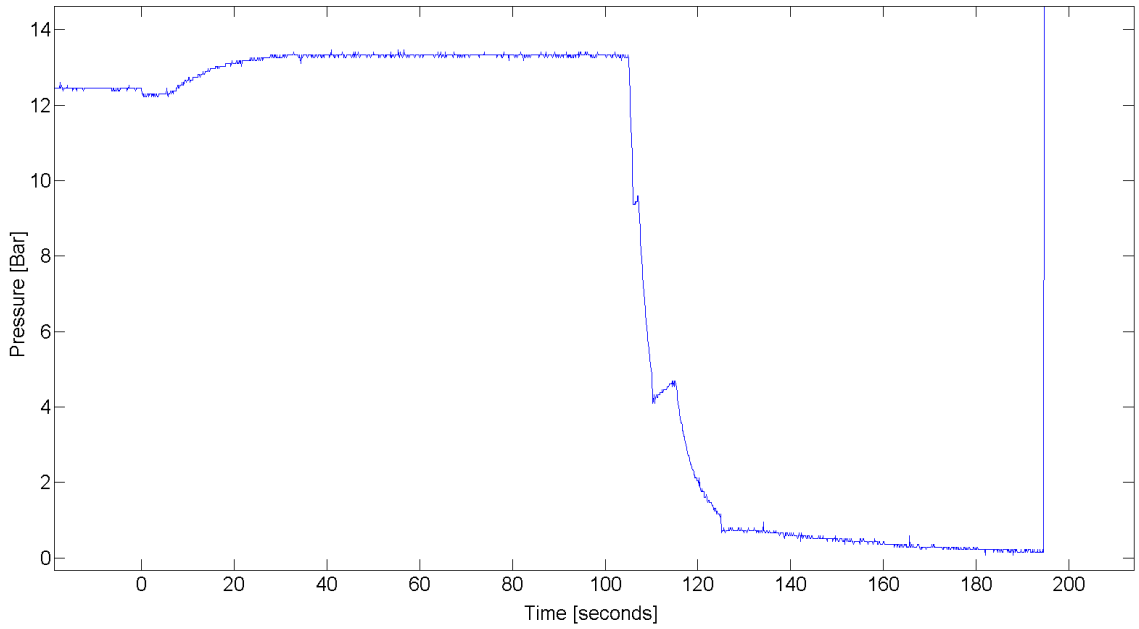

Figure 102. The graph shows the pressure within the gas system (Lift-off at T=0). Ejection can be seen at T+ 190s when the sensor value jumps high due to successful disconnection.

For completeness Figure 102 shows a graph of the reservoir pressure during the flight. The reservoir leak rate was carefully controlled to be very low (less than 0.5 bar in 24 hours). The apparent pressure increase after launch is an illusion caused by the relative pressure sensor used, being exposed to the external pressure drop during ascent. The pressure profile after inflation commences is consistent with the antenna pressure data (which used an internal vacuum reference).

Figure 103 shows the inflatable antenna post ejection. The compressed gas cylinder can be seen within the ejectable structure.

The mechanical dynamics observed during the data collection phase were very promising. The lack of oscillating motion suggests a more rigid connection than anticipated. The lack of deformation to the antenna shape is also ideal for RF performance. Based upon the re-entry drag disturbances seen on previous deployable REXUS experiments (Solar Sailors, 2013) it was expected that some deformation would have been observed just prior to ejection. However, no such behaviour was observed. Even during the ejection (Figure 103) no antenna deformation was observed from either camera. The internal antenna pressure

will dominate this initial structural stability though and so it is not possible to draw any conclusions concerning the long term stability based on these observations.

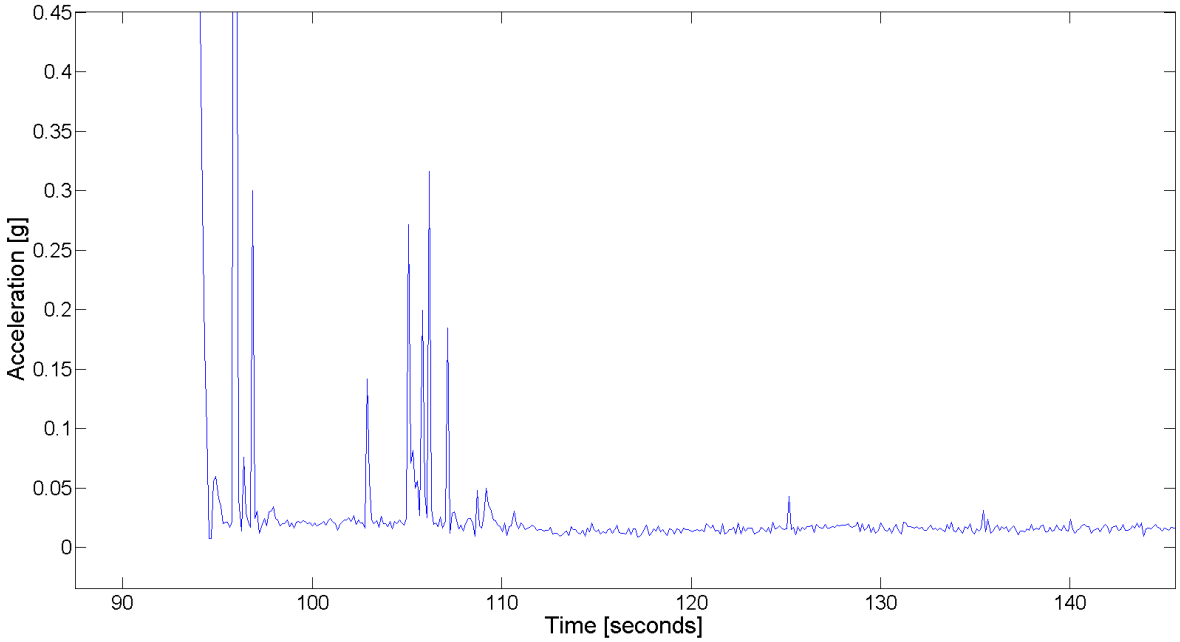

Figure 104. Accelerometer data for base of structure (total magnitude of x, y and z acceleration). Time is flight time in seconds; antenna inflation takes place from T+ 100s to T+125s.

Figure 104 shows the acceleration data recorded by an accelerometer mounted to the central RF subsystem mounting bracket, within the electronics housing of PICARD. The graph shows acceleration magnitude and focuses on the early milli-gravity phase. Data was captured from launch but is omitted prior to the Yo-Yo de-spin due to the high centripetal and motor thrust accelerations. The acceleration events located between 100-110 seconds are believed to be associated with PICARD as no other payload events occurred, by design, at that time. The spike at 103 seconds corresponds to the pyro shock release of the inflatable container door. The subsequent shocks correspond to the early stages of antenna inflation. Observation of the data shows no significant oscillations induced by the antenna movement or thrusts due to leaks from the antenna.

6.5.9) Flight results of Antenna RF measurement subsystem

In this section, the results from the antenna RF measurement subsystem of the PICARD experiment are presented. The experiment operated as expected, fully capturing all data to the micro SD card as well as sending a sample via downlink. The subsystem was named LAFORGE (See Appendix 1 for complete details) and operated with the aim of measuring the S11 of the inflated antenna in flight. It successfully activated just after antenna deployment was completed and operated for the full 120 seconds as planned.

Figure 105 shows all the raw data captured by the LAFORGE subsystem whilst the antenna was connected and active across multiple frequency sweeps (Blue). The graph also shows the results for the period after the antenna was ejected (Green), also for multiple frequency sweeps. After antenna ejection the coaxial cables are left as open circuits, completely reflecting the supplied power. The disparity therefore immediately verifies that the antenna was radiating and there was no damage/disconnection of the internal feed structure during launch and deployment.

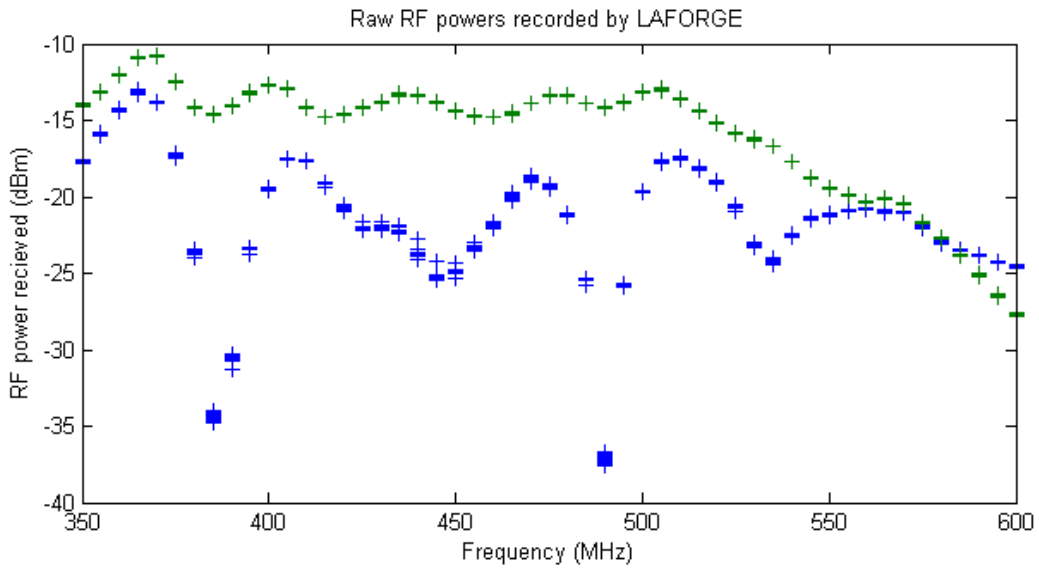

Figure 105 shows the raw data captured by the LAFORGE subsystem whilst the antenna was connected and active. Blue – antenna inflated. Green – antenna ejected. The data was stable, signifying no major reception of time varying external signals.

In order to determine the return loss of the antenna-balun system (which is equal to the negative of S11, which is in turn also equal to the reflection coefficient) we use the collected data and Equation 45. The result of which can be seen in Figure 106 (Green).

$$-S11\ (dB) = RL(dB) = P_{incident}(dBm) - P_{reflected}(dBm) \quad \textbf{Equation 45}$$

The next step is to remove the effect of the transmission line (also known as antenna feed line in this case) from the data. This effect, which was seen in the prototype tests, arises due to two factors: the length of coaxial cable required to traverse the ejectable structure and the impedance mismatch between the feed line and antenna. It is caused by the impedance mismatch generating reflections that travel back down the transmission line. This effectively changes the transmission line impedance at the input of the balun dependent on frequency as described in Equation 46.

$$Z_{in}(l) = Z_0 \frac{Z_{load} + jZ_0 \tan(\beta l)}{Z_0 + jZ_{load} \tan(\beta l)} \quad \textbf{Equation 46}$$

Where $\beta = \frac{2\pi}{\lambda}$ is the wavenumber, Z_0 is the transmission line characteristic impedance and l is the transmission line length. From this equation we note that for future antennas the effect can be minimised for any transmission line length if the transmission line impedance is finely tuned to the antenna impedance. However, it is difficult to remove completely due to the variation of antenna impedance with input frequency.

Once the effective transmission line impedance is calculated the resulting reflection coefficient can be determined with Equation 47. This calculation makes use of the known feed line length and constraints on the expected antenna impedance from simulation. It is noted that the transmission line fit in Figure 106 is somewhat lower than the measured S11

data. This is expected as the characteristics of the antenna itself are not included in the fit parameters.

$$\Gamma = \frac{Z_{load} - Z_0}{Z_{load} + Z_0}$$ **Equation 47**

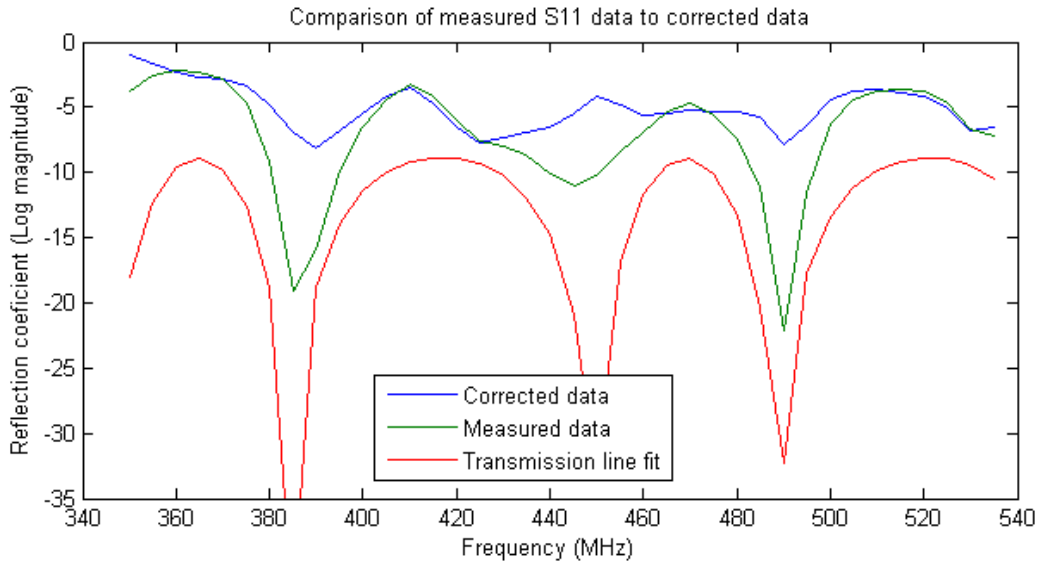

Figure 106 shows the S11 data measured by LAFORGE (green). It also includes the corrected data (blue) after removal of the frequency dependency of the transmission line (fitted transmission line curve (red)).

The correction procedure removes the frequency dependence from the impedance mismatch but specifically does not remove the mismatch itself from the system, showing the real performance of PICARD. The result of this process can be clearly observed in Figure 106, Figure 107 and Figure 108. Error bars are introduced to show the calculated systematic error from the correction process based on the limited knowledge of the transmission line length and the antenna impedance.

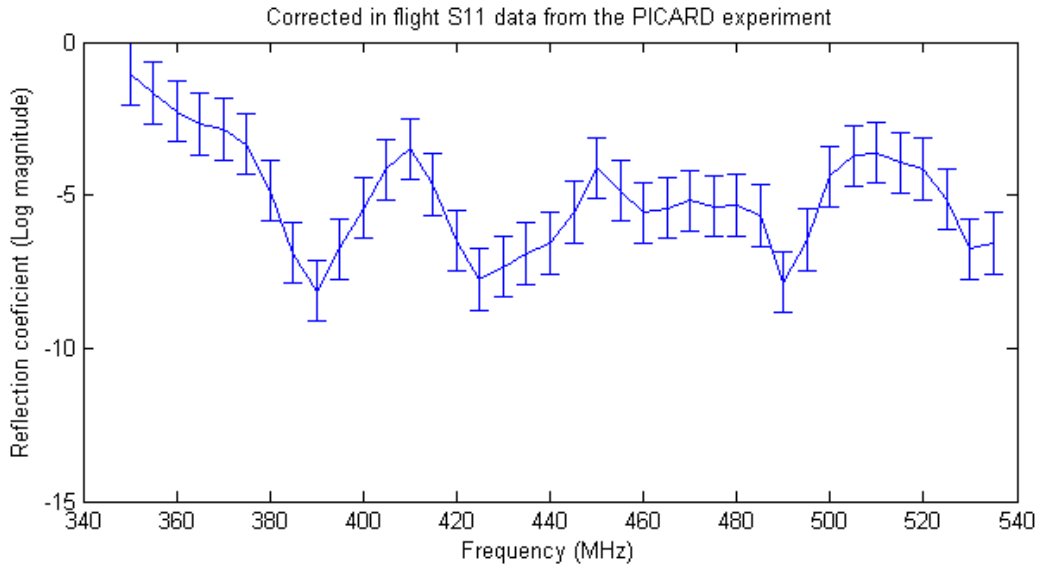

Figure 107 shows the final S11 result of the LAFORGE subsystem of the PICARD experiment. The antenna was functional and operated nominally.

Each of the PICARD antennas was single use due to the permanent deformation of strain rigidisation. Therefore prior to flight, in order to make a direct comparison, measurements were made of the flight antenna via ground based testing with a portable network analyser. We see this comparison in Figure 108, with the two results showing significant similarity. This similarity proves that the antenna was not significantly altered by the deployment process. The antenna was functional and did indeed inflate to the correct shape as seen in the video. Therefore, it is possible to conclude that the deployment mechanism deployed the antenna into the correct configuration without significant damage. However, due to the ±1dB systematic error of the correction method, we cannot rule out minor damage to the antenna elements, especially after the cable snag seen in the flight video. This event could very likely have caused small cracks in the aluminium elements due to over stress and therefore be responsible for some of the discrepancies.

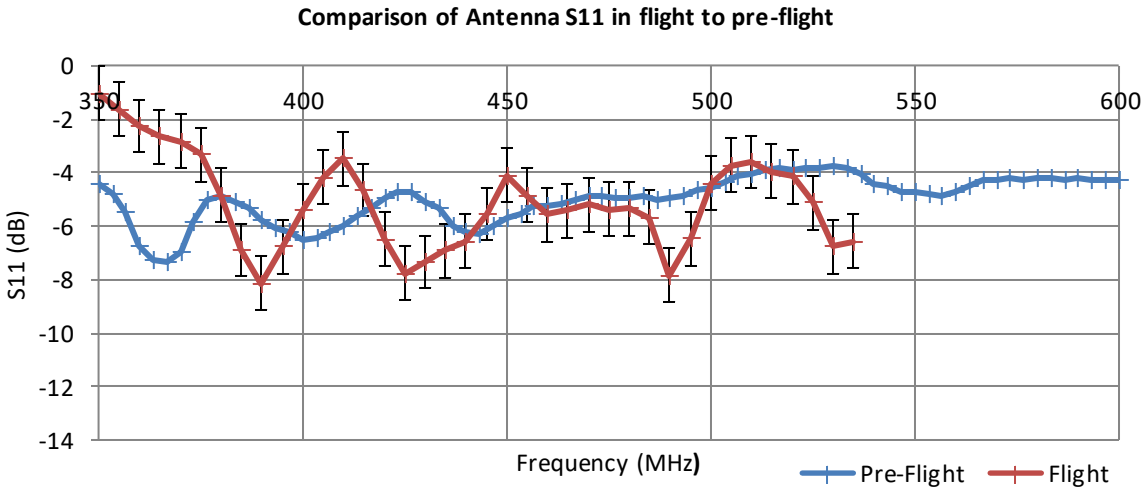

Figure 108 compares the S11 data recorded prior to the flight, via a portable scalar network analyser connected to the antenna feed line, to the corrected inflight measurements.

When compared to the predicted S11 results seen in Figure 109 (that have been corrected for the impedance mismatch) we can see that the results agree with the theoretical values. Another factor expected to contribute to the S11 variability in the post deployment results are the crinkles and small folds generated during packing of the antenna. Without time during the short REXUS flight for these folds to fully stretch out and settle, it should not be expected that the measured S11 be as smooth as the S11 measured before the flight, and not as smooth as predicted by the perfectly smooth antenna elements in the simulation.

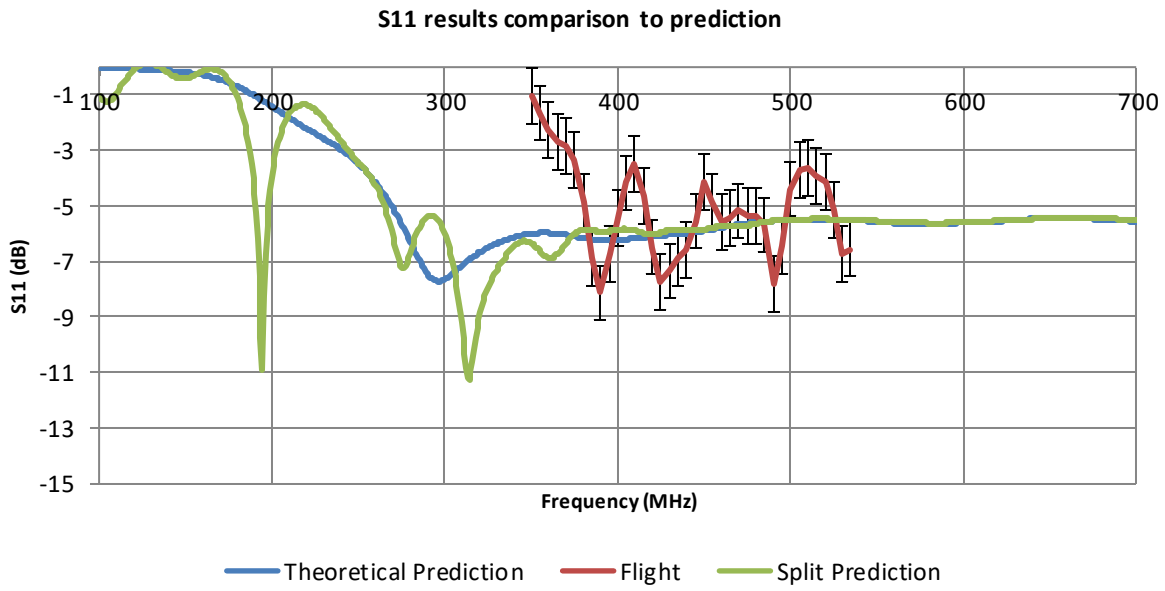

Figure 109 shows the corrected LAFORGE S11 flight data as compared to the predicted result of both a perfect theoretical antenna and one with a split arm near the base (after correction for impedance mismatch).

In conclusion the PICARD experiment successfully deployed and tested the antenna. The antenna deployed as planned apart from the damage to the strain sensor cables and the RF subsystem shows the antenna was radiating. Despite the failure of the strain sensors, the video evidence, accelerometer data and pressure logs support the conclusion that strain rigidisation was achieved without any rupture of the inflatable. The PICARD experiment not only showed successful results during flight but also provided valuable information on the construction methods required to build and operate such an antenna that will be an important foundation for any related inflatable structures.

Overall the conical helix antenna has been shown to be a viable candidate antenna for WISCER, yielding good RF performance. A novel inflatable deployment method has been explored and tested, providing the necessary results to further develop the antenna for this application.

CHAPTER 7) CROSSED MOXON ANTENNA

7.1) Introduction

A crossed Moxon antenna consists of a pair of bent dipoles orientated perpendicular to each other. This antenna type was first proposed by Moxon (1993) and since worked on by Tekin, Manzhura, & Niver (2011) for an application in UHF SATCOM. As part of the WISCER initial design study (Angling et al., 2013), the double vertical crossed Moxon antenna design was scaled for use in the WISCER frequency range. This design can be seen in Figure 110.

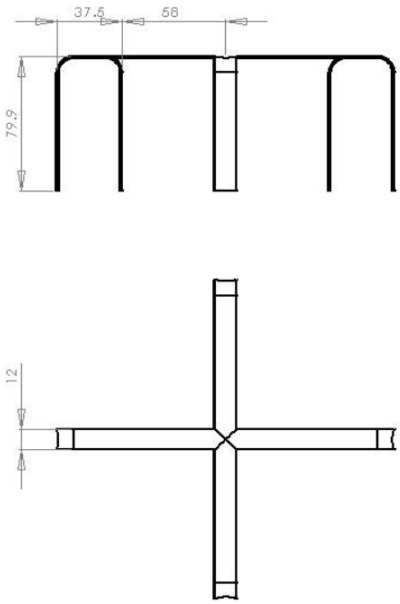

Figure 110 shows the initial crossed Moxon antenna elements configuration including the dimensions given in millimetres.

A prototype of a possible mechanical deployment method was created by the University of Glasgow to prove its viability. This design can be seen in Figure 111 and Figure 112 which show the packed and deployed states of the antenna.

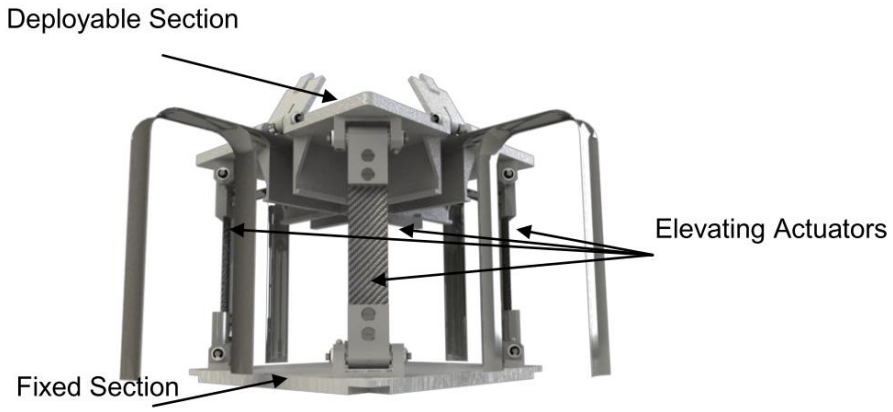

Figure 111 shows the deployed state of the crossed Moxon WISCER deployable. The main components of the deployable structure are labelled.

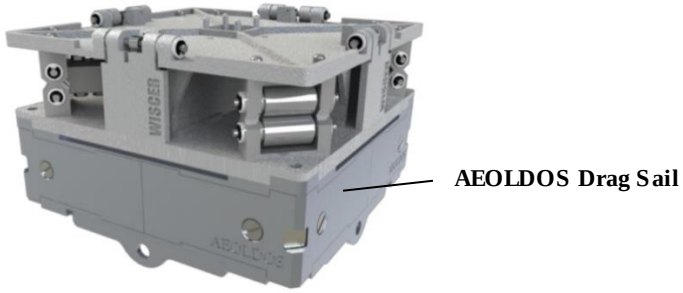

Figure 112 shows the packed state of the crossed Moxon WISCER deployable. The AEOLDOS drag sail is also included here in the undeployed configuration.

The prototype was used to perform deployment tests using a thermal knife release mechanism. A heater wire is wrapped around the mechanism restraining cable. When current is applied to the wire, the cable melts and the mechanism is released. The four actuating springs, in each corner of the deployer, then begin to push the top plate and antenna upwards. This releases the antenna door catches from the base plate, allowing the antenna arms to unfurl. During the test, this sequence was captured by a high-speed camera operating at 4000fps. Figure 113 shows the results of this test. As can be seen the deployment is very quick, releasing energy that must be dissipated without causing damage. For the flight model actuators, it is planned that a material with a lower spring constant be used. Despite the violence of the deployment, there is no risk of the CubeSat tumbling; as nothing is released and angular momentum is conserved within the system.

However, oscillations will occur due to the flexible nature of the springs until the energy is damped away by inelastic bending.

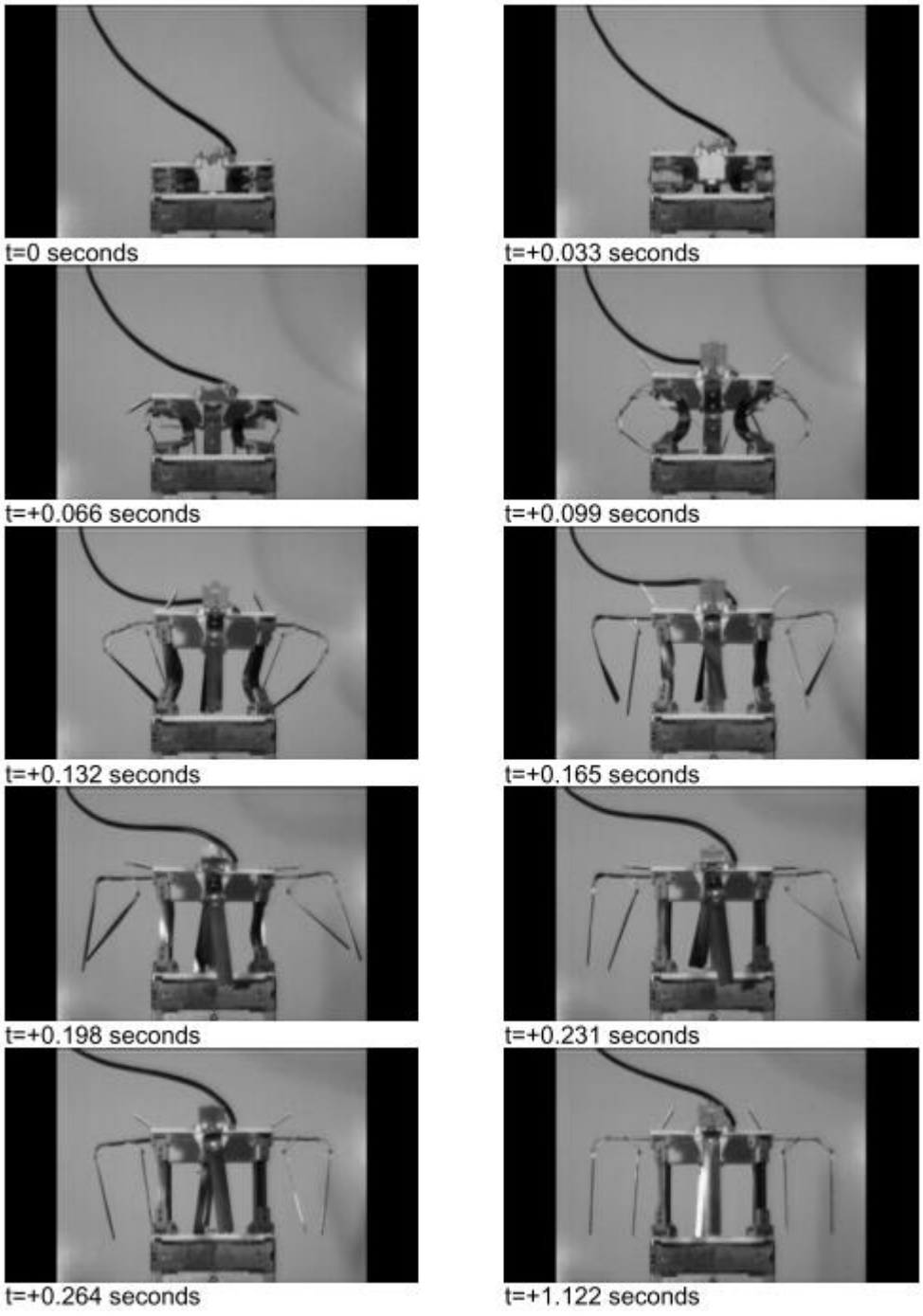

Figure 113 shows the stages of deployment during a test of the prototype mechanism.

The antenna is not by itself directional and requires a ground plane to radiate in the forward direction. This ground plane can be implemented using a repurposed AEOLDOS (Aerodynamic End Of Life DeOrbit System) unit (ClydeSpace, 2018a), which had the

added benefit of reducing the satellites lifetime as orbital debris after the one year mission. The fully deployed antenna can be seen in Figure 114.

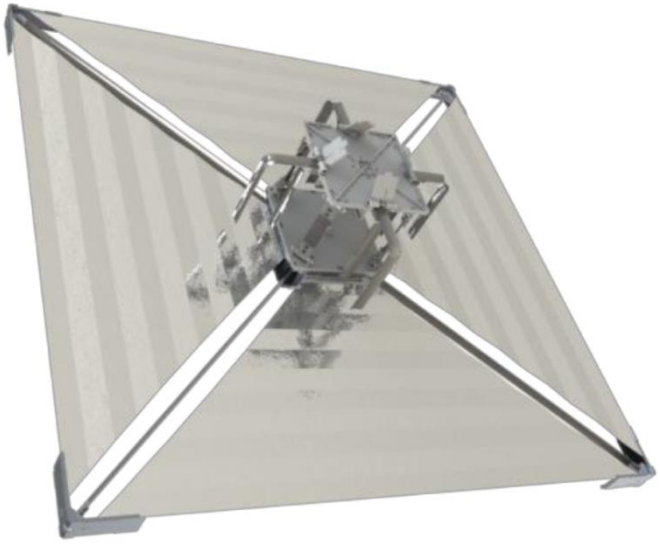

Figure 114 shows the fully deployed state of the initial crossed Moxon WISCER antenna including the active elements unit and the AEOLDOS ground plain (Angling, Harkness, & Drysdale, 2012).

The antenna-ground plane module is mounted onto the CubeSat service platform, which also holds the remaining payload electronics. The service platform structure is shortened so that the entire assembly fits within the 3U+ form factor. A schematic of the planned configuration can be seen in Figure 115, which also includes the intended layout of the feed-cable routing for the antenna.

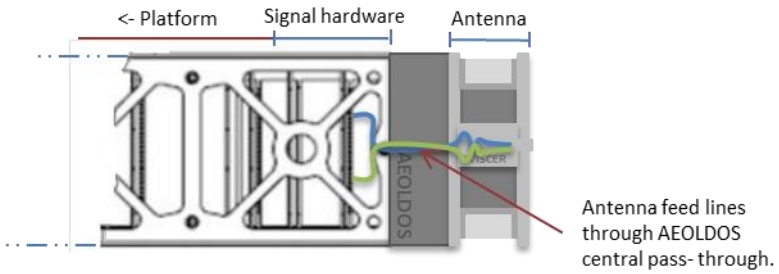

Figure 115 is a schematic of the crossed Moxon antenna attachment to the CubeSat service module.

7.2) Evaluation of the Crossed Moxon Design

The initial focus of investigation was to characterise the performance of the crossed Moxon as specified in Angling et al. (2013), with the objective of validating or correcting the assumptions made during its adaptation from the design (Tekin et al., 2011). The results from this evaluation could then act as a base line on which possible improvements could be made. The software package CST Microwave Office was used for this task via the same method as the conical helix antenna.

7.2.1) Validation of Current Concept

Simulations of increasing complexity starting from a simple dipole were carried out to gain a more rigorous understanding of the elements comprising the Moxon antenna. These included determining the effect of the arm width, height above the ground plane, bend location and the contribution of the inner arm. The effect of adding the inner arm is noteworthy and can be seen in Figure 116. It causes a slight increase in the antenna bandwidth but more importantly it lowers the resonance frequency of the antenna when added. This is caused by the added capacitive loading. This allows the antenna elements to be of a smaller size for a given required frequency range.

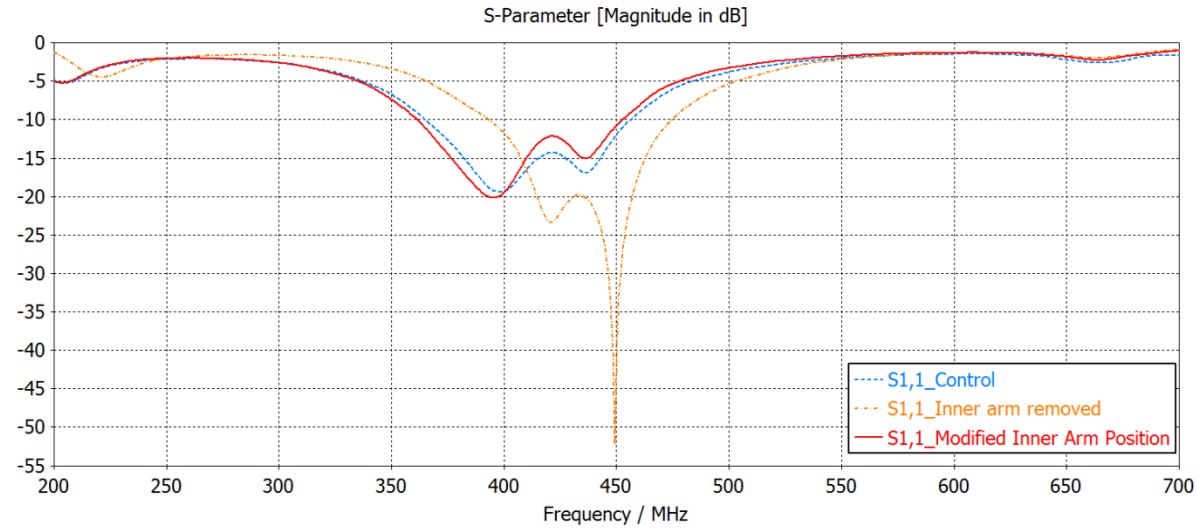

Figure 116 shows a series of linear S11 responses of the crossed Moxon antenna after modifications to the inner arm. The graph shows the effect of: removing the inner arm (orange), the inner arm position adjustment to prevent contact with the antenna mounting (red) and the original specification scaled from (Tekin et al., 2011) (Blue) as a control for comparison.

Figure 116 also provides data on the effect of the inner arm placement, where the blue curve shows the S11 profile for the original Moxon configuration. The CAD model used can be seen in Figure 117, which includes a one metre squared ground plane. Within Angling et al. (2013) it was suggested that the inner arm position be altered to prevent contact with the antenna mounting plate whilst still maintaining the 7mm distance to the AEOLDOS ground plane from the tips of the elements. The impact to the S11 profile is not significantly altered by this change (Figure 116).

It is noted here that, these results do not appear to agree with the experimental results of Tekin et al. (2011). Whilst the S11 profile looks similar in shape the bandwidth is significantly larger for their prototype. The model used here and the experimental setup used by Tekin et al. (2011) are not identical and most importantly there are no lossy materials in this simulation, but this is not expected to modify the results significantly. One potential explanation is the effect of the ground plane.

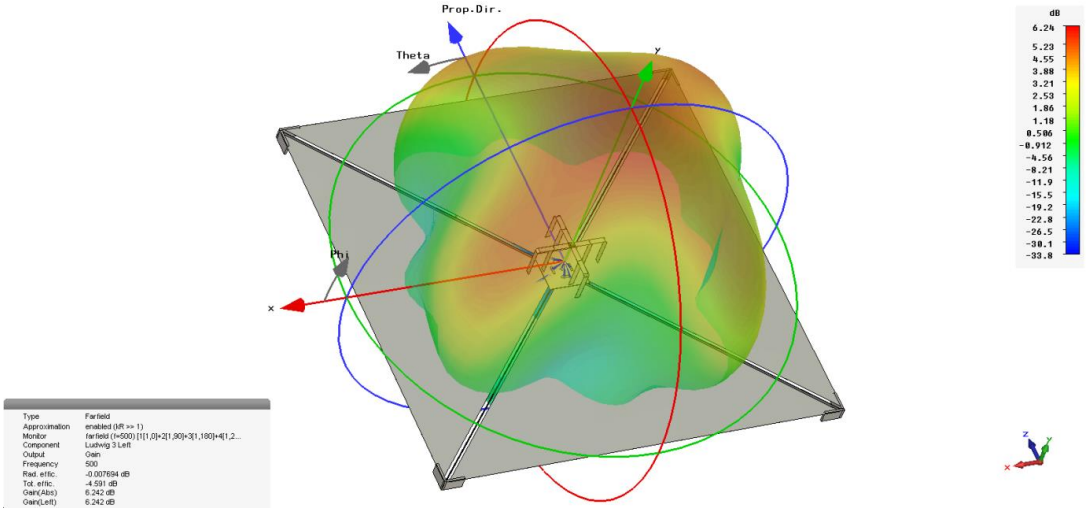

Figure 117 shows a 3D far-field plot of the crossed Moxon, similar to those seen in Figure 118 but with the inner arms in the original position. Across all three simulations the inner arm has a negligible effect on the radiation pattern.

Tekin et al. (2011) used a square ground plane of side length 4L (382mm) where L is the full horizontal length of a single antenna arm. In theory increasing the size of the ground plane should have a positive effect on antenna performance, increasing the forward transmitted power. Therefore, with AEOLDOS units available up to one metre squared this size was used in the initial RF and attitude control modelling. Figure 117 shows a 3D visualisation of the far-field pattern with the $1m^2$ ground plane which is also the same antenna specification used in the previous S11 results. Figure 118 shows the far-field plots for the same antenna with the modified position and removal of the inner arm. In all three plots, there is significant distortion of the expected circular pattern. Whilst the reason for this distortion was not fully investigated, reducing the size of the ground plane back to 4L by 4L does produce a smoothed radiation pattern and benefits the attitude control of the satellite. Figure 120 shows the new far field pattern, with the CAD model of the 4L ground plane in Figure 119.

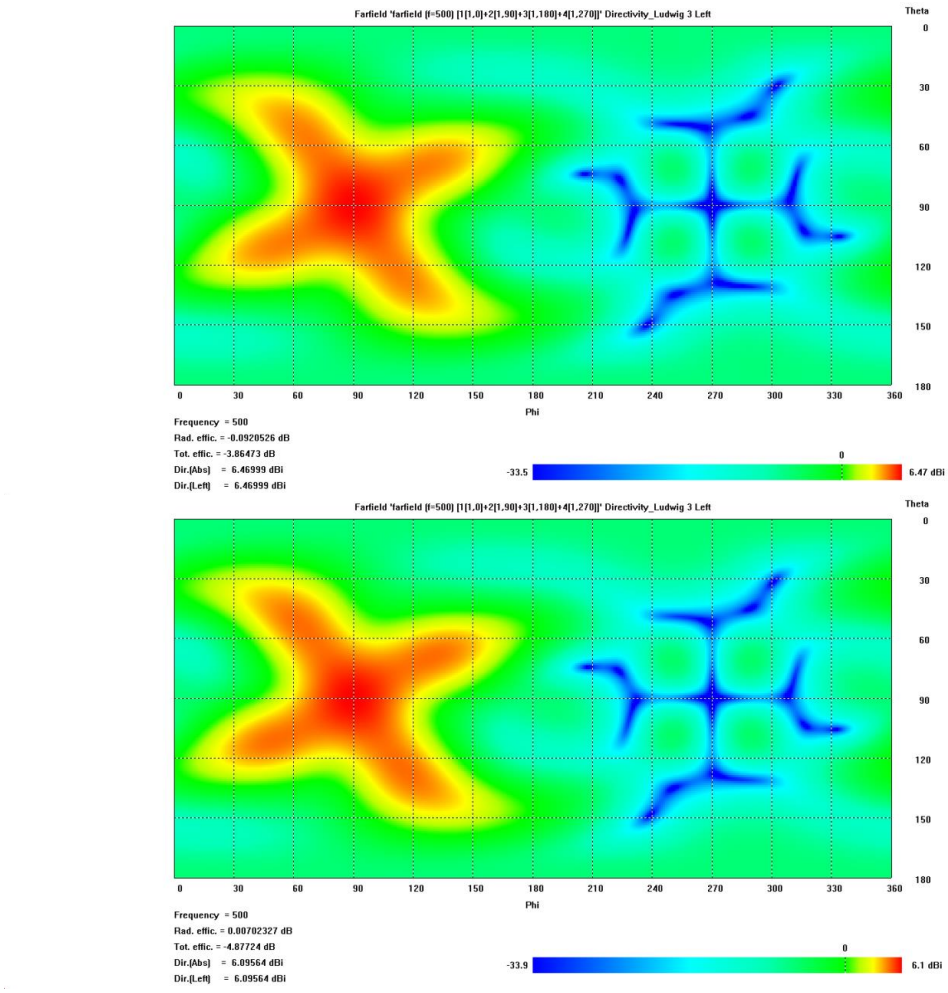

Figure 118 shows two 2D far-field plots of the crossed Moxon Antenna. The upper plot shows the directivity far-field pattern with the inner arm removed. The lower plot shows the directivity far-field pattern with the modification to the inner arm position suggested in (Angling et al., 2013).

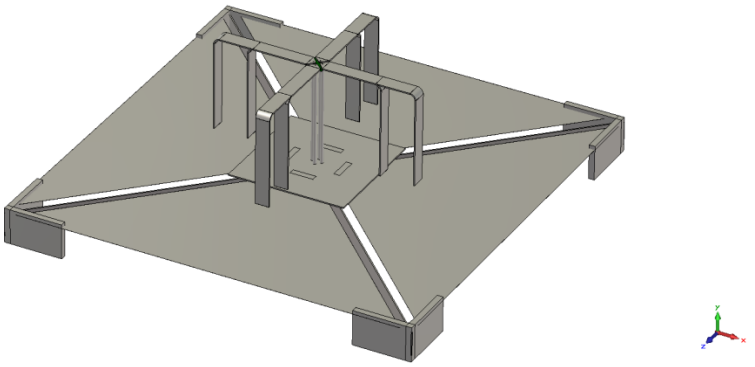

Figure 119 shows a 3D model of the reduced ground plane size. The ground plane dimensions seen here are consistent with the (Tekin et al., 2011) specifications.

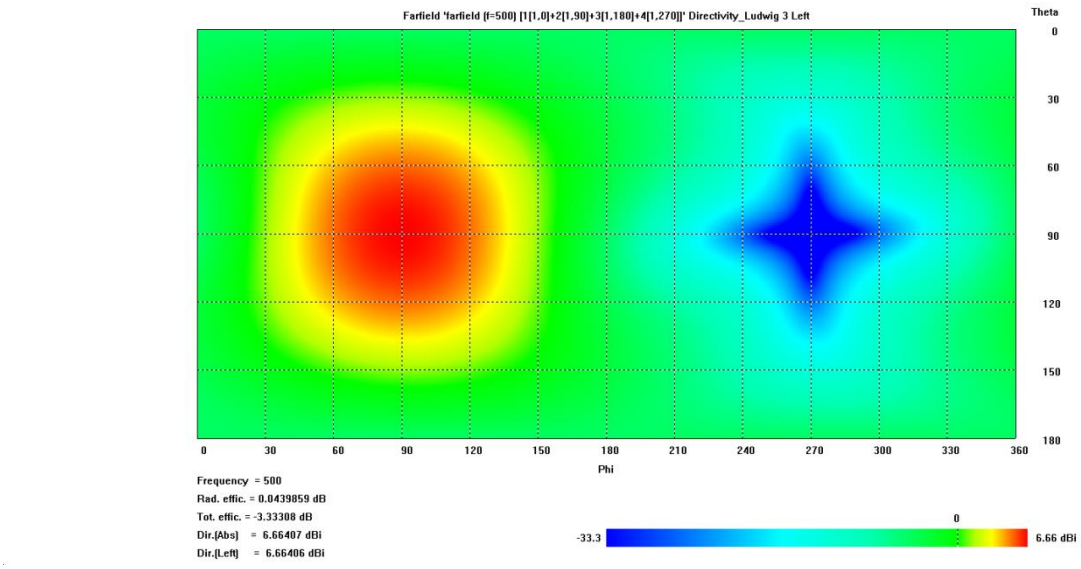

Figure 120 shows the Ludwig left hand polarised far-field pattern of the antenna shown in Figure 119 with the ground plane size defined by (Tekin et al., 2011).

The antenna design shown in Figure 119 represents the final evaluation of the basic antenna elements, having the specifications proposed in (Angling et al., 2013). To provide a baseline, the full set of antenna properties was determined for this model. Figure 120 shows that the left hand circularly polarised far-field pattern is uniform, with a full angular width (3dB) of 88.0°. This is less than the 90° requirement but still very applicable to the WISCER mission. The S11 profile, in Figure 121, is significantly affected by the reduction in the size of the ground plane and the bandwidth is reduced to 67 MHz (364MHz - 431MHz), for an input return loss below -10dB. For the WISCER experiment, the profile between 300MHz to 600MHz should ideally be smooth and flat to facilitate data analysis. The profile is smooth but not flat as seen in Figure 121. Whilst the response does drop to good levels within the stated bandwidth it steeply increases on either side.

The current radiative theory for the crossed Moxon is that it evolves from a dipole antenna, where the dipole arms are broadened to increase the antenna bandwidth. This is supported by the S11 profile in Figure 121, which approximates to that of a Lorentzian oscillator. One explanation for the increased bandwidth of the Tekin et al. (2011) antenna is possible

interaction with the ground plane or supporting structure used. This will therefore form a key consideration when modelling the antenna structure for WISCER.

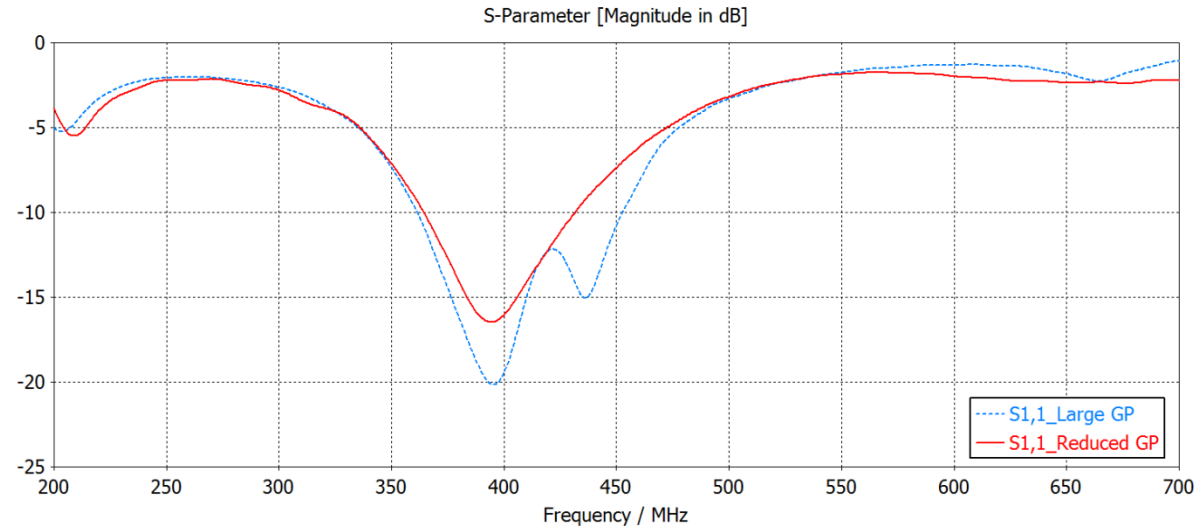

Figure 121 shows the S11 profile of both the 1m2 and 4Lx4L ground plane sizes of the crossed Moxon antenna.

The final antenna property considered here is the dispersion, or late time ringing of the antenna, of the antenna. A dispersion of less than 0.02μs is a requirement for WISCER. The graph in Figure 122 shows a simulated measurement of the radiated pulse waveform for the antenna. The antenna is seen to ring for the remainder of the simulation time, after the initial 4ns pulse. This is an issue as it means it cannot fulfil the dispersion requirement in Table 2.

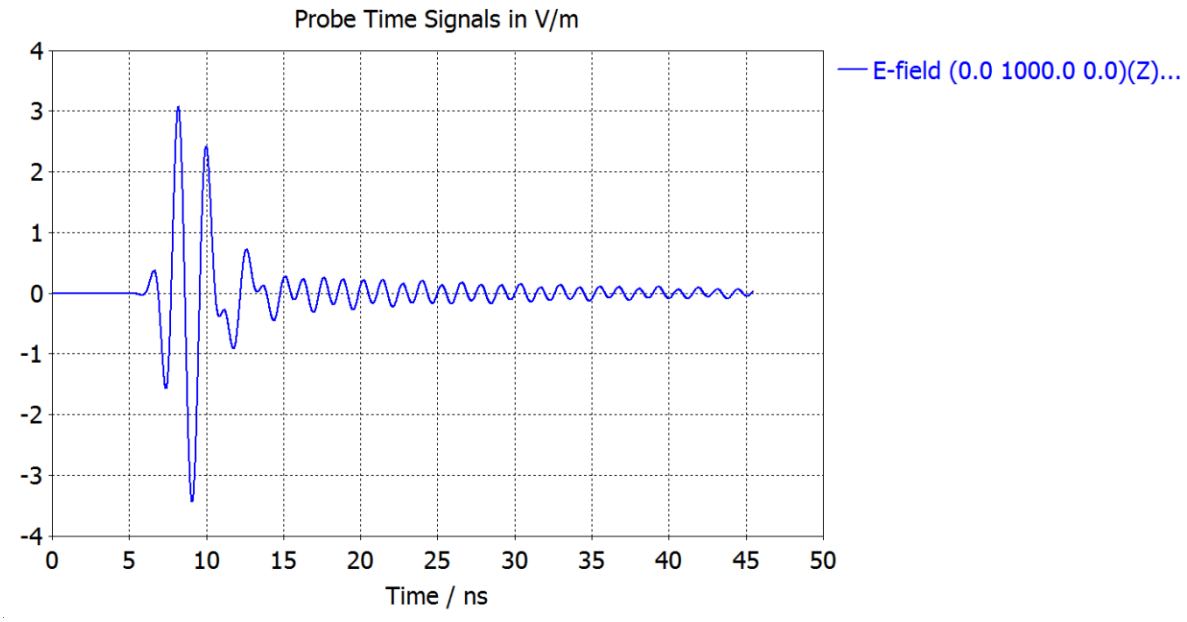

Figure 122 shows the time domain E field signals from the crossed Moxon as seen by a near field probe. The data in this graph is for a single antenna element.

7.2.2) Detailed RF Analysis of Preceding Mechanical Design

In collaboration with the University of Glasgow a detailed CAD model for this current crossed Moxon setup was created. The model includes all structural elements for the deployment system and can be seen in Figure 123. The AEOLDOS unit used was chosen to be the smallest available at 0.5m^2 in size, relating to a side length increase of 350mm to 700mm.

In order to simulate the antenna performance, using the CAD model provided by the University of Glasgow, the materials needed to be defined and the feed structure added. The choice of material for the support structure in the prototype was constrained by the separate decision to use a 3D printer. This support structure includes all the non-metallic parts that act to join the tape springs together. The choice of material for flight will depend not only on mechanical, survivability and manufacturing criteria but also of the RF performance. Therefore, for this preliminary simulation the representative material FR-4 was used, as its electromagnetic properties are well known due to its use as a PCB

substrate. It is very likely this will not be the material that will be used for construction, but it provides a good baseline for simulation. The remaining materials that were included in the model (primarily spring steel and aluminium) are well specified by the design and have well-known electromagnetic properties.

The antenna feed was designed and integrated within the CAD model. It makes use of four coaxial cables to carry the input signal to a small PCB to which the tape springs are electrically connected (Figure 123). This feed arrangement remained constant for all subsequent tests and is detailed more thoroughly in section 7.5. As four coaxial cables are used the outer conductors on each can be grounded to prevent radiation and minimise interaction with the antenna elements. Waveguide ports were used in this simulation to represent the connection with the matching and balancing circuitry that will be in the main body of the CubeSat. These ports, by definition, match the impedance of the geometry to which they are attached, which is in this case the termination of a coaxial cable designed to have an impedance of 50 Ohms.

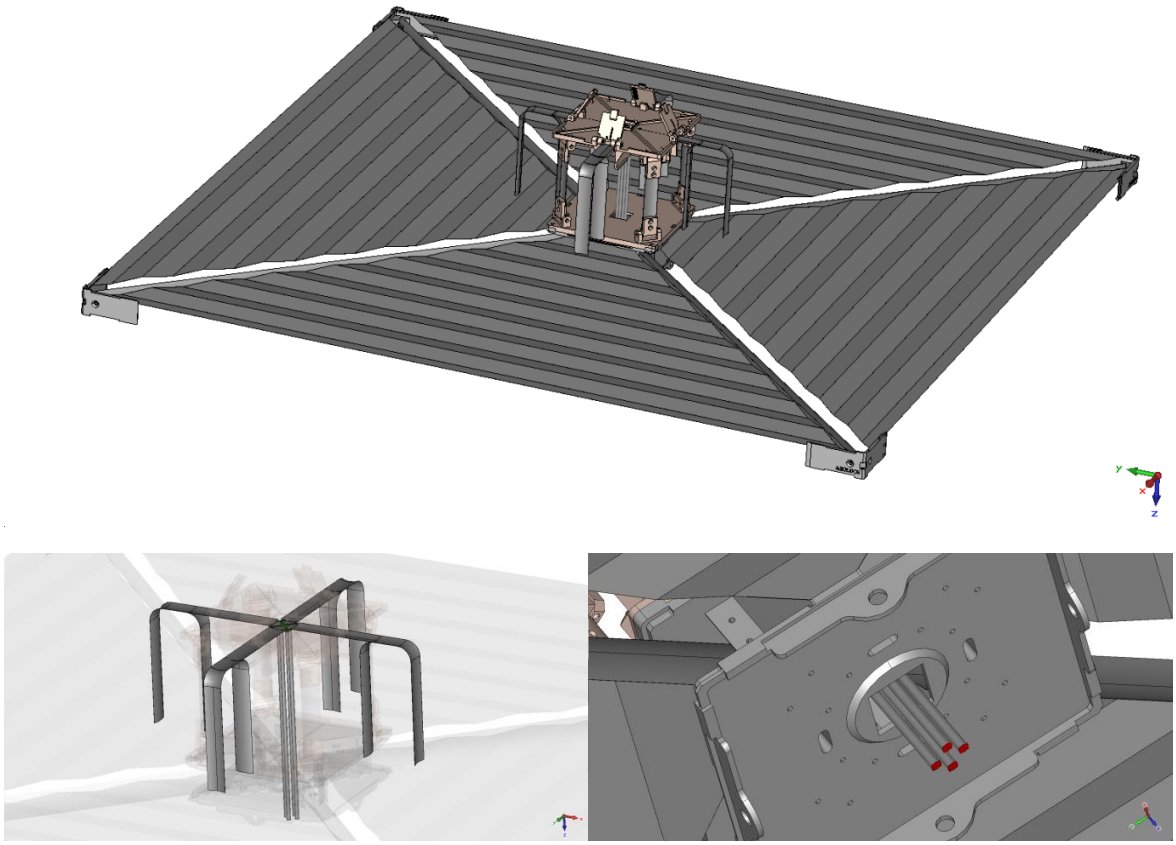

Figure 123 shows three images of the detailed crossed Moxon antenna CAD model. The top CAD model presents all antenna and structural elements of the (Angling et al., 2013) design but with a feed structure from this PhD work. The bottom left shows the primary antenna elements within the antenna structure. The bottom right image shows the waveguide ports used in this simulation that represent the connection to the matching and balancing circuitry.

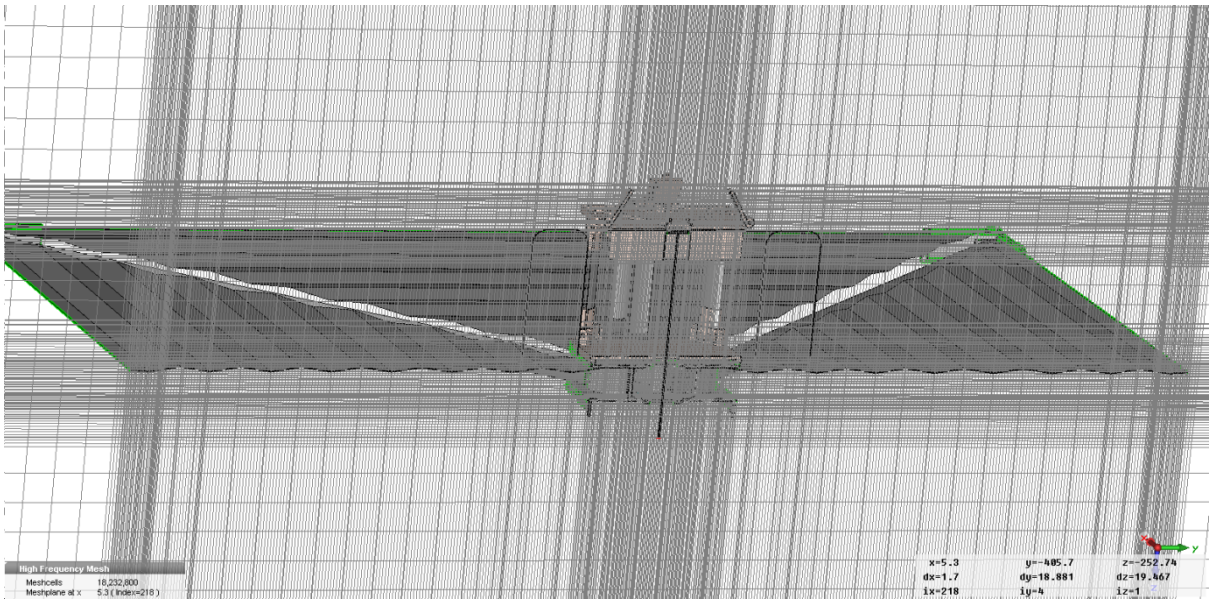

Figure 124 shows the mesh cell layout used to generate the hexahedral mesh for the simulation.

Although the antenna length is comparable to the wavelength of radiation being used, a dense mesh was required to provide sufficient detail for the simulation to model the electrical charge and current distributions. Figure 124 shows the layout and varying density of the cells used to generate the hexahedral mesh of the simulation. Due to the density of the mesh this model required approximately 30 hours to run on an Intel(R) Core (TM) i5-3570 3.4GHz CPU with 8GB of RAM.

The results from this simulation showed that the deployment structure has no significant effect on the antenna performance. The far-field pattern in Figure 125 shows no significant change over that of the simple model in Figure 120 (Note that the import of the CAD model has introduced a new co-ordinate system that explains the reversal in position on the graph). It is possible however to see the beginnings of the distortion caused by the increase in the ground plane size, most notably in the reverse transmission. This suggests that if other factors do not drive a reduction in size of the ground plane that the currently available $0.5m^2$ AEOLDOS unit may be suitable. The radiation efficiency has dropped from 0.98 to 0.89, which was expected due to the addition of the lossy FR4 material. At these frequencies FR4 has a non-negligible absorption spectrum and is unfortunately located in regions of high field strength. The choice of flight material should minimise this effect whilst also being resistant to the heat generated. A radiative thermal coating should be considered.

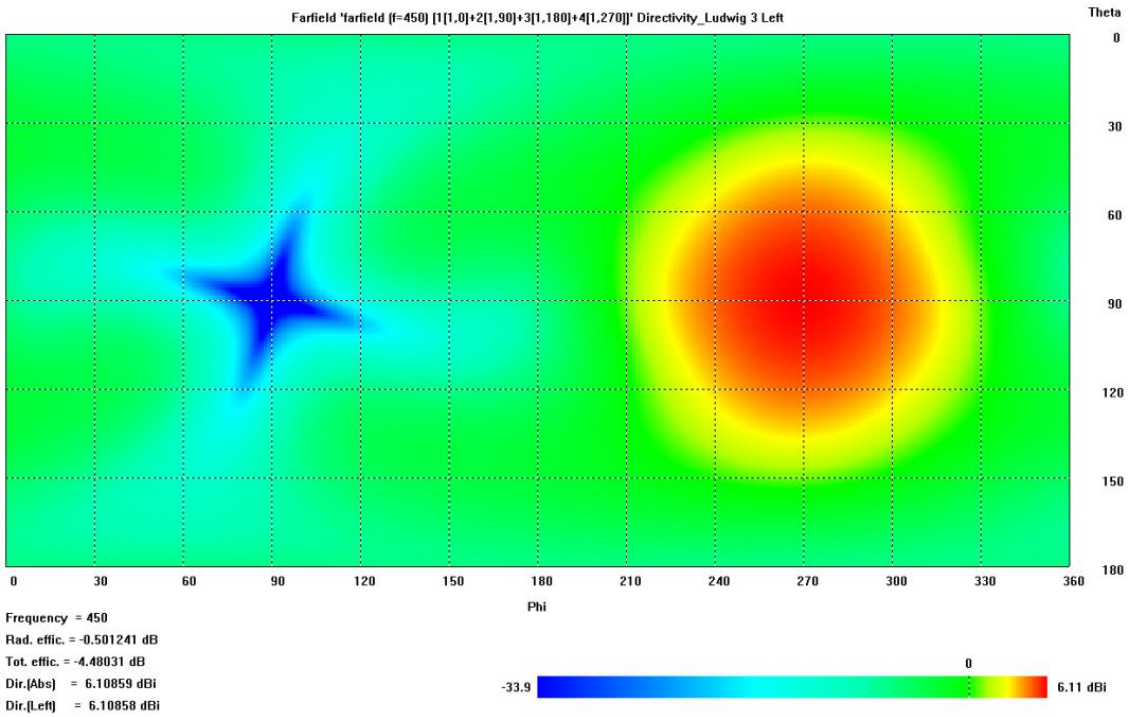

Figure 125 shows the far-field pattern of the detailed crossed Moxon CAD model with narrow antenna elements as seen in Figure 123. Note that the reversal of the propagation direction as compared to previous patterns is a result of the new co-ordinate system and not physically reversed transmission.

Figure 126 shows the S11 results for the simulation. The reflection of input power has greatly increased but the profile appears to still show the features of the simpler model suggesting that the results are physical and not an error in the simulation. It is therefore likely that, with the addition of the extra structure, the impedance of the antenna has changed and the reflection is occurring due to impedance mismatch between the antenna elements and the feed cables. Prototype investigation will be required to determine if this is the case or if there is another factor affecting radiation performance. Parametric sweeping to determine the optimal coaxial impedance has not been performed due to the long run time and complex nature of altering the physical dimensions of the cables.

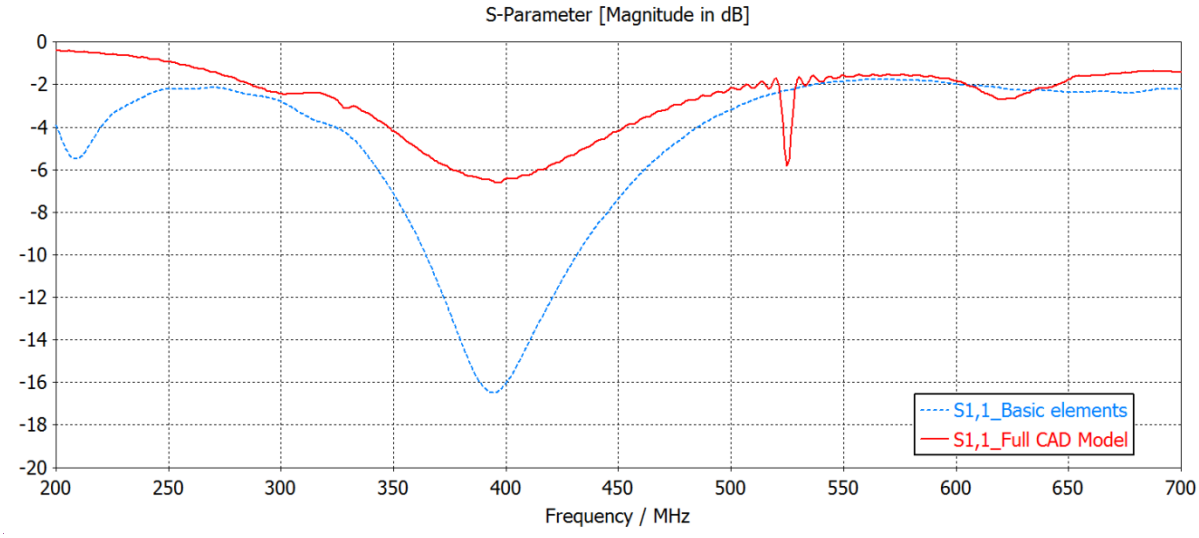

Figure 126 shows the S11 profile of the detailed narrow elements crossed Moxon simulation. The S11 of the basic simulation is provided for reference. The small oscillations in the results are not features of the S11 response but a product of the reduced simulation accuracy used to reduce run time.

7.3) Crossed Moxon antenna modifications and improvements

The results from the previous section show that there are areas of significant possible improvement of the crossed Moxon antenna, for application to the WISCER experiment. This section will describe the results of the RF simulations of the modified antennas. The aim is to improve the antenna RF performance whilst also optimising the overall satellite system performance (by reducing drag, mass, etc.).

7.3.1) Ground Plane Minimisation

The ground plane of the crossed Moxon is the largest contributor to the generation of disturbance torques on the satellite (see chapter 5). Reduction in its size or effective area will reduce the magnitude of the corrections required by the attitude control system which will in turn reduce the power, mass and volume requirements of that system.

An initial concept for reducing the effective area of the ground plane to both radiation pressure and aerodynamic drag was the addition of punched holes and can be seen in

Figure 127. As these holes are small compared to the operating wavelengths, the transmitted energy effectively sees a homogeneous ground plane to good approximation. The holes were intentionally placed away from the end points of the antenna elements to prevent changes to the element tip capacitance. This approach could be expanded to a wire mesh configuration, so long as enough material is present to maintain the reflection characteristics and structural integrity.

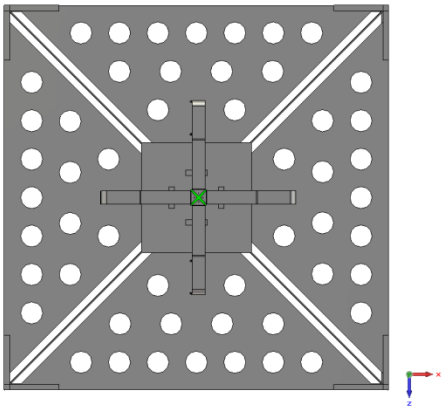

Figure 127 shows the crossed Moxon antenna with circular holes punched into the ground plane to minimise disturbance torques.

Figure 128 shows the far-field pattern results for the configuration shown in Figure 127. No effect is seen on the pattern smoothness or the peak directivity. This is as expected given the transmitted wavelength. From this it can be concluded that the structural integrity of the ground plane is likely to be compromised before the antenna performance is affected. The ground plane merely has to satisfactorily maintain the virtual images of the driven elements in order to preserve the radiation pattern. It is proposed that a fine wire mesh, with very high transparency, would be suitable for this purpose.

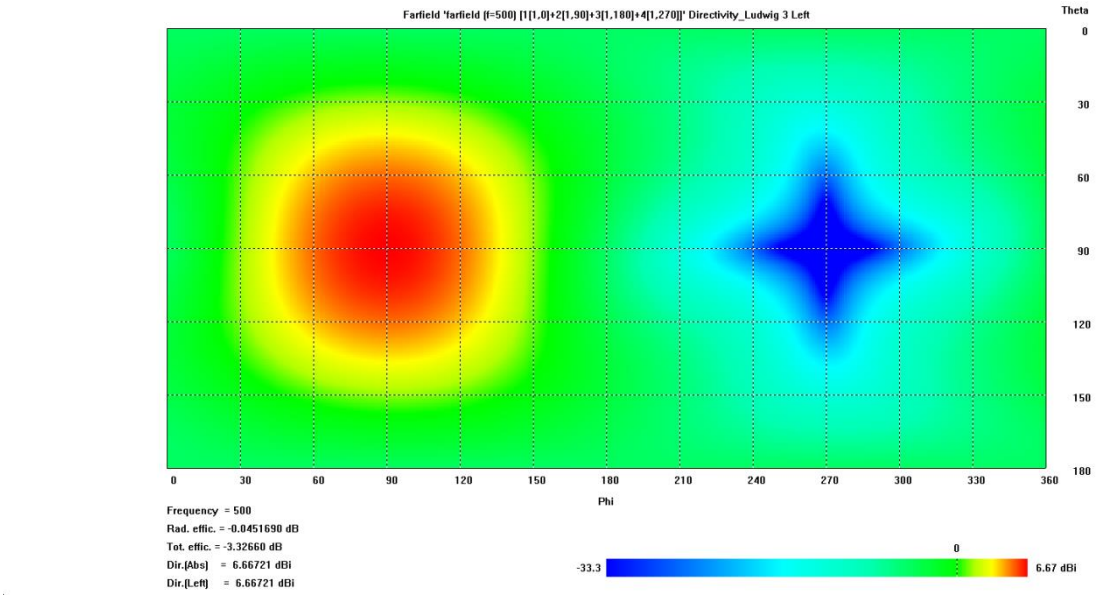

Figure 128 shows the left hand circularly polarised far-field pattern of the crossed Moxon antenna with holes punched into the ground plane. The configuration of these holes is shown in Figure 127.

7.3.2) Replacement of AEOLDOS with Solar Panel Ground Planes.

The crossed Moxon variant of WISCER will require deployable solar panels to meet its power demands. If the deployable solar panels can perform the dual use of also acting as the antenna ground plane, then the allocation of the mass and volume budgets for both systems together will be greatly reduced. An end of life de-orbit system may still be required but could potentially be of greatly reduced mass and complexity.

The requirement for an effective ground plane is that it should reflect the operational radio frequencies with minimal losses. Any metallic layer of sufficient thickness and smoothness can fulfil this requirement so long as there is not a lossy dielectric material between it and the antenna elements. There is no restriction to materials attached to the reverse side of the ground plane. Solar panels can therefore perform this role if they are facing away from the antenna elements. If there is no metallic layer already on the reverse of the panel one can be attached without affecting the energy collection requirement. The solar panels may potentially be affected by the induced voltages in the ground plane and so this should be investigated prior to the use of this design option, but it is not expected to be an issue.

The WISCER experiment will make measurements at approximately 22:00 local time over the equator to investigate the post sunset equatorial ionosphere. As this period is during eclipse there should be no conflict between the nadir pointing requirement of the antenna and the sun facing requirement of the solar panels. If for simplicity the nadir pointing of the satellite is maintained throughout the orbit there would also be significant exposure of this solar panel configuration to the sun as the two orientations align at local noon time. If the remaining body of the CubeSat were made up of solar panels this would lead to continuous power generation throughout the non-eclipsed phase of the orbit. The initial proposed design can be seen in Figure 129 and consists of four 2U solar panels. The solar panels in this model are represented simply by metallic panels which should be replaced with more realistic solar panel structures in future analysis. They provide sufficient accuracy for this initial test.

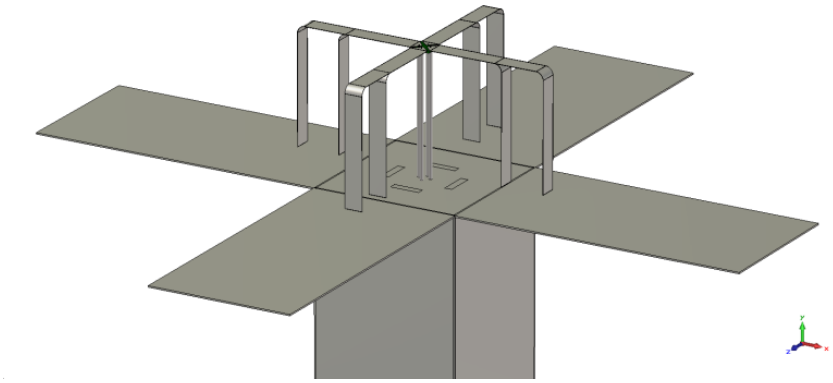

Figure 129 shows the 3D model used to simulate the antenna performance when using four 2U solar panels as the antenna ground plane.

Alteration of the ground plane presents the possibility of altering the radiation pattern of the antenna. In this case, as some of the reflective surface has been removed, a negative impact on the antenna forward gain and pattern smoothness is to be expected. Whilst we can see that this is the case in Figure 130, the effect is minor due to the alignment of the solar panels and the antenna elements. The peak directivity does drop from 6.66dBi to

5.32dBi but the radiation pattern remains smooth and circular. With the addition of more complex deployable geometries, further solar panels, the reduction in directivity could well be mitigated whilst also increasing solar power generation.

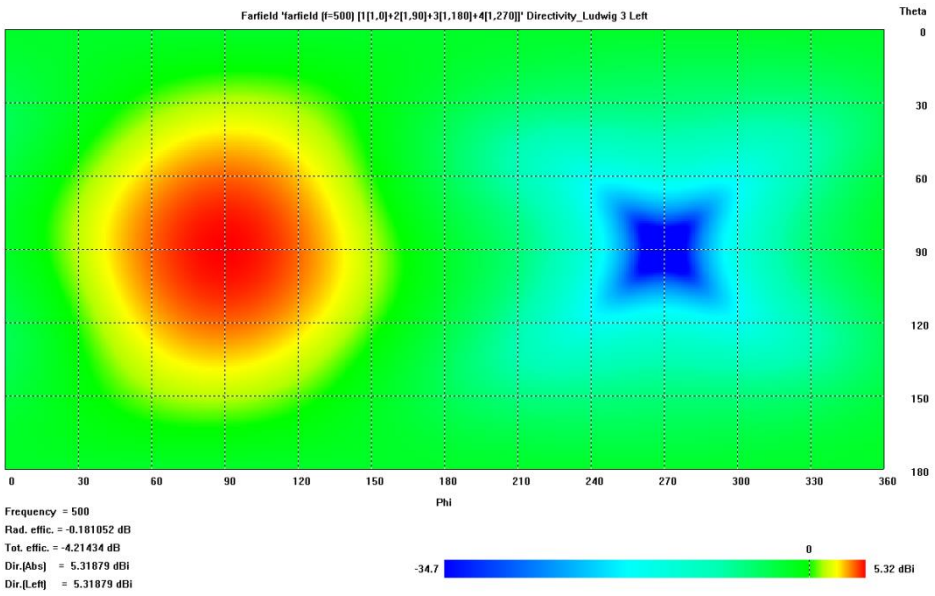

Figure 130 shows the left hand circularly polarised far-field pattern of the crossed Moxon antenna with four 2U solar panels acting as the antennas ground plane.

7.3.3) Antenna Element Shape Modification

Reducing reflections within an antenna is known to improve the antenna's wideband characteristics i.e. (Wu & King, 1965), (Lestari et al., 2004) and (Shlager, Member, Smith, & Maloney, 1994). These reflections are a characteristic of the resonance of narrowband antennas but also lead to the suppression of off resonance frequencies. Reducing reflections also reduces late time ringing which is a problem for the crossed Moxon antennas presented to this point as seen in Figure 122.

There are many ways to prevent reflections with a number discussed in chapter 4. The initial investigation here will look at low loss resistive loading through shape modification. The first and simplest alteration towards this goal is the conversion of the vertical antenna elements to tapers. This means the vertical section of the antenna reduces in width to a

point at the ground plane end of the element. Here a linear relationship is used for simplicity. The CAD model of this design can be seen in Figure 131.

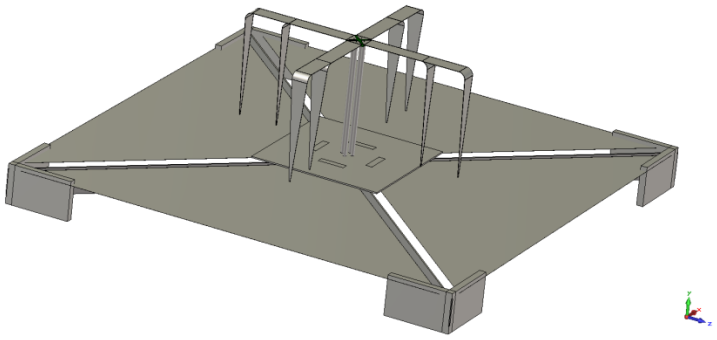

Figure 131 shows the crossed Moxon simulation model with ends that taper to a point on their vertical sections to prevent return signal reflections.

Looking at the S11 results, in Figure 132, from this model we can see that the bandwidth of the antenna has increased from 67MHz to 83MHz (-10dB) or in fractional bandwidth 1.184:1 to 1.204:1. The resonant behaviour is still clear though and the resonance frequency has shifted up due to the virtual shortening effect caused by the tapers. This is undesirable as the relative size of the antenna will increase for a given frequency.

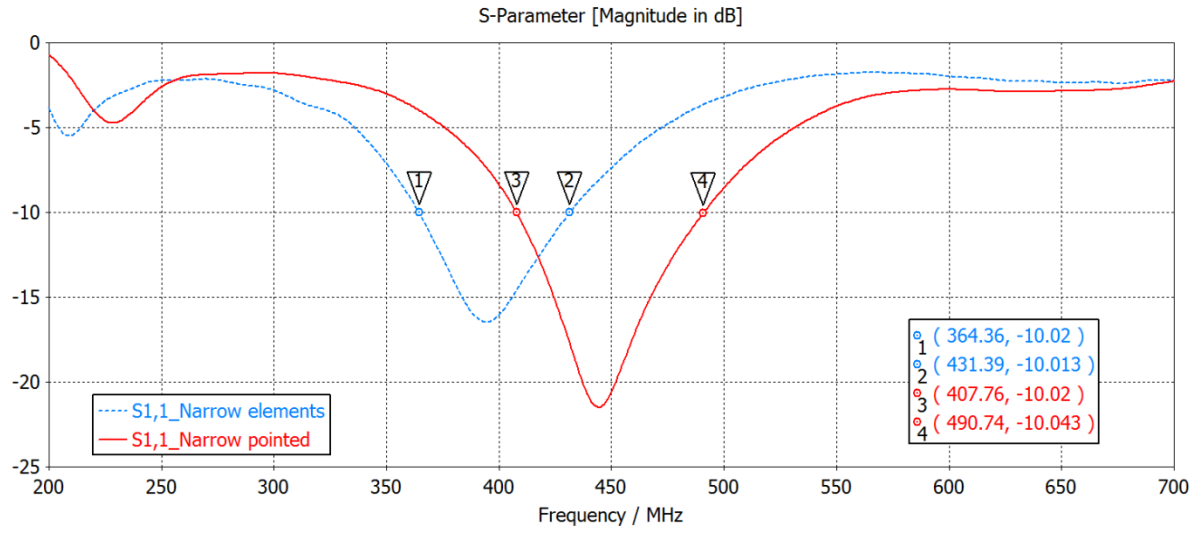

Figure 132 shows the S11 plot of the crossed Moxon antenna with the narrow, pointed vertical elements compared to the previous results from the model in Figure 119 with straight elements.

Further simulations were conducted on a model with parametrically defined elements in order to determine if further improvement was possible. Widening the horizontal arms was focused on to attempt to emulate a bow tie antenna for this section, nearest to the antenna feed. Parametric evaluation showed that the optimum location for the reversal in the taper direction is at the outer bends. Maintaining the 12mm end width also counteracts the virtual shortening and maintains antenna bandwidth.

Figure 133 shows the result of a parametric sweep of the antenna element width, widening from the original narrow elements to close to the maximum possible without contact between the four elements. As can be seen the narrowband nature smoothly transitions to a wideband profile as the element width is increased. The model labelled (9) was chosen for further investigation and can be seen in Figure 134.

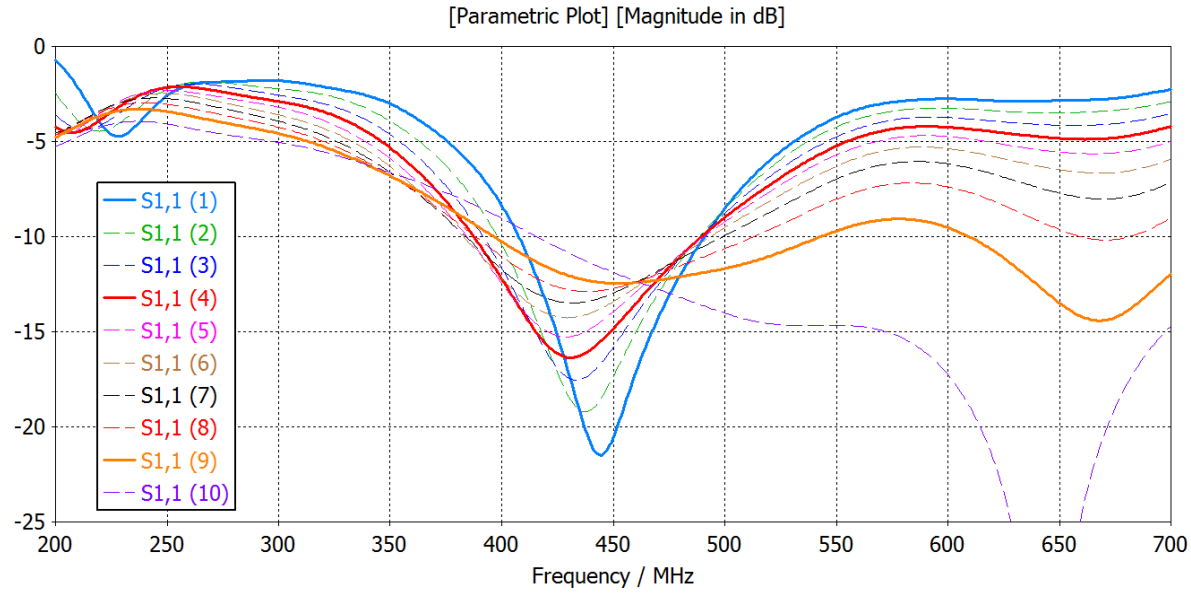

Figure 133 shows the S11 results from a parametric sweep of the antenna elements width. The range of this sweep runs from the straight elements seen in Figure 131 to close to the maximum possible without contact between the elements.

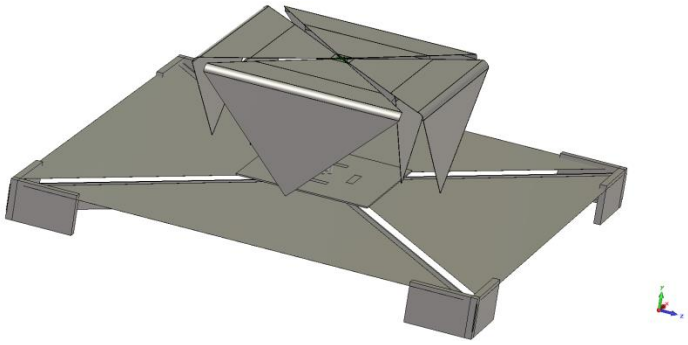

Figure 134 shows the wide antenna elements crossed Moxon CAD model that presented the optimum wideband properties from the parametric evaluation.

The S11 profile of the model shown in Figure 134 can be seen in Figure 135. It shows a greatly increased bandwidth over the previous results. The far-field pattern seen in Figure 136 shows no significant change despite the significant change to the antenna elements shape.

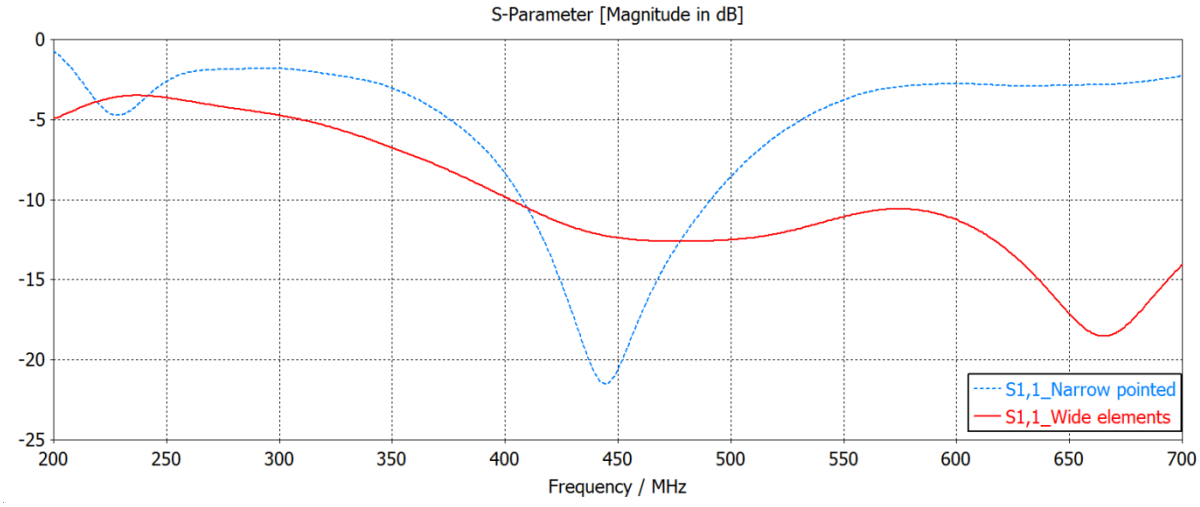

Figure 135 shows the S11 plot of the widened crossed Moxon antenna compared to the previous narrow points elements.

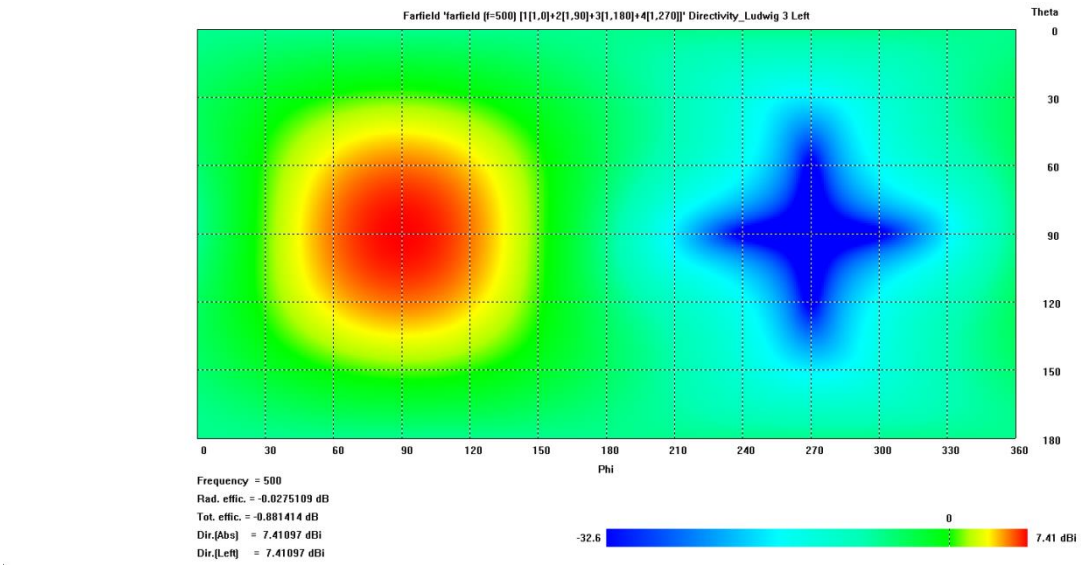

Figure 136 shows the left hand circularly polarised far-field pattern of the crossed Moxon antenna with widened arms.

The prototype deployable structure in Figure 111 would need a very significant redesign to accommodate the wide arms that produce the best wideband properties for the crossed Moxon. Therefore, it is necessary to compromise on the bandwidth of the antenna. The minimum required bandwidth viable for WISCER is 100MHz. The design shown in Figure 137 was designed to satisfy both constraints.

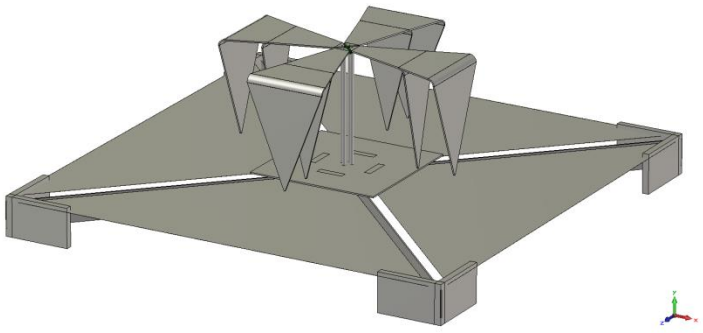

Figure 137 shows the CAD model of the compromised wide crossed Moxon antenna designed to provide the minimum WISCER requirement for bandwidth with the smallest antenna elements. Finalised measurement specifications are given in Figure 150.

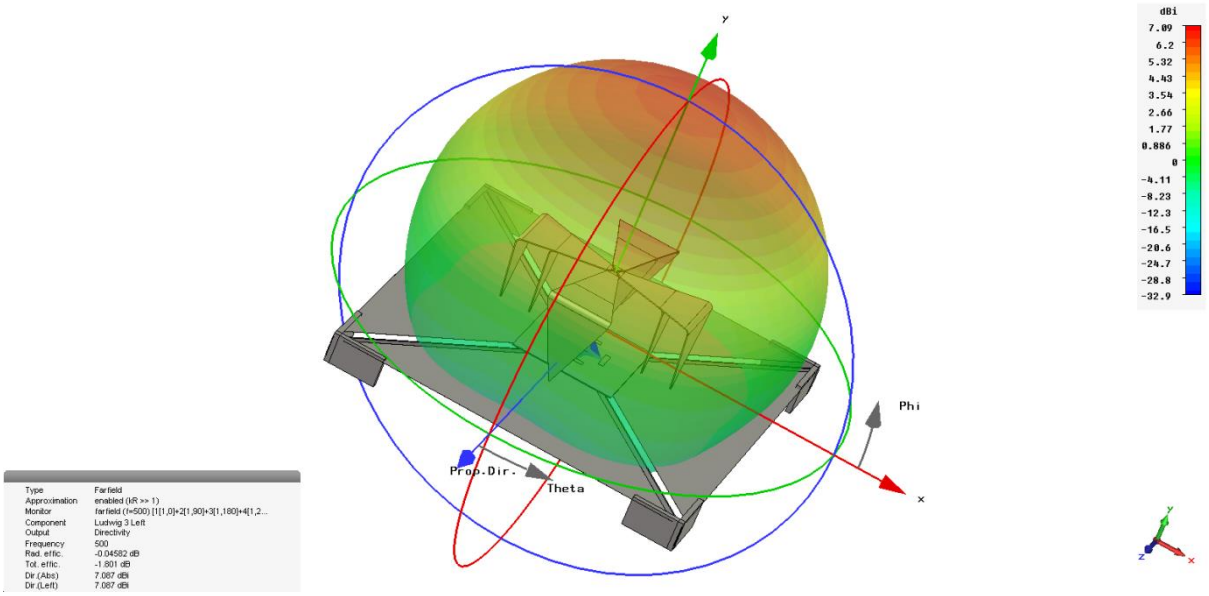

Figure 138 shows a 3D representation of the LHCP far-field pattern of the shown model. The orange to yellow transition shows the approximate position of the 3dB beam width edge.

The gain, far-field pattern smoothness and beam width of this antenna design have not been compromised as can be seen in Figure 138 and Figure 139 . The 3D representation in Figure 138 clearly shows the good alignment between the axial direction and the beam direction along with a scale of the beam width. A comparison of all antenna properties can be found in Table 7.

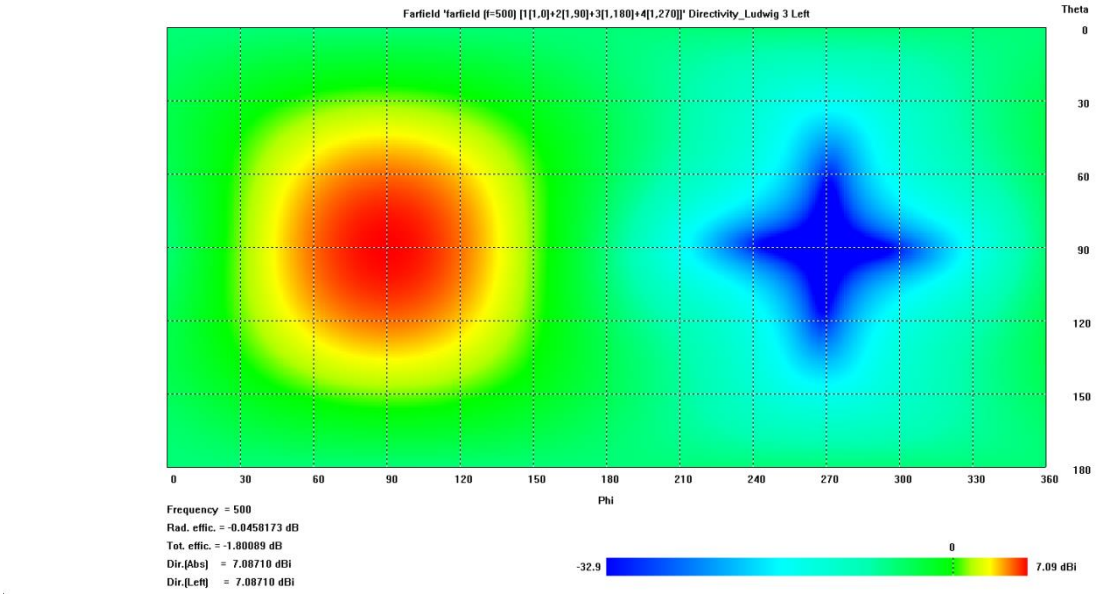

Figure 139 shows the LHCP far-field pattern for the compromised wide crossed Moxon antenna.

	Narrow elements (Figure 119)	**Modified widened elements (Figure 137)**
Radiation efficiency	0.9774	0.9895
Total efficiency	0.4496	0.6606
Peak Directivity	6.718dBi	7.087dBi
Angular Width (3dB)	88.2 deg.	84.7 deg.
Frequency range (-10dB)	364MHz - 431MHz	387MHz – 491MHz

Table 7 gives additional antenna property values on the compromised crossed Moxon design.

The simulated results give a bandwidth of 104MHz (fractional bandwidth 1.279:1) (Figure 140). The S11 plot in Figure 140 shows the ¼ wavelength harmonic resonance of the antenna at 200MHz. This could potentially be useful with the antenna being repurposed to operate at lower frequencies if the on-board signal generation can produce them, albeit at a much lower efficiency.

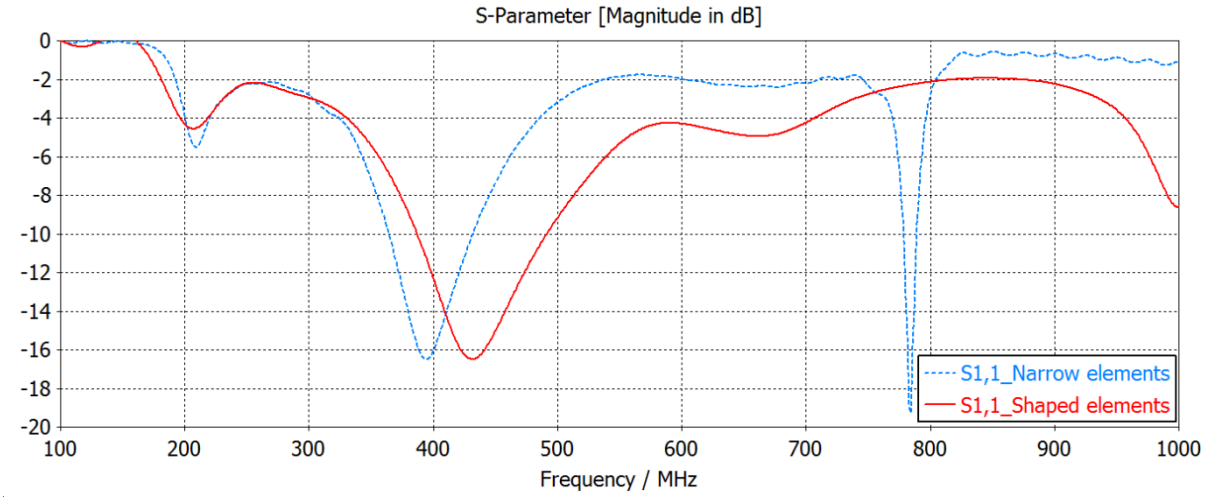

Figure 140 shows the S11 plots of the narrow and compromised crossed Moxon antenna elements over the full range of simulated frequencies.

It is concluded here that this design is sufficient to meet the WISCER requirements in theory. This simple design could be quickly prototyped, tested and made ready for flight

using the existing deployable structure. However, there is still potential for improvement and the investigation of this will be the focus of the remainder of the chapter.

7.4) Resistive Capacitive loading

A possibility of further improving the bandwidth is to implement aggressive loading of the antenna. Resistive loading is common despite the detrimental effects on efficiency. An alternative is RC loading, which attempts to reproduce the reflection suppressing properties of resistive loading whilst increasing antenna efficiency. It has been investigated by a number of sources including Lestari et al. (2004) and Kanda (1983). Modification of the crossed Moxon antenna was conducted and a full presentation can be found in Appendix 2. The work is not included here because whilst an improvement in RF performance was achieved it was not significant enough to warrant the greatly increased antenna design complexity it required. The final antenna design selected is shown in Figure 141 and a summary of the RF performance changes given by Table 8.

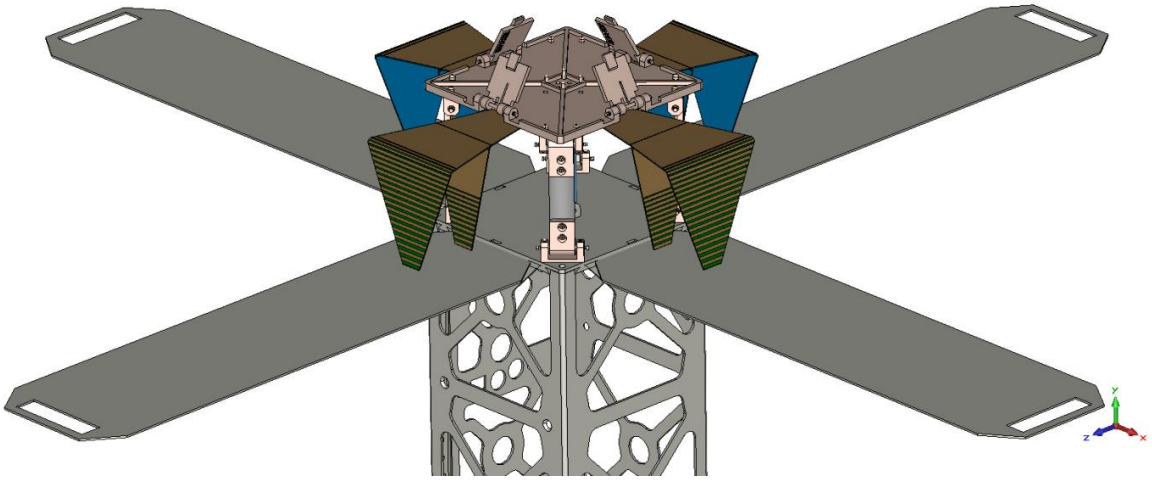

Figure 141 shows the modified crossed Moxon antenna with RC loading applied (Ref 0.7.5). The resistive loading now increases towards the ends of the antenna as the strip width remains constant.

	Control antenna	**Loaded antenna (Ref. 0.7.5 IncR-IncC)**
Radiation efficiency	-0.04842 dB	-2.839 dB
Total efficiency	-3.387 dB	-3.778 dB
Peak Directivity	5.66 dBi	6.03 dBi
Angular Width (3dB)	94.9 deg	91.9 deg
Frequency range (-10dB)	446.5-552.0 MHz (105.5 MHz)	440.5-553.0 MHz (112.5 MHz)

Table 8 details for comparison the antenna properties of the unloaded reference antenna and the increasing R increasing C (Ref 0.7.5) loaded antenna.

7.5) WCM Antenna

At the conclusion of work on the resistive capacitive loading for the crossed Moxon, notable complications arose due to the addition of the antenna loading pattern. Further analysis of the WCM antenna, used as the comparative bench mark, was therefore warranted. In this section the results of that analysis will be presented to provide detailed information for the systems level analysis in the next chapter.

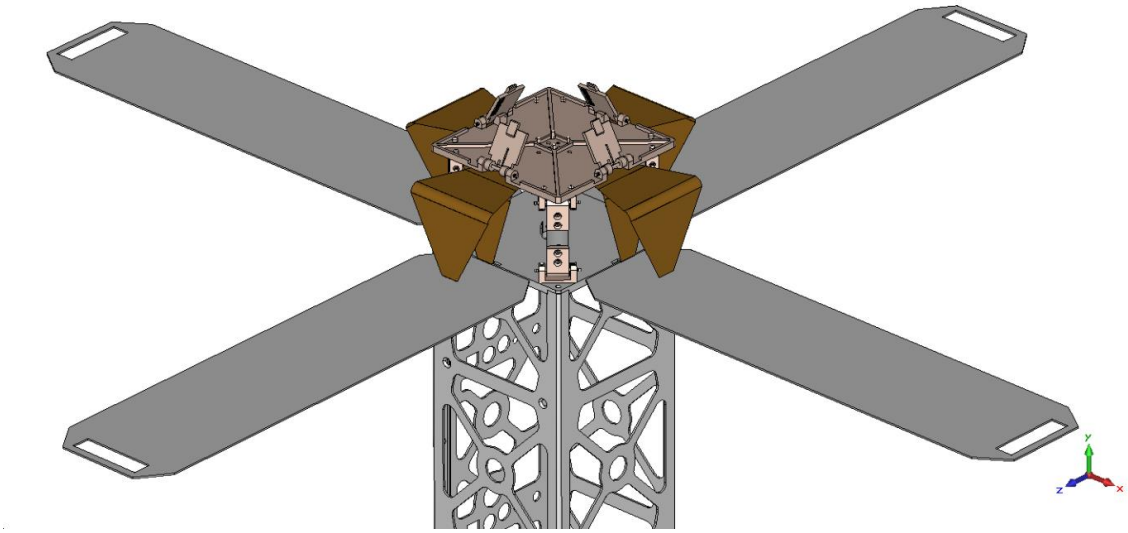

Figure 142 shows the Widened Crossed Moxon (WCM) antenna CAD model as used in the CST MWS simulations.

The WCM antenna design iteration was originally created to be an up to date, more detailed model of the final widened arms antenna in section 7.3.3. However, due to its good performance and simple design, it is now a primary candidate for the WISCER mission.

One alteration that was not detailed in the previous section was to cut-off the ends of the antenna element tapers. It was found during interim simulations that the capacitance with the ground plane, at the ends of the antenna elements, rendered the tapered tips unnecessary. Therefore, to remove the unnecessary mass and potential of damage to the ground plane the points were replaced by a 12mm cut-off width, seen in Figure 142.

The dimensions used in this antenna version were the result of further parametric studies on the more detailed model. The results of this showed again that the bandwidth grows with increasing element width. Hence, the width chosen is the largest that can be fitted within the deployment structure when rolled up. To achieve this estimate, the vertical actuators are used to construct diagonal cuboidal keep out zones within the deployer stowed volume. The maximum width of the rolled antenna element, simply the width at the widest point of the taper, can then be calculated from the resulting triangular spaces and the roll diameter. The resulting value was approximately 60mm, using the dimensions of the University of Glasgow prototype and based on a conservative estimate for the metal minimum bend radius.

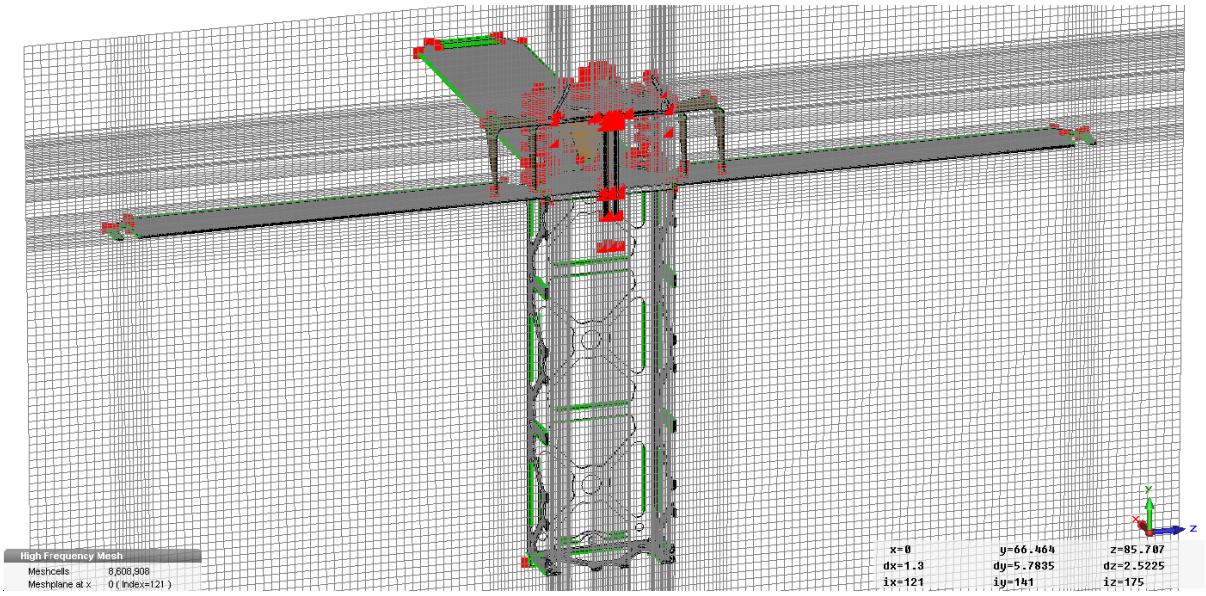

Figure 143 shows the mesh setup for the Widened Crossed Moxon (WCM) antenna CAD model as used in the CST MWS simulations.

The following results come from the time domain simulation of the CAD model in Figure 142 and the mesh setup in Figure 143. The internal electronics were not included in this simulation as the configuration has not been confirmed at the time of writing. However, as the internal volume of the CubeSat is shielded by both the ground plane and structural exoskeleton it is not expected that they would have any effect on the antenna properties. The connection to a signal generator will, however, have an impact that must be considered. This feed layout will likely be constrained further once the internal design progresses further. The setup used throughout this chapter is further detailed here and is partially shown in the image of the antenna feed structure (Figure 144) and the signal processing schematic (Figure 145). Four coax cables carry the 0, 90, 180 and 270 degree phase shifted signals, from the signal generator board to each of the antenna elements. In the simulation four 50Ω waveguide port are used to drive these lines.

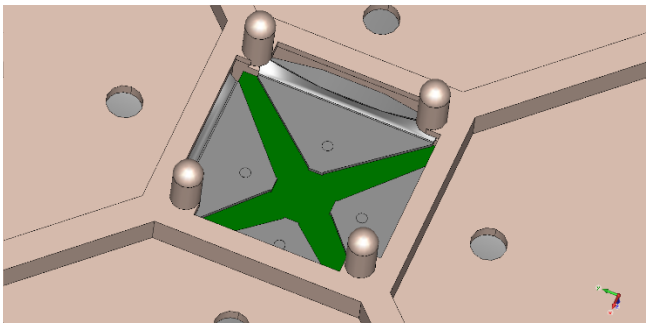

Figure 144 shows the connection arrangement for the feed to antenna elements. In this image, the upper structural (non-conductive) plate remains in place and the feed can be see through the central hole. Four coax cables connect to the underside, carrying the feed signal for each antenna element.

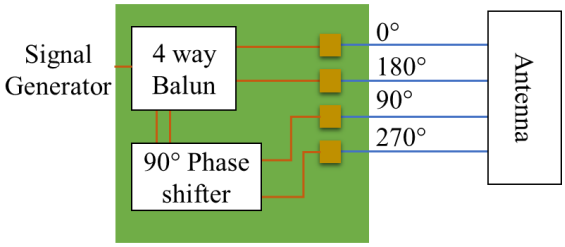

Figure 145 shows a schematic of the potential feed configuration for the crossed Moxon antenna.

An alternative setup to this would be to use two coaxial cables and feed two of the antenna elements with the induced signals on the shielding. Whilst this would simplify the setup, reducing the number of components and volume required, it would cause parasitic capacitance at the antenna feed input and generate undesirable changes to the antenna properties due to radiation from the cables. It is therefore not recommended for this situation but could be a potential point of compromise over the design used here.

Having described the features of the WCM antenna, the remainder of this section will be focused on detailing the results from the CST MWS simulation to provide a foundation for later comparison to the conical helix antenna. Figure 146 shows that S11 profile for the antenna as seen before in the comparison plots.

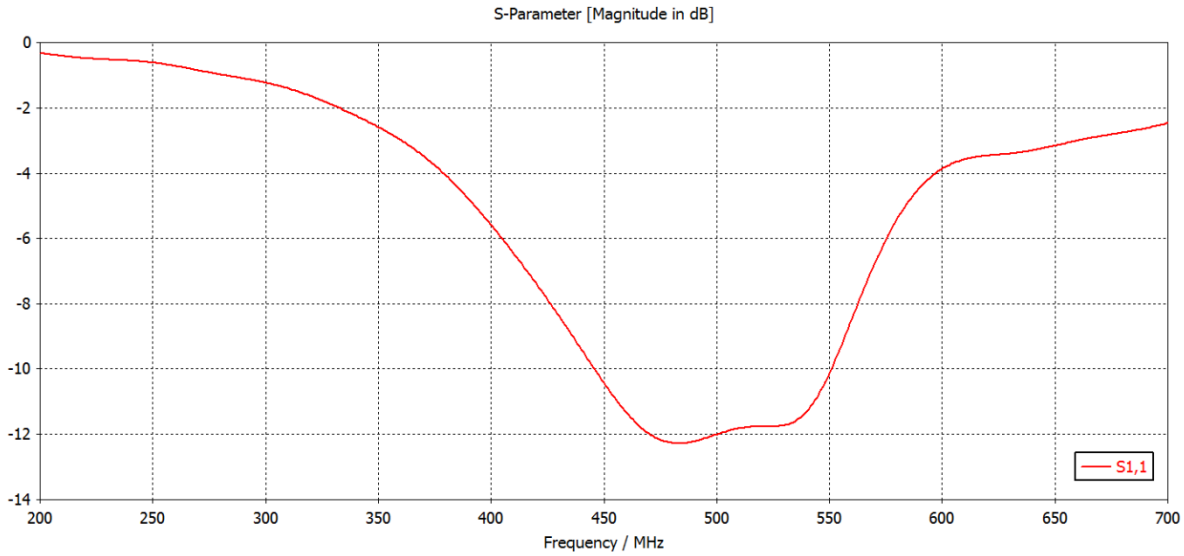

Figure 146 shows that S11 profile for the final WCM antenna.

Figure 147 and Figure 148 show the expected farfield pattern of the antenna. Using the 3D representation in Figure 147 it is easy to conceptualise the method of operation of the antenna: antenna points in the nadir direction; the underside of the deployable solar panels and the panels on the CubeSat body continuously capture energy from the sun in this attitude; captured energy is stored in a battery and is used to power the antenna burst transmission when it makes an over pass of the target ionosphere region. With the 90° beam width, the signal can be received for most of the over pass.

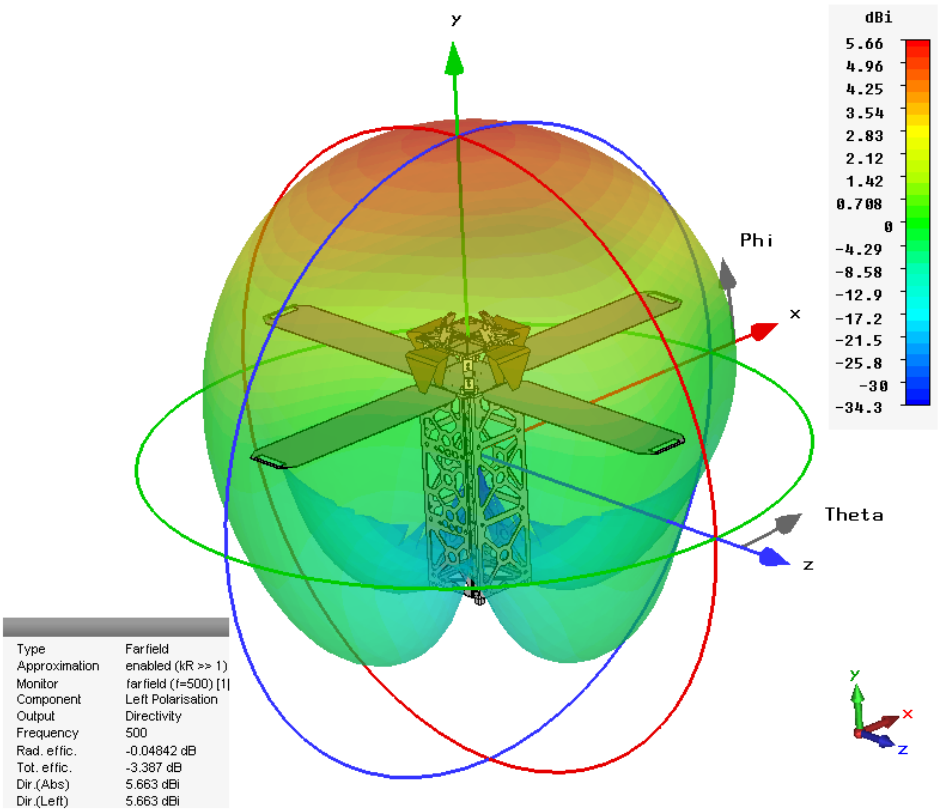

Figure 147 shows a 3D representation of the WCM antenna farfield pattern.

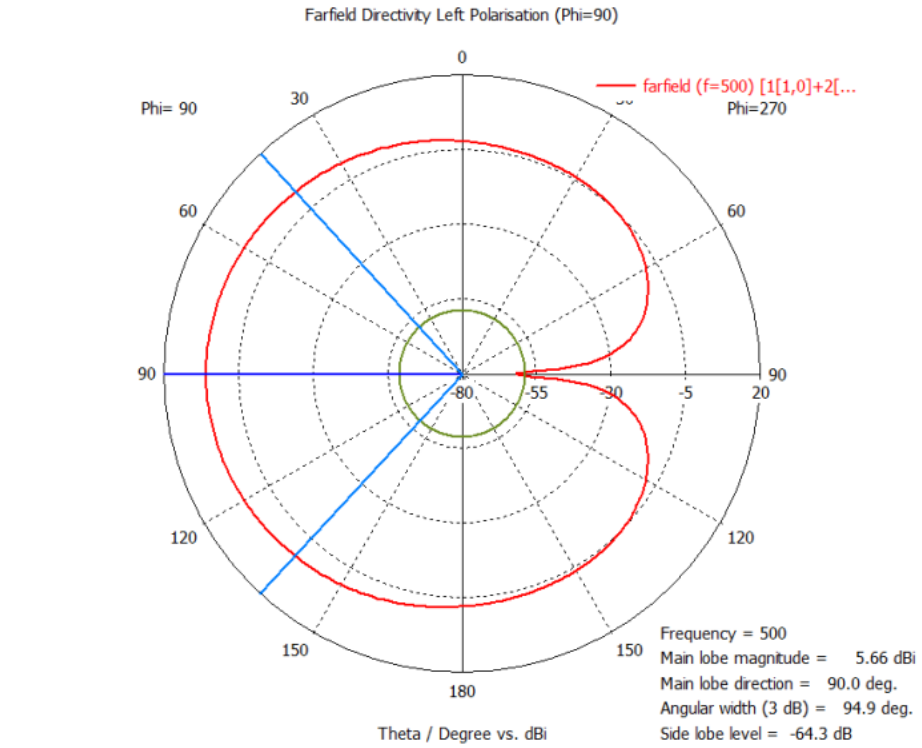

Figure 148 shows the farfield pattern of the final WCM antenna in polar plot form for clearer observation of the quantitative properties.

Then, as the transmitted signal traverses the ionosphere the signal scintillates because of the plasma turbulence. Time of flight frequency dispersion of the received signal is then observed when signals take differing paths to the ground antenna. Measurement of this multipath spreading can only be achieved if the dispersion of the transmitting antenna is small by comparison. Figure 149 shows the waveform of the radiated pulse from the WCM antenna (red), when subjected to a Gaussian input pulse (blue). The input pulse has a duration of approximately 6 ns. This is dispersed by the antenna and, when measured at 1m, yields a radiated pulse length of 8ns. The requirement for the WISCER experiment is less than 20ns and so, if the simulation is accurate, the WCM is expected to be more than suitable than the original narrowband design.

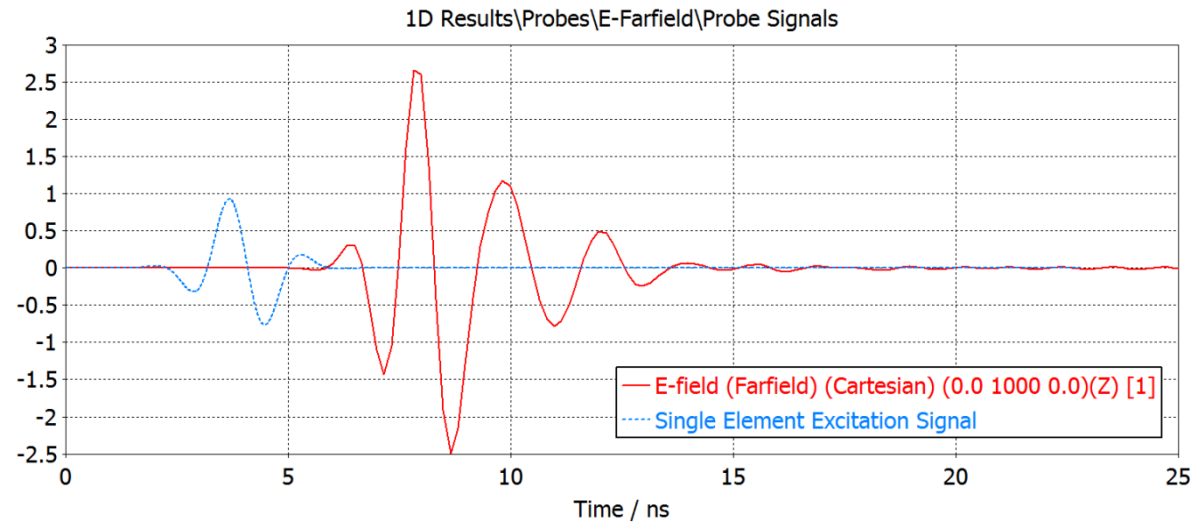

Figure 149 shows the radiated pulse response of the final WCM antenna, measured at 1m. The blue excitation signal is that for just one antenna element (1/4 amplitude of combined input pulse).

Taking all the above results, Table 9 can be compiled to provide a reference for further comparison to other antenna candidates. The WCM antenna is expected to be able to fulfil all the WISCER antenna performance requirements based on these simulation results.

Property	WCM antenna Value
Radiation efficiency	-0.04842 dB
Total efficiency	-3.387 dB
Peak Directivity	5.66 dBi
Angular Width (3dB)	94.9 deg
Frequency range (-10dB)	446.5-552.0 MHz (105.5 MHz)
Dispersion (Increase over original 0.006μs pulse)	0.008 μs

Table 9 details all antenna properties of the final WCM antenna simulation for comparison to those of the conical helix antenna.

To aid future work on this antenna design all the important design lengths are listed below, in Figure 150. To rescale the antenna, the lengths L, H and l should be proportionally scaled whilst leaving W, w and B constant. The later variables remain constant due to material properties (B) and the constraints from the deployment structure.

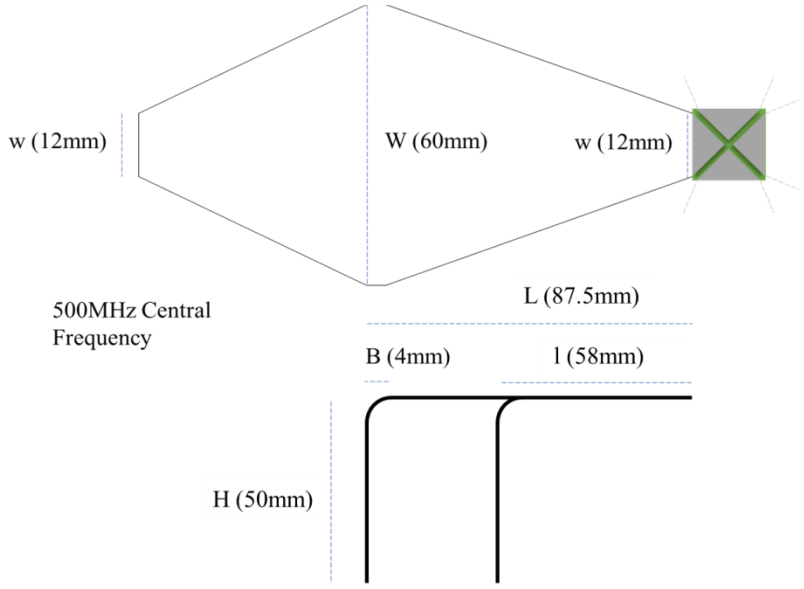

Figure 150 provides all critical design lengths for the WCM antenna.

For completeness, and to provide context for the RC loading results, an evaluation of antenna current in the WCM was also undertaken. The results of this run can be seen in Figure 151. The current pattern is very similar to that for the RC loaded antenna (Antenna Ref 0.7.5, Figure 141) in the previous section. The same cross-element induced current interaction can be seen, also aiding the generation of circularly polarised radiation for this antenna.

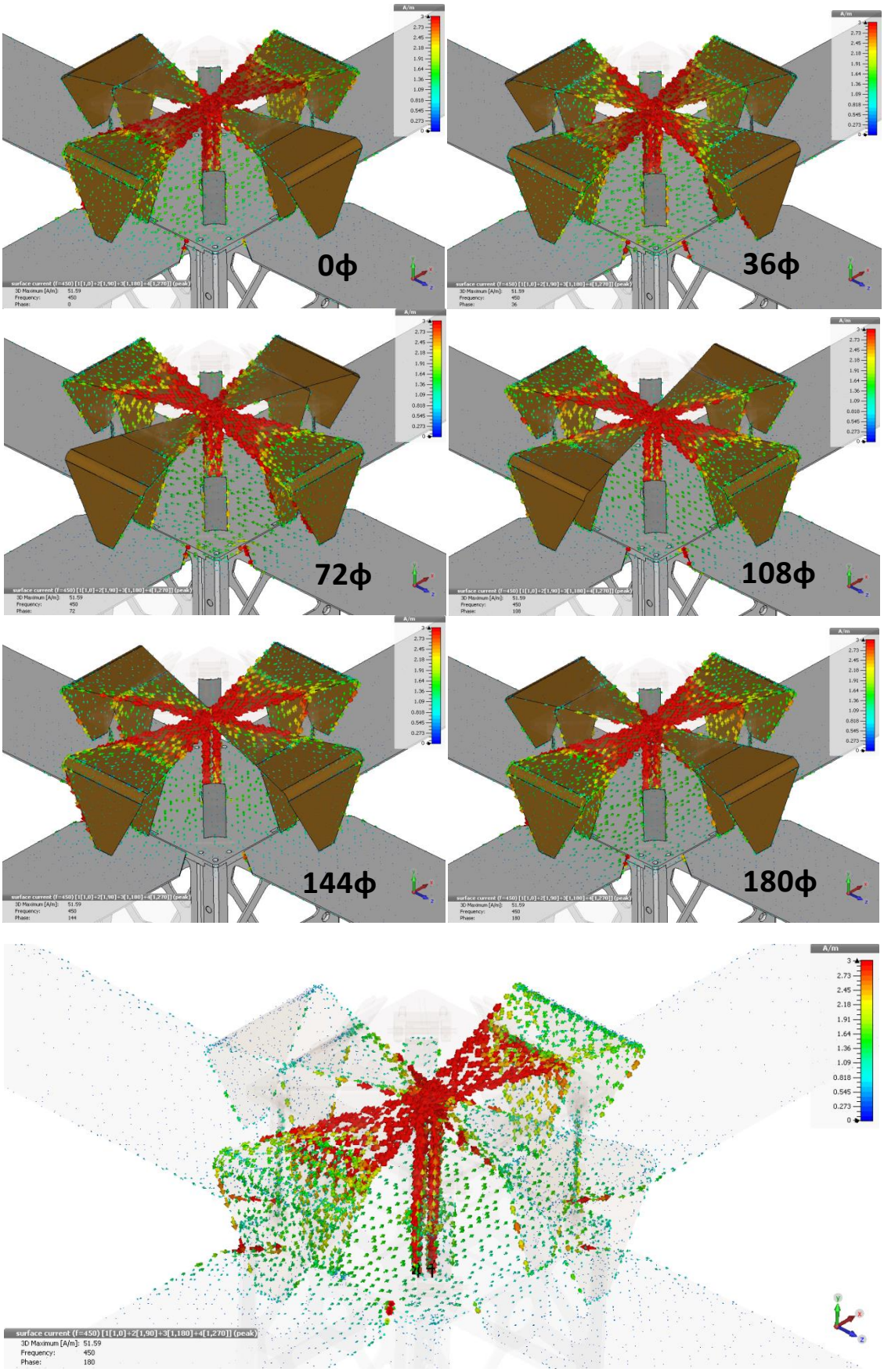

Figure 151. Surface current diagrams of the Widened crossed Moxon antenna. Scale limited to 3 A/m to maintain contrast.

This concludes the investigation into the properties and potential optimisation of the crossed Moxon antenna, for use in the WISCER experiment. Substantial changes to the design have been implemented that improve its performance. Multiple potential designs have been shown to be feasible, in theory. Selection of an optimal design requires systems level analysis based on the final flight platform. In the next chapter, such an analysis will be presented, along with a comparison to the conical helix antenna.

CHAPTER 8) SYSTEMS ANALYSIS AND CONCLUSIONS

8.1) Introduction

The individual lines of investigation have been analysed in isolation within the previous chapters. Here this information is combined in order to, by making use systems engineering techniques, determine the extent to which the WISCER antenna subsystem design can be finalised.

The intention of the WISCER mission concept is to provide significant design risk reduction of a future VHF-UHF FOPEN SAR satellite, using a simpler and much less costly precursor mission. For this plan of action to succeed, the proposed precursor mission is required to achieve the following:

1. WISCER must have a better risk to reward ratio than a fully-fledged FOPEN SAR precursor satellite.

2. The WISCER mission and development must be significantly less costly than that of a fully-fledged FOPEN SAR precursor satellite.

3. It must be shown that any proposed design can achieve the mission requirements. These mission requirements must ensure that sufficient data is collected to ensure value for any subsequent missions.

Considering the first requirement, it is apparent that an accurate quantitative analysis is difficult due to the unknowns prior to the commencement of such a project. But top-level considerations can be used to conclude which direction to proceed in.

For the second requirement it is again difficult to accurately predict the cost of undertaking such a mission. However, it is more than possible to reach conclusions based on

comparative analysis between the possible options. With knowledge of the CubeSat form factor, typical times to flight and mission independent costs, it is apparent that such a mission would be significantly less costly than a fully-fledged precursor FOPEN SAR satellite. It is therefore the third requirement that has dominated the work of this thesis.

A set of mission requirements were drafted, as a starting point, prior to the commencement of this research project. The requirements specifically relating to antenna performance, attitude control and system budgets have been evaluated independently in previous chapters. It is the aim of this chapter to determine any necessary changes to the requirements based on the systems analysis of, and identification of limiting factors from, the earlier analyses.

Firstly, we summarise the work of the previous chapters to show which of the requirements have been met and to what degree. A systems analysis of the satellite budgets will be discussed for each antenna based on the latest work, as well as an early risk analysis for the flight events (project risk will be omitted). These experimental and simulation results will then be tabulated into a trade-off table in order to best compare the two candidate antenna designs. A tailoring of the mission requirements will then be presented based on the table and previous results.

8.2) Systems Engineering principles

It is important to consider the systems engineering practices and philosophies commonly used in the design process of spacecraft. Spacecraft systems engineering refers to the process by which systems engineers ensure that the design of the spacecraft meets the mission objectives. It can most easily be understood by considering the way in which satellite programmes are broken down. Although there is some variability between

organisations and the exact nature of the spacecraft, the general pattern is the same and is shown below.

1) Phase A – Feasibility

    a) The goals and objectives of the satellite are outlined.

    b) Prototypes, experiments and simulations are carried out to ensure current technology can achieve the required accuracy and operational cycle.

2) Phase B – Preliminary definition

    a) Complete definition of system and subsystem requirements.

    b) Definition of system and subsystem designs to a level that will allow only minor alteration during the next phase.

    c) The preliminary design review (PDR) should be completed before proceeding onwards from this phase.

3) Phase C/D – Design, development, manufacture, integration and verification

    a) Completion of all designs and analyses before the critical design review (CDR)

    b) All preparations and instructions for manufacture and special procedures.

    c) Any final developmental tests to show integrated performance should be completed.

    d) Qualification testing should be undertaken.

    e) Manufacture for flight and acceptance testing.

4) Phase E – Mission operation, data analysis and end of life procedures

Systems engineering is applicable throughout all the design stages as it is the process by which the design is evaluated and self-checked for consistency between subsystems. In the early phases, systems engineering techniques are used to identify potential design road blocks and sets out the structure for mission requirements. In the later stages overarching design optimisation is implemented, followed by evaluation and testing of integrated systems prior to launch. Systems engineering heavily overlaps all other domains of spacecraft engineering, acting as a bridge between them. Due to the complex and highly constrained concept for the WISCER mission, systems engineering principles are necessary to ensure that a feasible design is found efficiently.

8.2.1) Systems engineering techniques

A list of systems engineering techniques is given in Table 10. These techniques will not be detailed here but they have been highlighted to show which have already been completed for the WISCER project and which have been the subject of this thesis. System optimisation, feasibility assessment and performance analysis have featured heavily in previous chapters and this chapter will focus on the employment of budget allocation and trade-off analysis.

Trade-offs	Cost estimation
Cost comparison	**System definition**
Feasibility assessment	Interface specification
Mission assessments	System Optimisation
Options identification	Performance analysis
System specification	Budget allocation
Requirements determination	**Concept selection**

Table 10. This table is a list of system engineering techniques. The underlined techniques are relevant to this thesis project and the bold techniques are ones that had been completed prior to the commencement of the PhD.

8.3) Summary of Results

In this section the primary conclusions from the previous chapters will be summarised and presented together. The implications of these conclusions will be discussed and a CubeSat configuration for each antenna type will be presented. These configurations will then be used as the basis for systems analysis in subsequent sections.

8.3.1) Implications for WISCER based on Crossed Moxon Results

The final iteration of the Crossed Moxon Antenna type (WCM antenna) can be seen in

Figure 152. Based on the conclusions from this design the impacts at systems level will be noted in this section.

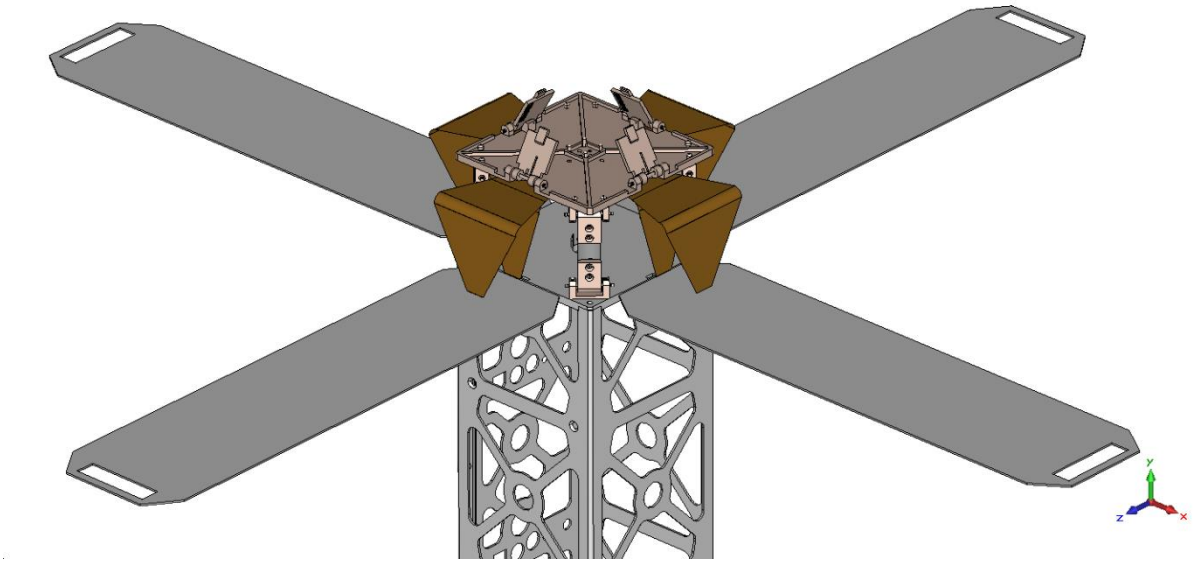

Figure 152 shows the CAD model of the final iteration of the Widened Crossed Moxon (WCM) antenna.

Firstly, the use of a drag sail as the antenna ground plane has been dropped in favour of using deployable solar cells. It was found during simulation that most standard drag sails were too large and caused distortion of the antenna's radiation pattern. Promising results were, however, obtained when 2U deployable solar panels were used. This configuration also yields a dual use approach that has significant mass and volume savings whilst also reducing the deployment risk (such panels are available as COTS components). Modifications to improve the panels RF reflectivity may be required based on further testing but this is not seen as a reason to avoid this approach. The minimal surface area of the panels also yields a benefit by reducing attitude perturbation torques. In the attitude simulations performed with 0.2Am max field strength, the control limit was still exceeded but only for small portions of the orbit. This could be rectified with the addition of more field coils (or a small set of reaction wheels) and so at this stage it is considered possible to use a magnetic only reaction system.

A parametric study of widening the antenna elements yielded very positive results with respect to improving the antenna bandwidth. The optimal width, if bandwidth is to be maximised, is constrained by the adjacent elements. Consideration of the practicalities of

storage and deployment led to the specification given in Figure 150, as a balance between this and achievable bandwidth. The bandwidth of the WCM antenna meets the requirement REQ-ANT-02 (Min 60MHz – ideal 100MHz). The element width could be reduced, if needed, if a bandwidth at the lower end of the range is acceptable.

8.3.2) Implications for WISCER based on Conical Helix Results

The PICARD antenna represents the final choice of this work for a volume-bandwidth optimised conical helix antenna design. A bandwidth of 300MHz (full width) was targeted whilst trying to minimise the volume of the antenna, and so minimise the quantity of gas required to inflate it.

If a reduced bandwidth is acceptable for the final WISCER mission, the antenna parameters should be re-optimised. The accuracy of the design charts from Hertel & Smith (2002) is supported by the simulation work undertaken up to this stage and so they should be used to optimise the antenna size. Size optimisation of the antenna should take place as it has a compound effect of: reducing the storage volume, reducing the inflation system mass and reducing the magnitude of the disturbance torques produced by the antenna. RF testing of a flight design antenna will be imperative to ensure that this optimisation has not been too aggressive, and that the radiation pattern is suitable for the mission.

The feed line running through the centre of the antenna has the potential to affect the radiation pattern. The feed should not have excess length that would allow it to rest within close proximity of the antenna elements, post deployment. In this configuration the feed line must also take the form of a balanced shielded coaxial line to prevent feed line radiation affecting the radiation pattern directly.

Impedance matching at the antenna tip will be required if a standard impedance of coaxial cable is used due to the 150-200Ω antenna input impedance.

8.3.3) Implications for WISCER based on PICARD Results

Strain rigidisation has been shown to be viable for the post deployment stiffening of the inflatable antenna. The data collected from the REXUS launch showed that the deployment process is achievable in a microgravity environment and that the antenna was effectively radiating after this process.

Verification of the cool gas inflation method should be undertaken if a down selection is made to the conical helix antenna but there are no issues expected based on current experience with inflating the antenna. A vacuum chamber test would be suitable for this and would also give the opportunity for a long-time scale deflation test to be carried out. This deflation test would quantify the expected leak rate and identify any potential issues related to attitude from the escaping gas.

During the PICARD experiment, the deployment method operated nominally resulting in a fully and correctly formed conical helix antenna. The S11 results show that the antenna was electrically functional after deployment, before then showing the characteristics of an open circuit once the antenna was ejected. It is recommended that future work on the conical helix antenna should focus on experimentally verifying the S21 parameter of a flight worthy inflatable conical helix antenna with a WISCER appropriate ground station in controlled conditions. This will verify that the antenna can achieve the required level of accuracy that is necessary to make the planned measurements of the ionosphere.

8.3.4) Resulting WISCER Variant Configurations

Using the results and conclusions of the investigations carried out to date it is possible to generate approximations of the whole satellite configuration for each antenna variant. Our intention now is to determine if there is sufficient justification to down select to one of these variants or if further research is required.

To provide an accurate systems analysis and comparison of the two antenna variants, as much information as possible about the resulting configurations should be considered. The first step towards this was to generate CAD models of the two variants, which can be seen in Figure 153 and Figure 154. Here a 3U CubeSat is chosen as the minimal viable design. Expansion to a 3U+ CubeSat or integration into a larger satellite are possible but have not been considered in the following analysis.

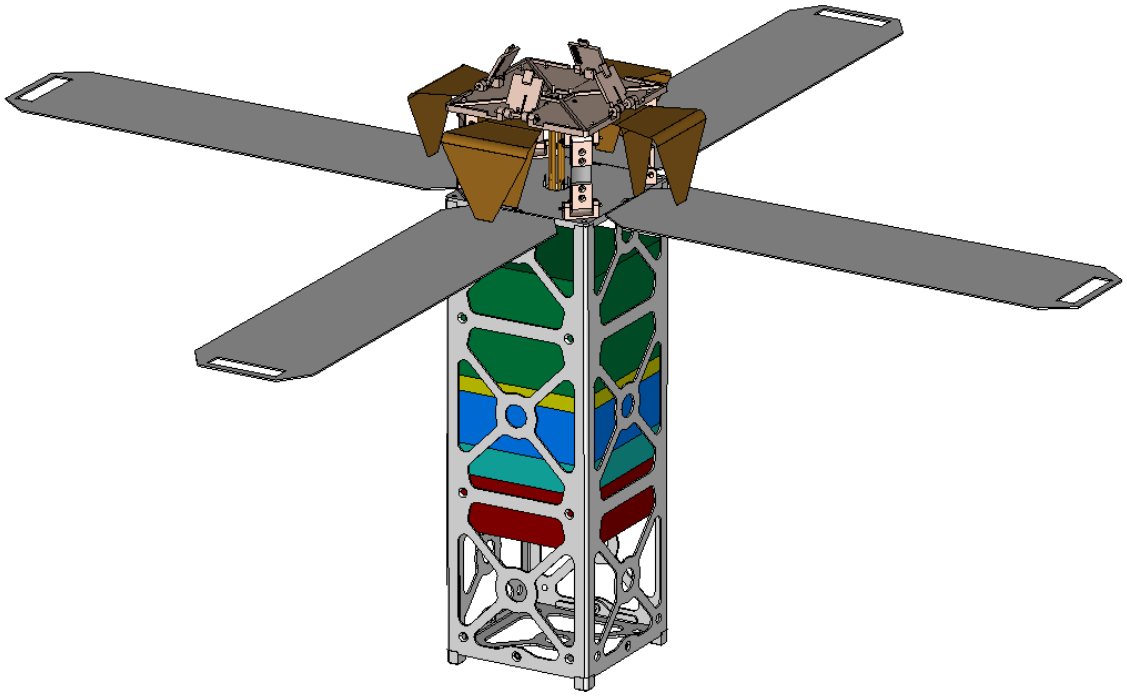

Figure 153 shows the concluding configuration of the Widened Crossed Moxon antenna CubeSat variant for the WISCER mission based upon the information collected during this investigation.

Figure 153 and Figure 154 show the antenna, solar cell and 3U CubeSat configurations of the two final variants. These models obviously omit a lot of detail that would be required

to construct the final satellite, but they do provide sufficient information to see the advantages and disadvantages of the two antenna designs in a system engineering setting. Simple rectangular representations of the internal components have been included to show their potential volumes and positions.

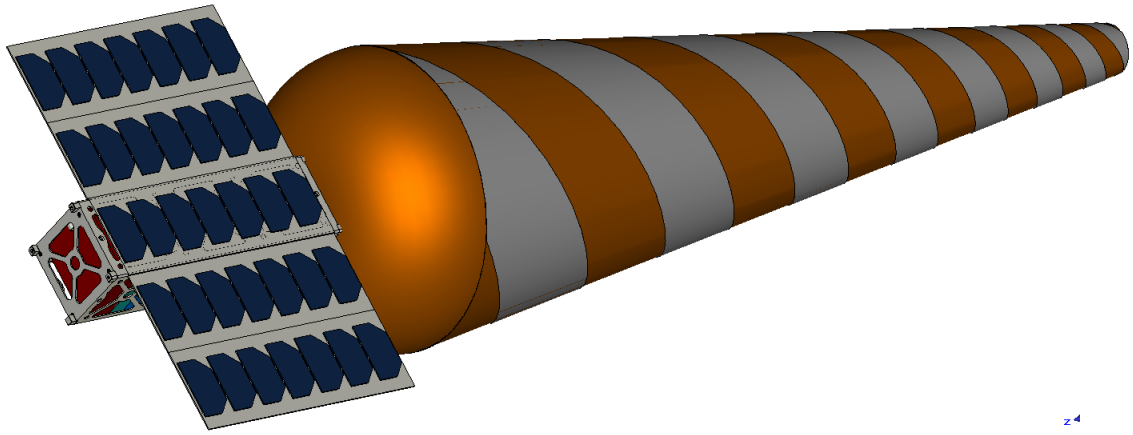

Figure 154 shows the concluding configuration of the conical helix antenna CubeSat variant for the WISCER mission based upon the information collected during this investigation.

The subsequent sections of this chapter detail the information collected that has not already been discussed in previous chapters. This data will then be processed to produce a weighted trade off analysis to compare the antennas and determine their relative performance.

8.4) Budget analysis

Budgets are a key part of satellite design due to the knock-on effects of the launch mass and volume limits. This section will present the current knowledge of the power, heat dissipation, attitude control, mass and volume budgets for the 3U WISCER CubeSat.

8.4.1) Power Generation

Power for WISCER will be generated via solar panels attached to the external surfaces. To generate enough power, unfolding solar panels will be used to increase the surface area. Preliminary modelling of these solar panels has been undertaken with SCT in MATLAB to validate an initial estimate for the power budget of the WISCER CubeSat. The simulation includes eclipsing of the satellite by the Earth and the location of the Sun based on the Julian date.

The solar panels intended for use on the conical helix antenna are the 3U 2-Sided Double Deployed panels manufactured by Clyde Space. The single 3U side panel solar array, seen in Figure 154, was not included in this simulation run. These panels have a quoted conversion efficiency of 0.283 and a total area of 0.12 m^2 each. For the initial simulations, an electrical conversion efficiency (from electrical power generated to energy stored in the battery) of unity is used; however, a value of 0.8 may be more realistic depending on the details of the final system. For the Cross-Moxon variant, the solar panels are necessarily shorter due to the antenna deployment structure. Therefore, a conservative length of 0.2 m was used for the Cross-Moxon solar panels. The panels will deploy about a hinge on their short edge and again Clyde Space provides such a configuration with the same performance values and an area of 0.08m^2.

Due to the nature of the deployed antennas it is possible for both designs to partially eclipse their own solar panels. However, under normal nadir pointing operations it is possible to avoid significant self-eclipsing of the solar panels if the correct attitude is maintained. This simulation assumes that the attitude can be maintained to achieve this criterion.

Figure 155 shows the instantaneous power collected and the energy stored for the low inclination orbit (candidate orbit O1) for both WISCER variants for an orbital altitude of 750 km. The profiles show the dominant factor is the expected 33% reduction in power and energy for the Cross-Moxon design due to the difference in panel area. This simulation was repeated for the other two candidate orbits, showing very similar relative differences but the optimised orientation for the panels in these orbits is more complex; depending on the exact orbit parameters as well as the Julian date. Candidate orbit O1 will therefore be used in the trade off analysis as it represents the simplest case, whilst also being the worst case in terms of the length of eclipse by Earth.

If nadir pointing is maintained throughout the orbit only the z-axis is available for rotation to optimise the solar energy interception. For this test the conical helix antenna panels were maintained in an orientation normal to the velocity vector but with their active faces always pointing towards the sun.

Using the total collected energy, it is possible to calculate the available steady state power for each configuration. This value is approximately 14W For the crossed Moxon WISCER and approximately 20W for the inflatable helix WISCER. It is expected that a 10W steady state power level will be required to store enough energy to operate the antenna during all possible ground station visibility windows.

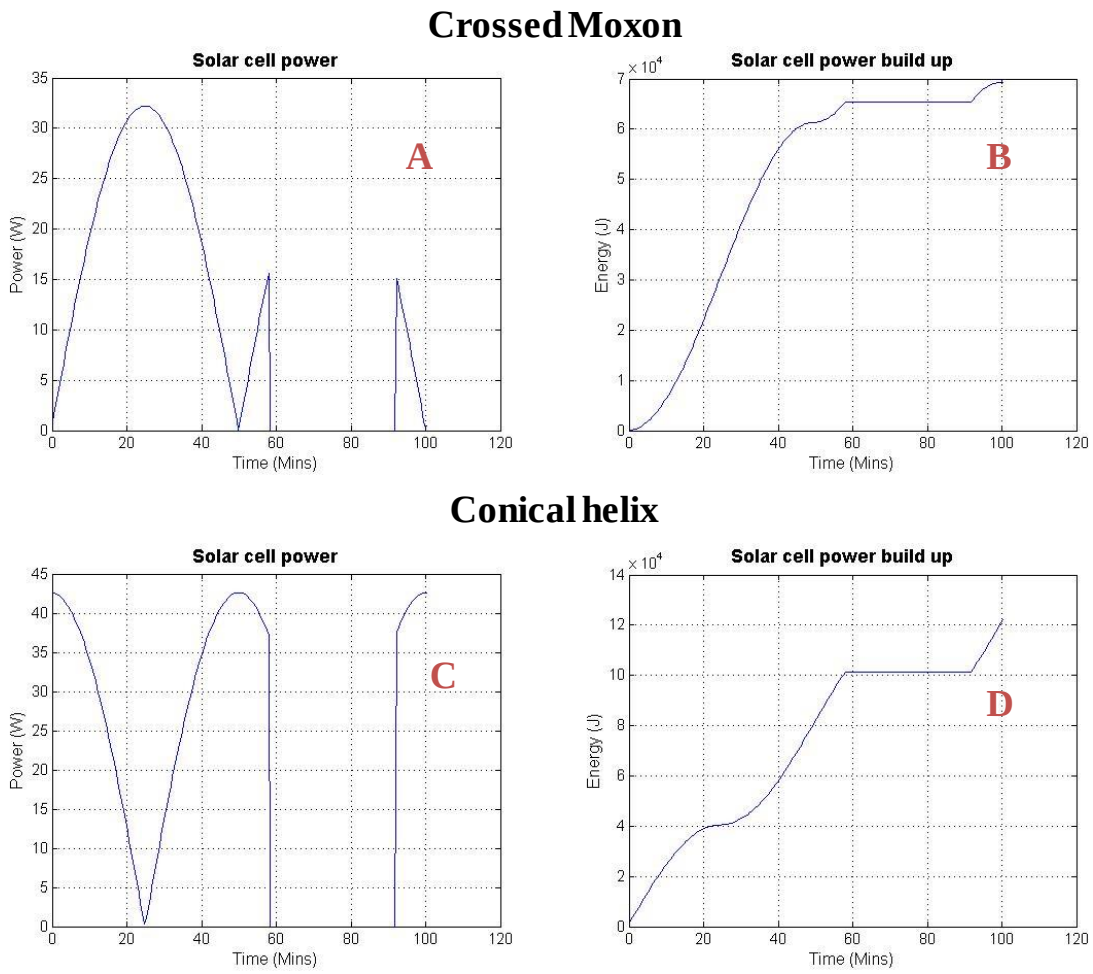

Figure 155 shows the instantaneous power (A, C) and stored energy (B, D) for both the cross-Moxon and inflatable helix WISCER variants (Low inclination orbit O1).

8.4.2) Heat Dissipation

A preliminary thermal analysis of the WISCER spacecraft has been completed using Thermica v3 (geometry for external flux calculation) and SINDA v2 by (Angling, Cruise, et al., 2012), prior to the commencement of this work. A basic concept of operation over a 14-day period was used to determine an operational profile for power dissipation.

The purpose of the thermal modelling was to investigate the thermal performance and thereby to provide confidence that the WISCER concept is viable. Preliminary results of the initial model are shown in Figure 156.

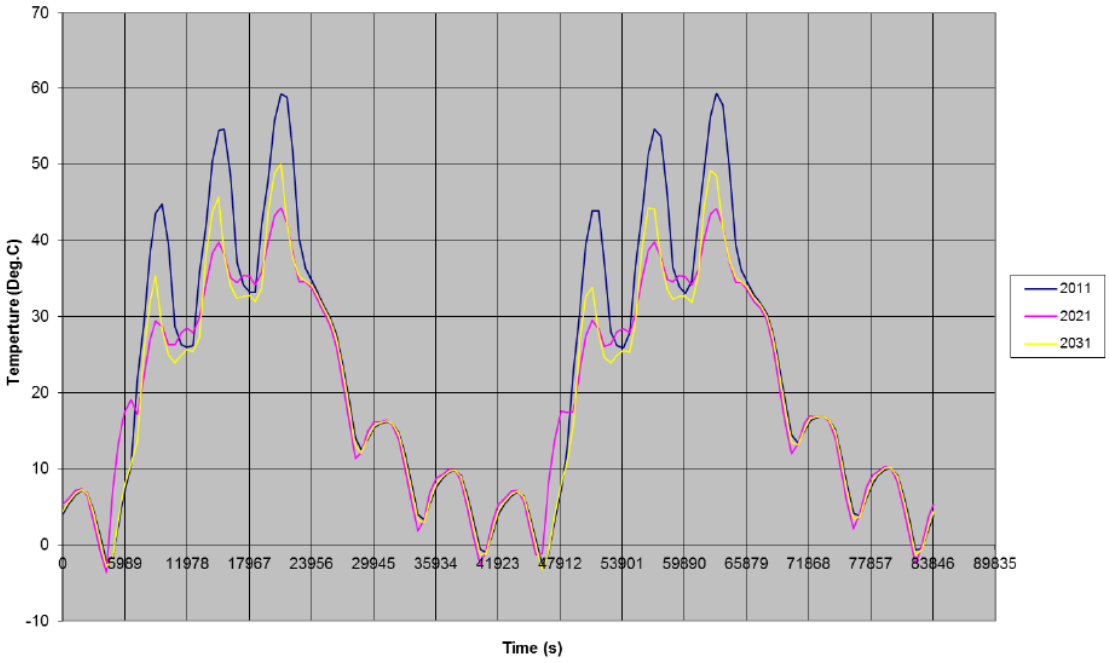

Figure 156. WISCER RF Payload Temperatures over the course of 14 orbits and 6 sounding periods. 2011=waveform generator, 2021=OCXO, 2031=PA.

The same thermal model was then modified to include 200 g of paraffin wax (specific heat capacity of 2900 J/kgK). This phase change material was selected to provide a heatsink for the highly inefficient broadband amplifier required by WISCER. The melting of the wax was not simulated in this model but even without this limitation the temperature rises were reduced. For example, the waveform generator temperature increase was reduced from 26ºC to 18ºC, as seen in Figure 157. It is, therefore, assumed that a heatsink of some type will be required to maintain the temperature of the waveform generator at acceptable levels. A heatsink mass of approximately 220g with a density of paraffin wax is therefore assumed henceforth.

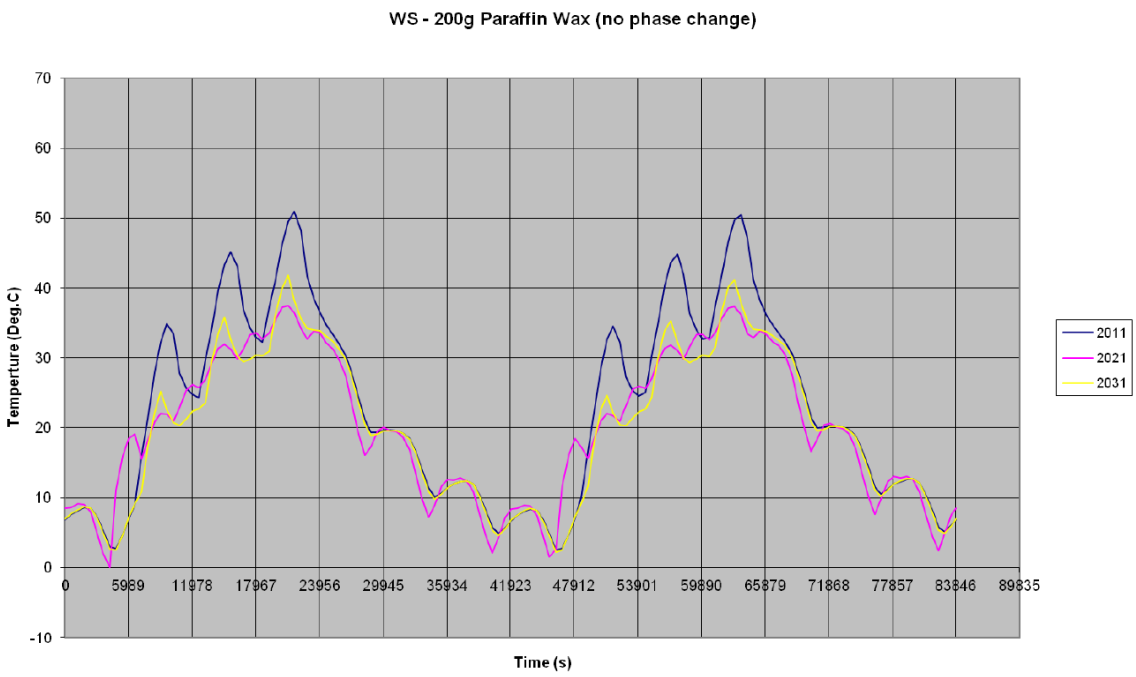

Figure 157 shows the WISCER RF Payload Temperatures over the course of 14 orbits and 6 sounding periods with a paraffin heat sink attached. 2011=waveform generator, 2021=OCXO, 2031=PA.

8.4.3) ADCS Pointing

Knowledge of the required strength of the ADCS needed for WISCER will determine the type of ADCS that is applicable and therefore the minimum mass and volume of this system. If this value is greater than the available budgets, then alterations to other systems will be required either to reduce their own mass and volume or to reduce the strength requirement on the ADCS. However, if the size of the ADCS system required to control WISCER is well within the parameters of current COTS systems then the opposite applies. The budgets of other systems can increase, potentially allowing increased performance and hence improving the results of the experiment.

The most compact ADCS system applicable to CubeSats is a magnetorquer system. If three axis magnetic control could be implemented on WISCER successfully then a significant mass and volume budget saving could be achieved. Based on the results of chapter 4 such a system is possible for the WCM antenna. Due to the nature of magnetic

control it should be expected that periods of unfavourable field alignment will occur. These periods will result in transient deviations from the ideal pointing vector. All such deviations seen in the testing completed here show only minimal angular deviation before the correct pointing is restored (<1°). If a conservative worst case scenario of ±10° error was used here with standard values for CubeSat attitude determination systems <1° (Janson & Welle, 2013) the result would still be well within the -3dB beam width of the WCM antenna.

The conical helix antenna however generates too great a disturbance torque to be controlled by a simple magnetorquer system. Use of reaction wheels in at least one axis would be required with de-saturation periods. The consequence of the added mass and volume of such a system will be discussed in the next section. The benefit of a reaction wheel system is that the periods of unfavourable geomagnetic field alignment can be absorbed, and a much smaller pointing error is achieved. Based on COTS ADCS systems an accuracy of less than 1° is achievable (Janson & Welle, 2013).

The power consumption of the two types of ADCS systems will obviously differ. As the reaction wheel system must also have magnetorquers, it is expected that the power consumption will be greater than that of the magnetic only system. However, the exact method of operation and duty cycle may lead to counter intuitive results. Review of COTS products suggests that a magnetic only system will consume approximately 1W of power (at maximum output). Adding a reaction wheel system (operating at maximum capacity) could then add a further 1W to 3W of power draw. At this design stage it is hard to quantify this difference in the context of the overall power usage by the different systems of WISCER. For subsequent trade off analysis 1W peak for the WCM and 3W peak for the conical helix have been used. To provide context, this accounts for a 30% power allocation

of the single orbit averaged power generation, after subtraction of the antenna payload usage.

8.4.4) Mass Properties

The mass and volume budgets of the WISCER CubeSat are much easier to quantify than the previous parameters due to the standardised CubeSat Specification (Munakata, 2009). In this study the 3U variant has been assumed due to its simpler design and the fact that the current estimations do not require the extra volume of a 3U+. The 3U+ design could well be used in the final WISCER design but would not significantly affect this analysis.

The maximum mass for the 3U and 3U+ CubeSat variants is 4kg, with the centre of gravity required to be located within 7 cm of its geometric centre in the Z direction. Calculation of the centre of gravity is omitted here due to the limited design certainty, but a mass budget has been formulated using available COTS components and estimations based on the current antenna designs. This budget can be seen in Table 10 and compares the WCM antenna variant to the conical helix variant as described in section 7.3.4.

Mass	Crossed Moxon (g)	Conical Helix (g)
Antenna	200	500
Attitude control	225	506
Communication system	80	80
Experiment system	200	200
Heat Sink	220	220
Battery and PCU	436	436
Solar Panels	592	888
Structure	390	390
Sub Total	2343	3220
Remainder	1657	780

Table 10 is the projected subsystem mass requirements for the antenna variants.

As can be seen in Table 10 both antenna variants are estimated to be viable using the 3U/3U+ form factor. The conical helix variant is significantly more massive than the WCM due to the antenna, attitude control system and larger solar panels but still has a contingency of 780g.

The maximum length of a 3U CubeSat body is 327.5mm (here used as a proxy for internal volume due to the constant cross section). Consideration of the structure thickness is omitted as it is not considered significant compared to the design uncertainty. The top hat section of a 3U+ CubeSat adds an additional 42.5mm of length, with a diameter of 64mm, should it be required. In this analysis it was not needed. Using the same methodology as the mass calculation an estimation of the WISCER volume budget situation is shown in Table 11. This table provides the worst-case estimations; in particular the conical helix

stowage volume is listed at 100mm. This length is required for the thicker walled PICARD prototype antenna but may not be necessary even when considering the volume required by the cool gas generators.

Subsystem	**Crossed Moxon (dm)**	**Conical Helix (dm)**
Antenna	0.50	1.00
Attitude control	0.34	0.59
Communication system	0.10	0.10
Experiment system	0.75	0.75
Heat Sink	0.196	0.196
Battery/PCU	0.366	0.366
Sub Total	2.25	3
Remainder	1.025	0.275

Table 11. Projected subsystem volume requirements for the antenna variants.

CAD model representations, using simple rectangles, are shown in Figure 158. These models provide a more intuitive appreciation for the contingency volume that is remaining for each option. The WCM variant has a significant advantage but the optional addition of the top hat volume does provide further contingency to both. It is expected that both designs are viable based on current knowledge, but it is apparent that the conical helix antenna could pose a project risk. This risk has not been calculated and it will not be included in the trade off analysis.

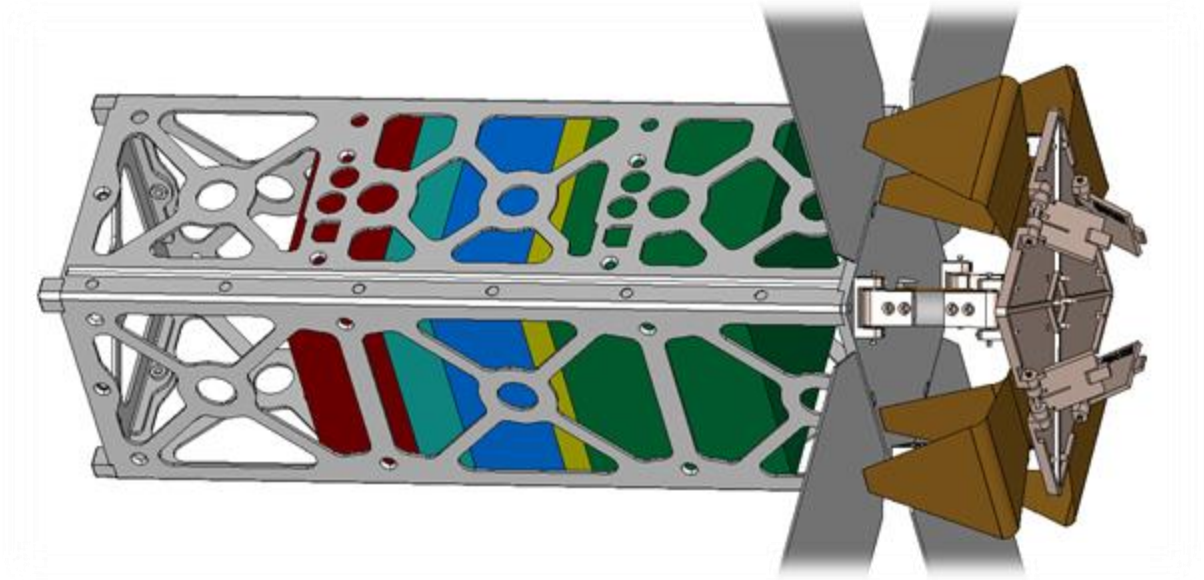

Subsystem	Reference Colour
Antenna Storage (Conical Only)	Grey
Attitude control system	Blue
Communication system	Yellow
Experiment system	Green
Heat Sink	Light Blue
Battery/PCU	Red

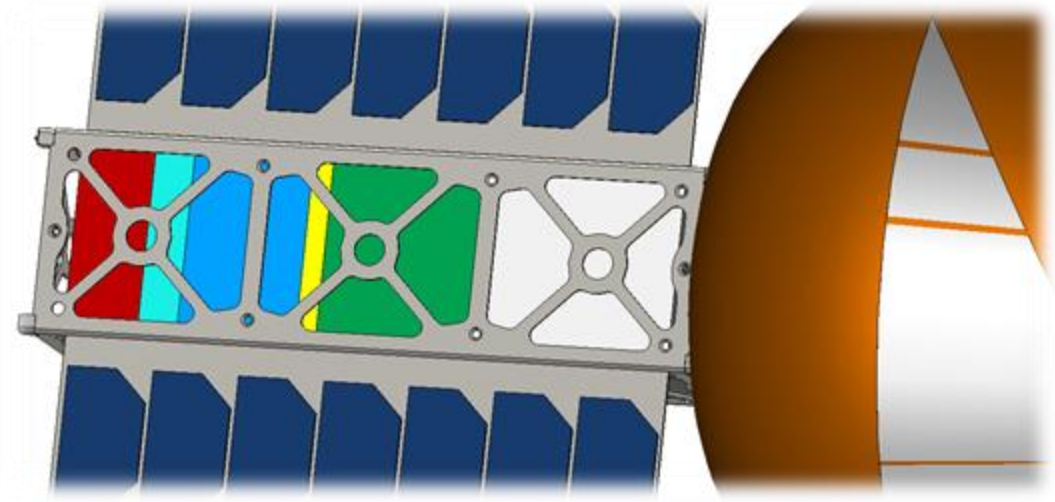

Figure 158. The crossed Moxon (Top) and conical helix (Bottom) design variants are shown with representations of the internal components included for the purpose of visualising the volume budget constraints.

8.5) Environmental analysis

The environmental factors of attitude control have previously been discussed and evaluated. However, there are other environmental factors that must be considered. The results of these supporting investigations are shown to provide information for the subsequent systems analysis and assessment of mission risk.

Orbit	Orbit type	Inclination	Altitude	Local time of descending node
O1	Low inclination	7°	750 km	N/A
O2	Mid inclination	60°	750 km	N/A
O3	Sun synchronous	99.4843°	750 km	2200

Table 12. The candidate orbits of WISCER.

The space environment is a key factor when designing any satellite and implications for the WISCER antennas must be considered. The environmental factors will vary between the candidate orbits and should therefore be evaluated for each one (the candidate orbits for WISCER are given in Table 12). As the final orbit that WISCER is inserted into is so heavily dependent on launcher availability and therefore is only known late in the process, the satellite must be designed for the worst case of each factor. To determine the environment of a given orbit SPENVIS can be used (provided by the European Space Agency (ESA)). It is a web interface for various models of the space environment and its effects (Heynderickx, Quaghebeur, Wera, Daly, & Evans, 2004). This includes models concerned with:

- Radiation sources and effects
- Spacecraft-plasma interaction
- The Earth's atmosphere
- The Earth's magnetic field
- Meteoroids and debris.

8.5.1) Meteoroids and Debris

The meteorite flux over the spacecraft orbit as a function of particle size (mass or diameter) can be estimated using the Grün interplanetary flux model (Grün, Zook, Fechtig, & Giese, 1985) for a given altitude. The meteorite fluxes for WISCER's altitude (750 km) were calculated as part of this thesis and are shown in Figure 159. WISCER will experience a large number of small particles – hence the importance of rigidising the inflatable antenna to avoid reliance on internal pressure to maintain its shape. SPENVIS is also able to output debris particle flux as a function of size, impact azimuth, elevation and velocity for several different types of debris, using the MASTER-2009 model. The debris fluxes for each candidate orbit are shown in Figure 160, Figure 161 and Figure 162.

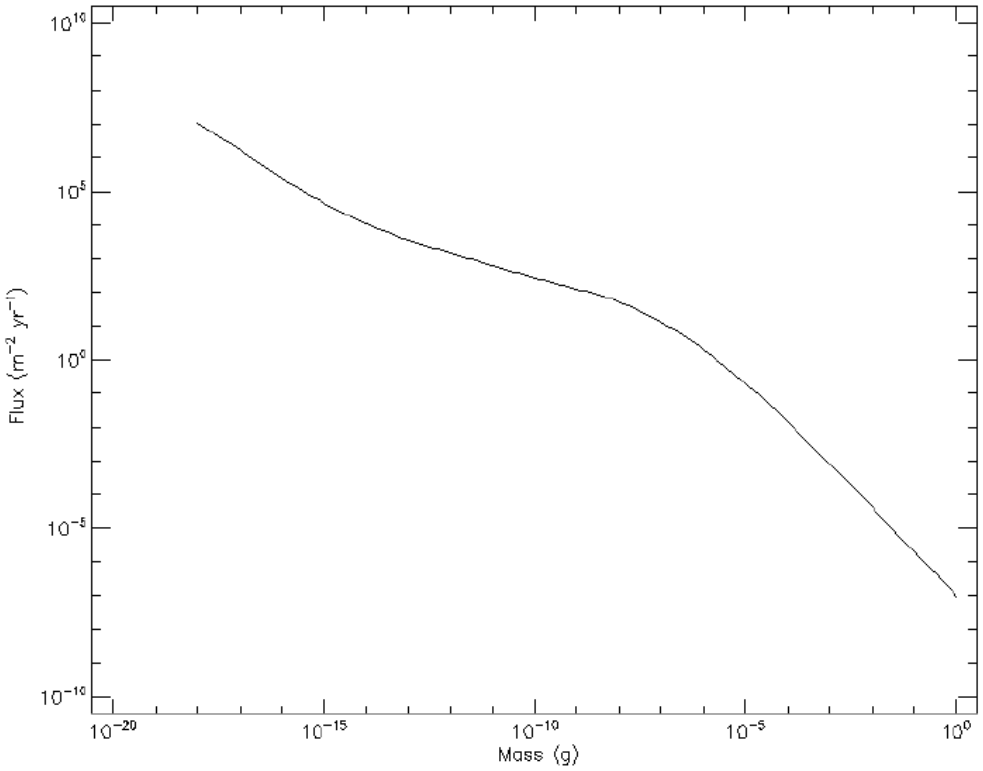

Figure 159. Meteorite flux as a function of mass at 750 km altitude (Grün model).

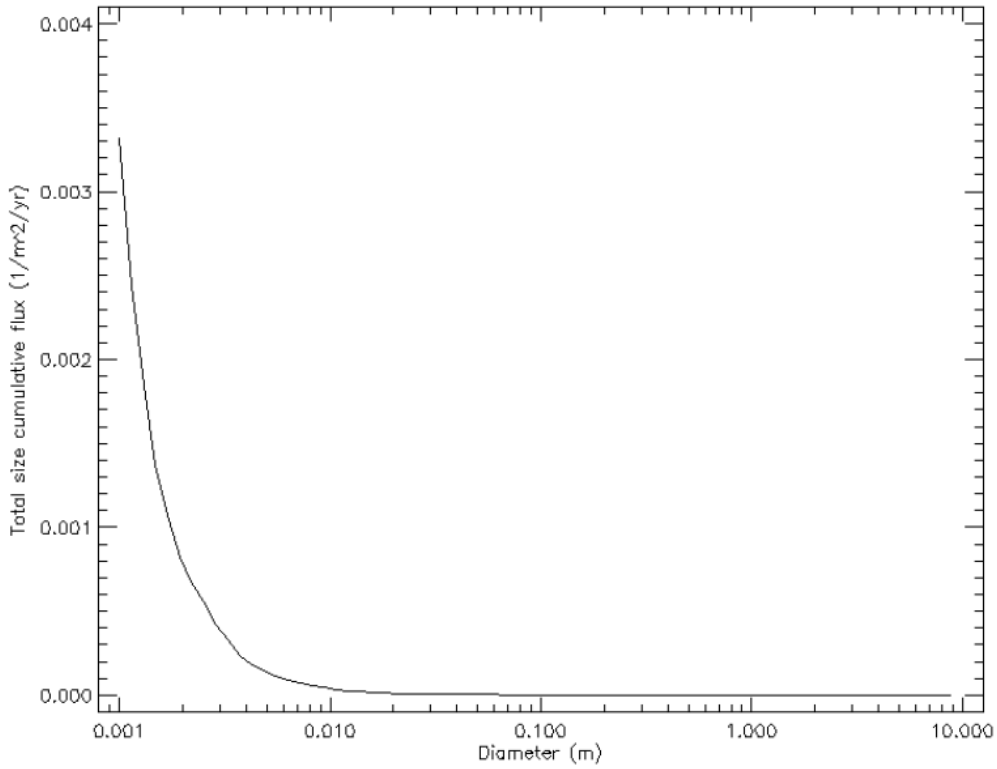

Figure 160. Flux of debris as a function of object size - candidate orbit O1.

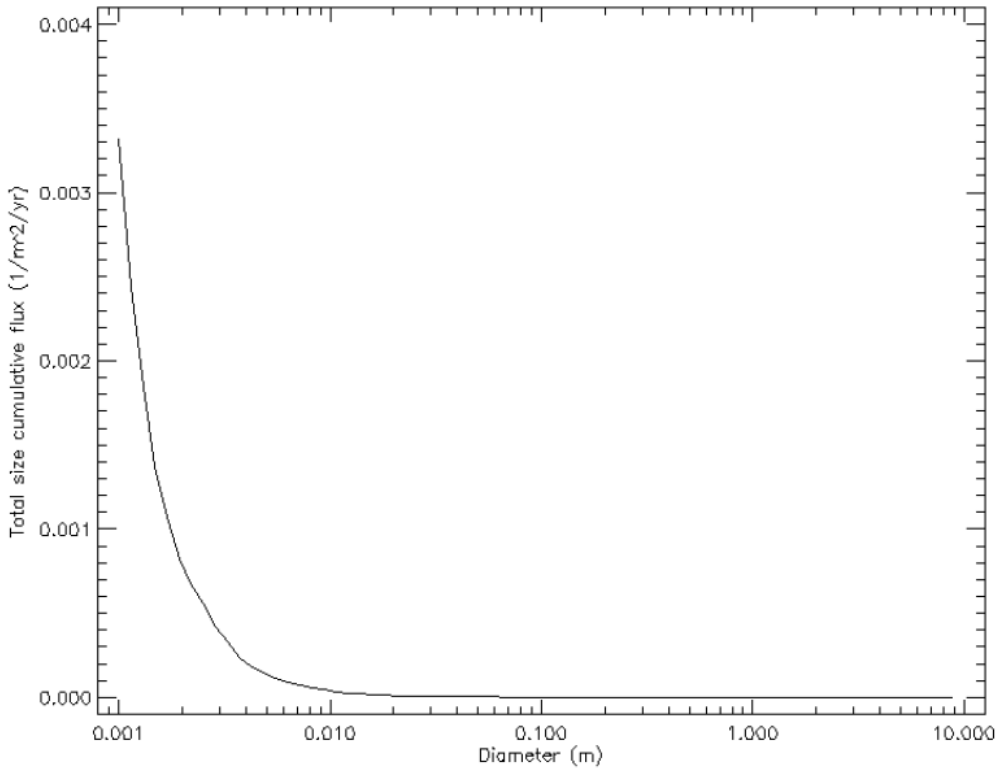

Figure 161. Flux of debris as a function of object size - candidate orbit O2.

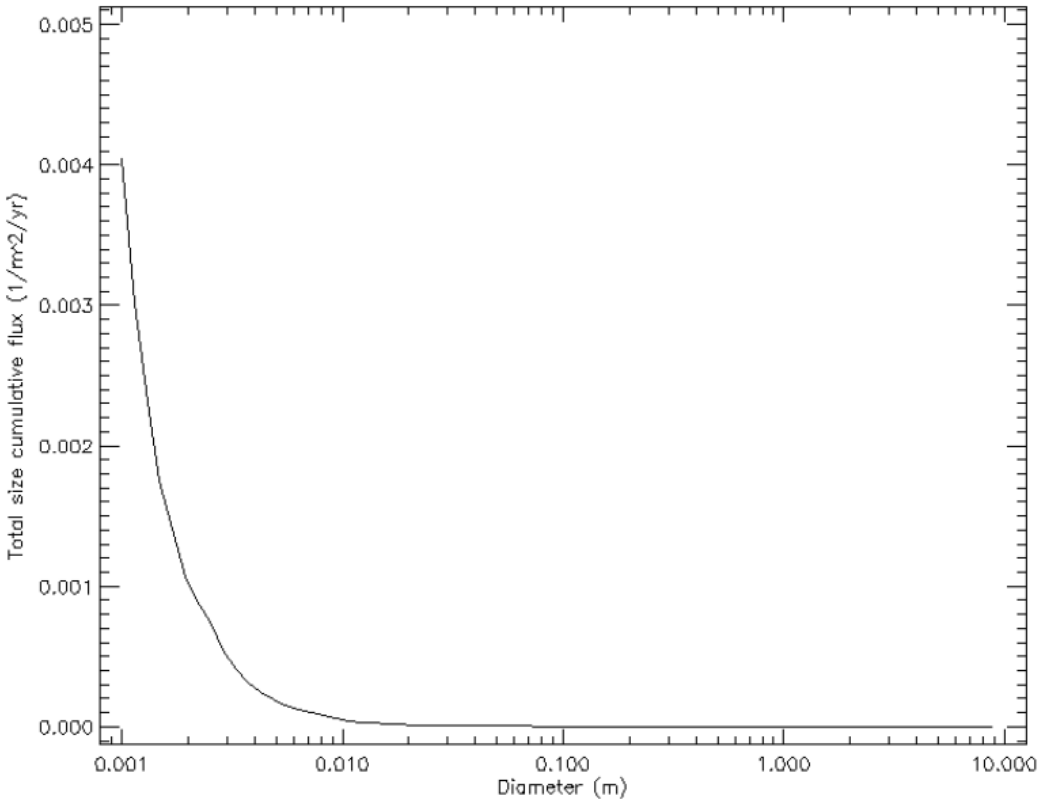

Figure 162. Flux of debris as a function of object size - candidate orbit O3.

The internal components of the spacecraft will be shielded by the structural and external elements for the more common smaller particles and so are not considered when comparing the differing designs due to the antennas. For the antennas themselves though, micrometeorite flux is an important consideration. This is especially true for the inflatable conical helix antenna as penetration through the antenna membrane must be considered at the commencement of design work. Using the micrometeorite fluxes as an input, an estimation of the worst-case mission risk due to impact damage can be calculated and a mission risk given.

8.5.2) Particle/Radiation Environment

SPENVIS includes models of radiation sources and models of the effects of radiation on spacecraft. The outputs of the source models are used as input to the effects models.

The source models can be run over the spacecraft trajectory to provide the average omnidirectional proton and electron fluxes for an entire orbit and the total fluence for the mission.

The AP-8 and AE-8 models were used to calculate the trapped electron fluxes. The AP-8 model provides spectra from 0.1 MeV (some via interpolation) but has limited accuracy at LEO. The only model available in SPENVIS for calculation of the electron spectra is the AE-8 model. AE-8 suffers from the same limited accuracy at LEO as AP-8; therefore, care must be taken when interpreting the results.

SPENVIS also provides both short and long-term solar particle flux models. This allows the impact of solar protons, and other ions to be assessed. For low altitude, low inclination orbits the Earth's magnetosphere will shield against these particles, but for high altitude or high inclination orbits it will not be as effective. The short-term models are relevant for estimating the rate of single-event upsets (SEU). The long-term models are more relevant for investigating the total radiation dose absorbed during the mission. Again, several models are available. For both the short and long-term effects, the default models (CREME-96 and ESP-PSYCHIC respectively) were used.

The final radiation source modelled by SPENVIS is galactic cosmic ray (GCR) fluxes. GCRs are high energy particles that originate from outside the solar system. The magnetosphere will provide some protection for low altitude, low inclination orbits. In this analysis, the ISO 15390 model was used.

The trapped particle and solar particle spectra are used as input to the radiation dose models (SHIELDOSE, SHIELDOSE2). These models calculate the absorbed dose as a function of depth of aluminium shielding material, given the electron and proton spectra from the source models. For the results shown in Table 13, Table 14 and Table 15 the

SHIELDOSE2 model was used to calculate the total ionizing dose in silicon over one year for each candidate orbit, as a function of shield thickness. The shield was modelled as a sphere of aluminium. The results show that WISCER will experience a much harsher radiation environment in candidate orbits O2 and O3 due to the reduced magnetospheric shielding.

Finally, the short and long-term SEU rates can be calculated based on the spectra of trapped protons, solar particles, and GCR particles. However, this requires specific details of the hardware to be used in the satellite and is beyond the scope of this thesis.

Al absorber thickness (mm)	**Total Dose (rad)**	**Trapped electrons (rad)**	**Bremsstrahlung (rad)**	**Trapped protons (rad)**	**Solar protons (rad)**
0.05	1082.0	899.8	1.9	180.6	0.0
0.10	829.0	668.6	1.4	159.0	0.0
0.20	576.7	433.1	0.9	142.6	0.0
0.30	398.2	261.5	0.6	136.1	0.0

Table 13. Ionizing dose in silicon over 1 year for candidate orbit O1.

Al absorber thickness (mm)	**Total Dose (rad)**	**Trapped Electrons** (rad)	**Bremsstrahlung (rad)**	**Trapped Protons** (rad)	**Solar Protons** (rad)
0.05	2.1×10^{6}	2.1×10^{6}	4.0×10^{3}	7.5×10^{3}	1.5×10^{4}
0.1	1.2×10^{6}	1.2×10^{6}	2.6×10^{3}	3.9×10^{3}	8.9×10^{3}
0.2	6.2×10^{5}	6.1×10^{5}	1.6×10^{3}	2.1×10^{3}	5.0×10^{3}
0.3	4.2×10^{5}	4.1×10^{5}	1.1×10^{3}	1.6×10^{3}	3.5×10^{3}
5.0	5.5×10^{3}	4.9×10^{3}	1.0×10^{2}	3.9×10^{2}	1.6×10^{2}
6.0	2.5×10^{3}	2.0×10^{3}	8.5×10^{1}	3.6×10^{2}	1.2×10^{2}
7.0	1.3×10^{3}	7.4×10^{2}	7.2×10^{1}	3.4×10^{2}	1.0×10^{2}

Table 14. Ionizing dose in silicon over 1 year for candidate orbit O2.

Al absorber thickness (mm)	**Total Dose (rad)**	**Trapped Electrons** (rad)	**Bremsstrahlung (rad)**	**Trapped Protons** (rad)	**Solar Protons** (rad)
0.05	2.1×10^{6}	2.0×10^{6}	4000	5100	4.2×10^{4}
0.1	1.1×10^{6}	1.1×10^{6}	2500	2800	2.5×10^{4}
0.2	6.0×10^{5}	5.8×10^{5}	1500	1700	1.4×10^{4}
0.3	4.1×10^{5}	3.9×10^{5}	1100	1400	9600
5.0	5100	4200	95	370	430
6.0	2500	1700	78	350	340
7.0	1300	630	67	330	280

Table 15. Ionizing dose in silicon over 1 year for candidate orbit O3.

The radiation levels and dose rates for the three candidate orbits are not expected to pose a major threat so long as they are considered during future WISCER design work. It is also expected that the effect of radiation on the antenna elements will have little impact when compared to that of SEUs and total dose damage on the other electrical hardware.

8.5.3) Spacecraft Charging

Spacecraft charging can be caused by the interaction between the spacecraft and the space environment. SPENVIS can evaluate the impact of deep dielectric charging and surface charging, as well as provide estimates of the current collection and power loss of a solar cell array along the orbit. The complete model requires detailed specification of the spacecraft geometry and materials. It was, therefore, beyond the scope of this thesis but should be considered when a more detailed design of the WISCER CubeSat is completed.

To gauge the likelihood and extent of surface charging for the candidate orbits, the EQUIPOT model can be used. It is made up of a simple geometry; an isolated patch of material on a sphere, which is used to estimate the currents in the sphere (representing the

body of the spacecraft) and the patch. The equilibrium potentials that are required to obtain zero net charge can then be calculated.

The environment variables were set up with the spacecraft at 750 km altitude (appropriate for all candidate orbits), in sunlight (as opposed to eclipse), with an isotropic distribution of incident particles and with ram/wake effects included. The plasma environment was modelled using the International Reference Ionosphere (IRI) at solar maximum. These options were chosen to create a 'worst-case' scenario for calculation of the equilibrium potentials found in Table 16. The SPENVIS documentation suggests that if no equilibrium potentials above 100 V are found, there will be no serious charging problems.

Structure	**Patch**
-0.4 V	-0.6 V

Table 16. Equilibrium potentials for aluminium sphere with Kapton patch.

At this time, it is therefore assumed that spacecraft charging poses no threat to either of the two antenna design variants. Consideration of spacecraft charging will, therefore, not make up part of the system analysis trade off table.

8.5.4) Atomic Oxygen

SPENVIS can model the density of a given particle at points along a satellite's orbit. The flux of the particle on an oriented plate is determined, as well as the fluence for both a single orbit and the entire mission duration. The particle fluxes can be generated using a variety of atmosphere/ionosphere models. These models take the F10.7 index, the Ap index, and/or the sunspot number as their input.

For atomic oxygen, the material loss due to oxidation can then be estimated using predefined erosion yields for many different materials. The erosion of the Kapton layer of

the conical helix antenna is of key importance due to its minimal thickness. If it were to erode completely the equally thin antenna elements that it protects would be exposed.

The particle fluxes were set up for a 'worst-case' scenario, with maximum values for F10.7 (380) and Ap (250) used as input to the model, whilst the test area was oriented to maximise the incident flux. More typical values of F10.7 and Ap (the yearly averages from 2013) were also used. Kapton was used as the material of the test area and has an erosion yield for atomic oxygen of 2.81×10^{-24} cm^3 (Banks, De Groh, Miller, & Waters, 2009).

The results for each candidate orbit are shown in Table 17, Table 18 and Table 19. It can be seen that the highest fluence of atomic oxygen would occur over candidate orbit O1, with the least over candidate orbit O3. The orbit O1 results (based on conditions in 2013) show an estimated erosion depth of approximately 3×10^{-5} cm (= 0.3µm) which is small compared to the thickness of Kapton proposed for use in the inflatable antenna (25µm). Based on these results it is proposed that neither antenna design is inherently susceptible to atomic oxygen erosion within the course of the planned one-year mission.

	Worst Case	**2013 (year)**
Average Density (cm^{-3})	1.9×10^{7}	4.7×10^{5}
Average Front Flux ($cm^{-2}s^{-1}$)	1.3×10^{13}	3.2×10^{11}
Average Back Flux ($cm^{-2}s^{-1}$)	2.4×10^{-2}	2.8×10^{-8}
Front Fluence (cm^{-2})	4.2×10^{20}	1.0×10^{19}
Back Fluence (cm^{-2})	7.6×10^{5}	0.88
Front Erosion Depth (cm)	1.2×10^{-3}	2.9×10^{-5}
Back Erosion Depth (cm)	2.2×10^{-18}	2.5×10^{-24}

Table 17. Atmospheric oxygen flux for candidate orbit O1.

	Worst Case	2013 (year)
Average Density (cm^{-3})	1.6×10^{7}	5.0×10^{5}
Average Front Flux ($cm^{-2}s^{-1}$)	7.0×10^{12}	2.3×10^{11}
Average Back Flux ($cm^{-2}s^{-1}$)	3.4×10^{7}	2.2×10^{4}
Front Fluence (cm^{-2})	2.2×10^{20}	7.1×10^{18}
Back Fluence (cm^{-2})	1.1×10^{15}	6.9×10^{11}
Front Erosion Depth (cm)	6.2×10^{-4}	2.0×10^{-5}
Back Erosion Depth (cm)	3.0×10^{-9}	1.9×10^{-12}

Table 18. Atmospheric oxygen flux for candidate orbit O2.

	Worst Case	2013 (year)
Average Density (cm^{-3})	1.4×10^{7}	3.3×10^{5}
Average Front Flux ($cm^{-2}s^{-1}$)	3.9×10^{12}	9.8×10^{10}
Average Back Flux ($cm^{-2}s^{-1}$)	6.3×10^{9}	2.9×10^{7}
Front Fluence (cm^{-2})	1.2×10^{20}	3.1×10^{18}
Back Fluence (cm^{-2})	2.0×10^{17}	9.1×10^{14}
Front Erosion Depth (cm)	3.5×10^{-4}	8.7×10^{-6}
Back Erosion Depth (cm)	5.5×10^{-7}	2.6×10^{-9}

Table 19. Atmospheric oxygen flux for candidate orbit O3.

8.6) Mission Risk Analysis

The level of risk that each antenna poses to the successful completion of the WISCER mission is of key importance when accessing the candidates. If one of the designs has a significant chance of failure, whilst the other is much more likely to succeed, it may be favourable to go with the variant with reduced electromagnetic performance in order to ensure mission success. The tables in this section detail potential mission risks arising

from each antenna design, with the failure rate given for the worst-case scenario. The estimation has been achieved through a combination of measured flux data from the SPENVIS database, comparison of failure rates in similar mechanical systems and estimation of key system volumes. It is expected that all values will be refined before flight. Potential mitigations are included in some cases, as a guide for future work. The list of risks is not intended to be exhaustive, merely to provide an insight into the relative risk between the two WISCER variants. The system failure chance is calculated by summing the subsystem chances.

8.6.1) Crossed Moxon Risk Table

ID No. (Crossed Moxon Risk)	Potential Risk Description	Subsystem failure chance	System failure chance	Potential Mitigation
CMR-001	Failure of thermal knife release mechanism	<1/400 (Thurn et al., 2012)	<3/800	Tests of COTS device with flight like engineering model.
CMR-002	Failure of stored energy deployment mechanism	~<1/800		Limit excess stored energy and quality check rotating joints.
CMR-101	Catastrophic micrometeorite damage to antenna within nominal mission (worst case orbit). (Dikarev, Grün, Landgraf, & Jehn, 2005)	N/A	<1/227250	Shield the antenna feed line with additional material.
Total			<0.00375	

Table 20. Mission risk values for the current crossed Moxon antenna design variant.

The failure chance of CMR-101, in Table 20, was calculated using Figure 162 and the assumption that a micrometeorite of 1mm in diameter or larger, impacting the antenna feed

assembly would significantly degrade the antenna performance. The antenna feed assembly is approximated to have an area equal to 11cm^2.

The simplicity of the deployment design, and the fact that many features of the release mechanism have been tested in orbit, act to minimise the number of risk risers.

8.6.2) Conical Helix Risk Table

ID No. (Conical Helix Risk)	Potential Risk Description	Subsystem failure chance	System failure chance	Potential Mitigation
CHR-001	Failure of door release mechanism	<1/400 (Thurn et al., 2012)	<3/800	Test correct integration of COTS device
CHR-002	Failure of cool gas generator deployment mechanism	~<1/800		
CHR -101	Catastrophic micrometeorite damage to antenna within nominal mission, post deployment. (Dikarev et al., 2005)		<1/23584	Shield the antenna feed line with structural material.
CHR-201-a	Material failure upon inflation (strain-rigidisation)	~<1/100	<11/1000	Create a process to reduce the likelihood of manufacturing defects.
CHR-202-a	Rigidisation failure (strain-rigidisation)	~<1/1000		A vacuum chamber inflation test should be implemented to measure localised material strain.
CHR-201-b	Material failure upon inflation (UV cure resin)	~<1/500	<11/500	As in CMR-201-a
CHR-202-b	Rigidisation failure (UV cure resin)	~<1/50 (Many system unknowns)		A vacuum chamber inflation test should be implemented to monitor cure process.
Total (Strain)			<0.0148	
Total (Resin)			<0.0276	

Table 21. Mission risk values for the current conical helix antenna design variant.

The failure chance of CHR-101, in Table 21, was calculated using Figure 162, as with the crossed Moxon analysis. The antenna feed assembly is approximated to have an area equal to 106cm^2. The difference in the calculated area arises due to the much longer length of the conical helix antenna and its feed line.

At this stage the final rigidisation technique for the inflatable has not been defined. The two most promising candidates have been included in Table 21. Due to the risk reduction activities undertaken for the PICARD REXUS sounding rocket flight, the values for strain rigidisation are lower than their equivalents for resin rigidisation. This could change if further work on resin curing was undertaken.

Solar UV driven curing of resin in orbit is a topic of current research at other institutions (Babuscia et al., 2013) (Maessen, van Breukelen, Zandbergen, & Bergsma, 2007), the results of which should be considered when they become available. The associated rigidisation failure (CMR-202-b) value is particularly uncertain due to the minimal work performed to date on this method. This essentially disqualifies this method until further work is performed. For this reason, the strain rigidisation risk value will be used in the trade-off analysis. It is important to note though that, due to the reduced inflation pressure, the risk of material failure during inflation will always be less than that of strain rigidisation.

8.7) Trade-off Analysis of Candidate Antennas

A wide variety of data has been collected for the two WISCER candidate antennas. The antennas have been simulated, prototypes have been produced and tested, and the necessary support systems have been characterised to a first approximation. At this stage a

comparison is necessary in order to determine if a down selection should be made. This section will present a trade-off analysis that compares all key factors using a percentage score method. This method quantifies the known/anticipated performance variables against the relevant requirement. If no requirement has currently been set, the lowest value is used as the bench mark for comparison. A score of 0% represents fulfilling the requirement with no extra margin. A negative score is therefore not permitted, as it would indicate that the requirement has not been met, and so that variant should be ruled out immediately.

The key areas that have been selected for this analysis are: cost, antenna performance, physical characteristics (mass properties etc.), availability of hardware/software and failure risk during the one-year mission. This list is not exhaustive but does cover the key deciding factors and all relevant information collected to date. At this stage of a project it is hard to be quantitative in all regards, particularly with regards to the cost difference of the antennas. Qualitative approximations have been used to capture existing experience on cost and hardware/software availability. Weighting of the factors will not be implemented in this analysis. Therefore, the section conclusions will emphasize attention on the individual comparisons rather than focusing solely on the final totals.

Table 22 shows the trade-off scoring for the first criteria area: RF performance. The values included in the table come directly from simulation of the final antenna designs detailed in previous chapters. The values are analysed, yielding the percentage score values which are then totalled. As expected, it can be clearly seen that whilst both antennas fully satisfy the requirements the conical helix has significantly better bandwidth performance (width and flatness). However, this extra bandwidth performance is likely not a major advantage due to other limitations and so, with the remaining criteria being closely matched, either antenna could be justified in terms of RF properties.

RF performance	**WCM**	**Conical**	**Percentage Score - Moxon**	**Percentage Score - Conical**
Bandwidth	105.5 MHz	300 MHz	5.5%	200%
Ring time	0.008 μs	0.014 μs	60%	30%
Angular width (3dB) (as a measure of Forward gain smoothness)	94.9°	129.4°	5.44%	43.78%
Peak directivity	5.66 dBi	5.54 dBi	2.17%	0%
Radiation efficiency	-0.0484 dB	-0.0028 dB	0%	4.80%
Total			**73.11%**	**278.57%**

Table 22. RF performance trade off table for the WISCER antenna candidates.

Next, Table 23 details the comparison between the physical aspects of the antenna and the supporting CubeSat. The WCM offers significant advantages for the mass and volume budgets, providing significant contingency compared to that of the conical helix. The WCM antenna performs very well with regards to ADCS, generating much reduced attitude disturbance torques. This would likely make up for the reduced solar panel area available for this design. Based on this the WCM is superior in this category.

Physical Characteristics	**Moxon**	**Conical**	**Moxon**	**Conical**
Mass	2343 g	3220 g	31.09%	5.29%
Volume	2.25 dm	3 dm	31.30%	8.40%
Power	30W (Peak)	45W (Peak)	0%	50%
Thermal	1	1	0%	0%
ADCS	3×10^{-8} Nm	5×10^{-7} Nm	94%	0%
Total			**156.39%**	**63.69%**

Table 23. Physical characteristics trade off table for the WISCER antenna candidates.

Availability of hardware and software has not been discussed previously in this thesis but has been included here with approximate values in order to indicate the experience gained during the construction of the WCM mechanical prototype and the construction of the PICARD experiment. The results are shown in Table 24, with a simplified calculation method.

Availability of Hardware and Software	**WCM**	**Conical Helix**
Support systems	1	1.1
Antenna elements and structure	1	2
Deployment mechanism	1	2
Software	1	1
Total	4	6.1
Percentage Score	**34.43%**	**0%**

Table 24. Availability of hardware/software trade off table for the WISCER antenna candidates.

The support systems are largely common between antennas and COTS components are available for most of the systems. This leads to a near identical relative rating for

availability. However, there may be stricter limitations on the heat sink size and mass for the conical helix antenna resulting in extra design work. A suitable reaction wheel system for the conical helix may also pose more work to successfully source, size and integrate.

Secondly in Table 24 the antenna elements and structure are considered. The conical helix represents a larger construction task than the WCM, which is compounded when considering the further prototypes and test articles required. The conical helix manufacturing quality will also need to be significantly higher in order to control the leak rate from the antenna post inflation. WISCER also intends to use thinner balloon materials than those used for the PICARD experiment. Thick materials were used in PICARD due to sourcing issues, but the increased cost budget of WISCER will likely alleviate this issue.

The deployment mechanism for the inflatable conical helix antenna is more complex than the WCM. Software will need to be written for both but will be necessarily more complicated for the conical helix.

Table 25 shows the mission risk probabilities resulting directly from the failure modes of the two antennas. The individual probabilities have been combined (using the strain rigidisation method for the conical helix) to give a failure probability during the nominal one year mission. The WCM antenna has a major risk mitigation factor due to its simpler design.

Risk	**Probability - Moxon**	**Probability - Conical**	**Percentage Score - Moxon**	**Percentage Score - Conical**
One Year Mission Failure Risk	0.00375	0.0148	74.66%	0%

Table 25. The mission risk probabilities resulting directly from antenna failure modes.

Combining the above data with an approximation of the relative cost, yields the results in Table 25. Design and manufacture labour hours are expected to be the largest project cost and they will depend largely on costs not directly related to the antennas. It is expected that the conical helix does represent the more expensive option but the uncertainty on this relative value is too large to estimate here.

WISCER Antenna Trade Off Table	**Percentage Score - Moxon**	**Percentage Score - Conical**
Cost	-	-
RF Performance	73.11%	278.57%
Physical Characteristics	156.39%	63.69%
Availability of Hardware/Software	34.43%	0%
Mission Failure Risk	74.66%	0%
Total	**338.58%**	**342.27%**

Table 25. Final trade-off analysis results for the WISCER antenna candidate designs.

Figure 163 shows how evenly matched the two antennas are, based on total score alone. The RF performance advantages of the conical helix antenna are essentially balanced by the physical properties and mission risk advantages of the WCM antenna design. It is key to note that the WCM scores evenly across the categories, showing multiple advantages in several areas. The conical helix, however, collects two thirds of its score from a single category: antenna bandwidth. If this large bandwidth does not truly represent an advantage to the mission or does not materialise fully in future testing, as indicated by the subscale and PICARD prototypes, then the result becomes very different with the WCM clearly favoured.

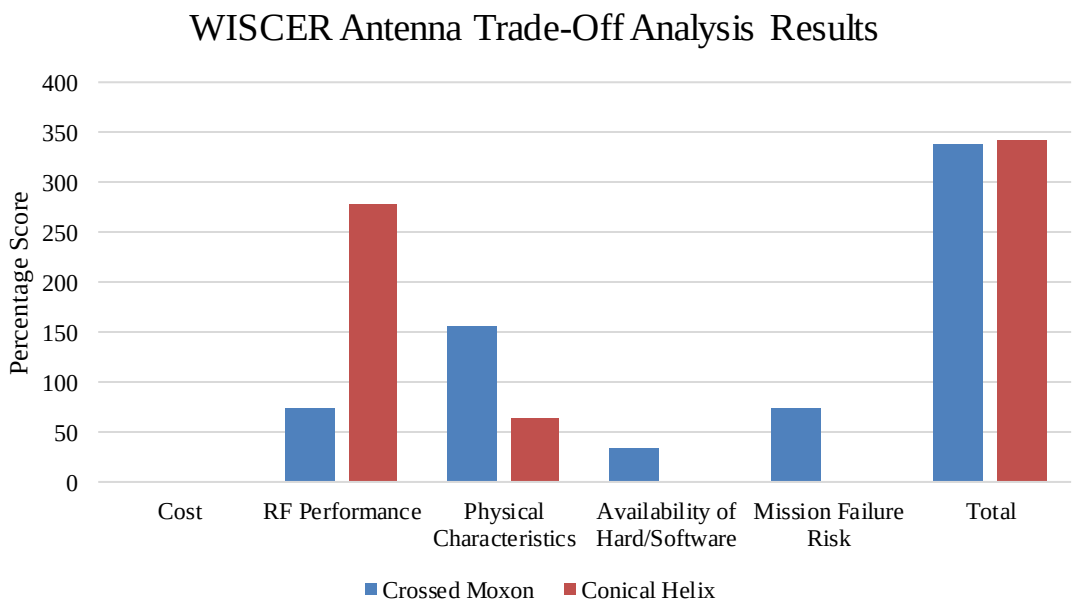

Figure 163. Visualisation of the final WISCER candidate antenna trade-off analysis results.

The WCM antenna provides solid advantages via: a simple release and deployment mechanism design, reduced attitude disturbance torques, small stored volume and dual use of the solar panels as a ground plane. If the 100MHz antenna bandwidth is sufficient, these varied design resiliencies and contingencies are critical in reducing project risk. In conclusion, if a down selection is required at this time, the WCM antenna design should be chosen.

The conical helix is still a viable antenna candidate and would provide a backup option should further work on the WCM yield significant issues.

CHAPTER 9) CONCLUSIONS

To conclude, the trade-off analysis of the two candidate antennas shows that both antennas are viable options. Interrogation of the results shows that the scoring of the conical helix antenna is heavily dependent on the superior antenna bandwidth alone, which may not materialise into actual benefit for the mission. If this is the case and the WCM is shown to be viable in subsequent RF ground testing, a down selection to the WCM should be made to efficiently use project resources.

Attitude simulations show that both antennas are viable given current control technologies, but the conical helix is at a disadvantage due to its large surface area and highly offset centre of mass, causing high radiation pressure torques. Simulations showed that using solar panels in dual use as the WCM antenna's ground plane appears viable and greatly reduces the torque generated compared to that of the AEOLDOS drag sail.

Improvements and optimisations to the crossed Moxon antenna design, yielding the WCM antenna, have led to significantly better (simulated) RF performance. These performance values include: a bandwidth improvement from 65 MHz to 105 MHz, significantly smoothed forward gain and a reduction of antenna dispersion to 0.008μs.

The RF properties and design curves for the conical helix antenna are well understood (Hertel & Smith, 2002, 2003) (Dyson, 1965) so the work here focused on the deployment method and its effect on RF performance. Two ground based sub-scale prototypes were created and tested in an anechoic chamber. This was done to inform the antenna feed design and investigate the impact of the dielectric inflatable material. This work culminated in the sub-orbital flight and successful S11 test of the full-scale inflatable PICARD conical helix antenna on a REXUS sounding rocket. The inflatable antenna

deployed as intended, provided key information on deployment dynamics and validated the novel use of strain rigidisation for a partial metal coverage inflatable structure.

APPENDIX 1) PICARD RF SUBSYSTEM DESIGN

1.1) Introduction

In this appendix the design of the RF S11 measurement subsystem for the PICARD experiment will be described in detail. The system was specifically designed for PICARD in order to meet the strict mass and volume limitations imposed. The integrated system can be seen in Figure 164. The experiment subsystem flew on the REXUS 19 rocket in March 2016 and performed nominally during flight, collecting all the planned data.

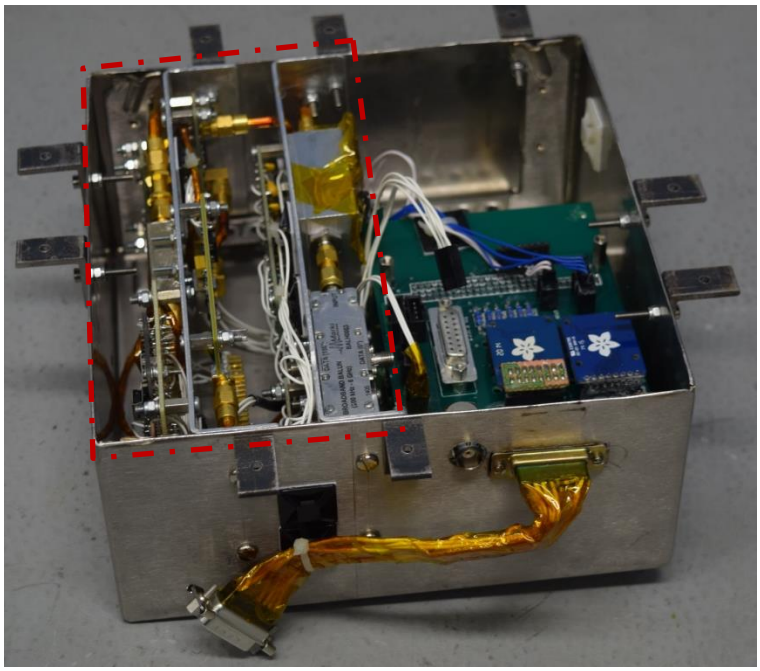

Figure 164 shows the PICARD electronics housing prior to integration with the rest of the experiment. The highlighted area is the RF subsystem.

1.2) PICARD RF performance measurement

A measurement of the antenna reflection coefficient spectrum, in the frequency range 350 – 600 MHz, allows validation of an operational antenna in milligravity deployment conditions. Without such a measurement, correct antenna operation cannot be proved (only

inferred) by a successful inflation and rigidisation of the antenna structure alone. Due to the measurement being made on the antenna feed line the power delivered to the antenna can be extremely small. Therefore, the antenna produces only a small amount of radiated power whilst active, which will not interfere with other systems. The signal should not be detectable on the ground. In order to achieve this measurement, three key operations need to be completed:

- Control and data logging
- Signal generation
- Antenna feeding and connection

The control and logging are performed using the central Arduino. The Arduino controls the sequential switching of frequencies through the chosen spectrum, by commanding the signal generator using one digital output port. It then co-ordinates this with the recording of data from the RF power meters.

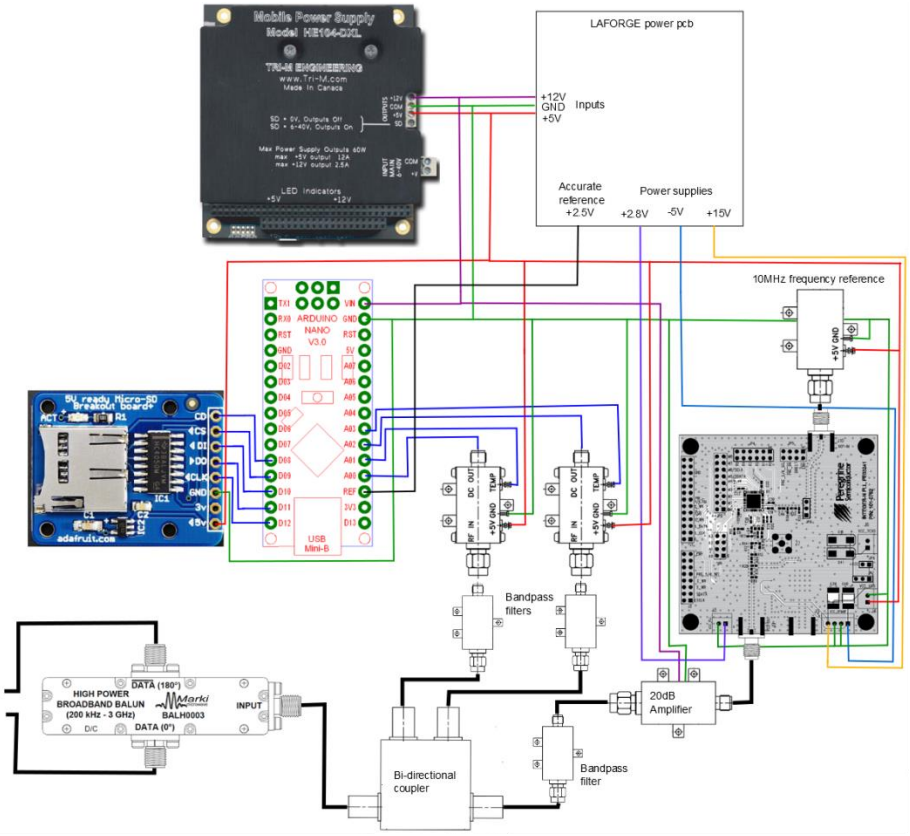

Figure 165 shows a wiring diagram for LAFORGE including the power supply. Serial connections between the Arduino-signal generator and Arduino-Control Arduino have been omitted.

Two RF power meters are required for accurate results of the reflection coefficient. The fed power and reflected power must be measured simultaneously as the provided power from the amplifier could drift. Measurements of these powers can then be combined on the ground, post flight, to generate the reflection coefficient spectrum using

Equation 48.

$$\Gamma = \sqrt{\frac{Prev}{Pfwd}} \qquad \textit{Equation 48}$$

Measurements made by the power meters are converted in to an output voltage which responds linearly to a logarithmic change in the power. The dynamic range of the power meter is therefore very high. Two analogue voltage input ports can be used by the Arduino

to record the output voltage from the meters and store it to a memory card. Built in to the power meters are temperature sensors which also output a voltage that can be recorded by the Arduino. Measuring the temperature allows us to compensate for any temperature dependant drift in the voltage of the power reading. The model of RF power meter used and its maximum ratings, can be seen below in Figure 166 and Figure 167 respectively.

Figure 166 RF power meter ZX47-40+ from Mini Circuits suitable for flight. Calibrated voltage output for RF power and temperature will be captured by the Arduino.

Maximum Ratings

Operating Temperature	-40°C to 85°C
Storage Temperature	-55°C to 100°C
DC Power:	
Max. voltage	5.7V
Max. current	120mA
Internal Power Dissipation	0.73W
Input Power	+27dBm

Permanent damage may occur if any of these limits are exceeded.

Figure 167 Maximum ratings for the ZX47-40+ RF power meter from Mini Circuits.

The RF power meters are be fed from the antenna feed line using a bi-directional coupler. The bi-directional coupler to be used by PICARD is the ZFBDC20-62HP-S+ from Mini Circuits seen in Figure 168. It has an operating and storage temperature of -55 to +100 degrees Celsius.

Figure 168 The bi-directional coupler ZFBDC20-62HP-S+ that will feed forward and reflected power to the RF power meters.

The antenna has two arms requiring two balanced RF feed lines which are 180° out of phase with each other. In order to achieve this, we use a balun to split the single feed line from the signal generator. The chosen balun is be a BAL-0003 as seen in Figure 169.

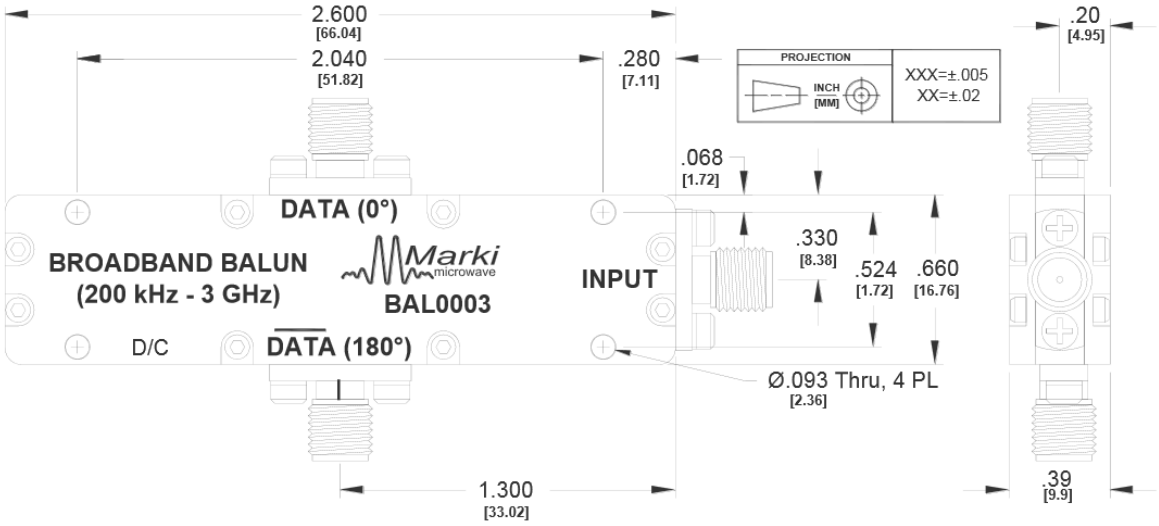

Figure 169 BAL-0003 balun from Marki microwave. The balun splits the single feed from the signal generator into 2 balanced feeds for each arm of the antenna, whilst also including the required 180° phase shift to one line.

Just prior to the bi-directional coupler in the antenna feed line is an amplifier. In a transmission system, like WISCER, a high power amplifier is placed here to amplify the signal to transmission power levels. In this system the amplifier is required merely in order to ensure there is sufficient signal reaching the reflected RF power meter after it has been through the antenna.

A multilayer circuit board produced by Peregrine Semiconductor fulfils the signal generation requirements. The board integrates the PE33241 PLL chip with a VCO capable of producing frequencies in the 350-700 MHz range. Whilst a VCO range of 200-700 MHz would be more favourable, this COTS system offers many benefits in terms of reliability and improved operating parameters. An image of the board with USB interface chip can be seen in Figure 170 and a schematic of the board layout in Figure 171.

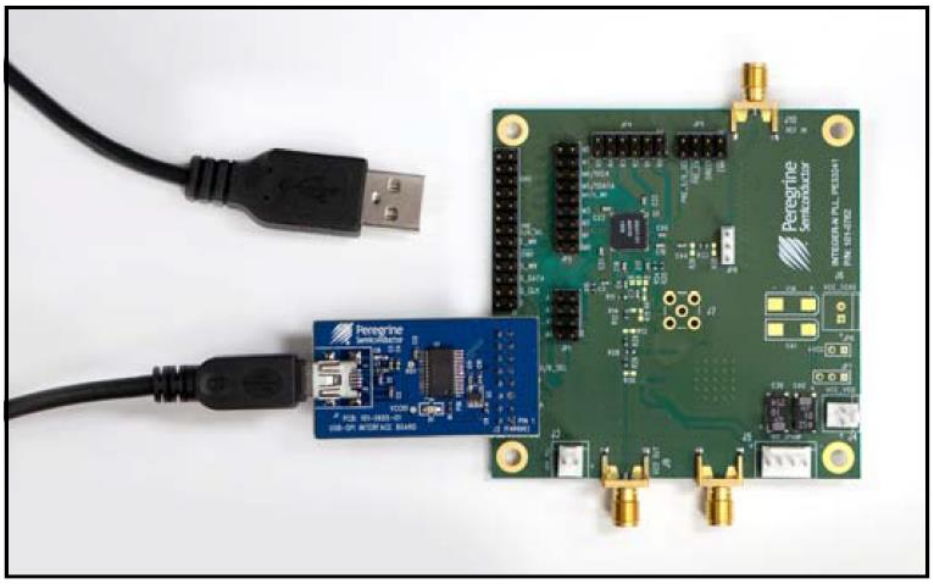

Figure 170 Peregrine Semiconductor PE33241 Integer-N PLL development board. The board combines the PE33241 PLL with an appropriate VCO and the necessary filters.

This board produces the required signal frequency using a voltage controlled oscillator (VCO). The voltage applied to the VCO is determined using a phase locked loop (PLL) and reference oscillator. The PLL compares the phase difference (and therefore any difference in frequency) between the reference and VCO output in order to keep the VCO output at constant frequency. In order to achieve the shifting of the VCO output frequency, counters are used within the PLL. This allows the PLL to stabilise frequencies generated by the VCO that are multiples of the reference frequency. The counter values are set via the serial input pins seen on the left of the board in Figure 171. The Arduino will be used to alter the counter values approximately once every $1/10^{th}$ of a second. A multitude of

filters are also included on the board that are needed to attenuate and balance the circuits between the PLL and VCO.

The reference oscillator will be a TXC 7W 10MHz crystal oscillator. It has an operating temperature range of -40 to +85°C at a stability of ±25ppm. The oscillator will be attached to a small PCB to provide it with voltage and connect it to an SMA connector.

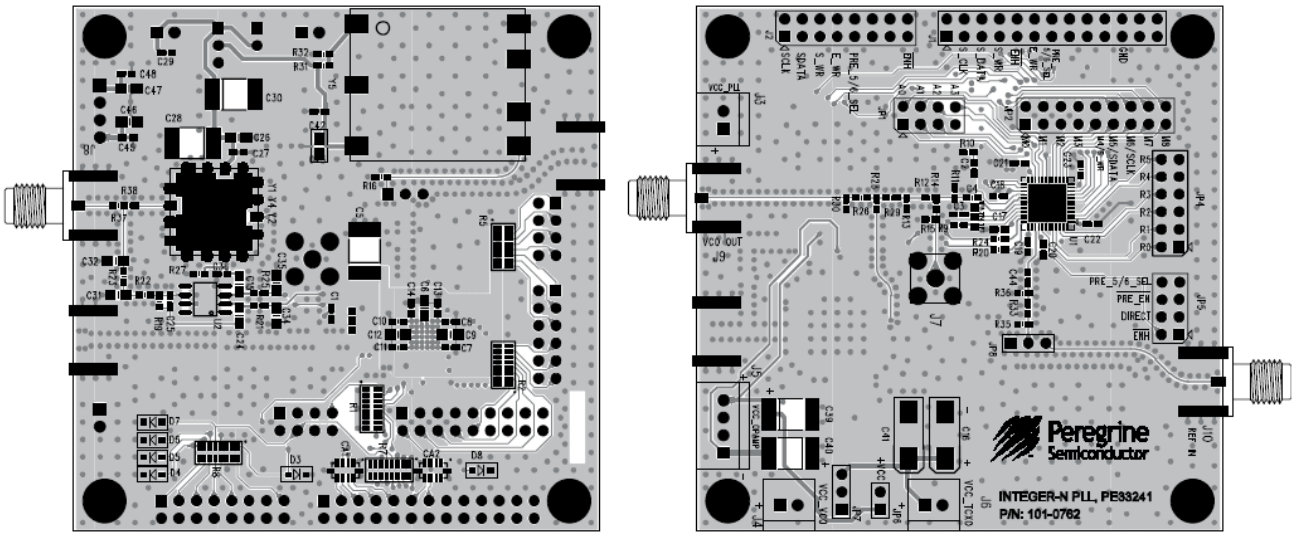

Figure 171 A schematic of the multilayer PE33241 development board (top – topside, bottom – bottom side).

The COTS components in LAFORGE will be connected via 50Ω SMA coaxial cables for the RF transmission. The notable exceptions are the power and data output connections. The individual components will be linked together directly where possible and standard SMA coaxial cables will be used where a bend or length is required. The SMA cables running from the balun will interface with the antenna system.

The full electronic schematic for the PE33241EK board can be found in its data sheet in the appendix. Figure 172 shows an extract for that schematic, showing the three VCOs included on the board. For PICARD the highlighted 350-700MHz VCO will be used.

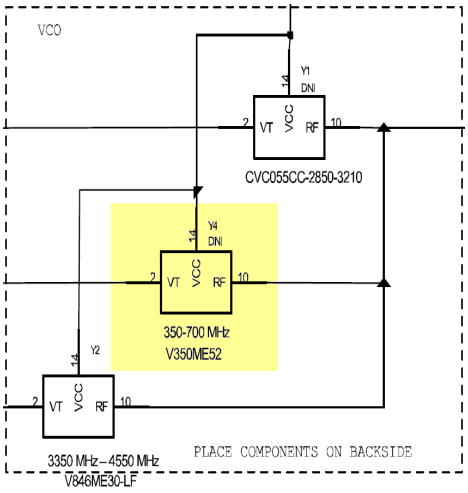

Figure 172 Extract from the PE33241EK circuit schematic. There are three VCOs included with the board. The yellow highlighted area shows the VCO that will be used for PICARD.

The reference oscillator requires the addition of a PCB mount for electrical and mechanical connections. A schematic of the PCB design can be seen in Figure 173. The trace widths have been impedance matched to 50 ohms with respect to the board parameters. The ground plated FR4 substrate will be 1.6mm thick and the copper traces will have a thickness of 35um. Only the frequency output trace to the SMA connector will be carrying the 10MHz signal.

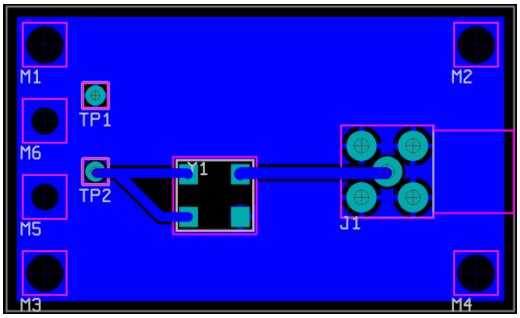

Figure 173 shows the PCB design for the reference oscillator used by the signal generator.

As seen in Figure 174 and Figure 175 filters are included in the RF circuitry. The low pass filter prevents super harmonic generation being sent to the antenna. This therefore prevents interference with the REXUS service module GPS receiver. The low pass filter is a Chebyshev filter with 5 poles. It is constructed on a PCB using surface mounted SMD type components. At the 2.3 GHz GPS frequency band the attenuation should be approximately

-60db of attenuation. The circuit diagram and simulated performance can be seen in Figure 174.

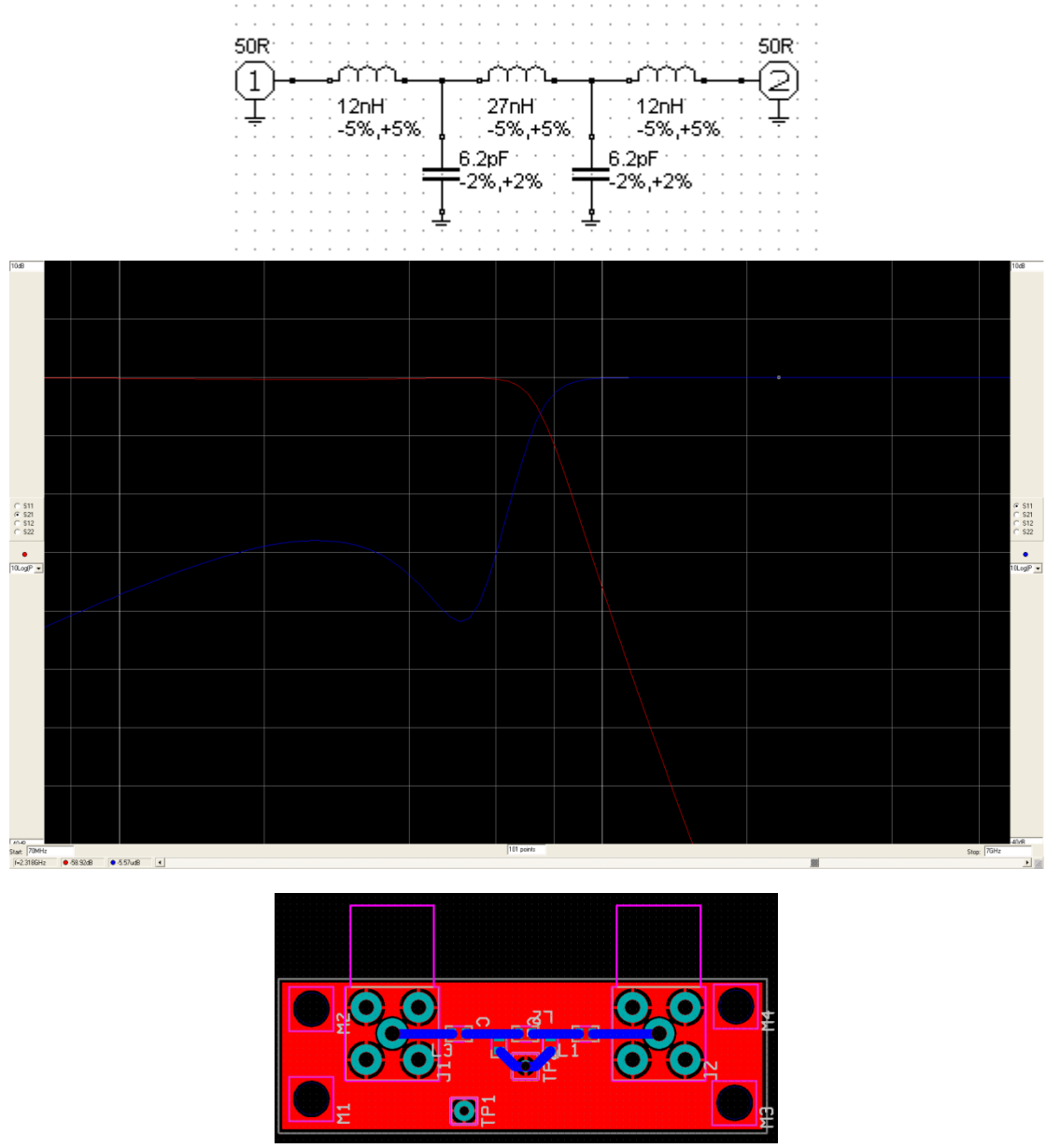

Figure 174 (Top) Circuit diagram for the 700MHz low pass filter. (Middle) The simulated results for this circuit design. The attenuation in the 1.5GHz frequency range is approximately -40db. (Bottom) PCB design.

The band pass filters included in the design reduce unwanted RF energy from entering the power detectors. These filters also use the SMD attachment and Chebyshev design but with just 3 poles. The bandwidth (-10db) has been simulated to be 250-780 MHz with an attenuation of -40db in the 1.5GHz frequency range. The circuit diagram for both is

identical and is shown in Figure 175. There is some rippling in the pass bandwidth which should but noted when interpreting the data. Testing showed that the rippling in the constructed components has a negligible effect on the overall system and can be discounted.

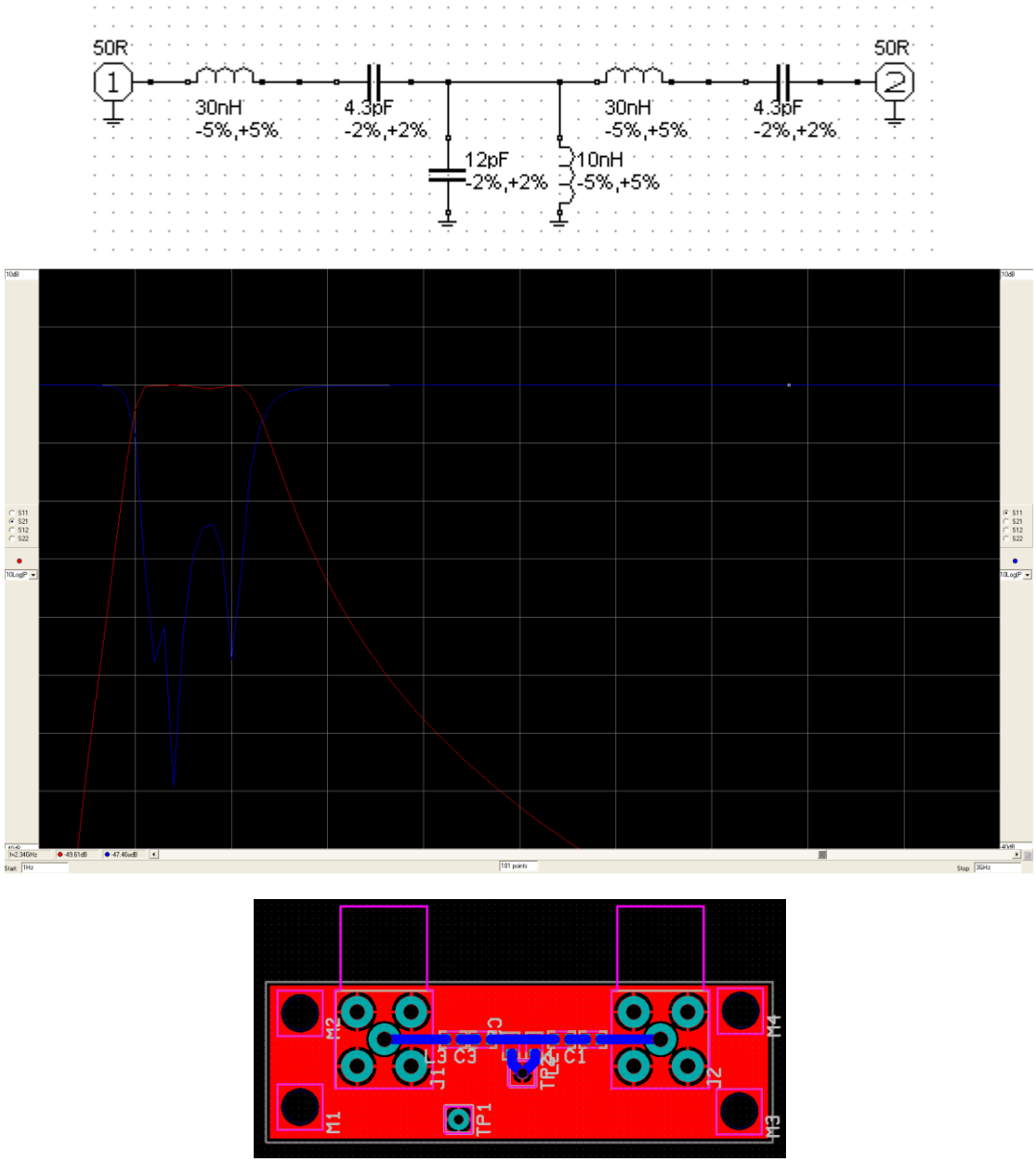

Figure 175 (Top) Circuit diagram for the band pass filter. (Middle) The simulated results for this circuit design. The attenuation in the 2.3GHz frequency range is approximately -50db. (Bottom) PCB design.

The PICARD design calls for multiple data logging Arduinos. These data loggers are controlled by a central Arduino Nano that provides timing and the experimental signals.

The LAFORGE Arduino logs the RF power measurements and controls the signal generator frequency.

Once the subsystem is powered up it begins reading the temperature sensors on the RF power meters in an idle mode. This data is then outputted to the serial port D1 and not recorded. The control Arduino samples this data for inclusion in the downlink format. The start of experiment signal will be accepted on pin D2 (05). This triggers the signal generation and data logging program that will run until just after the antenna is jettisoned. During that time the program repeatedly records S11 data at 5MHz discrete steps over the 350MHz – 600MHz range.

Serial communication (SPI) is used to set the register values on the signal generation board during each loop. Pins: D4 (SDATA), D5 (SCL), D6 and D7 are used for this communication. The data logging is achieved through the addition of a micro-SD breakout board to the Arduino.

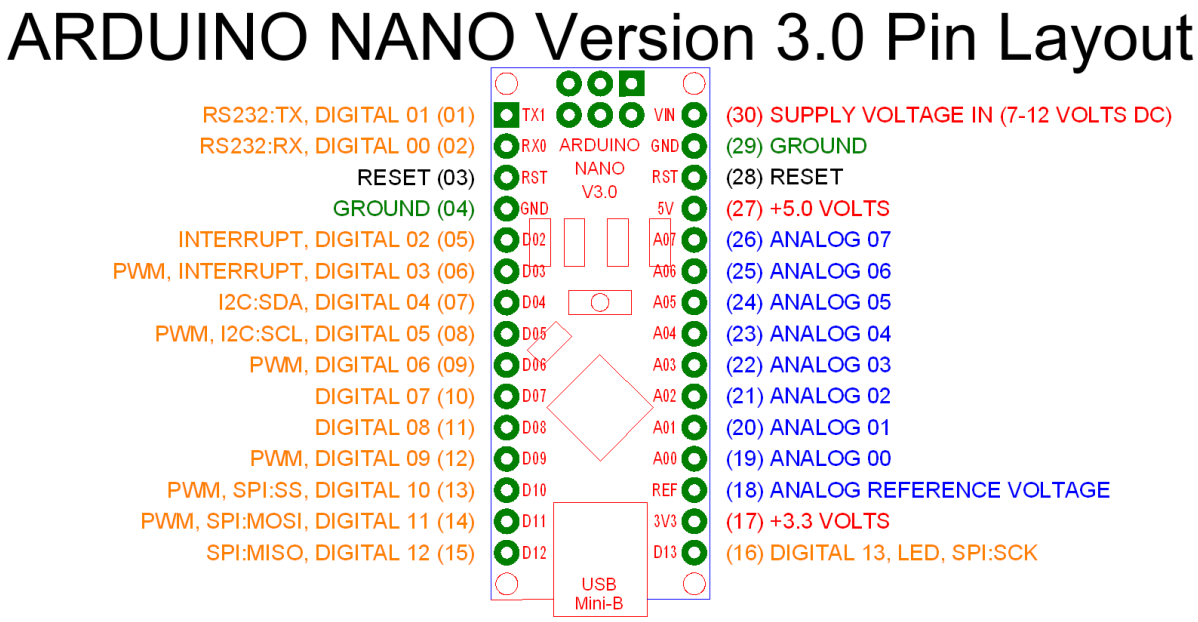

Figure 176 The pin layout of the V3 Arduino Nano.

A reference voltage of 2.5 volts is used for the analogue measurements to increase measurement accuracy. Based on the expected voltage range from the reflected RF power sensor, this gives the 10 bit analogue to digital converter a resolution of 2.44E-3 volts per division. This gives 184 levels across the expected voltage range and a resolution of 0.11dB for the S11 measurements which is sufficient for analysis of the results. The voltage reference is provided by an ADR441A voltage reference chip on the LAFORGE power board.

The 1.1V internal reference is used when making measurements of the temperature during standby mode, increasing the temperature resolution. The system should achieve a temperature resolution of 0.52°C across the -40°C to 100°C range, if the Arduino were to remain operational.

Only every 10th data point will be output on digital pin 1 (01), as the frequency sweep proceeds, for downlink. Serial output is a time consuming process and this method allows for a much greater volume of data capture to the SD cards.

Connection	**Arduino Pin Reference**
Micro-SD board 5V	5V (27)
Micro-SD board GND	GND (29)
Micro-SD board CLK	D13 (16)
Micro-SD board DO	D12 (15)
Micro-SD board DI	D9 (14)
Micro-SD board CS	D10 (13)
Micro-SD board CD	D9 (12)
Data TX	D1 (01)
Signal generation on (testing)	D3 (06)
Start of experiment	D2 (05)
Signal generator - Serial Output	D4 (07)
Signal generator – Clock	D5 (08)
Signal generator - E_WR	D6 (09)
Signal generator - S_WR	D7 (10)
2.5 volts reference voltage	AREF (18)
Forward RF power	A0 (19)
Reflected RF power	A1 (20)
Forward meter temperature	A2 (21)
Reflected meter temperature	A3 (22)

Table 26 shows a list of the pin connections for the LAFORGE Arduino.

Using the datasheet values provided, expected signal levels throughout the system have been calculated. The final power levels at both RF power meters under the full range of

operating conditions determine if the system is capable of recording the possible results. For these conditions we use the expected reflection magnitude values from modelling of the conical helix antenna.

The minimum expected reflection power is expected to be approximately -22dB. In a real system the reflection is likely to be higher than this ideal case simulation. Still in Table 27 we use this value to determine the power level seen at the RF meter of -32.53dBm.

Component	**Gain (dBm)**	**Evolving power level (dBm)**
PLL-VCO	+9	9
Amplifier	+10	19
Output Filter	0	19
Bi-directional coupler mainline	-0.53	18.47
Balun	-4.5	13.97
Antenna (approx. max)	-22	-8.03
Balun Return	-4.5	-12.53
Bi-directional coupler Out-Cpl Rev	-20	-32.53
Measurement filter	0	-32.53
RF power meter (reflected)	0	**-32.53 (1.8 Volts)**

Table 27 Power budget table for reflected power meter (minimum expected reflection)

The worst case scenario for maximum reflected power from the antenna is that of complete reflection. This gives an effective value for the gain of 0 dBm. Table 28 shows the power flow calculation resulting in a value of -10.53dBm at the power meter. We can also deduce from this calculation that the RF power meters are safe from power received by the

antenna. They have a maximum input power of +27dBm, requiring a captured power from the antenna of +51.5dBm for damage.

Component	**Gain (dBm)**	**Evolving power level (dBm)**
PLL-VCO	+9	9
Amplifier	+10	19
Output Filter	0	19
Bi-directional coupler mainline	-0.53	18.47
Balun	-4.5	13.97
Antenna (approx. min)	0	13.97
Balun Return	-4.5	9.47
Bi-directional coupler Out-Cpl Rev	-20	-10.53
Measurement filter	0	-10.53
RF power meter (reflected)	0	**-10.53 (1.3 Volts)**

Table 28 Power budget table for reflected power meter (maximum expected reflection)

Table 29 shows the same calculation performed for the forward power meter. Due to the reduced losses through the path to this power meter the power measured here is much higher. The calculation gives a value of 9dBm. This is still well within the power meter range and so should not require attenuation.

Component	Gain (dBm)	Evolving power level (dBm)
PLL-VCO	+9	9
Amplifier	+10	19
Output Filter	0	19
Bi-directional coupler In-Cpl Fwd.	-20	-1
Measurement filter	0	-1
RF power meter (forward)	0	**-1 (1.05 Volts)**

Table 29 shows the power budget for the forward power meter.

Using the data provided in the datasheet of the ZX47-40+ RF power meter, Figure 164, we can convert the calculated input RF power levels into the expected output voltages. From the tables we see that the predicted voltage range is 1.8 volts to 1.3 volts for the reflected power measurement and the forward power measurement will be approximately 1.05 volts.

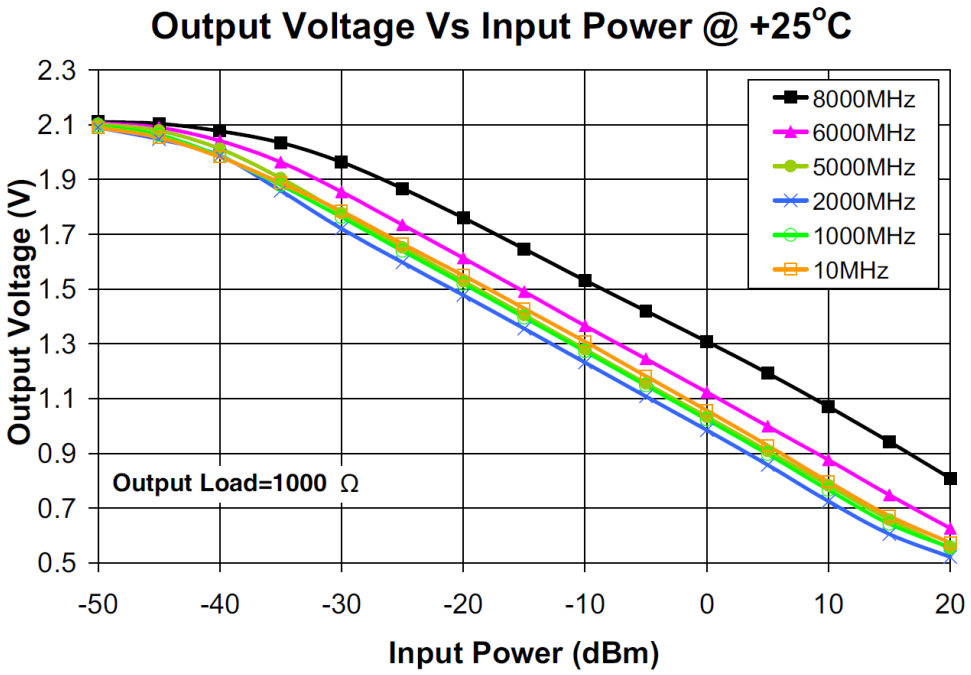

Figure 177 Graph from the ZX47-40+ RF power meter datasheet. The graph shows the output voltage for a given input RF power in decibel milliwatts.

Data is also recorded from temperature sensors built into the power meters. Figure 178 shows the change in output voltage for a given RF input power dependant on the temperature. In the lower frequency range, where LAFORGE will operate, the effect is minimal. Temperature information is still useful as a systems status check and was included in the downlink telemetry via the used of the power meter's temperature sensor (Figure 179).

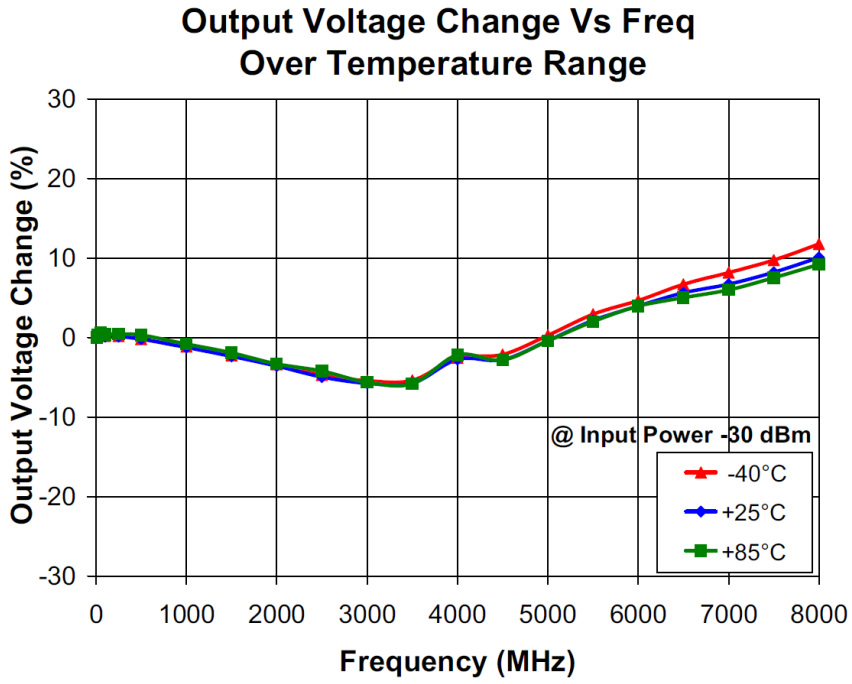

Figure 178 Graph of the output voltage change depending on ambient temperature for RF power meters.

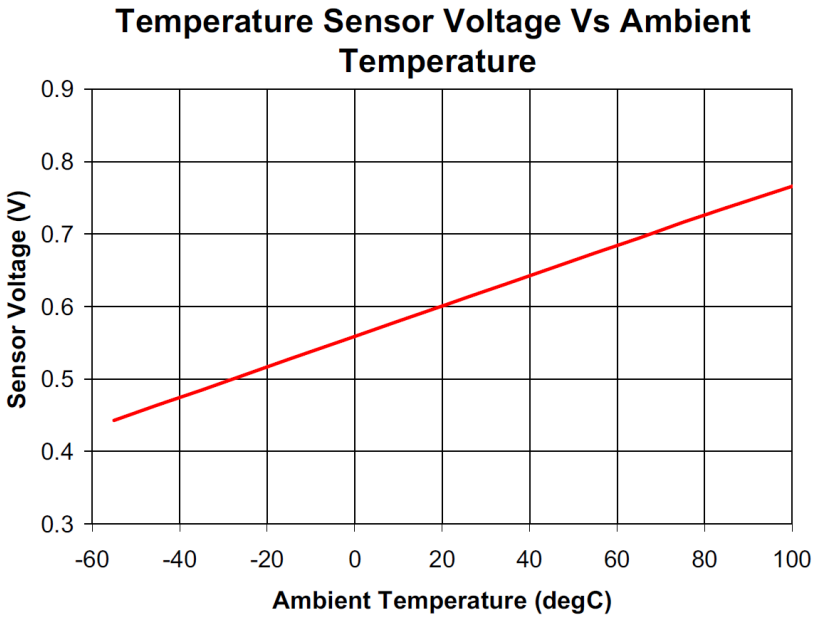

Figure 179 Output voltage for the temperature sensor on the ZX47-40+ RF power meter.

The full range of output voltages (0.8 – 0.4 volts) can be recorded by the Arduino. The low temperatures will be experienced on the launch pad. The high temperatures will be experienced as the heat from the sonic shock radiate to the rocket skin and subsequently permeate through the structure to the components. The internal structure has been designed to reduce thermal conductivity between the skin and the components to prevent component temperature exceeding 80°C during the flight.

1.2.1) Power System

The main power is provided by a commercially available DC-DC converter/power supply taking input from the REXUS service module. The power supply has built-in features to limit voltage ripple (both feedback and to the experiment) to levels within the 100mV tolerance for REXUS. LAFORGE has a separate power supply to provide the more specific voltages required by the RF components; this runs from the 12V output of the main experiment power supply. Table 30 summarises the power consumption of the primary system components; power for each sensor is drawn from the Arduino Nano

voltage out pin, and hence they are not required to be considered separately in the power plan. The measured peak power usage from all the electronics systems (excluding solenoid activation) was 11W. According to its spec, the solenoid valve for the inflation system requires an additional 18W; this (including losses from the MOSFET) was measured by the service module as 24W at its peak. The RF systems activate only once the solenoid is no longer powered, ensuring that the experiment power drain did not exceed 35W during the inflation cycle and 17W after this.

Component	**Voltage (V)**	**Amps (mA)**	**Power Consumption (mW)**
PLL Evaluation Board	2.8 (PLL) 5 (VCO)	75 (PLL) 17 (VCO)	295 (Combined)
RF power meter (x2)	5	100	1000
LAFORGE Power board losses	-	-	950
Amplifier	12	450	5400
TCXO reference oscillator	5	45	225
Arduino Nanos	5	50	250
HackHD cameras	5	400	2000
TOTAL			**10,120**

Table 30 Expected electronics power usage breakdown

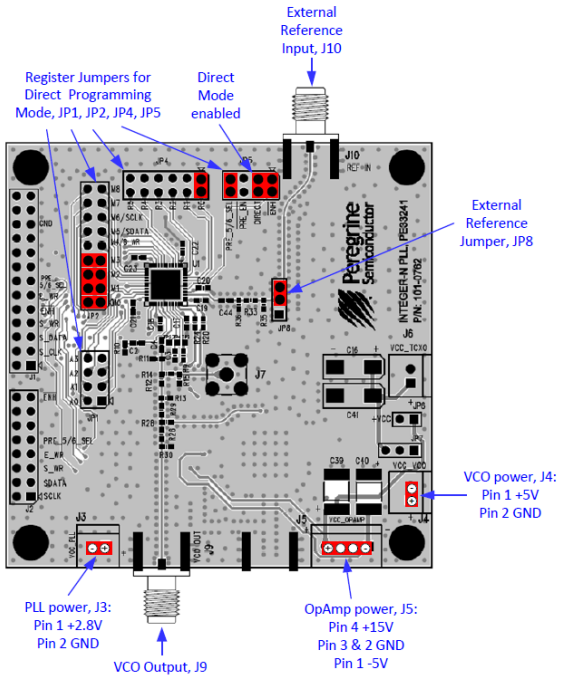

Figure 180 is a schematic of the PE33241 development board with labelled connections and pins.

Figure 180 shows a schematic with the input ports of the PLL/VCO board. For operation it requires voltages not supplied by the HE104-DXL power regulator used by the rest of the PICARD systems. A list of the required components to provide these voltages is provided in Table 31. Also included on this board is the accurate 2.5V reference source for the Arduino measurements. The PCB design is shown in Figure 181.

Component	**Reference number**	**Voltage supplied**
Voltage Reference	ADR441	2.5V ref
Voltage Inverter	LT1026	-5V
DC-DC converter	1PB1215LD	15V
LDO regulator	LT1764	2.8V

Table 31 Primary LAFORGE power supply components.

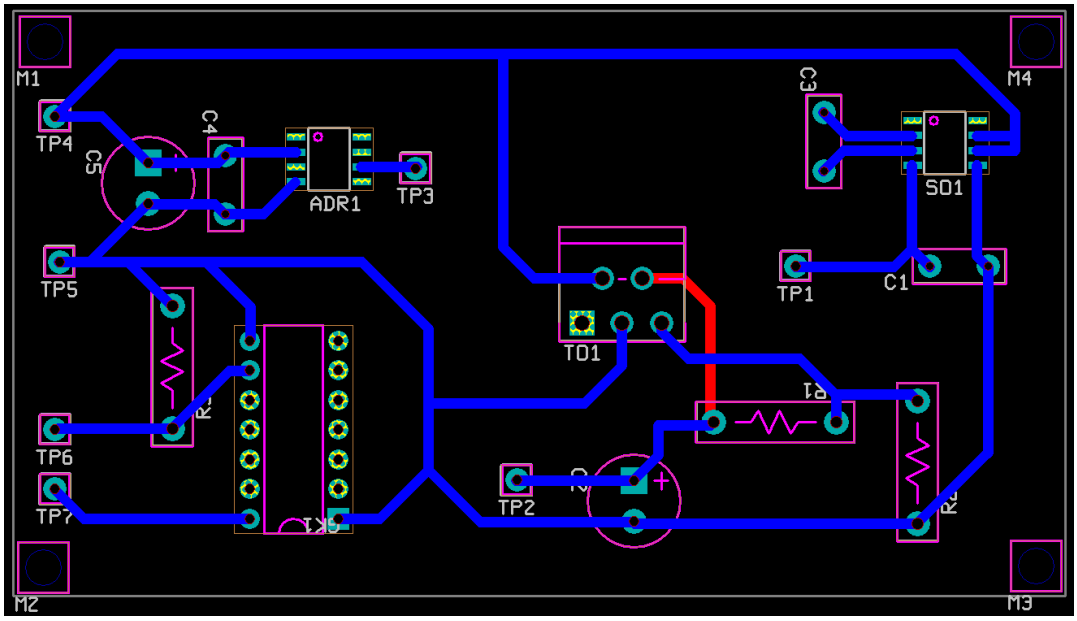

Figure 181 is the LAFORGE power supply PCB required to power the signal generator.

APPENDIX 2) RESISTIVE CAPACITIVE LOADING

2.1) Introduction

The work included in this appendix was completed with the goal of improving the bandwidth and reducing the dispersion of the crossed Moxon antenna. Despite improved results, they were not a significant enough improvement over the base design to warrant the extra complexity. The investigation is included here for completeness as it represents a large volume of work.

2.2) RC Loaded Bow Tie Antenna

The following section describes the methodology used to apply the RC loading technique to the crossed Moxon antenna. The Lestari method is most applicable due to the similarities between the design requirements of that study and WISCER. The method is used as a starting point from which necessary modifications for the crossed Moxon are made. To explain the concept prior to describing the changes made, a test simulation is outlined below.

This test simulation models the performance of a Bow Tie antenna identical to that considered by (Lestari et al., 2004) except that it has been rescaled to use frequencies of interest to WISCER. Figure 182 shows the antenna model where blue is the substrate and the gold is the metal antenna elements. The absorber has been removed in this image to allow a view of the antenna elements and their distribution, but if it were present it would cover the entire top surface in the same way as the substrate below. (Lestari et al., 2004) gives detailed information on the exact physical layout of the materials so it is omitted here.

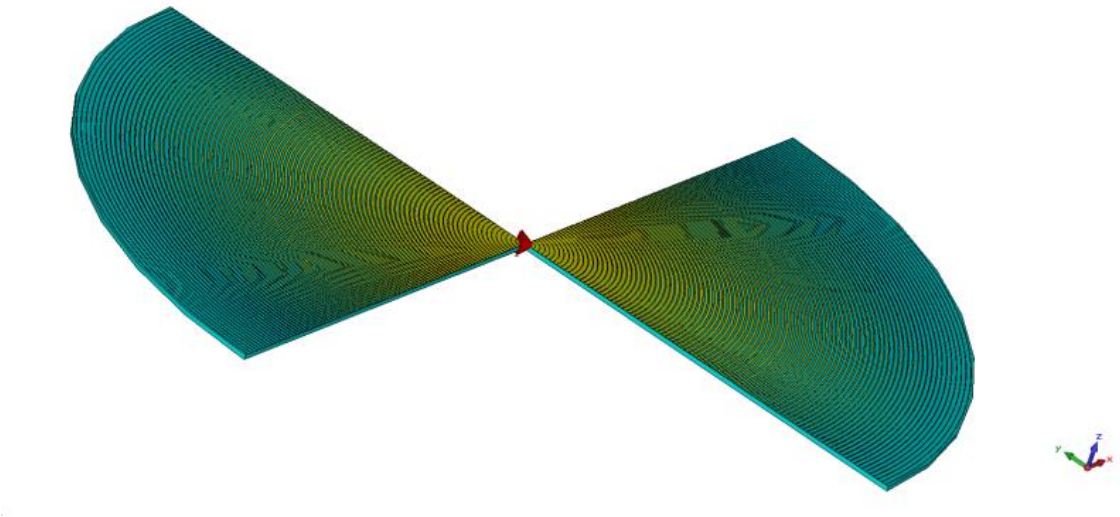

Figure 182 shows the CAD model of the RC loaded circular ended bow tie antenna.

Constant resistive and linearly increasing capacitive profiles are used for this simulation in line with (Lestari et al., 2004). More effective profiles have been suggested for resistive loading pattern such as the Wu-King profile (Wu & King, 1965) but were beyond the scope of this investigation. The profiles are achieved through etching of concentric slots which cut through the antenna. The capacitance of such slots has been shown to decrease approximately proportional to the width of the slot (Lestari, Yarovoy, & Ligthart, 2003) and in agreement with classical microstrip theory. Therefore, to achieve linearly increasing capacitance towards the ends the slots widths should also linearly increase.

To achieve the resistive loading at the required frequency an applicable volumetric absorber is used to cover the conducting side of the antenna. The equivalent surface resistance per square meter is inversely proportional to the area of the strips. Therefore, to achieve a constant resistive profile radially outward along the antenna the areas of the strips must remain constant, due to their changing cross section.

An initial investigation into possible materials for the thin sheet RF absorber used to apply resistive loading yielded several flexible possibilities. For this test, the electrical properties of a material set called the AB7000 series which was designed to be effective in the

frequency range of 200+MHz. Thicknesses commercially available as of 12/09/2016 were 0.16, 0.25, 0.35 and 0.55mm. A parametric sweep analysis of these material thicknesses, as applied to the bow tie antenna, yielded that a thickness of 0.35mm would be optimal in this case. It gave the best balance between radiation absorption and generated loading.

Figure 183 shows the supplier power loss data that was used to select the optimal absorber material type (AB7050). This material was manually entered to the CST library so that it could be included in the simulations. Figure 184 shows the absorption data programmed into CST for all subsequent simulations runs in this chapter that make use of the AB7050 absorber.

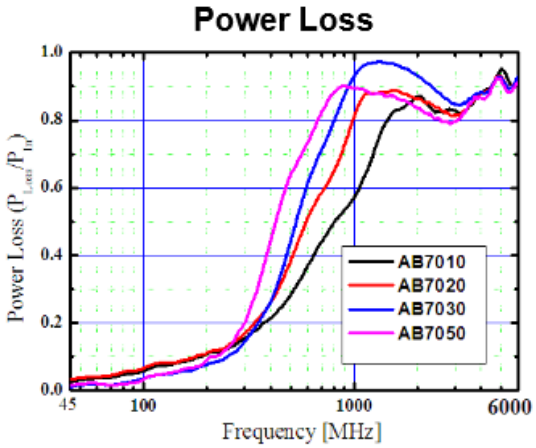

Figure 183. Graph of absorbing power of differing thicknesses of AB7000HF series absorber (3M, 2009). Power loss here is measured using the 50 ohm microstrip line standard 3M TM K-RD-EMC-AB-01.

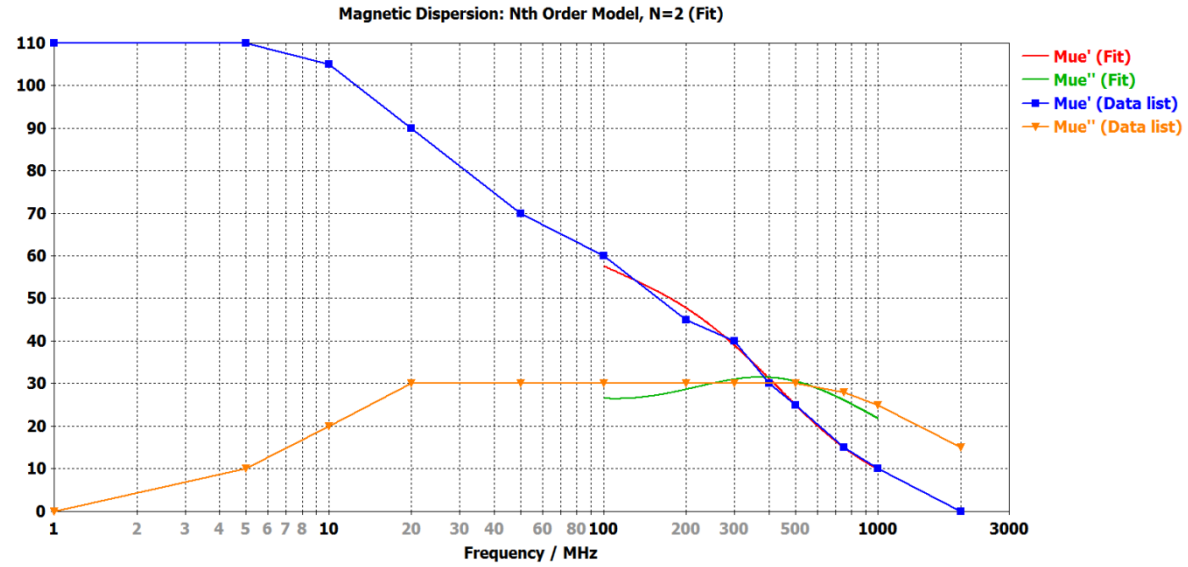

Figure 184 shows the Mue data used in all the CST simulations with the volumetric absorber. This data was supplied by the manufacturer.

Theoretical analysis by (Lestari et al., 2003) and (Lestari et al., 2004) suggests that the impedance at the ends of the antenna should be 25jkΩ/m. Using the same loading calculation as (Lestari et al., 2004) and also following the assumption that a first slot width of 0.2mm corresponds to an impedance of 1jKΩ/m we arrive at the slot loading pattern seen in Figure 182. Note that the slot widths increase, and the strip widths decrease leading to a simple formula for their calculation as the slot-strip width remains constant. This will not be the case for the crossed Moxon and is discussed subsequently in this section.

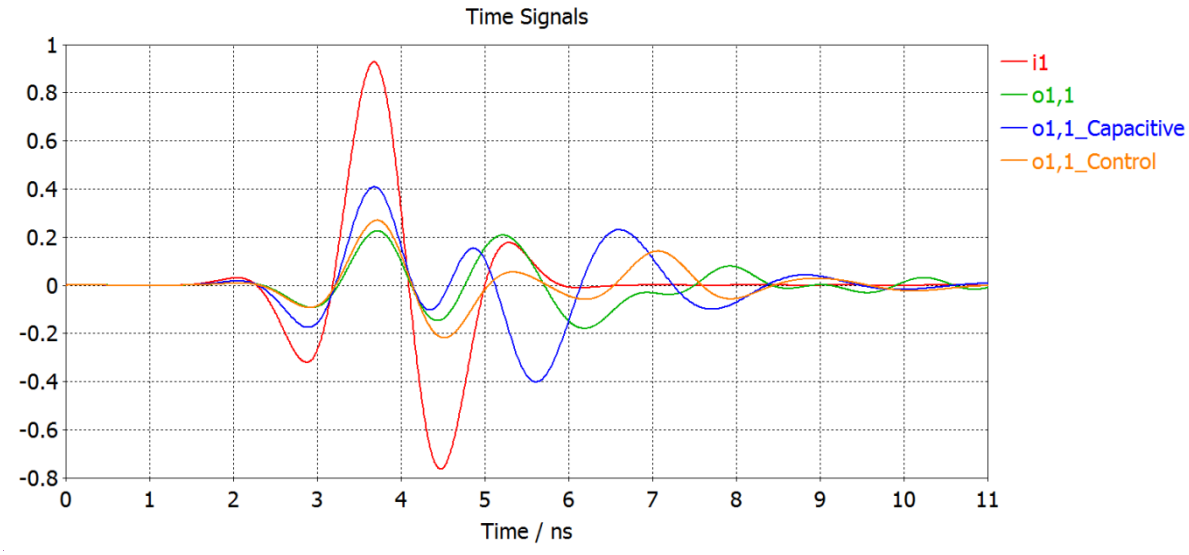

Figure 185 shows the modelled bow tie antenna time signal response to the input pulse. The outputs signals shown here are for one of the four feed points.

The results of this simulation can be seen here in Figure 185, Figure 186 and Table 32. Whilst the results shown here are not as pronounced as those in (Lestari et al., 2004), the expected effect was observed. The reflected signals in Figure 185 reduced and the -10dB bandwidth increased by 66%. Ideally further work would have been performed here to attempt to replicate the (Lestari et al., 2004) results but the simulation setup for this particular case is extremely time consuming, due to the antenna size. It was therefore deemed more effective to progress with the smaller crossed Moxon antenna. We also note here that in this early model the first slot distance from the feed was only approximated. This is a significant contributor to the reduction in gain seen in Table 32. To calculate the distance from the feed to the first slot Equation 49 is used.

$$2l_{max} = \frac{C_{subst}}{2f_c} \qquad \textbf{Equation 49}$$

Where C_{subst} is substrate dielectric constant, f_c is the intended central frequency and l_{max} is the value of feed point-first slot distance for which the pulse radiated from the feed

point, in the broadside direction, combines constructively with the pulse from slot one. Further research refined the calculation for the chosen materials and dimensions of later simulations leading to improved gains.

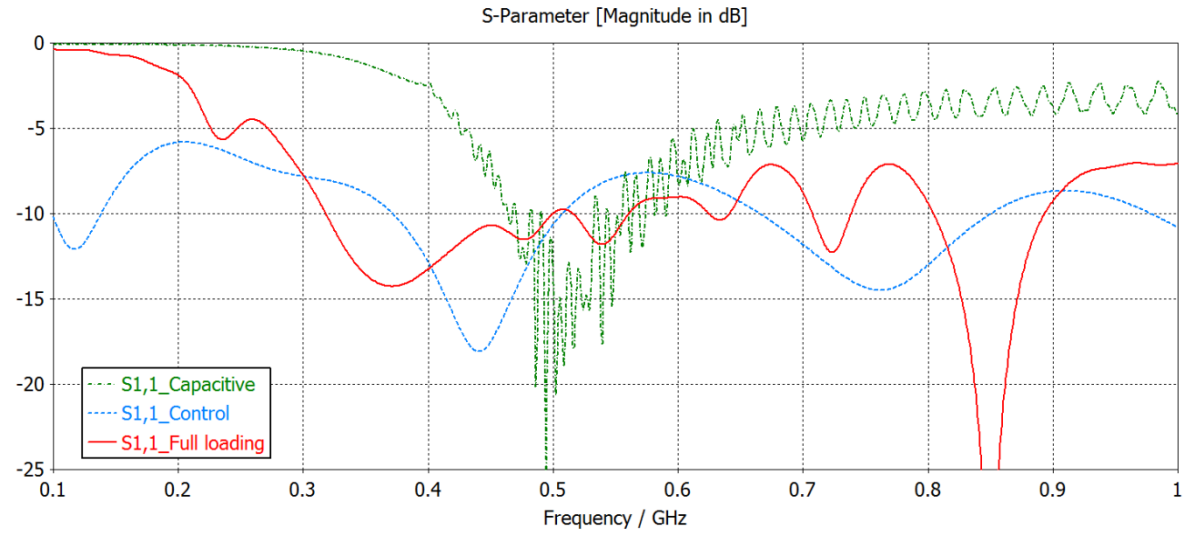

Figure 186 is a linear graph of the S11 results for RC loaded bow tie antenna simulation.

Values for 450MHz simulation	**Bow tie antenna**	**RC loaded bow tie antenna**
Radiation efficiency	0.98	0.65
Total efficiency	0.97	0.60
Directivity	3.133dBi	3.471dBi
Gain (IEEE)	3.065dBi	1.606dBi
Realised gain	2.987dBi	1.220dBi

Table 32 gives a comparison of the simulated efficiency, directivity and gain values of the loaded and unloaded bow tie test antennas.

2.3) RC Loading of Crossed Dipoles

To develop a better understanding of, gain experience with and explore the necessary differences in loading profiles between the bow tie antenna and the crossed Moxon,

simulations of a simple crossed ribbon dipole were performed. This section does not directly link to the conclusions presented at the end of this chapter on the crossed Moxon but does provide detail on the instrumental steps taken to decide on the final loading pattern.

The first results presented are that of the control test. The crossed tape spring dipole antenna, seen in Figure 187 was created. Using such a simple, well documented antenna design reduces the number of variables within the system. It allows us to develop an understanding of the processes that are occurring within the antenna during operation based on well know principles. From this point forward, we also finalise the WISCER CubeSat structure, the antenna support structure and the use of solar panels as ground planes. This design will be used in all subsequent simulations as it is the most likely candidate for a 3U WISCER variant and has not changed between the date the simulation has run and the time of writing. Whilst there are obvious omissions in the design, especially within the CubeSat itself, these components are not expected to have a significant impact on the final antenna performance. This allows us to provide a consistent background for comparison between results and make definitive conclusions for the final design based upon detailed antenna properties.

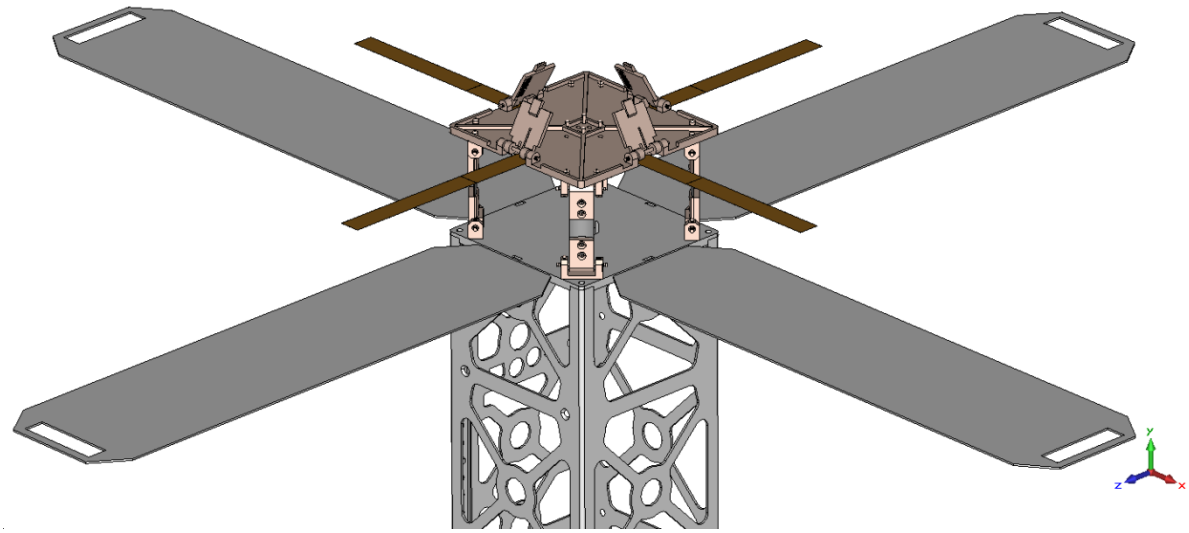

Figure 187 shows the crossed tape spring antenna. This antenna provides a baseline for which all subsequent RC loaded versions can be compared and for a working theory of operation to be created.

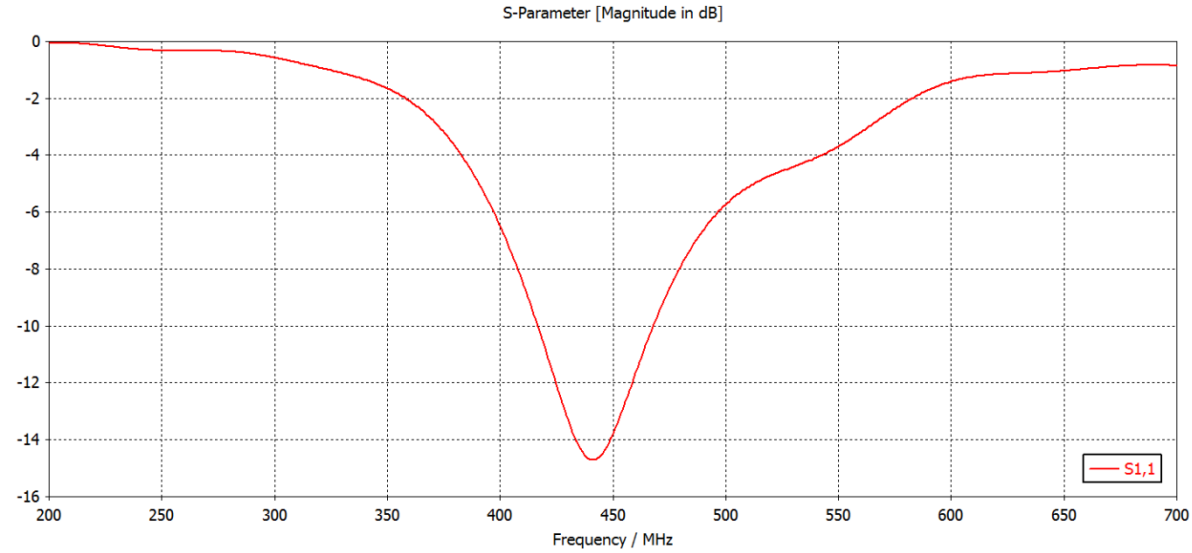

Figure 188 shows the S11 profile simulation results for the crossed tape spring antenna reference model.

Above in Figure 188 we see the S11 results of the now standard time domain FEM analysis performed by CST. The electrical resonance is wider than a classical rod dipole as expected due to the width of the elements. If the bandwidth requirement for WISCER were reduced from its current level this antenna design would provide a significantly simplified design. It also has significant flight history due to its similarity to the common deployable tape spring dipole used on many CubeSats.

To progress from here we must now determine the correct loading profiles for this antenna. Following the method from the previous section but adapting it to the constant width of the tape spring dipole yields the following requirements for the loading in Table 33.

Desired RC profile	**Profile comment**	**Slot/Strip Profile**
Constant resistive profile	Achieved via constant strip area	Constant slot-strip length
Linearly increasing capacitive profile		Increasing slot width

Table 33 details the loading profiles required for the loaded crossed dipole antenna.

The outcome of this loading pattern can be seen in Figure 189. Calculation of the first slot distance, using **Equation 49** and n=1.7, yields 9.7cm for the Kapton substrate tape spring. As can be seen this is a significant fraction of the antenna due to its electrically small nature.

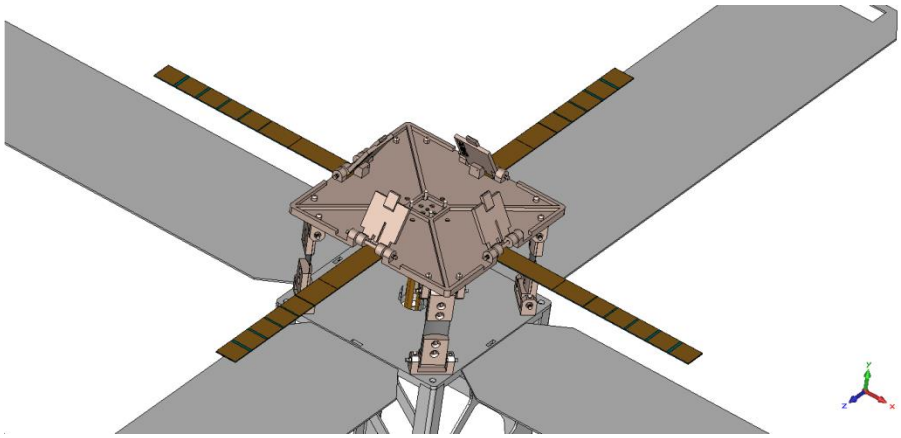

Figure 189 shows the RC loaded crossed tape spring antenna.

Figure 190 and Figure 191 show the comparative results between the loaded and unload simulations. The -10dB S11 bandwidth has increased by 200% and the late time ringing has been suppressed as desired. It can be inferred from this result that the resistive and capacitive loading is indeed reducing the reflections from the ends of the antenna as

desired. We must note however that some of the S11 bandwidth improvement will be arising from the newly introduced losses of the absorber material. Simulation of the absorber alone, however, suggests that this accounts for less than 10% of the improvement seen.

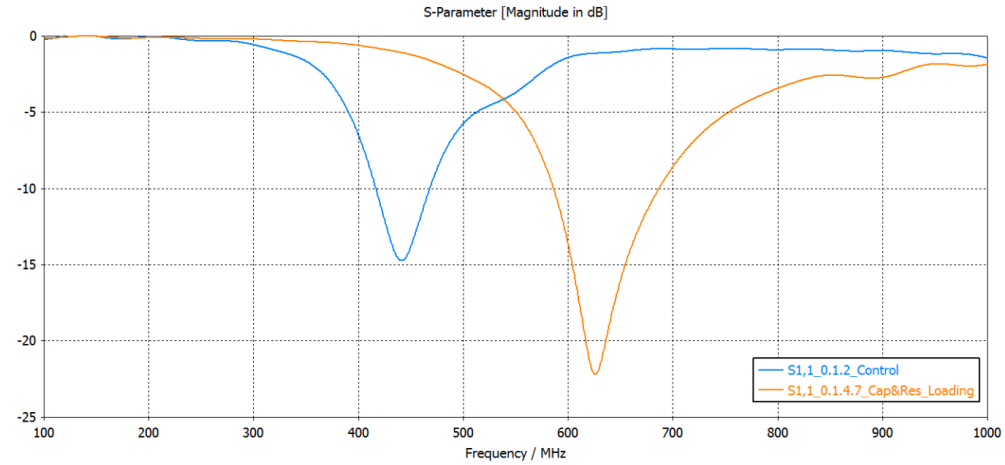

Figure 190 shows the comparison of the S11 for the loaded and unloaded crossed tape spring antenna.

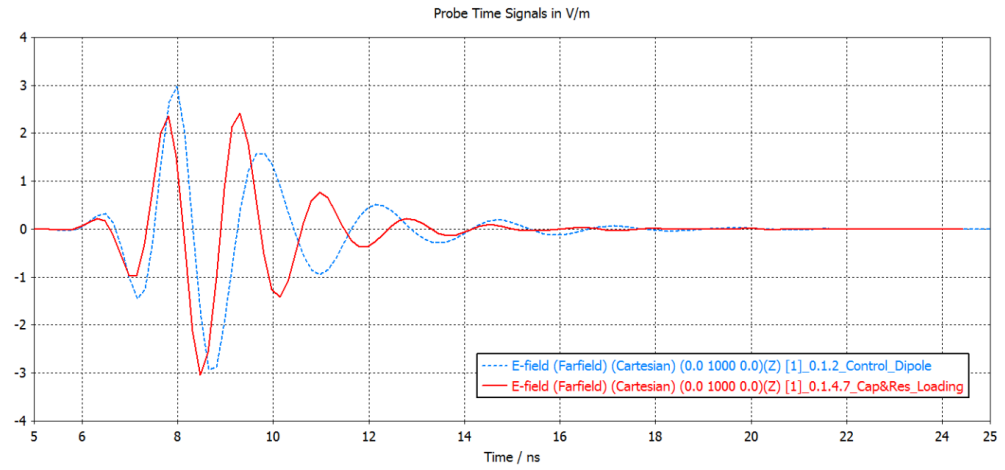

Figure 191 shows the late time ringing comparison of the loaded and unloaded crossed tape spring antenna.

A concern arising from these results is that the loading has electrically shortened the antenna. Mitigating this requires that the antenna arms are lengthened, which is undesirable in terms of mass and volume constrictions. The extra size requirement is small so this may be an effective trade-off if a larger bandwidth is required.

A range of further simulations on this dipole setup were performed. They validated the first slot distance and explored the performance relation to the strip width. (Lestari et al., 2004) states that a smaller slot distance results in reduced discontinuity at the slot positions. However, the absolute value of strip width is not constrained. The simplicity of dipole antenna was used to investigate this property. Multiple factors affect the optimisation of this parameter, which are listed below:

- Increasing the number of slots and strips provides a favourable smoother capacitance and resistance profile along the antenna.
- Increasing the number of slots and strips provides a favourable smoother capacitance and resistance profile along the antenna.
- Reducing the number of slots and strips reduces antenna complexity; minimising manufacture time, project risk and simulation time.
- Reducing the number of slots and strips minimised the shifting of the antenna resonant frequency.

The factors that affect antenna performance directly were found to only have a small impact on the actual antenna properties. Therefore, if the increase in antenna size is accommodated for with the intention of maximising bandwidth, the slot with can be reduced until other factors constraint the design. Such factors may include resolution of lithography manufacture.

A complete practical theory of RC loading implementation is beyond the scope of this thesis and so at this point it was decided to progress to the loading of the crossed Moxon antenna. The information gathered from this model allowed for validation of the concept

as applied to none bow tie antennas and sufficiently constrained the design too permit investment of resources into creating the necessary loaded crossed Moxon CAD models.

2.4) RC Loading of the Modified Crossed Moxon Antenna

In this section the antenna resistive and capacitive loading concept will be applied to the best performing modified version of the crossed Moxon antenna. This version of the antenna will remain constant during all the simulation runs shown here and only the loading features will be altered. This allows a comparative method to be implemented in the analysis and improvement verification process. After a first run loading trail the electrical shortening effect, seen in the previous section, was observed. The antenna, and therefore also the loading pattern, were rescaled until the antenna central frequency matched the required value. The resulting loading patterns can be seen in Figure 193. Due to the nature of the widened crossed Moxon antenna, the resistive profile naturally increases towards the ends of the tapered tips by design. It was therefore theorised that attempting to implement a constant resistive profile would be counterproductive in this case. Hence two loading patterns were generated, and both were simulated to test the theory.

Due to the change of antenna shape from that of a bow tie, to the crossed Moxon, the loading rules must be modified. The slots in the antenna act as microstrip gap capacitors, with their capacitance increasing with gap width (s) and track width (w). The relationship holds so long as $s < w$ which is ensured for the loading pattern. The relationship to gap width is dominant and so just as in (Lestari et al., 2004) the slots will increase in width along the antenna here also to achieve a linearly increasing capacitive profile. The resistive profile however is completely dependent on strip area. Therefore, to create a constant resistive profile, the strip width must increase along the taper to maintain constant strip

area. The result of these loading rules is the profile seen in the top graph of Figure 192 (Antenna Ref. 0.9.0). However, if the above theory is correct an increasing resistive profile would be a better choice. To achieve this, the strip width is simply held constant leading to a reducing strip area. This profile can be seen in the lower graph of Figure 192 (Antenna Ref. 0.7.5). The resistance profile is then a combination of the taper shape and surface resistance from the absorber. As the absorber creates an effective surface resistance per square meter that is inversely proportional to the area of the strip, we observe increasing resistance for decreasing area. We note here however that the conclusions of (Lestari et al., 2003) is that a constant resistive profile should, in general, be theoretically superior.

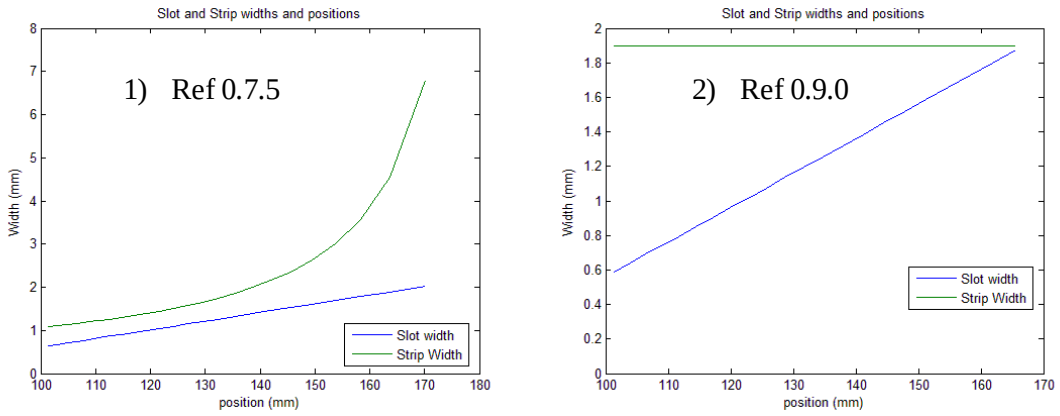

Figure 192 shows the slot-strip profiles for: 1) the constant resistive and Increasing capacitive loading scheme (Ref 0.7.5), 2) the increasing resistive and increasing capacitive loading scheme (0.9.0).

The original loading profile of (Lestari et al., 2004) was simple enough to calculate by hand. Due to the new loading rules for the crossed Moxon and the number of variations to be trailed this was no longer the case. An iterative MATLAB program was created that can automatically generate the slot/strip widths and positions. The program works outward along the antenna calculating the appropriate slot and strip widths based on the distance along the antenna.

Figure 193 shows the resulting antenna CAD model used for the simulation of the constant R, increasing C profile. The profile has also been repeated on the interior arms, beginning

at the same first slot distance from the feed point. In the figure, the green substrate has been removed for the metal sections to make them visible. It would normally cover the upper surface, encasing the antenna elements between itself and the absorber below.

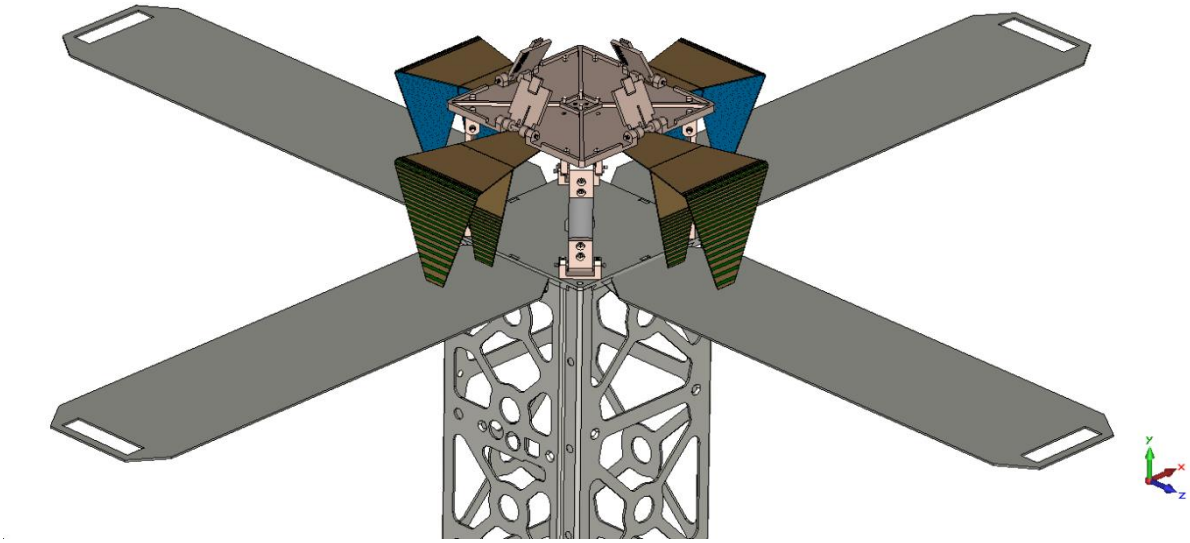

Figure 193 shows the CAD model of the loaded modified crossed Moxon antenna (Ref 0.9.0). The antenna has been modified to include capacitive loading slots and resistive loading volumetric absorber.

The simulation generated the S11 results in seen in Figure 194. Comparing with the control S11 of the unmodified antenna, there is significant alteration. The resonance profile has been significantly changed and no longer appears to display a double lobe characteristic. The bandwidth improvement is minor, increasing by only 6.5% (-10dB).

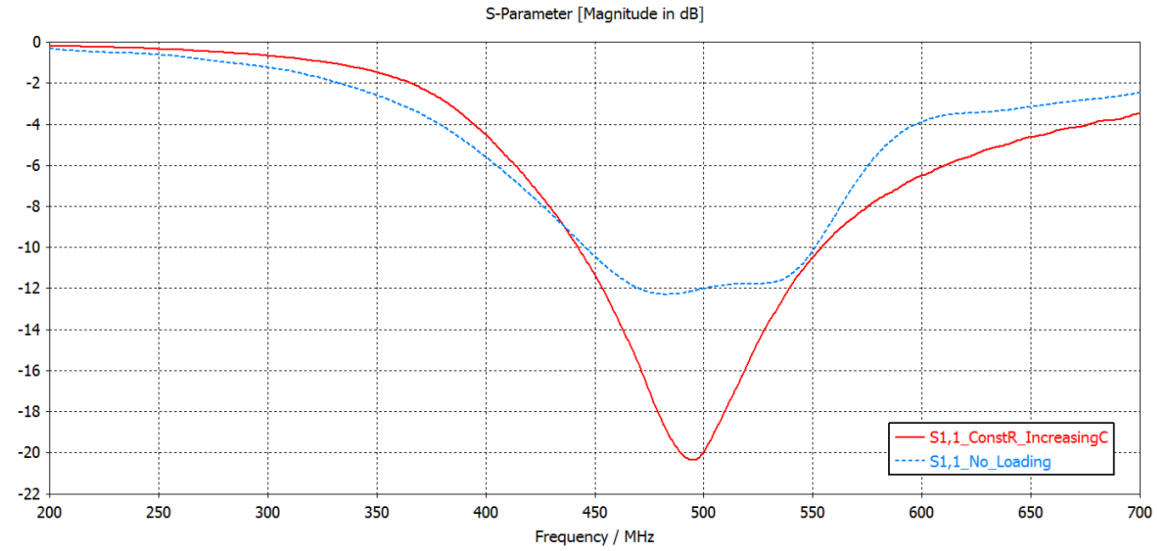

Figure 194 shows the comparison between the S11 of the unloaded antenna and the S11 of the loaded antenna.

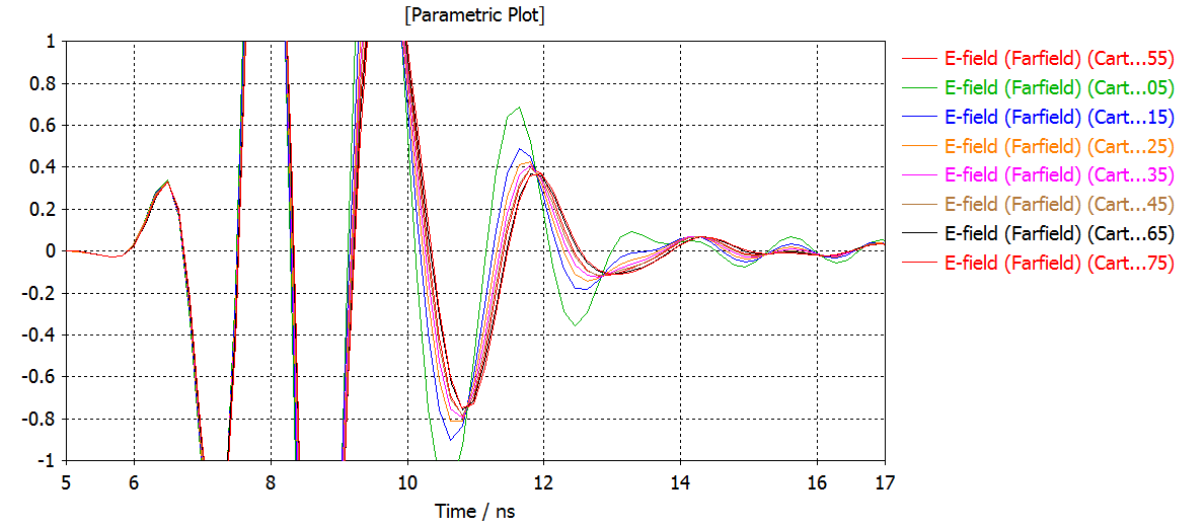

Figure 195 shows the farfield pulse results for a parametric sweep analysis of the absorber thickness. The units of the key are 100ths of a millimetre.

As the approximation for absorber thickness was originally determined via analysis of the tape spring antenna a new parametric sweep was performed at this point to ensure optimal performance. The results however yielded that the 0.35mm thickness was still the optimal choice. Figure 195 shows the pulse waveform of the antenna. Whilst the effect is small, improvement of the late time ringing is clearly observable. At approximately 0.35mm the benefit of absorber thickness plateaus and further absorber material only serves to parasitically absorb radiated energy.

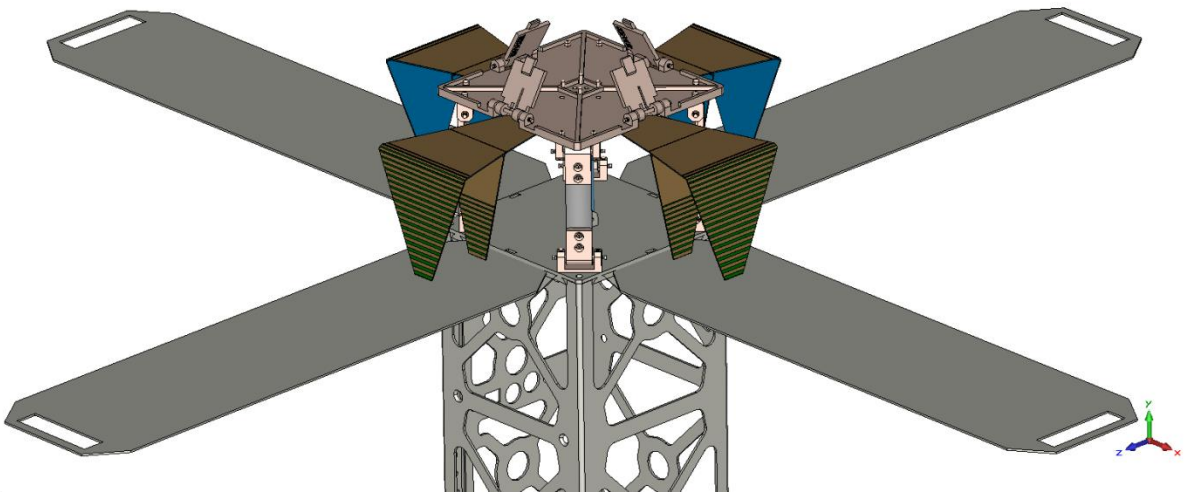

Figure 196 shows the modified crossed Moxon antenna with RC loading applied (Ref 0.7.5). The resistive loading now increases towards the ends of the antenna as the strip width remains constant.

Moving quickly to the competing loading pattern before making any conclusions, Figure 141 shows the model with constant strip widths (Antenna Ref 0.7.5). In Figure 197 the S11 profile is near identical for the two antennas, with only a slight improvement for the new pattern. This is suggestive that the resistive profile has minimal effect in this regime and that the strip widths are not crucial.

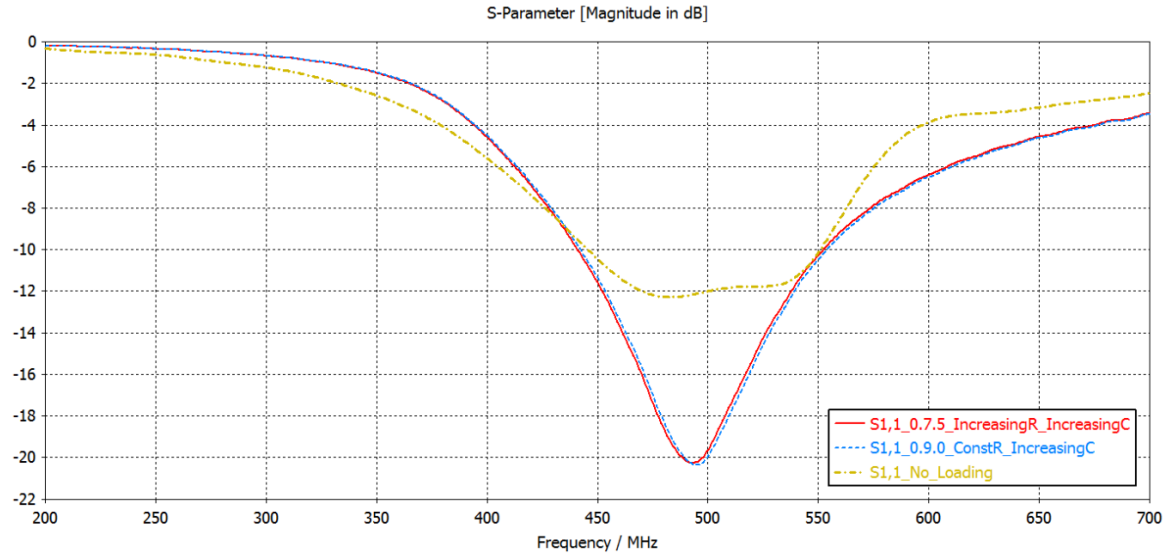

Figure 197 shows the S11 comparison between the loaded crossed Moxon antenna variants and the reference unloaded antenna.

Several further simulations were carried out at this point, to explore the design space. As the process could not be fully automated an optimisation method was not implemented. Both the capacitive and resistive profiles were altered without yielding results that improved upon the 0.7.5 design. The efforts to further improve the antenna bandwidth were concluded here in favour of a full analysis of the 0.7.5 design, for consideration at system level.

Table 8 gives the final properties of the constant strip width, increasing slot width antenna loading pattern design (0.7.5). The bandwidth improvement over the control antenna is 6.6% (-10dB) and the directivity is increased due to a reduction in the main lobe width. However, these benefits are opposed by the reduction in radiation efficiency. With the addition of the volumetric absorber energy is being lost as heat.

Values for 500MHz simulation	**Control antenna**	**Loaded antenna (Ref. 0.7.5 IncR-IncC)**
Radiation efficiency	-0.04842 dB	-2.839 dB
Total efficiency	-3.387 dB	-3.778 dB
Peak Directivity	5.66 dBi	6.03 dBi
Angular Width (3dB)	94.9 deg	91.9 deg
Frequency range (-10dB)	446.5-552.0 MHz (105.5 MHz)	440.5-553.0 MHz (112.5 MHz)

Table 34 details for comparison the antenna properties of the unloaded reference antenna and the increasing R increasing C (Ref 0.7.5) loaded antenna.

Angular beam width given in Table 8 is that for 500MHz. Figure 198 shows the beam pattern cross sections across the full range of operating frequencies. It can be seen that the pattern remains, for the level of detail included in the model, consistent across these frequencies. The beam width varies by only 2.7^0 which is well within the requirements.

Even if the variation for a real antenna is many times larger the beam width requirement, of 60°, will be satisfied.

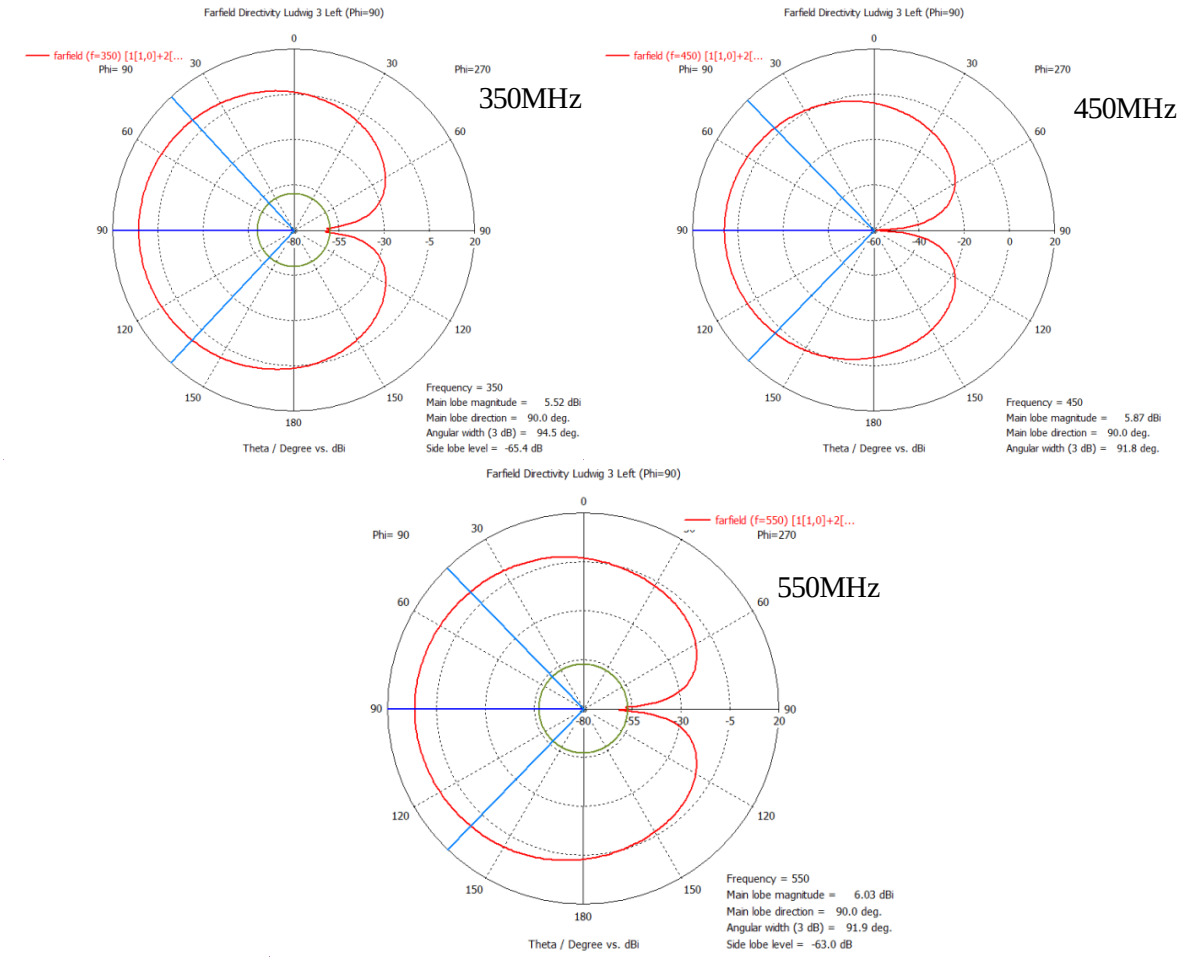

Figure 198 shows the farfield beam patterns for the Const R - Inc C (0.7.5) loaded crossed Moxon antenna version. As can be seen the beam pattern is stable over the required frequencies.

One of the primary drivers for attempting RC loading was the reduction of late time ringing in the antenna. Figure 199 shows the antenna dispersion and the improvement of the pulse characteristics of the loaded vs the unloaded antenna. From this graph, we can analysis the dispersive properties of the two antennas, based on the method of (Schantz, 2004). To generate this data a pulse was supplied to the antenna in the simulation. A field probe was placed in the model, at 1m, directly in front of the antenna. This allows the radiated pulse to be recorded. Ideally this would be recorded at a true farfield distance of $> 5\lambda$. However, due to the simulation setup this would have unavoidably increased the

number of mesh cells (greatly increasing simulation time). After experimentation, it was found that for this situation the field probe gave near identical results at this distance, so the run time impact could be minimised over the number of simulations performed.

The output waveform matches closely the input Gaussian pulse (Green) to the antenna output, where this input pulse is that supplied to a single antenna element (1/4 magnitude). As predicted by (Lestari et al., 2003) and (Lestari et al., 2004), the radiated pulse from the loaded antenna has an amplitude that is increased over that of the unloaded antenna. This shows that the first slot distance has been implemented correctly for the modified crossed Moxon antenna shape and is successfully achieving constructive interference of the energy radiated from the feed point and first slot.

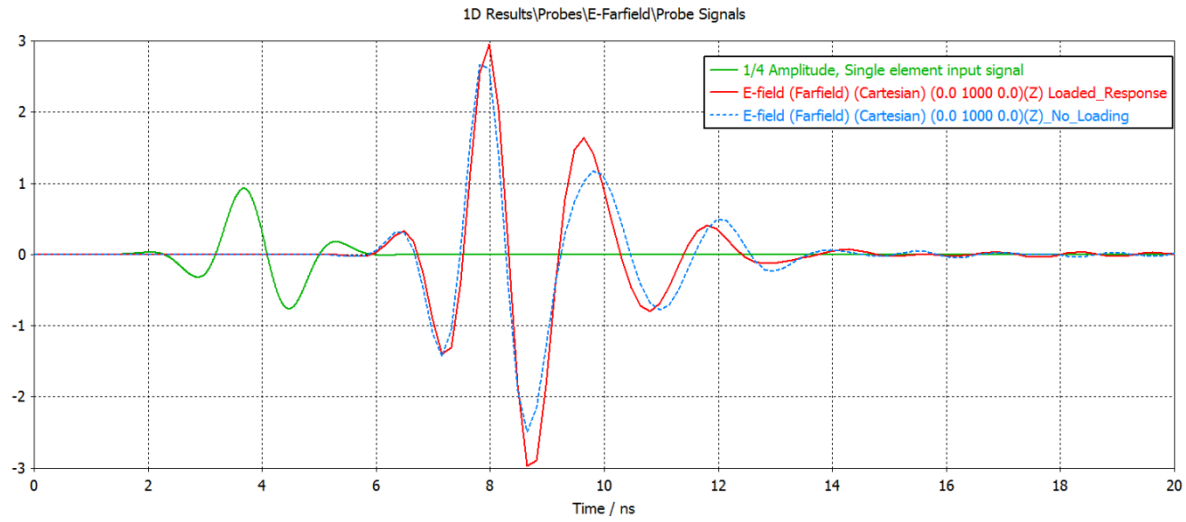

Figure 199 shows the Const R - Inc C (0.7.5) loaded crossed Moxon antenna pulse characteristics compared to an unloaded antenna.

There is still observable ringing in the antenna, but this is greatly reduced, for both antennas, over the earlier results in this chapter for the original crossed Moxon (Figure 122). The dispersion spreading is well within the 0.020µs requirement for both antennas, at ~0.003µs for the loaded antenna and ~0.004µs for the unloaded antenna. The most likely theory to explain these results is that the reflection from the end of the WCM is already

uncoherent and so whilst the capacitive and resistive loading does prevent energy from being reflected into the antenna feed, the potential for further significant improvement antenna properties is limited. A bow tie antenna has a very sharp discontinuity at the end that provides a coherent reflection. However, there are two factors that mean this is not the case for the WCM: the taper constantly partially reflects the waves along its length due to the changing resistive impedance; the capacitance between the antenna tip and the ground plane reduces the reflections coherence. So the end reflection, which is primarily targeted by RC loading is already minimised, given the input impedance dependence on the primary antenna length. Widening the taper would, by this theory, improve the antenna properties in a much more significant way and has indeed been shown to do so in previous sections. This realisation therefore concludes our attempts to optimise the late time ringing through RC loading.

To conclude an investigation of the currents within the antenna was performed in order to ensure that that antenna is performing as expected. Based on the previous results and conclusions of this chapter, it should be expected that:

1. Current is distributed throughout the entire antenna length (Slots do not cause complete reflection of the signal), but does diminish towards the tips, as the signal is continuously reflected along the length.

2. Current is distributed across the full width of each antenna elements. The exact distribution not being predicted here, but potentially diminishing towards the centre based on the (Lestari et al., 2003).

3. Current is distributed to the inner arm.

4. Current smoothly transitions from the feed to the antenna without an impedance mismatch.

5. The mechanism for circular polarisation is apparent (as opposed to the antenna merely radiating in two orthogonal polarisation axes).

6. No obvious discontinuities based on simulation errors.

Determination of the current distribution is a key part of the time domain simulation method. The data is not normally recorded however, due to its quantity, and so a specialised simulation run was performed. The results for the current distribution, over 6 equispaced phases in one half wave cycle, are presented in Figure 200 and Figure 201. It is readily apparent that points 2, 3, 4 and 6 are satisfied. Point 2 suggesting that future work may find a benefit to including a slit in the centre of each element.

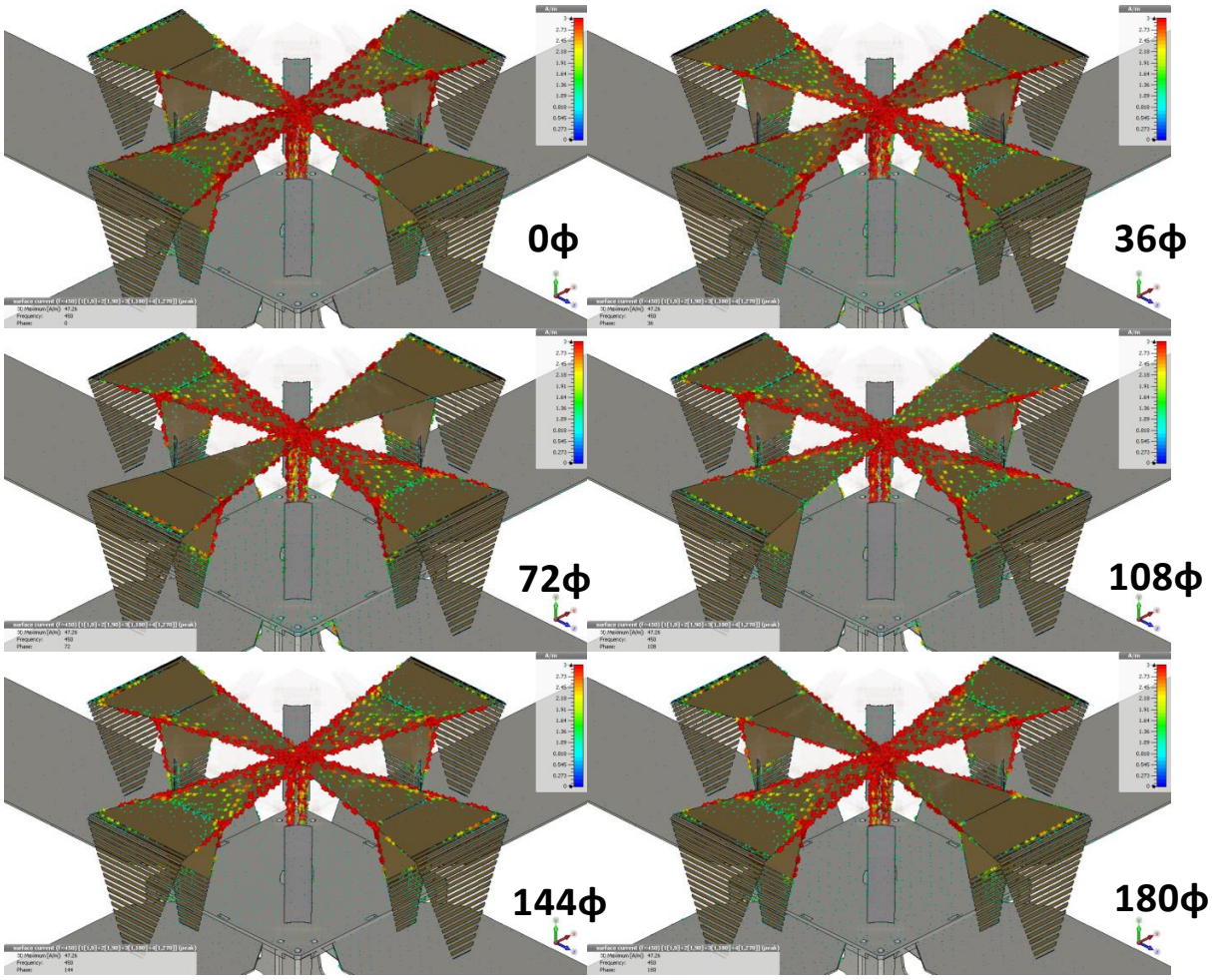

Figure 200 shows the antenna (Ref 0.7.5) current distribution across half of the phase cycle. The current range displayed is limited to 3A/m in order to maintain contrast.

Whilst determining the exact distribution of the current along the length of the antenna fell beyond the scope of this work, point one can be accepted based on detailed observations of the current magnitude in the strips of each element. The nature of the loading pattern does create a not insignificant discontinuity at the first slot location. It is proposed that this is the primary reason for the central frequency shift, but it cannot be avoided for this antenna format. The loading changes the effective length of the antenna by changing the properties of the tapered end of the antenna elements. It, therefore, also modifies the operating principle of the antenna, reducing the capacitive effect of the ground plane. The S11 characteristics change rather than directly building on the base antenna operating mechanisms.

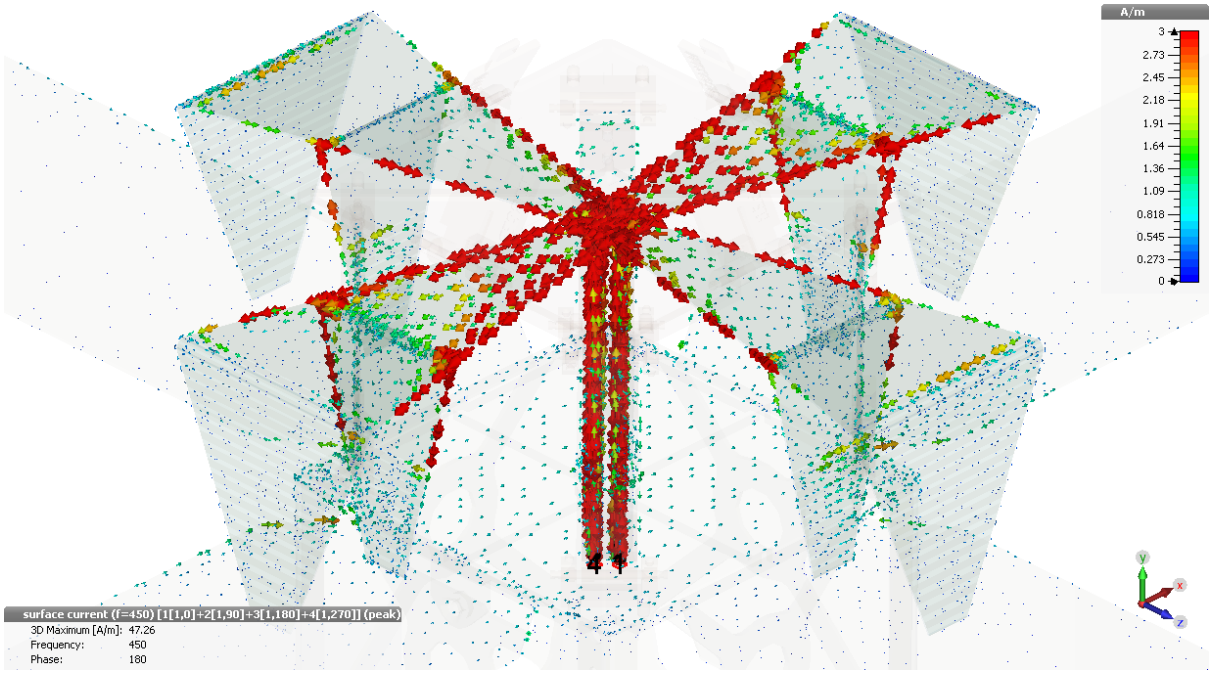

Figure 201 shows the unobscured current distribution in the final loaded (Ref 0.7.5) WCM antenna. The current range displayed is limited to 3A/m in order to maintain contrast.

An insight provided by the analysis of the current distribution is that of the mechanism by which the antenna radiates circularly polarised waves. Consider an infinite number, of infinitely narrow, radiating element pairs arranged in a circular formation, each fed sequentially in phase. In a simplified model this would yield an ideal circular polarisation profile. For two orthogonal pairs, as with the crossed Moxon, the circular polarisation profile would be a diamond shape in this simplified view. However, each pair of elements does not radiate independently of the other and there is an induced cross interaction. As the current grows or diminishes in one element this drives a current in the near side neighbouring element, as the elements are of extended width. The effect is to smooth the effective rotation of the current flow axis, around the antenna. The animation feature in CST makes the effect more apparent than the still pictures in Figure 200, but the uneven current distribution can still be observed in the images for 36,72,108 and 144 degrees of phase. This effect smooths the polarisation profile, leading to a larger RHC component than would be expected for the number of implemented elements.

In conclusion the constant strip width, linearly increasing slot width, loaded WCM antenna (Ref 0.7.5) was found to be the optimal loaded design based on simulation results. The loading pattern generated benefits to the antenna dispersion and bandwidth properties but at the cost of added complexity and radiative losses. The antenna size also had to be rescaled to account for the shift in central frequency. The operating principles of the antenna were changed significantly more than expected by the loading pattern and so a systems level analysis is required to determine if this antenna variant is most suitable for the mission.

10) REFERENCES

3M. (2009). AB7000HF Series EMI Absorber Data sheet.

Anderson, D., & Fuller-Rowell, T. (1999). *The Ionosphere*. Space Environment Centre - Boulder, CO (325 Broadway, Boulder 80303-3326).

Angling, M. J., Cannon, P. S., & Bradley, P. (2007). Ionospheric propagation. In *Propagation of Radio Waves (2nd Edition)* (pp. 199–233). https://doi.org/10.1049/PBEW056E_ch12IET Digital Library

Angling, M. J., Cannon, P. S., Davies, N. C., Willink, T. J., Jodalen, V., Lundborg, B., … Willink, J. (1998). Measurements of Doppler and multipath spread on oblique high-latitude HF paths and their use in characterizing data modem performance. *Radio Science*, *33*(1), 97–107.

Angling, M. J., Cruise, A. M., Hoyland, D. H., Harkness, P., & Drysdale, T. (2012). *Wideband Ionospheric Sounder Cubesat Experiment (WISCER): Initial design study*. Poynting Institute, University of Birmingham.

Angling, M. J., Harkness, P., & Drysdale, T. (2012). The Wideband Ionospheric Sounder Cubesat Experiment. In *European Space Weather Week*. Brussels, Belgium.

Angling, M. J., Hoyland, D. M., Cannon, P. S., Harkness, P., Mcrobb, M., Vasile, M., & Sinn, T. (2013). *Wideband Ionospheric Sounder Cubesat Experiment (WISCER): Phase II study*.

Babuscia, A., Corbin, B., Knapp, M., Jensen-Clem, R., Van De Loo, M., & Seager, S. (2013). Inflatable antenna for cubesats: Motivation for development and antenna design. *Acta Astronautica*, *91*, 322–332. https://doi.org/10.1016/j.actaastro.2013.06.005

Babuscia, A., Van de Loo, M., Wei, Q. J., Pan, S., Mohan, S., & Seager, S. (2014). Inflatable Antenna for CubeSat: Fabrication, Deployment and Results of Experimental Tests. *2014 IEEE Aerospace Conference*. https://doi.org/10.1109/AERO.2014.7024296

Banks, B. A., De Groh, K. K., Miller, S. K., & Waters, D. L. (2009). Lessons learned from atomic

oxygen interaction with spacecraft materials in low earth orbit. In *AIP Conference Proceedings* (Vol. 1087, pp. 312–325). https://doi.org/10.1063/1.3076845

Bernasconi, M. C. (2002). Flexible-wall expandable structures for space applications: forty years of trying. In *1st European Workshop on Inflatable Space Structures* (pp. 21–22). Noordwijk, The Netherlands.

Bilitza, D., & Papitashvili, N. (2015). DGRF/IGRF Geomagnetic Field Model 1900 - 2020 and Related Parameters. Retrieved July 27, 2017, from https://cohoweb.gsfc.nasa.gov/vitmo/igrf_vitmo.html

Bilitza, D., Rawer, K., Bossey, L., & Gulyeava, T. (1993). International reference ionosphere — past, present, and future: I. Electron density. *Advances in Space Research*, *13*(3), 3–13.

Bruzzi, S., Louet, J., & Pfeiffer, B. (1995). Envisat-1 system and mission. *Space Technology*, *15*(3), 145–155. https://doi.org/10.1016/0892-9270(95)00024-Y

Cannon, P. S., Groves, K., Fraser, D. J., Donnelly, W. J., & Perrier, K. (2006). Signal distortion on VHF/UHF transionospheric paths: First results from the Wideband Ionospheric Distortion Experiment. *Radio Science*, *41*(RS5S40). https://doi.org/doi:10.1029/2005RS003369

Chamberlain, J. W., & Hunten, D. M. (1987). *Theory of Planetary Atmospheres* (1st ed.). International Geophysics, Academic Press.

Chu, L. J. (1948). Physical limitations of omni-directional antennas. *Journal of Applied Physics*, *19*(12), 1163–1175. https://doi.org/10.1063/1.1715038

ClydeSpace. (2018a). Aerodynamic End of Life Deorbit System for CubeSats. Retrieved March 22, 2018, from https://www.clyde.space/products/59-aerodynamic-end-of-life-deorbit-system-for-cubesats

ClydeSpace. (2018b). Products - Spacecraft Engineering. Retrieved March 21, 2018, from https://www.clyde.space/products/76-triple-deployable-solar-panels

Collin, R. E., & Rothschild, S. (1964). Evaluation of Antenna Q. *IEEE Transactions on Antennas and Propagation*, *12*(1), 23–27. https://doi.org/10.1109/TAP.1964.1138151

Córdoba, S. S. F. de. (ICARE P. (2013). 100km Altitude Boundary for Astronautics. Retrieved July 27, 2017, from http://www.fai.org/icare-records/100km-altitude-boundary-for-astronautics

CubeSat Shop. (2018). Cube ADCS - CubeSat Shop. Retrieved March 21, 2018, from https://www.cubesatshop.com/product/cube-adcs/

Davis, M. E. (2009). Developments In Foliage Penetration Radar. In *Radar Conference - Surveillance for a safer world, 2009. RADAR. International* (pp. 1–6).

Di Paolo, F. (2000). *Networks and devices using planar transmission lines*.

Dikarev, V., Grün, E., Landgraf, M., & Jehn, R. (2005). Update of the ESA meteoroid model. In *European Space Agency, (Special Publication) ESA SP* (pp. 271–276). https://doi.org/10.1016/j.asr.2005.05.014

Drinkwater, M. R., Haagmans, R., Muzi, D., Popescu, A., Floberghagen, R., Kern, M., & Fehringer, M. (2007). The GOCE gravity mission: ESA'S first core earth explorer. *European Space Agency, (Special Publication) ESA SP*, (SP-627), 1–7. https://doi.org/ISBN 92-9092-938-3

Dyson, J. (1965). The characteristics and design of the conical log-spiral antenna. *Antennas and Propagation, IEEE Transactions On*, *13*(4), 488–499. https://doi.org/10.1109/tap.1965.1138471

Freeland, R. B. (1998). Inflatable deployable space structures technology summary. In *49th International Astronautical Congress*. Melbourne, Australia.

Goode, P. R., Qiu, J., Yurchyshyn, V., & Hickey, J. (2001). Earthshine Observations of the Earth's Reflectance. *Geophysical Research Letters*, *28*(9), 1671–1674.

Groves, K. M., Basu, S., Weber, E. J., Smitham, M., Kuenzler, H., Valladares, C. E., … Kendra, M. J. (1997). Equatorial scintillation and systems support. *Radio Sci*, *32*, 2047–2064.

Grün, E., Zook, H. A., Fechtig, H., & Giese, R. H. (1985). Collisional balance of the meteoritic complex. *ICARUS*, *62*(2), 244–272.

Guo, Y., & Shi, X. (2006). Improved Resistive Loading Profile for Ground-Penetrating Radar Antenna Applications. *2006 CIE International Conference on Radar*, (2), 543–546. https://doi.org/10.1109/ICR.2006.343219

Harrington, R. F. (1960). Effect of antenna size on gain, bandwidth, and efficiency. *Journal of Research of the National Bureau of Standards, Section D: Radio Propagation*, *64D*(1), 1. https://doi.org/10.6028/jres.064D.003

Hertel, T. W., & Smith, G. S. (2002). Analysis and design of two-arm conical spiral antennas. *IEEE Transactions on Electromagnetic Compatibility*, *44*(1), 25–37.

Hertel, T. W., & Smith, G. S. (2003). On the Dispersive Properties of the Conical Spiral Antenna and Its Use for Pulsed Radiation. *IEEE Trans. Ant. Prop.*, *51*(7).

Heynderickx, D., Quaghebeur, B., Wera, J., Daly, E. J., & Evans, H. D. R. (2004). New radiation environment and effects models in the European Space Agency's Space Environment Information System (SPENVIS). *Space Weather - the International Journal of Research and Applications*, *2*(10), 2–5. https://doi.org/10.1029/2004SW000073

Huang, Y., & Boyle, K. (2008). *Antennas: From theory to practice*. Wiley.

Hunt, G. W., & Ario, I. (2005). Twist buckling and the foldable cylinder: An exercise in origami. *International Journal of Non-Linear Mechanics*, *40*(6), 833–843. https://doi.org/10.1016/j.ijnonlinmec.2004.08.011

Ishida, S., Nojima, T., & Hagiwara, I. (2014). Mathematical Approach to Model Foldable Conical Structures Using Conformal Mapping. *Journal of Mechanical Design*, *136*(9).

ITU-R. (2007). *Ionospheric propagation data and prediction methods required for the design of satellite services and systems*. Geneva.

Janson, S. W., & Welle, R. P. (2013). The NASA Optical Communication and Sensor Demonstration Program. *27th Annual AIAA/USU Conference on Small Satellites*, 1–10.

JAXA, & EORC. (2006). ALOS Project. Retrieved August 26, 2016, from http://www.eorc.jaxa.jp/ALOS/en/about/about_index.htm

Kallenrode, M. (2004). *Space Physics: An Introduction to Plasmas and Particles in the Heliosphere and Magnetospheres*. *Space physics : an introduction to plasmas and particles in the heliosphere and magnetospheres, 3rd, enlarged ed., by May-Britt Kallenrode.~Advanced texts in physics.~Berlin: Springer, 2004*. https://doi.org/10.1007/978-3-662-04443-8

Kanda, M. (1983). Time Domain Sensors for Radiated Impulsive Measurements. *IEEE Transactions on Antennas and Propagation*.

Kirkby, G., Tester, B., Angling, M., McCallum, M., Jackson, C., Lund, A. G., … Lima, A. G. (2015). Strain-Rigidised Wideband Conical Helix Antenna for CubeSat Deployment. In *International Astronautical Congress*.

Klopfenstein, R. W. (1956). A Transmission line taper of improved design. *Proceedings of the IRE*, 31–35.

Knipp, D. (2011). *Understanding space weather and the physics behind it*.

Kopp, G., & Lean, J. L. (2011). A new, lower value of total solar irradiance: Evidence and climate significance. *Geophysical Research Letters*, *38*(1), n/a-n/a. https://doi.org/10.1029/2010GL045777

Kraus, J. D. (1988). *Antennas. McGraw Hill*. Retrieved from http://www.sciencemag.org/cgi/doi/10.1126/science.113.2927.131

Lestari, A. A., Yarovoy, A. G., & Ligthart, L. P. (2003). Analysis of RC loading profiles for

antenna bandwidth improvement. *IEEE Antennas and Propagation Society International Symposium. Digest. Held in Conjunction with: USNC/CNC/URSI North American Radio Sci. Meeting (Cat. No.03CH37450)*, *3*, 632–635. https://doi.org/10.1109/APS.2003.1219927

Lestari, A. A., Yarovoy, A. G., & Ligthart, L. P. (2004). RC -Loaded Bow-Tie Antenna for Improved Pulse Radiation. *IEEE Transactions on Antennas and Propagation*, *52*(10), 2555–2563.

Li, J., Post, M., Wright, T., & Lee, R. (2013). Design of attitude control systems for CubeSat-class nanosatellite. *Journal of Control Science and Engineering*, *2013*. https://doi.org/10.1155/2013/657182

Maessen, D., van Breukelen, E., Zandbergen, B. T. C., & Bergsma, O. K. (2007). Development of a generic inflatable de-orbit device for CubeSats. In *Proceedings of the 58th International Astronnautical Congress* (pp. 1–11). Retrieved from http://lr.tudelft.nl/fileadmin/Faculteit/LR/Organisatie/Afdelingen_en_Leerstoelen/Afdeling_SpE/Space_Systems_Eng./Expertise_areas/Space_propulsion/Research/Thermal_thrusters/doc/Presentation.pdf

Mannix, C. (2016). Measuring and modelling the impact of the ionosphere on space based synthetic aperture radars. *Thesis*, (July), Page 207. https://doi.org/10.1016/0197-3975(91)90016-E

Mannix, C. R., Belcher, D. P., & Cannon, P. S. (2014). Estimating the impact of the ionosphere on space-based SAR autofocus using GPS signals. In *2014 XXXIth URSI General Assembly and Scientific Symposium (URSI GASS)* (pp. 1–4).

Mannix, C. R., Belcher, D. P., Cannon, P. S., & Angling, M. . (2016). Using GNSS signals as a proxy for SAR signals: Correcting ionospheric defocusing. *Radio Science*, *51*, 60–70. https://doi.org/10.1002/2015SRS005822

McLean, J. S. (1996). A re-examination of the fundamental limits on the radiation q of electrically

small antennas. *IEEE Transactions on Antennas and Propagation*, *44*(5), 672–676. https://doi.org/10.1109/8.496253

Mini-Circuits. (2018). *Application note on transformers*. Retrieved from https://ww2.minicircuits.com/app/AN20-002.pdf

Montoya, T. P., Member, S., & Smith, G. S. (1996). A Study of Pulse Radiation from Several Broad-Band Loaded Monopoles. *IEEE Transactions on Antennas and Propagation*, *44*(8).

Moxon, L. A. (1993). *HF Antennas for All Locations* (1st Editio). Radio Society of Great Britain.

Munakata, R. (2009). Cubesat design specification rev. 13. *The CubeSat Program, California Polytechnic State*, *8651*, 22. Retrieved from http://www.cubesat.org/images/developers/cds_rev12.pdf

Nava, B., Coisson, P., & Radicella, S. (2008). A new version of the NeQuick ionosphere electron density model. *Journal of Atmos. and Solar-Terr. Physics*. https://doi.org/10.1016/j.jatsp.2008.01.015

NOAA. (2019). Ionospheric Scintillation. Retrieved February 2, 2019, from https://www.swpc.noaa.gov/phenomena/ionosphere-scintillation

Olson, G., Pellegrino, S., & Costantine, J. (2012). Structural Architectures for a Deployable Wideband UHF Antenna. *Pellegrino.Caltech.Edu*, *50*, 1–10. https://doi.org/10.2514/6.2013-1671

Pillai, S. U., Li, K. Y., & Himed, B. (2008). *Space Based Radar - Theory & Applications*. McGraw Hill.

Quegan et al, S. (2012). *Report for mission selection: CoReH2O* (Vol. ESA SP-132).

Rao, B., Ferris, J., & Zimmerman, W. (1969). Broadband Characteristics of Cylindrical Antennas with Exponentially Tapered Capacitive Loading. *IEEE Transactions on Antennas and Propagation*, *17*(2), 145–151.

Reddy, M. R. (1995). Effect of low earth orbit atomic oxygen on spacecraft materials. *Journal of Materials Science*, *30*(2), 281–307.

Sakovsky, M., Maqueda, I., Karl, C., & Pellegrino, S. (2015). Dual-Matrix Composite Wideband Antenna Structures for CubeSats. In *2nd AIAA Spacecraft Structures Conference* (pp. 1–27). American Institute of Aeronautics and Astronautics.

Saunders, R. S., & Pettengill, G. H. (1991). Magellan: Mission Summary. *Science*, *252*(5003), 247–249.

Schantz, H. G. (2004). Dispersion and UWB antennas. *2004 International Workshop on Ultra Wideband Systems Joint with Conference on Ultra Wideband Systems and Technologies. Joint UWBST & IWUWBS 2004 (IEEE Cat. No.04EX812)*, 161–165. https://doi.org/10.1109/UWBST.2004.1320956

Schenk, M., Viquerat, A. D., Seffen, K. a., & Guest, S. D. (2014). Review of Inflatable Booms for Deployable Space Structures: Packing and Rigidization. *Journal of Spacecraft and Rockets*, *51*(3), 762–778. https://doi.org/10.2514/1.A32598

Schwering, F. (1976). Workshop on electrically small antennas: Background and purpose. In *Proceedings of the ECOM-ARO Workshop on Electrically Small Antennas*. Fort Monmouth, NJ.

Shlager, K. L., Member, S., Smith, G. S., & Maloney, J. G. (1994). Optimization of Bow-Tie Antennas for Pulse Radiation, *42*(7).

Solar Sailors. (2013). *Solar Sailors - SED V5*. Germany.

Stimson, G. W., & Griffiths, H. (2014). *Introduction to Airborne Radar*. (C. Baker & D. Adamy, Eds.) (3rd Editio). SciTech - IET.

Swartwout, M. (Saint L. U. (2017). Cubesat Database. Retrieved from https://sites.google.com/a/slu.edu/swartwout/home/cubesat-database

Tekin, I., Manzhura, O., & Niver, E. (2011). Broadband circularly polarized antennas for UHF

SATCOM 2 . Prototype Antenna topologies, 9–12.

Thurn, A., Huynh, S., Koss, S., Oppenheimer, P., Butcher, S., Schlater, J., & Hagan, P. (2012). A Nichrome Burn Wire Release Mechanism for CubeSats. In *41st Aerospace Mechanisms Symposium*.

Turner, S. (2018). Dipole Current Voltage. Retrieved March 23, 2018, from http://blog.hamradioschool.com/wp-content/uploads/2014/03/dipole_current_voltage.png

Viquerat, A., Schenk, M., Sanders, B., & Lappas, V. (2014). Inflatable Rigidisable Mast For End-Of-Life Deorbiting System. *European Conference on Spacecraft Structures, Materials and Environmental Testing (SSMET)*, 1–10.

Wheeler, H. a. (1947). Fundamental Limitations of Small Antennas. *Proceedings of the IRE*, *35*(12), 1479–1484. https://doi.org/10.1109/JRPROC.1947.226199

Wu, T. T., & King, R. W. P. (1965). The Cylindrical Antenna with Nonreflecting Resistive Loading. *IEEE Transactions on Antennas and Propagation*, *13*(3), 369–373.

Xu, Z.-W., Wu, J., & Wu, Z.-S. (2004). A survey of ionospheric effects on space based radar. *Waves in Random Media*, *14*, S189–S273.